Shock and Vibration

Automated Operational Modal Analysis and its Applications in Structural Health Monitoring

Special Issue Editor in Chief: Carlo Rainieri
Guest Editors: Filipe Magalhaes and Filippo Ubertini

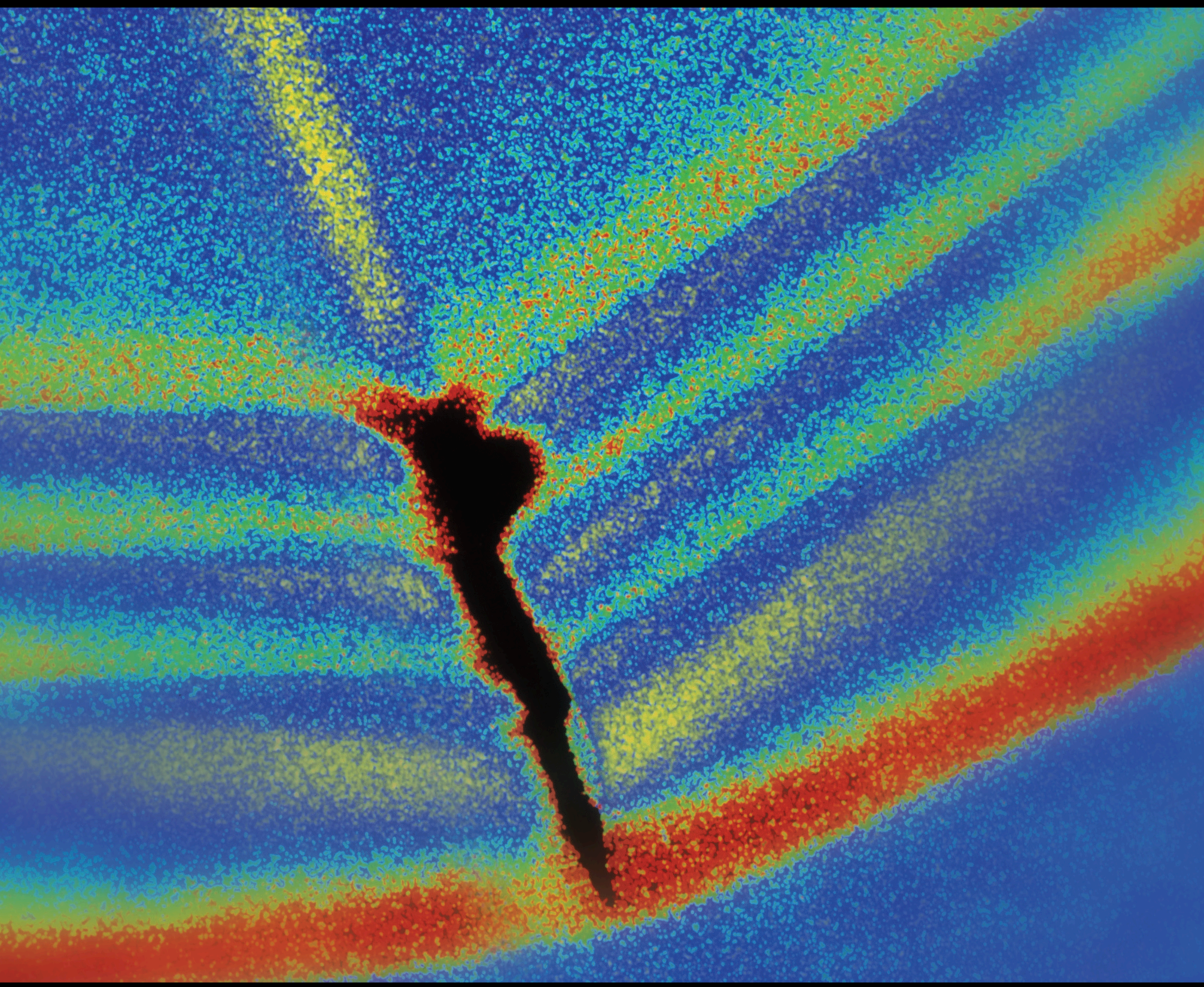

Automated Operational Modal Analysis and its Applications in Structural Health Monitoring

Shock and Vibration

Automated Operational Modal Analysis and its Applications in Structural Health Monitoring

Special Issue Editor in Chief: Carlo Rainieri
Guest Editors: Filipe Magalhaes and Filippo Ubertini

Contents

Hindawi
Shock and Vibration
Volume 2019, Article ID 5497065, 3 pages
https://doi.org/10.1155/2019/5497065

Editorial

Automated Operational Modal Analysis and Its Applications in Structural Health Monitoring

Carlo Rainieri,[1] **Filipe Magalhaes**,[2] **and Filippo Ubertini**[3]

[1]*University of Molise, Campobasso, Italy*
[2]*University of Porto, Porto, Portugal*
[3]*University of Perugia, Perugia, Italy*

Correspondence should be addressed to Carlo Rainieri; carlo.rainieri@unimol.it

Received 20 August 2019; Accepted 23 August 2019; Published 6 November 2019

Research in operational modal analysis (OMA) and its applications in structural health monitoring (SHM) have experienced significant efforts in the last decade. The development of methods able to provide, eventually in a fully automated way, accurate estimates of the modal parameters from structural response only measurements opened new applicative perspectives in the field of structural condition assessment. In fact, while visual inspections, typically in combination with destructive and nondestructive investigations on selected portions of the structure, and scheduled maintenance are the conventional approaches to damage detection and management, the local nature of tests, the subjectivity of the expert judgment, and the costs and very limited frequency of inspections have solicited strong research efforts to change the paradigm, leading to the development of innovative structural health monitoring strategies relying on the analysis of the global, continuously measured, response of the structure. Among the developed approaches, modal-based damage detection is probably one of the most popular for SHM of civil structures. The recent developments in the field of OMA, including in particular several robust automated OMA algorithms, make modal-based SHM an attractive and fairly mature technology. However, in spite of the significant advantages and proved effectiveness of the technique, limitations to its extensive application still come from the accuracy and reliability of the (automated) OMA results, which can affect the damage-detection performance. Moreover, extending the potentialities of the technique to deal with time-varying structures or to support the setting and refinement of numerical models is also a significant research challenge.

This special issue collects five original research contributions that present recent advances in OMA as well as important applications in the context of SHM. In particular, the papers address the following relevant research issues: improving the quality of estimates, dealing with non-stationarities and/or time-varying systems, on-line identification of modal parameters from strong motion records, enhancing FE models by reducing epistemic uncertainties. The collection of papers focused on different aspects and applications of OMA clearly remarks that, even if the technology is mature for applications, several aspects can still be improved, and they are worthy of additional research efforts. It is the hope of the editors that this special issue will contribute to the development of the discipline and the enhancement of its already promising applicative perspectives in SHM.

The paper by B. Zhou et al., entitled "The tunnel structural mode frequency characteristics identification and analysis based on a modified Stochastic Subspace Identification method," deals with a challenging modal-identification problem, that is the modal identification of underground tunnels based on processing of ambient responses as well as of hammer test records. The challenging nature of the investigated problem is related to the coupling between structural and soil vibrations and to the need of selecting the appropriate eigenproperties for condition monitoring. The topic is highly relevant in view of continuous SHM applications of underground tunnels to detect faults, damages, and the effects of nearby soil excavations. To effectively identify the fundamental natural frequencies of underground tunnels, a combined method based on the

natural excitation technique (NExT) and the stochastic subspace identification (SSI) method is proposed. After the introduction, the paper presents the mathematical formulation of the new proposed identification method. Afterwards, the efficacy of the method is demonstrated in application to real data acquired on a concrete power tunnel having a 3.2 m external diameter and on a subway tunnel where each ring is made of six different concrete segments resulting in an external diameter of 6.2 m. The proposed NExT-SSI method results in quite clear stabilization diagrams, whereby the same stabilization diagrams based on covariance-driven SSI (SSI-COV) are quite poor and fail to provide evidence of eigenfrequency stability with increasing model order. The paper ends with an elegant model-based validation using dispersion analysis based on the so-called pipe-in-pipe analytical model, where dispersion analysis is the analysis of the relationship between wave number and frequencies of propagating waves. The results demonstrate that the first natural frequency of the underground tunnels can be effectively identified by the proposed method, although daytime traffic may lead to wrong estimates. Hammer test also allows higher-order modal identification with good consistency against dispersion analysis, and its use is therefore recommended for providing additional information for condition assessment.

The paper by F. Liu et al., entitled "An introduction of a robust OMA method: CoS-SSI and its performance evaluation through the simulation and a case study," addresses the challenge of nonstationarity. Most of the OMA techniques have been developed under the assumption of linear and stationary system. However, the monitoring data are often nonstationary, as shown in the paper for the cases of platforms under wave excitations, and bridges under time-varying traffic loading. As a result of nonstationarity, the identified modal parameters might be unreliable, or part of the modes could be missed. An improved OMA method based on SSI is therefore proposed to analyze the dynamic response of nonstationary systems. The proposed method is denoted as correlation signal subset-based SSI (CoS-SSI) as it divides correlation signals from the system responses into several subsets based on their magnitudes; then, the average correlation signals with respect to each subset are used as the inputs of the SSI method. The performance of CoS-SSI has been evaluated first against simulated data, considering also different levels of noise, and it has been validated afterwards through an experimental study. Both simulation analysis and the experimental results remark the promising performance of CoS-SSI method in dealing with nonstationary systems and noisy signals, thus overcoming some inherent limitations of the traditional SSI-COV as well as of the average correlation signal based SSI (ACS-SSI) method, which is another variant of the SSI method specifically developed to deal with nonstationary data. The CoS-SSI method seems to be able to provide more accurate and reliable modal identification results with respect to the latter reference methods, thus resulting in a promising solution for reliable SHM.

The paper by H. Jin et al., entitled "Modal Parameters Identification Method Based on Symplectic Geometry Model Decomposition," proposes a novel method for operational modal analysis with the ability to identify the modal parameters of time-invariant structures and also track the evolution of the dominant frequencies of time-variant systems. This is achieved with the use of symplectic geometric model decomposition (SGMD). The authors advocate that compared with other decomposition methods, SGMD does not need user-defined parameters, has better robustness and suppresses modal aliasing. The methodology is validated with both simulated and measured data. Simulation studies are performed on a time-variant multi-DOFs shear-type structure, considering periodical and smooth variations on the springs that connect the vibrating masses, to explore the effectiveness of the proposed method for time-variant system identification. The validation with measured data encompasses a laboratory experiment with a dissected vehicle underframe crossbeam of high-speed train tested under time-invariant conditions and a time-variant wheel-rail coupling system. In the latter the moving vehicle vibrations were monitored during a field braking test and the instantaneous frequencies of the system were tracked during 9 seconds. The authors concluded that experiments using simulated and real data show that the proposed method can make good use of the limited bandwidth of each model for signal decomposition, and it can also accurately extract the instantaneous frequency of the time-variant system.

The paper by L. Cheng et al., entitled "Online Modal Identification of Concrete Dams using the Subspace Tracking based Method," proposes an online modal identification procedure based on strong-motion records to investigate the time-varying dynamic characteristics of concrete dams under the excitation of earthquakes. The online modal identification is expressed as a subspace tracking problem, and a newly developed recursive stochastic subspace identification (RSSI) method based on the "Generalized Yet Another Subspace Tracker" (GYAST) algorithm, which exploits both the accuracy of the subspace identification and fast computational capability, is used to extract the time-varying modal parameters of concrete dams during earthquakes. Firstly, the method is validated with numerically simulated vibration response records to verify its accuracy, robustness, and efficiency. Then, several strong-motion records collected at the Pacoima arch dam are analysed using the proposed modal-identification procedure, and the time-varying characteristics of the concrete arch dam during three different earthquakes are analysed. The authors conclude that the GYAST is a good tool to track different modes, since it shows good identification accuracy, robustness, and computation efficiency. They also report that the identification accuracy of the frequencies and modal shape vectors is sufficient, while for the damping ratios, the performance of the proposed online modal identification method still needs to be improved.

The paper by M. Juul et al., entitled "One-step updating using local correspondence and mode shape orthogonality," deals with the topic of FE model updating based on results of OMA aimed at improving an FE model in order to enhance its agreement with test results and reduce modeling errors (epistemic uncertainties). Particularly, the paper proposes a

one step updating technique where mass and stiffness matrices are corrected using experimentally identified mode shapes. These last are appropriately smoothed and are initially mass normalized to the first guess mass matrix through a fixed-point iteration procedure that is also illustrated in the paper. The one-step principle is based on expressing the inverse of the mass matrix as a sum of the contributions of lower order modes (those that are actually identified by OMA) and of higher-order modes (those that are not identified), with the same being done also for stiffness matrix. After the introduction, the paper illustrates the mathematical formulation of the proposed one step updating procedure, which exploits the circumstance that the mode shape matrix of a perturbed system can always be expressed as a linear transformation of the mode-shape matrix of the unperturbed system. The second part of the paper contains a validation of the proposed method considering both simulated and real test data on a *T* steel frame structure arranged in the lab and a section presenting the discussion of the obtained results. The discussion covers two main aspects. First of all, it comments on the fact that the proposed one step method assumes small distributed perturbations. This implies that when perturbations are localized and significant, the method may fail in handling epistemic uncertainties. Furthermore, the discussion contains very useful computational hints when dealing with applications of the proposed method to systems having a large number of degrees of freedom, where the inversion of very large dimensional matrices is required. The results show that, after mass scaling with respect to the updated mass matrix, the eigenvalue analysis using the updated FE model provides the "correct" (identified) undamped modal frequencies. A notable result of the paper is that in the case of perturbations distributed along the structure, the updating procedure is effective even when experimental information is limited to lower-order modes, while keeping higher-order modes unchanged.

In conclusion, it is clear that the above papers address relevant research issues in the field of OMA and its application to SHM, contributing to the development of the discipline and the enhancement of its already promising applicative perspectives. These editors, therefore, are confident that this special issue will be useful for researchers and practitioners working in the field.

Conflicts of Interest

The editors declare that they have no conflicts of interest regarding the publication of the special issue.

Acknowledgments

The guest editors would like to thank all distinguished authors contributing to this special issue for the high scientific quality and diversity of their papers, successfully addressing and effectively responding to the special call. The guest editors would also like to acknowledge the work made by all referees, who have completed the peer-reviewing tasks of all papers in a professional and timely fashion. Finally, a special recognition is because of the editorial staff at Shock and Vibration for welcoming the special issue proposal and for providing valuable and continuous support during the entire publishing effort.

Carlo Rainieri
Filipe Magalhaes
Filippo Ubertini

Hindawi
Shock and Vibration
Volume 2019, Article ID 5018732, 26 pages
https://doi.org/10.1155/2019/5018732

Research Article

Modal Parameters Identification Method Based on Symplectic Geometry Model Decomposition

Hang Jin, Jianhui Lin, Xieqi Chen, and Cai Yi

State Key Laboratory of Traction Power, Southwest Jiaotong University, Chengdu 610031, China

Correspondence should be addressed to Xieqi Chen; shayshe@msn.cn and Cai Yi; yicai@swjtu.edu.cn

Received 16 November 2018; Revised 13 May 2019; Accepted 15 July 2019; Published 11 September 2019

Guest Editor: Filipe Magalhaes

This paper proposes a novel method of structural system modal identification, where the iterative method is introduced in symplectic geometric model decomposition (SGMD). The proposed method can decompose the measured response into finite symplectic geometric components and identify the modal parameters of time-invariant structures and the instantaneous frequency of time-variant system through each symplectic geometric component. To obtain the shape information of the structural model, the SGCs of the same frequency at different measuring points are subjected to singular value decomposition (SVD). Both simulated data verification and measured data verification were used to verify if the method proposed in this article is effective for time-invariant system and time-variant system identification. For the simulated data, we study on a structural system which is set up with time-variant stiffness and time-invariant system. The measured vibration data of beam structure and time-variant wheel-rail coupling system were also tested and varied. Compared with the results of empirical model decomposition, the proposed method is capable of identifying instantaneous frequencies with better accuracy.

1. Introduction

The dynamic parameters are determined by the measured input and output of the vibration to establish a mathematical model for vibration systems. This method can be referred as the inverse problem of dynamics. Meanwhile, the experimental modal analysis was developed to solve this inverse problem. Also, structural damage can be identified and evaluated by its modal parameters. Hence, the accurate modal parameters identification of structure has great significance [1]. For integral structures, like gearboxes and equipped vehicles, it is difficult to apply artificial excitation during modal testing. Therefore, modal parameters would be identified by using the output signals directly under environmental excitation. Compared with the traditional modal test of input and output, the direct identification of modal parameters using output signals has the advantages of simple measurement, neighbour sensitivity, repetition frequencies, and much closer to the real dynamic characteristics [2].

Since structures are usually influenced by the environmental excitations, operational modal recognition methods, for example, the time-domain decomposition method [3], frequency domain decomposition method [4], and the stochastic subspace recognition method [5], were utilized in mechanical engineering structures by means of only output responses. For the problem of modal identification of structure which has a free vibration response, eigensystem realization algorithm (ERA) [6] was proposed. The applicability of the algorithm described above has been increased for using modal parameters identification under environmental excitation. Additionally, two methods, i.e., the random decrement method [7] and natural excitation method [8], were developed. It was shown that the random decrement function and correlation function have similar properties as the free decay vibration responses. This property can be employed in the identification of modal information. Dohler et al. [9] quantified the uncertainty effect in the modal identification by improving the traditional stochastic subspace identification method. Bayesian methods [10–13] were also proposed for identification of operational modals, which consider the noise effect as well as the uncertainty emerged in the real data. The above-mentioned methods were successfully employed to identify the vibration property for real structure [14–16].

However, it is known that the abovementioned methods mainly dealt with the problem of modal identification of time-invariant linear systems. When the tests are applied to the first structure prototype, nonlinearity is usually encountered [17]. Nonlinearity can obtain complicated dynamic phenomena, e.g., modal interactions, quasiperiodicity, and chaos subharmonic and superharmonic resonances, besides distorted resonances as well as the jumps between low- and high-amplitude responses. Therefore, essentially linear models are difficult in predicting the structural response [18]. For example, changes in the locations of the moving vehicle can lead to variations in the frequencies of a bridge-vehicle system [19]. Meanwhile, track irregularity would also be the cause of nonlinearity [20]. In this condition, proper understanding and identification of the vibration characteristics are significant. For example, time-variant frequency is essential to identify possible damage in the structure and to monitor the structural operational conditions.

The instantaneous frequency (IF) and instantaneous amplitude (IA) of system responses depend on damping and stiffness of the systems [21]. For this reason, Mihalec et al. [22] studied the synchrosqueezing wavelet transform (SWT) to apply free-response signal to recognize the damping ratio in the vibrating system.

It was shown that SWT with a proportional criterion gave relatively improved localization and estimation of damping ratios for close model, to minimize frequency-shift errors in original SWT. Montejo and Vidot-Vega [23] tested SWT by means of the estimated damping values of the structure from its noise-contaminated response, and it was concluded that SWT outperformance was greater than CWT and Hilbert–Huang transform when estimating the modal damping ratio. Li et al. [24] monitored the variations in structural responses by means of the EMD and wavelet analysis. Shi and Law [25] employed HHT to obtain the structural parameters in time-variant structure which have complete measurement responses. This technique is more accurate than traditional methods in identifying the damage occurrence and severity. Also, Ni et al. [26] employed variational model decomposition (VMD) to produce a few intrinsic model functions by decomposing the real responses and then utilized the Hilbert transform of each intrinsic model function to identify the instantaneous frequencies of time-variant systems. In the experiments, we analyze the real vibration data in the laboratory from a time-variant bridge-vehicle and a steel frame structure system. Unfortunately, the existing methods have at least one of the following defects:

(1) This method inevitably decomposes it to inaccurate components in the case of a complex (nonsinusoidal) waveform

(2) This method does not have noise robustness as it cannot effectively decompose signals with noises

(3) This method is very sensitive to the parameters, which are required to be defined by users

The analysis method proposed in this paper, which is based on symplectic geometry, has a protective effect on geometry structure of phase space, which represents system state variables. Also, the symplectic geometric decomposition method is primarily utilized to solve eigenvalue problem $2n \times 2n$. Hamiltonian matrix has been commonly used in dynamics and control systems, and rapidly employed to describe partial and singular differential equations, as well as other systems. In the method of symplectic geometric analysis, symplectic geometry spectrum analysis (SGSA) can preserve the essential characteristics of measurement and keep the main time series same as before; therefore, it is suitable for analyzing nonlinear systems [27, 28]. SGMD uses symplectic geometry spectrum analysis (SGSA) to solve the eigenvalues of the Hamiltonian matrixes and reconstructs individual symplectic geometric component signals (SGCs) with the corresponding eigenvectors. According to the authors' knowledge, there are no studies which use relatively new techniques to modal parameters identification. This paper applies the newly proposed SGMD technique to perform the signal decomposition of real responses from the structure systems and then their modal parameters identification.

This paper firstly introduced the theoretical analysis as well as the detailed algorithm process of symplectic geometric modal analysis. It is also proposed an improved iterative termination conditions for SGMD. We considered the modal responses on a structure, which is found in all sensor locations, to acquire the model shape corresponding to a particular model. The same frequency at different locations has been processed to singular value decomposition (SVD) in SGCs for obtaining modal models. Secondly, we analyzed the simulation study of structural response under impact force and verified the effectiveness of this method in identifying time-invariant modal parameters and time-variant instantaneous frequencies. Finally, the experimental research is implemented on beam structure and time-variant vehicle body vibration data. Compared with the existing technique, the proposed method is much better.

2. Theoretical Background

2.1. Motion Equation of Time-Variant Structure. The motion equation of a time-variant structure with n degrees of freedom (DOFs) is described by

$$M\ddot{x}(t) + C\dot{x}(t) + K(t)x(t) = BF(t), \tag{1}$$

where $K(t)$, C, and M mean stiffness matrices, damping, and $n \times n$ time-variant mass, respectively; $\ddot{x}(t)$, $\dot{x}(t)$, and $x(t)$ mean displacement response vectors, velocity, and acceleration of structure, respectively; and $F(t)$ is the applied excitation force on the structure with mapping matrix B and relates the applied excitation force to the corresponding DOFs. In this paper, the mass and damping matrices are time invariant, the variations of which are generally much smaller and insignificant compared to that of structural stiffness.

The frequency (variation) of each model will be narrow band if the coefficient has a minor time variation. According to the modal superposition method with n vibrational modal responses, we can obtain the structural displacement and

acceleration responses based on the principle of modal superposition. The signal is expressed with

$$x(t) = \sum_{i=1}^{n} \mathbf{\Phi}_i(t) q_i(t),$$
$$\ddot{x}(t) = \sum_{i=1}^{n} \mathbf{\Phi}_i(t) \ddot{q}(t), \tag{2}$$

where $\mathbf{\Phi}_i$ means i-th model shape and $q_i(t)$ is corresponding modal response. Based on the orthogonal property of model shape, equation (1) can be decoupled into equations of n models after substituting equation (2) in equation (1):

$$\ddot{q}_i(t) + 2\xi_i \omega_i(t) \dot{q}_i(t) + \omega_i^2 q_i(t) = \frac{\mathbf{\Phi}_i^T(t) F(t)}{m_i}, \tag{3}$$

where m_i, ξ_i, and ω_i are circular modal frequency, modal damping ratio, and the i-th modal mass, respectively. After an impulse force is employed to the z-th DOF, the the i-th generalized modal coordinate will have an acceleration response described as

$$\ddot{q}_i(t) = \frac{F_0 \phi_{zi,t=0} \omega_i(t)}{m_j \sqrt{1-\xi_i^2}} \exp\left(-\xi_i \omega_i(t)\right) \cos\left(\omega_{di}(t) t + \nu_i\right), \tag{4}$$

where $\phi_{zi,t=0}$ denotes the z-th item of the i-th modal vector $\mathbf{\Phi}_i(t)$ at time $t = 0$, $\omega_{di} = \omega_i \sqrt{1-\xi_i^2}$, and ν_i is the phase angle.

The acceleration response $\ddot{x}_p(t)$ of the structure at the p-th DOF is as follows:

$$\ddot{x}_p(t) = \sum_{i=1}^{n} \phi_{pi}(t) \ddot{q}_i(t). \tag{5}$$

We can further write equation (5) as the superposition of amplitude-modulated-frequency-modulated signals:

$$\ddot{x}_p(t) = \sum_{i=1}^{n} S_i(t) = \sum_{i=1}^{n} A_i(t) \cos\left(\omega_{di}(t) t + \nu_i\right),$$
$$A_i(t) = \frac{\phi_{pi}(t) F_0 \phi_{zi,t=0} \omega_i(t)}{m_i \sqrt{1-\xi_i^2}} \exp\left(-\xi_i \omega_i(t)\right). \tag{6}$$

2.2. SGMD for Signal Decomposition. A trajectory matrix has been built by the SGMD method in the original time series during embedding. Firstly, the power spectral density (PSD) method is employed for obtaining the embedding dimension and the trajectory matrix. Then, the symplectic matrix is constructed, and the eigenvalues of Hamiltonian matrix are solved by symplectic geometric similarity transformation. Traditional SGMD obtains all SGC by similarity comparison. In this paper, SGC is extracted by merging all similar vectors of the maximum eigenvalue from the original signal and re-symplectic geometric model decomposition of residual components, which is an iterative process. To estimate the original time series in this study, we apply a diagonal averaging method to every symplectic principal component matrix. Figure 1 shows the diagram of SGMD technique.

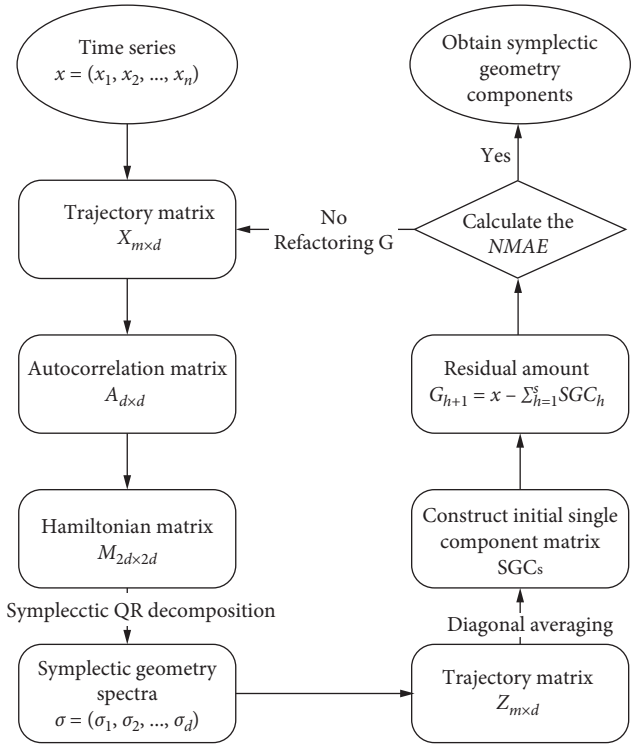

Figure 1: Block diagram of SGMD.

Before analyzing SGMD method, some definitions and theorems are introduced as follows.

Definition 1. S is a symplectic matrix if there is $JSJ^{-1} = S^{-T}$.

Definition 2. H is a Hamiltonian matrix if there is $JHJ^{-1} = -H^{-T}$.

Theorem 1. *For any symplectic matrix $A_{n\times n}$, construct a new matrix $M = \begin{bmatrix} A & 0 \\ 0 & -A^T \end{bmatrix}$; M is also a Hamilton matrix.*

Theorem 2. *Suppose the Householder matrix is supposed as*

$$H = H(k, w) = \begin{bmatrix} P & 0 \\ 0 & P \end{bmatrix},$$
$$P = I_n - \frac{2\overline{w}\overline{w}^{\mathrm{T}}}{\overline{w}^{\mathrm{T}}\overline{w}}, \tag{7}$$

where $\overline{w} = (0, \ldots, 0; w_k, \ldots, w_n)^T \neq 0$ and H is a symplectic unitary matrix.

Theorem 3. *Suppose an $m \times n (m > n)$ dimension real trajectory matrix X and $A = X^T X$ is a real symmetry matrix. Then, the Hamilton matrix M can be constructed from the symmetric matrix A, namely, $M = \begin{bmatrix} A & 0 \\ 0 & -A^T \end{bmatrix}$.*

There is a Householder matrix H; then, an upper Hessenberg matrix B is constructed via HMH^T, namely,

$$
\begin{aligned}
HMH^T &= \begin{pmatrix} P & 0 \\ 0 & P \end{pmatrix} \begin{pmatrix} A & 0 \\ 0 & -A^T \end{pmatrix} \begin{pmatrix} P & 0 \\ 0 & P \end{pmatrix}^T \\
&= \begin{pmatrix} PAP^T & 0 \\ 0 & -PA^TP^T \end{pmatrix} \\
&= \begin{pmatrix} B & 0 \\ 0 & -B^T \end{pmatrix}, \\
\lambda(A) &= \lambda(B), \\
\sigma &= \lambda^2(X) = \lambda(A).
\end{aligned} \tag{8}
$$

The upper Hessenberg matrix B is an n-dimension space matrix. Therefore, the primary $2n$-dimension space Hamilton matrix M can be resolved via transforming it into n-dimension space.

The key of symplectic geometry model decomposition is to utilize symplectic geometry spectrum analysis (SGSA) for solving the eigenvalues of Hamiltonian matrix and reconstructing the single component signals via its corresponding eigenvectors. Therefore, the power spectral density (PSD) method is applied to adaptively obtain embedding dimension of the studied time series. Then, symplectic geometry is constructed, and SGSA is used to deal with the eigenvalues of Hamiltonian matrix. Finally, the diagonal averaging and adaptive reconstruction are employed to obtain symplectic geometry components. Therefore, the SGMD may fit for nonlinear signal analysis.

The symplectic geometry model decomposition method usually can be divided into four parts: adaptive determining embedding dimension of the time series, solving the eigenvalues of Hamiltonian matrix via symplectic geometry similarity transformation, diagonal averaging, and adaptive reconstruction of components.

Briefly, any original signal time series are expressed as $x = x_1, x_2, \ldots, x_n$, ($n$ means data length). Based on Takens' theorem, a time-series delay topology equivalent method is used to reconstruct the multidimensional signals via one dimensional signal. That is to say the original time series can be projected to the trajectory matrix X which has all the dynamic information of time series x:

$$
X = \begin{bmatrix} x_1 & x_{1+\tau} & \cdots & x_{1+(d-1)\tau} \\ x_2 & x_{2+\tau} & \cdots & x_{2+(d-1)\tau} \\ \vdots & \vdots & \vdots & \vdots \\ x_m & x_{m+\tau} & \cdots & x_{m+(d-1)\tau} \end{bmatrix}, \tag{9}
$$

where d is the embedding dimension, τ is the delay time, $m = n - (d-1)\tau$, and the appropriate embedding dimension d and the delay time τ are chosen to get the corresponding reconstruction matrix. The idea of determining embedding dimension in the existing studies [29] is employed to calculate the PSD of the initial time series x. Subsequently, $f_{\max}$, frequency of the maximum peak, is estimated from PSD. d is set to $n/3$ where n is the length of data if the normalized frequency is less than the given threshold 10^{-3}. Otherwise, it is set to $d = 1.2 \times (Fs/f_{\max})$.

To obtain Hamiltonian matrix, autocorrelation analysis is implemented on the trajectory matrix to get the covariance symmetric matrix A:

$$
A = X^T X. \tag{10}
$$

Then, the Hamilton matrix M will be obtained based on the symmetric matrix A:

$$
M = \begin{bmatrix} A & 0 \\ 0 & -A^T \end{bmatrix}. \tag{11}
$$

After constructing Hamilton matrix, the square of M is N, i.e., $N = M^2$, and the matrices M and N are Hamilton matrices by the definition of Hamilton matrix. Therefore, a symplectic orthogonal matrix Q can be obtained from the following equation:

$$
Q^T N Q = \begin{bmatrix} B & R \\ 0 & B^T \end{bmatrix}, \tag{12}
$$

where Q means an orthogonal symplectic matrix with the property of its prototype, to protect the structure of Hamilton matrix when it is transformed. Here, B means upper triangular matrix, i.e., $b_{ij} = 0\,(i > j+1)$. It can be transformed via utilizing the Schmidt orthogonalization to matrix N, and the eigenvalue of the upper triangular matrix B can be calculated as $\lambda_1, \lambda_2, \ldots, \lambda_d$. Indeed, the eigenvalues of A will equal those of B if A is real symmetric. Based on the properties of Hamilton matrix, the eigenvalues of the matrix A are obtained:

$$
\sigma_i = \sqrt{\lambda_i}, \quad i = 1, 2, \ldots, d. \tag{13}
$$

The symplectic geometry of X is made by eigenvalues of A in descending order, i.e.,

$$
\sigma_1 > \sigma_2 > \cdots > \sigma_d. \tag{14}
$$

The distribution of σ_i is the symplectic geometry spectra of A, with its smaller values to be usually treated as noise components. $Q_i\,(i = 1, 2, \ldots, d)$ means eigenvectors which correspond to eigenvalue of matrix A.

Matrix Q is constructed as Householder matrix H from equation (14), where the theory of symplectic geometry can be employed to solve the embedding dimension time series. Therefore, the Householder matrix H, rather than the symplectic orthogonal matrix Q, has been selected. H is easy to be verified as the unitary matrix, and H can be obtained from real matrix. This is helpful for researching the time series. Moreover, let $S = Q^T X$, $Z = QS$, and Z be the reconstructed trajectory matrix. Each component matrix is reconstructed as per the following steps.

Firstly, based on the unitary matrix eigenvectors and trajectory matrix, the transformation coefficient matrix S is obtained as follows:

$$
S_i = Q_i^T X^T. \tag{15}
$$

Then, to obtain reconstruction matrix Z, the transformation coefficient matrix is transformed:

$$
Z_i = Q_i S_i, \tag{16}
$$

where Z_i $(i = 1, 2, \ldots, d)$ is the initial single component. Similarly, trajectory matrix Z is

$$Z = Z_1 + Z_2 + \cdots + Z_d. \tag{17}$$

The obtained initial single component matrix Z is $m \times d$ matrix. Therefore, the initial single component should be reordered, and the reconstructed matrix Z should be transformed by the diagonal averaging into a new set of time series of length n. Meanwhile, that of new time series d can be achieved as well, where the sum of new time series d is the original time series.

Additionally, we define the elements of matrix as z_{ij} for any initial single component matrix Z_i, where $1 \le i \le d$, $1 \le j \le m$, and $d^* = \min(m, d)$, $m^* = \max(m, d)$, and $n = m + (d-1)\tau$. Let $z^*_{ij} = z_{ij}$ if $m < d$; otherwise, $z^*_{ij} = z_{ji}$. Thus, the diagonal averaging transfer matrix is

$$y_k = \begin{cases} \dfrac{1}{k} \displaystyle\sum_{k}^{p=1} z^*_{p,k-p+1}, & 1 \le k < d^*, \\ \dfrac{1}{d^*} \displaystyle\sum_{d^*}^{p=1} z^*_{p,k-p+1}, & d^* \le k \le m^*, \\ \dfrac{1}{n-k+1} \displaystyle\sum_{n-m^*+1}^{p=k-m^*+1} z^*_{p,k-p+1}, & m^* < k \le n. \end{cases} \tag{18}$$

The matrix Z_i is transformed to a series of $Y_i(y_1, y_2, \ldots, y_n)$ based on equation (20). Thus, by diagonal averaging, we can transform the reconstruction matrix Z into a new series of matrix Y with the length $d \times n$. Additionally, it can decompose the original time series into d independent superimposed components with various trends and frequency bands.

d single component signals are acquired via diagonal averaging:

$$Y = Y_1 + Y_2 + \cdots + Y_d. \tag{19}$$

After construction of the trajectory matrix and implementation of diagonal averaging, d single components are obtained, whereas the components are not totally independent as they may have same characteristics, periods, and frequency components, which means that the initial single components with same characteristics need reconstructing. The component correlation and frequency similarity are employed to rebuild the components. Also, the components divided from a component will be rebuilt via calculating their frequency and correlation. Additionally, the signal usually includes numerous noise components irregularly, such as frequency and correlation as the interference of environmental factors. Therefore, it is urgent to set the iterative stopping conditions.

Firstly, the correlation was calculated with Y_1 and other reconstructed signals $Y_{k \ne l}$, and the highly similar Yk is composed of the first SGC component. Then the SGC_l is removed from the source signal x, and the residual signal is recorded as g_{h+1}:

$$g_{h+1} = x - \sum_{l=1}^{h} \mathrm{SGC}_l, \tag{20}$$

where h means number of iterations. Finally, the calculation would be made for normalized mean absolute error (NMAE) of the participating signals:

$$\mathrm{NMAE}_h = \frac{1}{t} \sum_{t=1}^{n} \left| \frac{g_{h+1}(t)}{x(t)} \right|. \tag{21}$$

The whole decomposition process will continue until the normalized mean absolute error is smaller than the predetermined threshold $\mathrm{NMAE}_h = 1\%$. Otherwise, the reconstructed residual signal g_h is the trajectory matrix X and the above $\mathrm{NMAE}_h = 1\%$ iterative process is repeated until the iteration termination condition is satisfied. And, the final decomposition result is obtained as follows:

$$x(t) = \sum_{h=1}^{N} \mathrm{SGC}_h(t) + g_{N+1}(t), \tag{22}$$

where N means number of identified component series. Different from the traditional SGMD method, the newly proposed SGMD removes the reconstructed signal Y_1 with the largest feature and its similar signal from the source signal. It also needs to take the judgement which reiled on the NMAE of residual signal for completing the decomposion, still, the method by continuing to search for the new SGC is replaced as the new trajectory matrix recalucation. This can be more accuary compared with combing the reconstructed signal Y in the conventional SGMD method for obtaining SGC. Hence, the iterative process has been added to improve the traditional SGMD.

2.3. Hilbert Transform. It is widely accepted that time-frequency analysis methods have advantages over the traditional methods. By using fast Fourier transformation (FFT), energy distribution in the time and frequency scales can be visualized with an adjustable resolution. Additionally, the signal in the frequency scale can be investigated with multiresolution analysis from time-frequency analysis via the time scale information. In areas of damage identification, modal identification, and signal processing, the time-frequency analysis methods are widely utilized. Performing the signal decomposition with SGMD, several SGCs are obtained and employed for obtaining Hilbert spectrum. Both nonlinear and non-stationary signals can be analyzed by Hilbert transform. To perform Hilbert transform using the extracted the SGCs from a vibration response signal, it is required to obtain frequency and time-domain information with the instantaneous frequencies and amplitudes. The following equation can be used to define Hilbert transform of a specific SGC:

$$\widetilde{\mathrm{SGC}}_k(t) = H\left[\mathrm{SGC}_k(t)\right] = \frac{1}{\pi} P \int_{-\infty}^{+\infty} \frac{\mathrm{SGC}_k(\tau)}{t - \tau} d\tau, \tag{23}$$

where $\widetilde{\mathrm{SGC}}_k(t)$ is the Hilbert transform of symplectic geometry components $\mathrm{SGC}_k(t)$ and P is the Cauchy principle value. The analytical signal is

$$z_k(t) = \mathrm{SGC}_k(t) + \widetilde{\mathrm{SGC}}_k(t) = A_k(t)e^{j\theta_k(t)},$$
$$A(t) = \left[\mathrm{SGC}_k(t)^2 + \widetilde{\mathrm{SGC}}_k(t)^2\right]^{1/2}, \quad (24)$$
$$\theta_k(t) = \arctan\left(\frac{\widetilde{\mathrm{SGC}}_k(t)}{\mathrm{SGC}_k(t)}\right).$$

Finally, the identified instantaneous frequency $\omega_{id}^k(t)$ of k-th component is expressed by

$$\omega_{id}^k(t) = \frac{\partial\theta_k(t)}{\partial t}. \quad (25)$$

2.4. Modal Data Identification Algorithm. Figure 2 shows the diagram for identifying modal characteristics by means of SGMD method for system identification. The diagram contains the following five main steps:

(1) The SGMD has been processed on n point sensor data $(x_1, x_2 \ldots, x_n)$ for test structure, each measurement point retains k SGC scale components, and data length is N:

$$\mathrm{SGC}_n = \begin{bmatrix} \mathrm{SGC}_n(a_1,t_1) & \mathrm{SGC}_n(a_1,t_2) & \cdots & \mathrm{SGC}_n(a_1,t_N) \\ \mathrm{SGC}_n(a_2,t_1) & \mathrm{SGC}_n(a_2,t_2) & \cdots & \mathrm{SGC}_n(a_2,t_N) \\ \vdots & \vdots & \vdots & \vdots \\ \mathrm{SGC}_n(a_k,t_1) & \mathrm{SGC}_n(a_k,t_2) & \cdots & \mathrm{SGC}_n(a_k,t_N) \end{bmatrix}_{k\times N}. \quad (26)$$

(2) Since the symplectic geometric decomposition will disturb the order of scales, it is necessary to compare the correlation coefficients of the SGC components of all sensors and select one SGC component with the largest correlation coefficient from different measuring points n to form N new matrices A_k:

$$A_k = \begin{bmatrix} W_1(a_k,t_1) & W_1(a_k,t_2) & \cdots & W_1(a_k,t_N) \\ W_2(a_k,t_1) & W_2(a_k,t_2) & \cdots & W_2(a_k,t_N) \\ \vdots & \vdots & \vdots & \vdots \\ W_n(a_k,t_1) & W_n(a_k,t_2) & \cdots & W_n(a_k,t_N) \end{bmatrix}_{n\times N}. \quad (27)$$

Thus, A_k can form a singular value decomposition matrix which can ensure to contain the same instantaneous frequency.

(3) Singular value decomposition for each combined matrix is carried out:

$$A_k = U_k S_k V_k^T, \quad (28)$$

where $U_k = \{u_{1k}, u_{2k}, \ldots, u_{nk}\}$; $S_k = (\sum_{\lambda k} O)$, $\sum_{\lambda k} = \mathrm{diag}(\sigma_{1k}, \sigma_{2k}, \ldots, \sigma_{nk})$; $V_k = \{v_{1k}, v_{2k}, \ldots, v_{nk}\}$.

(4) The judgement matrix is reconstructed by using the first singular value σ_{1k}:

$$B[\sigma_{11}, \sigma_{12}, \ldots, \sigma_{1k}]_{1\times k}. \quad (29)$$

In this formula, B represents the obtained first singular value of different scales decomposition.

(5) The first singular value vectors u_{1k} and v_{1k} are reconstructed to obtain the reconstructed matrix:

$$D_1 = [u_{11}, u_{12}, \ldots, v_{1k}]_{n\times k},$$
$$D_2 = [v_{11}, v_{12}, \ldots, v_{1k}]_{k\times N}. \quad (30)$$

When the scale point position of local maximum in B corresponds to a_l, D_1 contains structural point vibration model information and D_2 contains the natural frequency of structural modal point and its damping ratio:

$$\{\Phi_i\} = D_{1l},$$
$$\begin{cases} \omega_i = \sqrt{\left(\dfrac{d}{dt}\angle D_{2l}\right)^2 + \left(\dfrac{d}{dt}\left(\ln|D_{2l}|\right)\right)^2}, \\ \xi_i = \dfrac{-(d/dt)\left(\ln|D_{2l}|\right)}{\omega_i}. \end{cases} \quad (31)$$

l is the scale corresponding to the column a_l. $D_{1l} = u_{1l}$, $D_{2l} = v_{1l}$, and $\angle$ represents the phase angle.

3. Simulation Studies

Simulation studies are performed on a time-variant multi-DOF shear-type structure to explore the effectiveness of the proposed method for time-variant system identification. To verify the proposed method, a simulation model of 5-DOF mass-spring-damper is fabricated first, which is shown in Figure 3.

Also, based on equation (1) and the mass matrix M,

$$M = \begin{bmatrix} 4.9895 & 0 & 0 & 0 & 0 \\ 0 & 4.9895 & 0 & 0 & 0 \\ 0 & 0 & 4.9895 & 0 & 0 \\ 0 & 0 & 0 & 4.9895 & 0 \\ 0 & 0 & 0 & 0 & 4.9895 \end{bmatrix}, \quad (32)$$

and the stiffness matrix K of the model is

$$K = \begin{bmatrix} k_1 + k_{12} & -k_{12} & & & \\ -k_{12} & k_{12} + k_{23} & -k_{23} & & \\ & -k_{23} & k_{23} + k_{34} & -k_{34} & \\ & & -k_{34} & k_{34} + k_{45} & -k_{45} \\ & & & -k_{45} & k_5 + k_{45} \end{bmatrix}, \quad (33)$$

where $k_{12} = 17{,}110$ N/s, $k_{23} = 8005$ N/s, $k_{45} = 5632$ N/s, $k_5 = 13{,}300$ N/s, and k_1 and k_{34} are the time-variant stiffness parameters. Three cases with periodical and smooth variations are researched, respectively. The variant stiffnesses in Case 1 are set as $k_1 = 2000$ N/m and $k_{34} = 48{,}000$ N/m, which is a time-invariant system, and defined as $k_1 = (5 - 0.08t) \times 10^3$ N/s and $k_{34} = (4.8 - 0.12 * t) \times 10^4$ N/s in Case 2. The corresponding values in Case 3 are $k_1 = (2 + 0.6\sin(2\pi t)) \times 10^3$ N/m and $k_{34} = 48{,}000$ N/m.

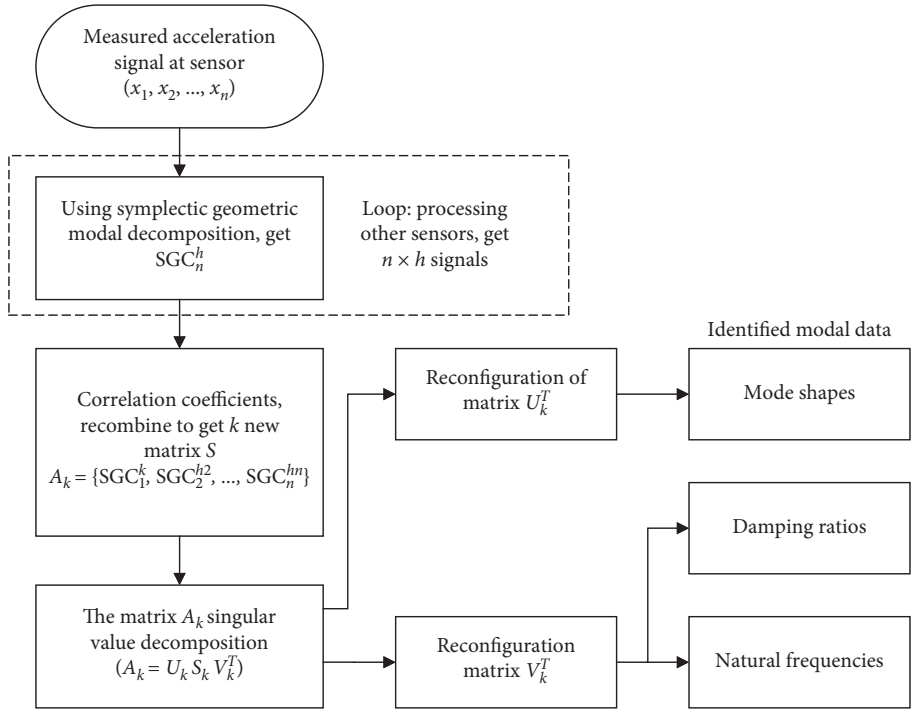

Figure 2: Workflow of the proposed modal data identification method.

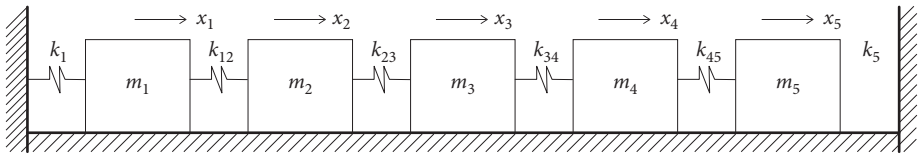

Figure 3: The 5-DOF simulation model.

Proportional damping $C = 0.08M$. The following impulse force is applied at the fourth layer:

$$BF(t) = \begin{Bmatrix} 0 \\ 0 \\ 0 \\ f(t) \\ 0 \end{Bmatrix}, \quad f(t) = \begin{cases} 500\,\text{N}, & t = 0, \\ 0, & t \neq 0. \end{cases} \tag{34}$$

Newmark beta method, a time-stepped integration method, is used to solve the analytical responses of time-variant system. 200 Hz is set as the sampling frequency. The acceleration signal from the top level is chosen to decompose signals and identify the following instantaneous frequencies. Moreover, the signal-to-noise ratio of vibration signals in both three cases is 30 dB, which is considered the noise effect in measurement.

3.1. Linear Structure Modal Identification. According to the structural parameters of Case 1, the modal shape can be obtained as

$$\Phi = \begin{bmatrix} 1.0000 & 1.5690 & -0.4609 & 4.4280 & 0.3353 \\ 1.0352 & 1.0000 & 0.0231 & -5.3460 & -1.6530 \\ 0.9295 & -1.2411 & 1.0000 & 0.3206 & 15.4604 \\ 0.8848 & -1.4027 & 0.7469 & 1.0000 & -15.0077 \\ 0.2842 & -0.7365 & -4.0584 & -0.2703 & 1.0000 \end{bmatrix}. \tag{35}$$

The natural frequencies can be obtained as $f_1 = 2.66438$ Hz, $f_2 = 6.4540$ Hz, $f_3 = 10.0685$ Hz, $f_4 = 14.2087$ Hz, and $f_5 = 22.9175$ Hz. The damping ratios for each order are obtained as $\xi_1 = 0.1066$, $\xi_2 = 0.2582$, $\xi_3 = 0.4027$, $\xi_4 = 0.5683$, and $\xi_5 = 0.9167$. Still, the modal assurance criterion (MAC) is utilized for the evaluation of the errors of identified model shape:

$$\text{MAC}_i = \frac{\left(\phi_i^T \widehat{\phi}_i\right)^2}{\phi_i^T \phi_i \widehat{\phi}_i^T \widehat{\phi}_i}, \tag{36}$$

where ϕ_i is the estimated model vector and $\widehat{\phi}_i$ is the theoretical one. Figure 4 shows the Fourier transform spectrum and time history of the response signal from Case 1. The Fourier spectrum clearly indicates five frequencies.

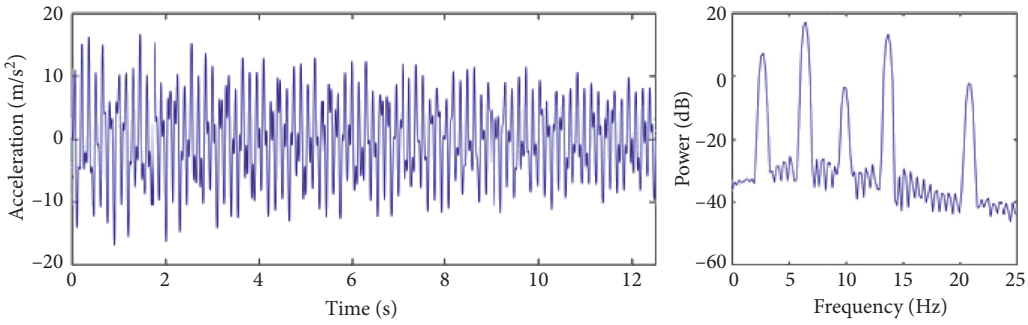

Figure 4: Time-domain response signals as well as the fast Fourier transform spectrum in the simulation study (Case 1).

Unlike the SGMD method introduced in reference [28], in order to suppress overdecomposition, equation (23) described in this paper is used as the iteration termination condition, and the simulation signal is decomposed into five SGCs. The symplectic geometric decomposition of the vibration signal on the fifth degree of freedom is shown in Figure 5. After the decomposition, the order of each layer for SGC is not arranged in the sequence of frequency but followed the energy distribution; the order of sequences has been rearranged in order to natural frequency identification. The SGMD can decompose each order of vibration into independent components. Meanwhile, modal shapes cannot be obtained after decomposing a single signal. This paper proposes to combine SGMD with SVD and identify the modal parameters of the reconstructed matrix D_2 as shown in Figure 6. Also, each individual component is close to the vibration of a single degree of freedom. At the same time, according to D_1, the model shape can be obtained.

The modal parameters of linear simulation signal are identified by the methods of SVD, SGMD, and SGMD-SVD, respectively. The results are shown in Table 1. The SVD can effectively identify the model shape, but the natural frequency and damping ratio recognition effect are very unsatisfactory. After SGMD classifies a single simulation signal, the identified natural frequency and damping are more accurate and the fifth-order natural frequency identification result has a larger deviation, owing to fact that the simulation signal has a shorter step size and the affected recognition frequency is lower. The combination of SGMD and the SVM, not only effectively identify models but also can be effective for identifying the natural frequency and damping for simulation modal identification signals. Therefore, the SGMD can decompose the measured signals into each effective frequency single signal, which is convenient for the identification of modal parameters. Still, the vibration models were extracted by SVD, and MAC values were all greater than 0.898. As a result, the proposed method is suitable and applicable to the identification of linear modal parameters.

3.2. Nonlinear Structure Instantaneous Frequency Identification. Figure 7 shows the Fourier transform spectrum and the time history of the response signal in Case 2. The Fourier spectrum has five frequencies, as shown in Figure 7. Thus, signal decomposition is implemented via SGMD. The decomposed SGCs as well as their corresponding frequency spectra are shown in Figure 8. Four independent frequency components are decomposed in the Fourier spectra, which are well separated. The true and identified instantaneous frequencies of time-variant structure are shown in Figure 9. Note that the "freezing method" is used to obtain the theoretical instantaneous frequency [30]. Assume that, in each time interval, the structural physical parameters are unchanged, and the theoretical instantaneous frequency is solved from the solution of eigenvalue analysis problem. The finite duration of measured signals will have an end effect, which may bring certain errors, especially when the response signals begin and stop, which is shown in Figure 9. In general, with the associated FFT analysis, the end and leakage effects are significant. In addition, employing FFT with band-pass filters cannot identify the instantaneous frequency of time-variant systems. Meanwhile, the proposed approach can successfully identify the smooth decreasing time-variant frequencies.

From the Fourier transform of SGCs in Figure 8(c), the decomposed signals still have a modal aliasing problem. Observing the time-domain map is not difficult to find, which is caused by modal aliasing caused by the endpoint effect.

Figures 10–12 show the identified instantaneous frequencies, decomposed SGC via SGMD, and the response signal in time and frequency domains for Case 3, respectively. As shown in Figure 11, the Fourier spectra of the decomposed SGCs indicate that the five models are clearly decomposed. Similar to Figure 8(c), the end effect mode results still lead to the certain aliasing in Figure 11(c) and 11(d).

Moreover, Figure 12 shows the identified instantaneous frequencies where the lower frequency component has larger variation compared to its higher counterpart. Nevertheless, the identified first models are the best among all the models. The high model offsets the central frequencies caused by noise, while the identified low model frequency fluctuates around the central frequency.

Empirical model decomposition (EMD), a typical method for signal decomposition, is also employed in this study for the vibration response of Case 3 (Figure 13 shows the obtained IMFs). The results of the first two decomposition in EMD are similar to those in the proposed method in this paper. The instantaneous frequency of IMF1

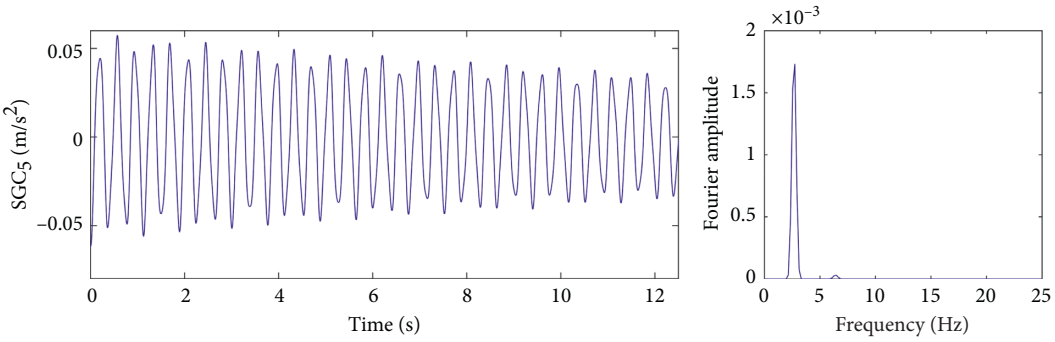

(a)

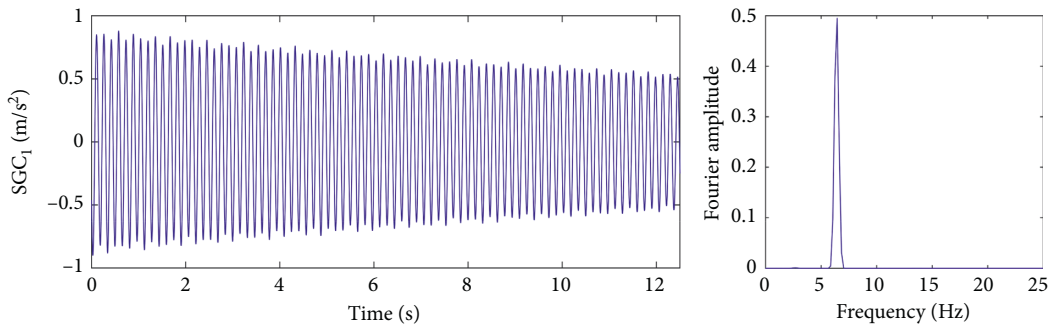

(b)

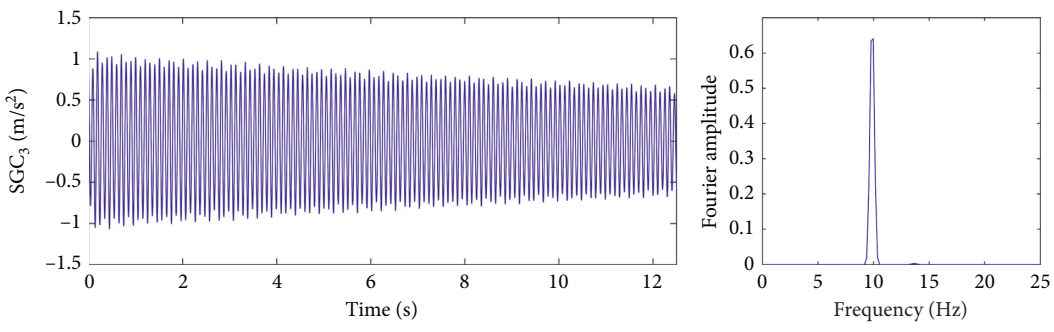

(c)

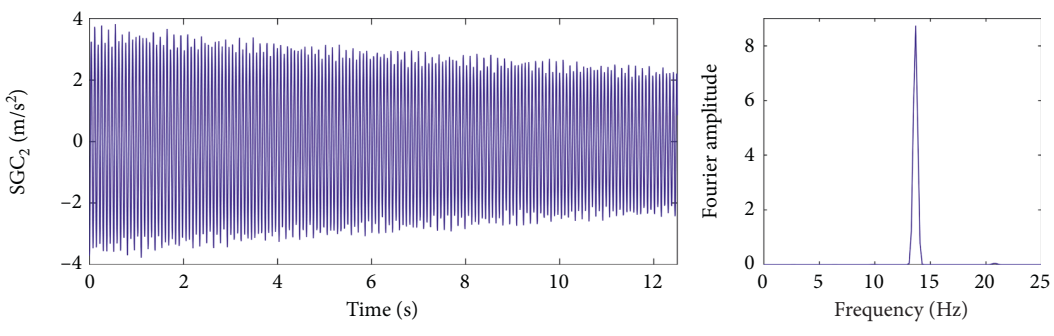

(d)

Figure 5: Continued.

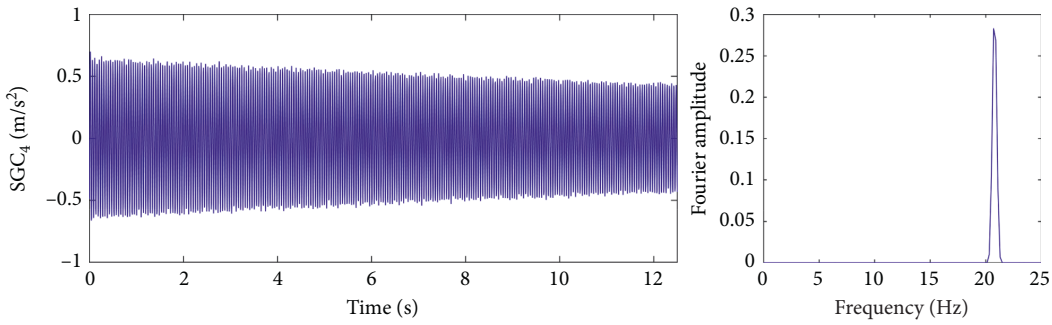

(e)

Figure 5: The results of the symplectic geometry decomposition and power spectrum for DOF5.

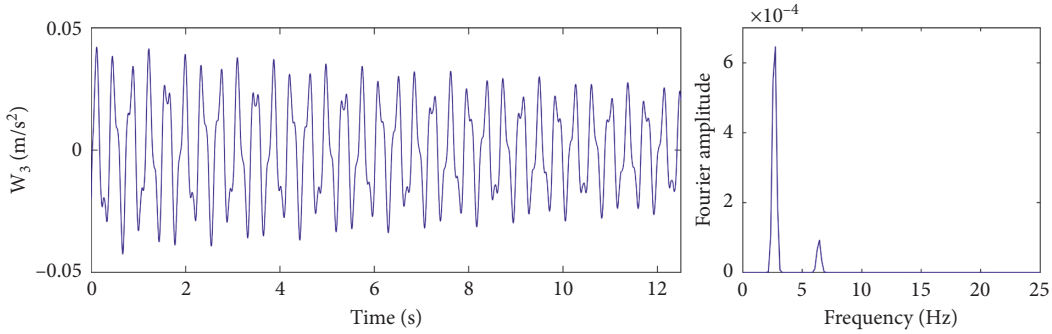

(a)

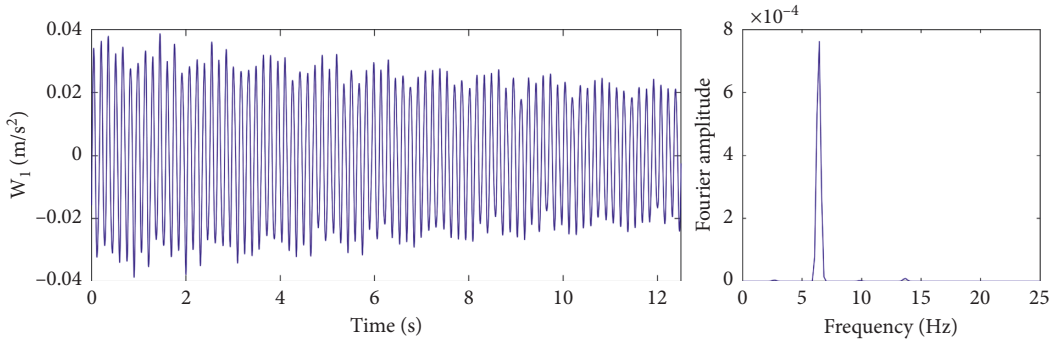

(b)

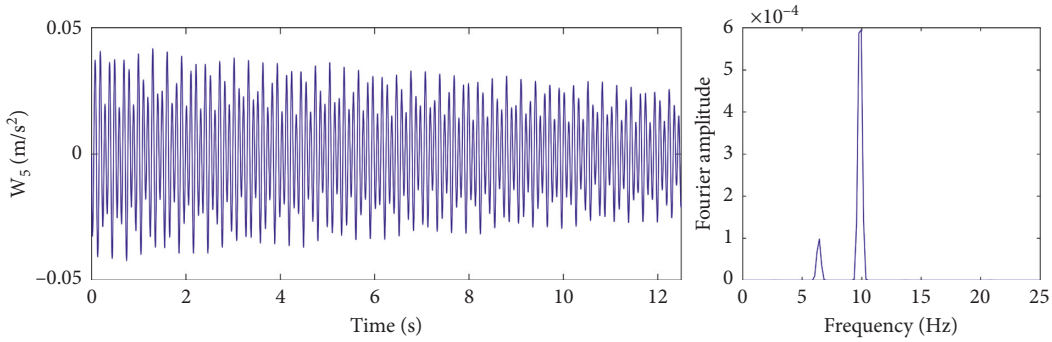

(c)

Figure 6: Continued.

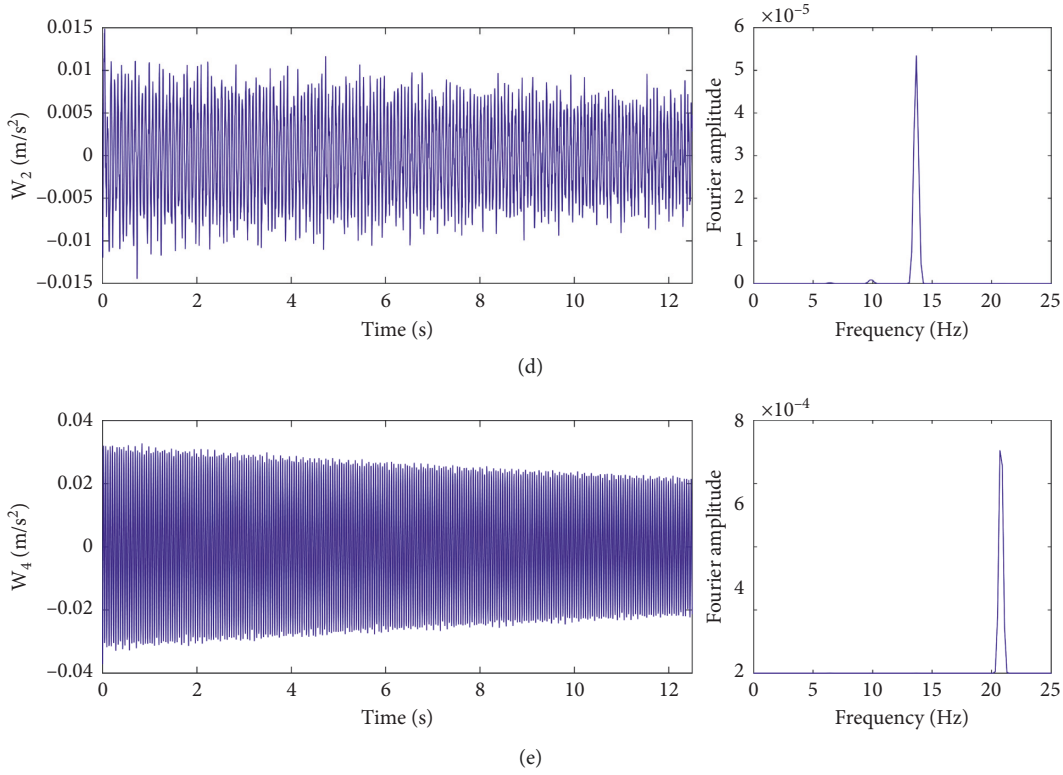

Figure 6: The matrix reconstruction for D_2 in SGMD-SVD.

and IMF2 has been overlapped, which is approximated as the component of theoretical instantaneous frequency 5. In the results of EMD decomposition, there is no component that coincides with the theoretical instantaneous frequencies 3 and 4. Therefore, it is difficult to decompose signals from time-variant systems. Figure 10 demonstrates that the Fourier spectrum has several peaks within a scope of the most significant frequency components, which means that it is relatively difficult for the traditional methods to realize the signal decomposition. As shown in Figures 13 and 14, significant fluctuations are observed as the noise in measurements influences the performance of EMD in signal decomposition.

As shown in Figures 12 and 14, comparing the results of SGMD and EMD, SGMD has much better performance for instantaneous frequency identification and the signal decomposition.

3.3. Effect of Measurement Noise. Noise was added to the response simulation of Case 3 to carry out the further study on robustness of method for modal identification using SGMD, and the signal-to-noise ratio was 10 dB and 20 dB, respectively. To decrease the high frequency noise, the noisy responses are processed by a band-pass filter with a frequency range of 1 ~ 30 Hz due to the fact that the first five are observed within 30 Hz. For SGMD employed for signal decomposition, the same procedure is followed, and the obtained instantaneous frequencies are recognized and shown in Figure 15. As shown in Figure 15, all the five frequency models are in a complete separation state and the true values are close with the identified instantaneous frequencies. As a result, the results on the first model show the best agreement. Therefore, it can be seen from the above that the first model dominates the vibration. Moreover, the results of models 2 and 5 under such high noise effects are also satisfactory.

It can be seen that the SGMD method is applicable to both modal parameter identification of linear systems and instantaneous frequency of nonlinear systems. Compared with the traditional EMD and SVD identification methods, SGMD has better robustness and adaptability.

4. Experimental Verifications

SGMD can be used to decompose linear and nonlinear signals. The existing methods, due to end effects or time-variant systems with nonstationary signals, still have some limitations when it comes to processing signals from time-invariant systems. In order to explore the performance of instantaneous frequency identification in the mechanical structure using the proposed method in this case, experimental studies on both time-variant and time-invariant systems were performed in the laboratory. The proposed method is used to extract the instantaneous frequency of the structure, and the real vibration data are used for signal decomposition. An experimental study of the first invariant structure was employed to prove the accuracy of proposed method, with particular attention on how to use the

Table 1: Comparison of modal parameter identification results.

Model	SVD					SGMD				SGMD-SVD				
	Natural frequency	Error (%)	Damping ratio	Error (%)	MAC	Natural frequency	Error	Damping ratio	Error (%)	Natural frequency	Error (%)	Damping ratio	Error (%)	MAC
1	2.204774	17.25	0.128879	20.90	0.904	2.660464	0.15%	0.105204	1.31	2.660789	0.13	0.10789	1.21	0.959
2	6.433347	0.32	0.267495	3.60	0.77	6.39942	0.85%	0.255257	1.14	6.399353	0.85	0.254756	1.33	0.898
3	9.653678	4.12	0.488475	21.30	0.973	9.864816	2.04%	0.396764	1.47	9.864922	2.04	0.407428	1.17	0.952
4	24.27983	70.88	0.20743	63.50	0.964	13.65411	3.98%	0.558576	1.71	13.67084	3.86	0.553462	2.61	0.914
5	56.19371	145.20	0.035751	96.10	0.958	20.79091	9.73%	0.796246	13.14	20.79083	9.73	0.777912	15.14	0.948

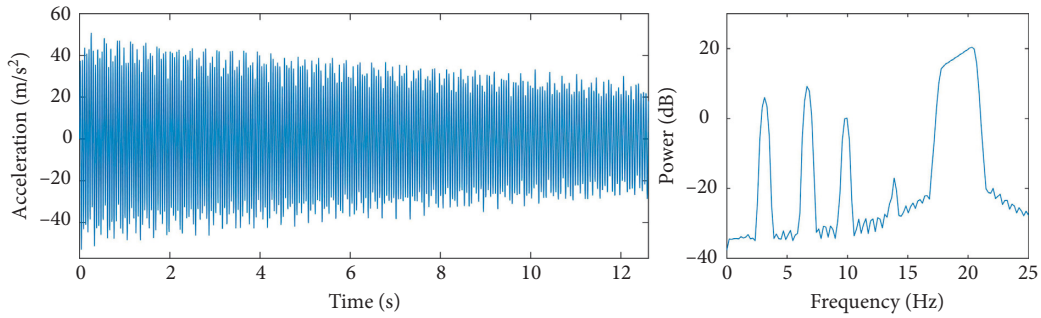

Figure 7: Time-domain response signal and its fast Fourier transform spectrum in the simulation study (Case 2).

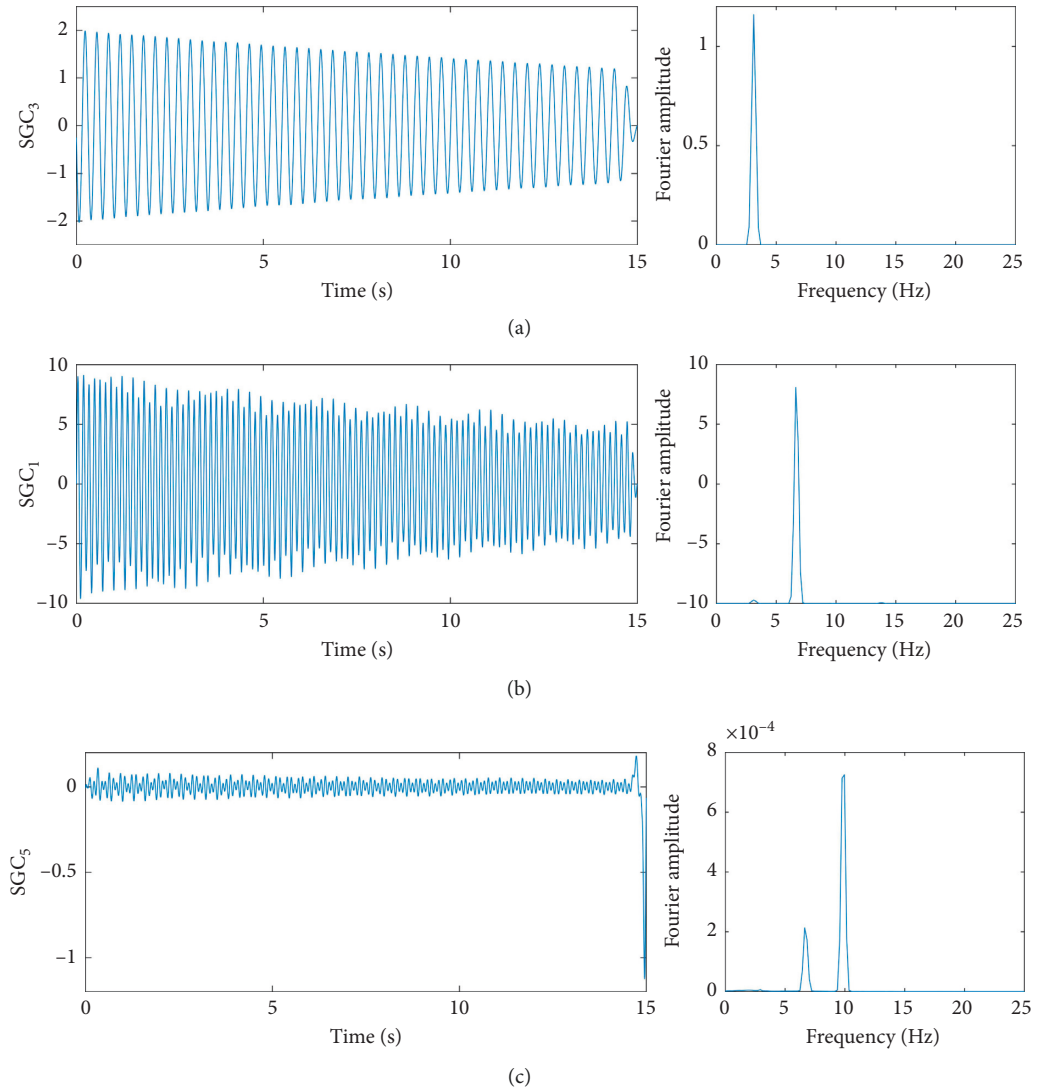

Figure 8: Continued.

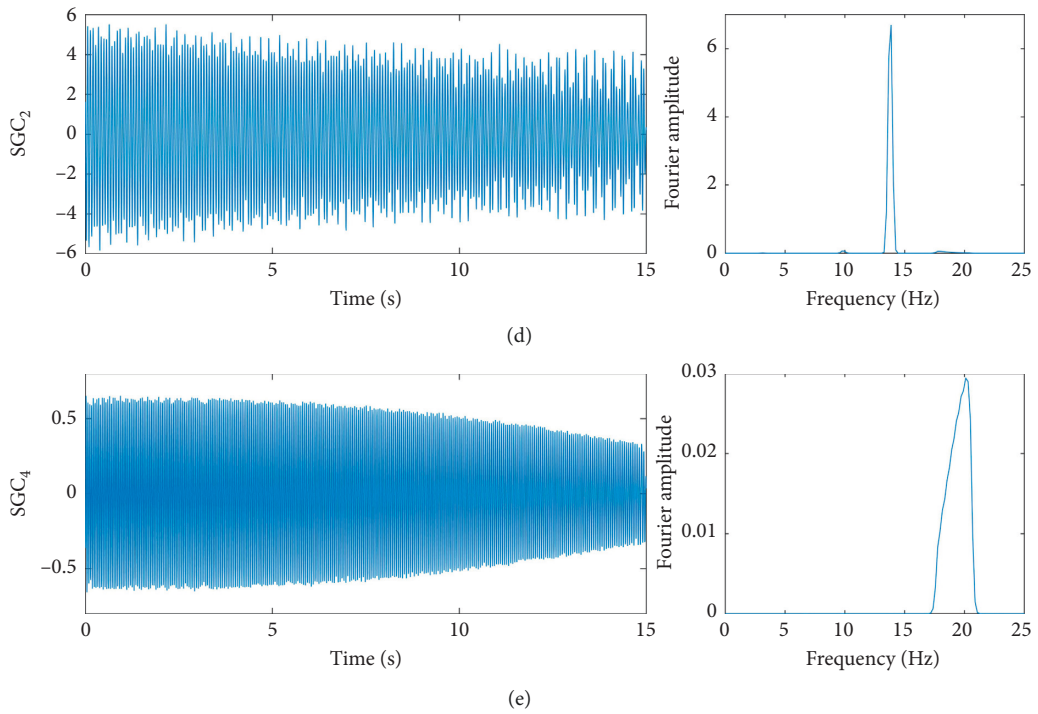

Figure 8: Decomposed symplectic geometric components (SGCs) of the response signal with symplectic geometric model decomposition in the simulation study (Case 2).

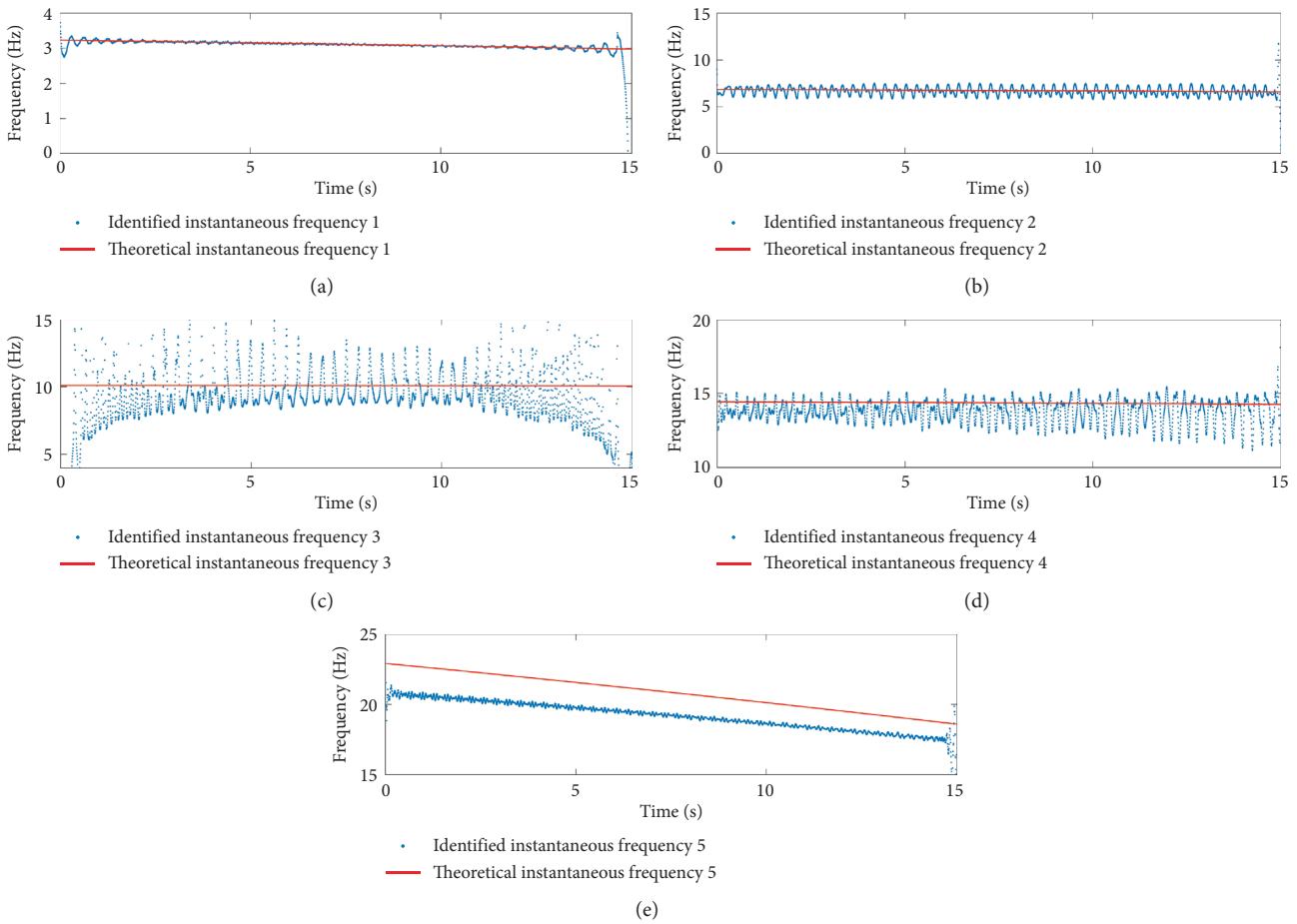

Figure 9: Symplectic geometric model decomposition applied to identify instantaneous frequencies in the simulation study (Case 2).

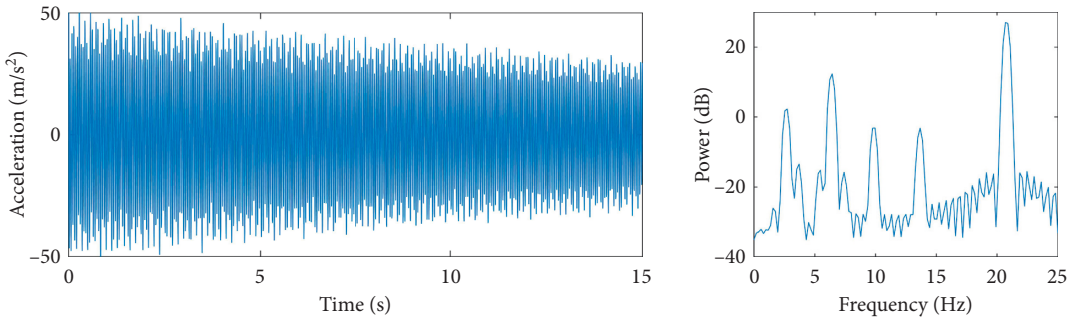

FIGURE 10: The results in the simulation study (Case 3): time-domain response signal as well as the fast Fourier transform spectrum.

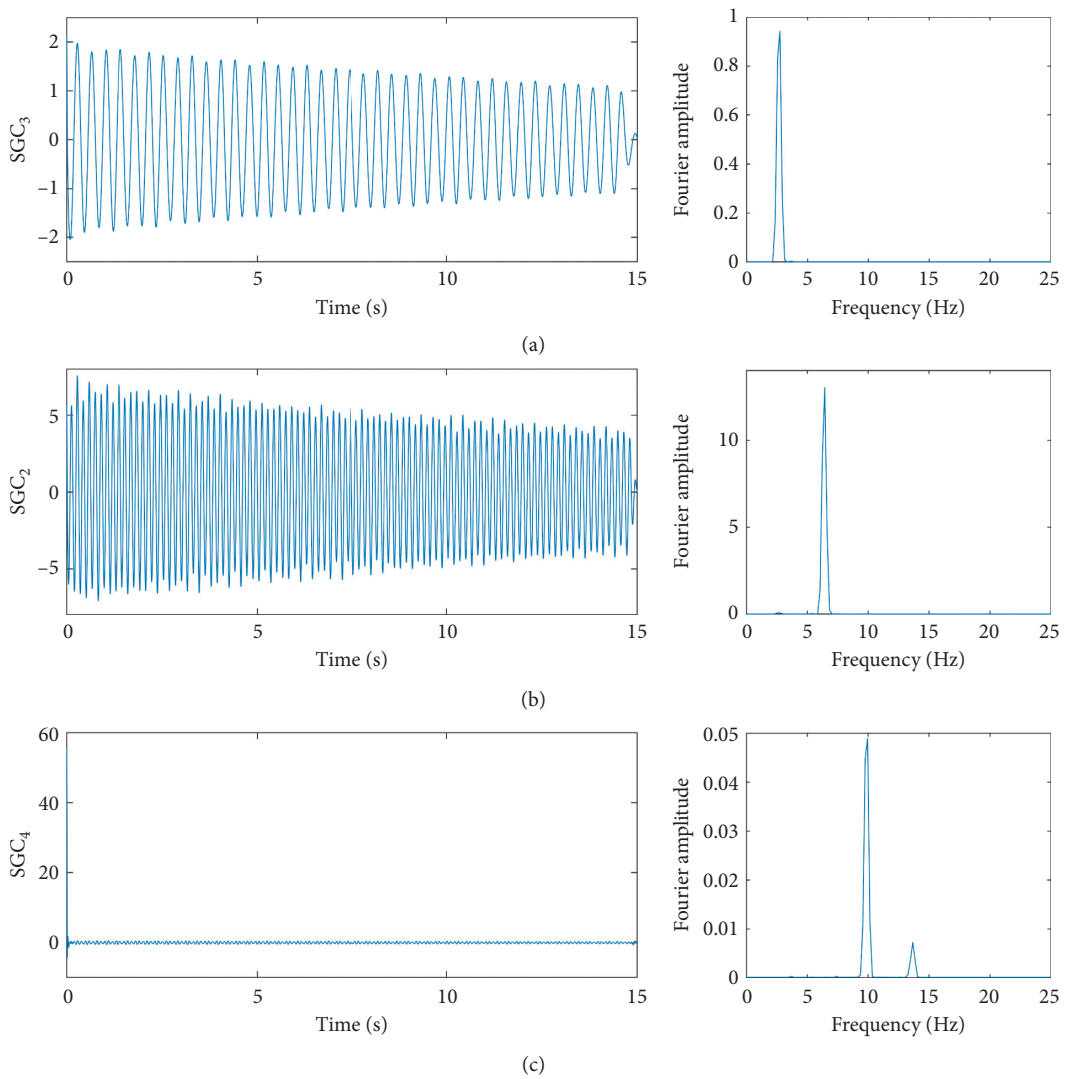

FIGURE 11: Continued.

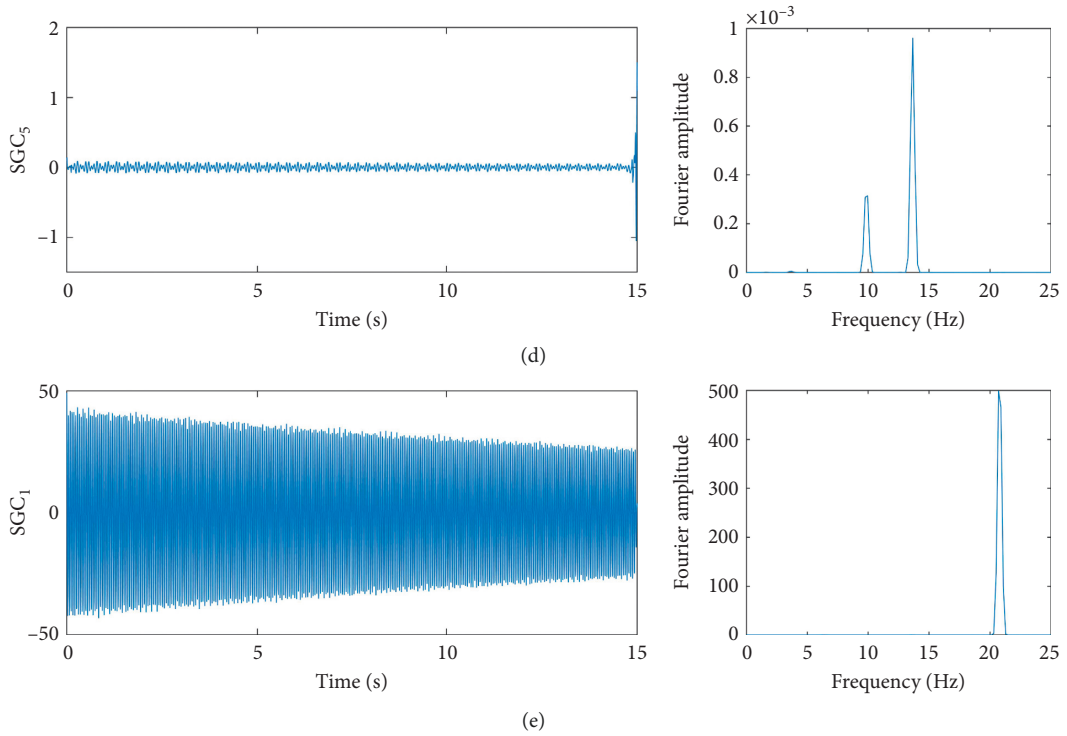

Figure 11: Decomposed symplectic geometric components (SGCs) of the response signal with symplectic geometric model decomposition in the simulation study (Case 3).

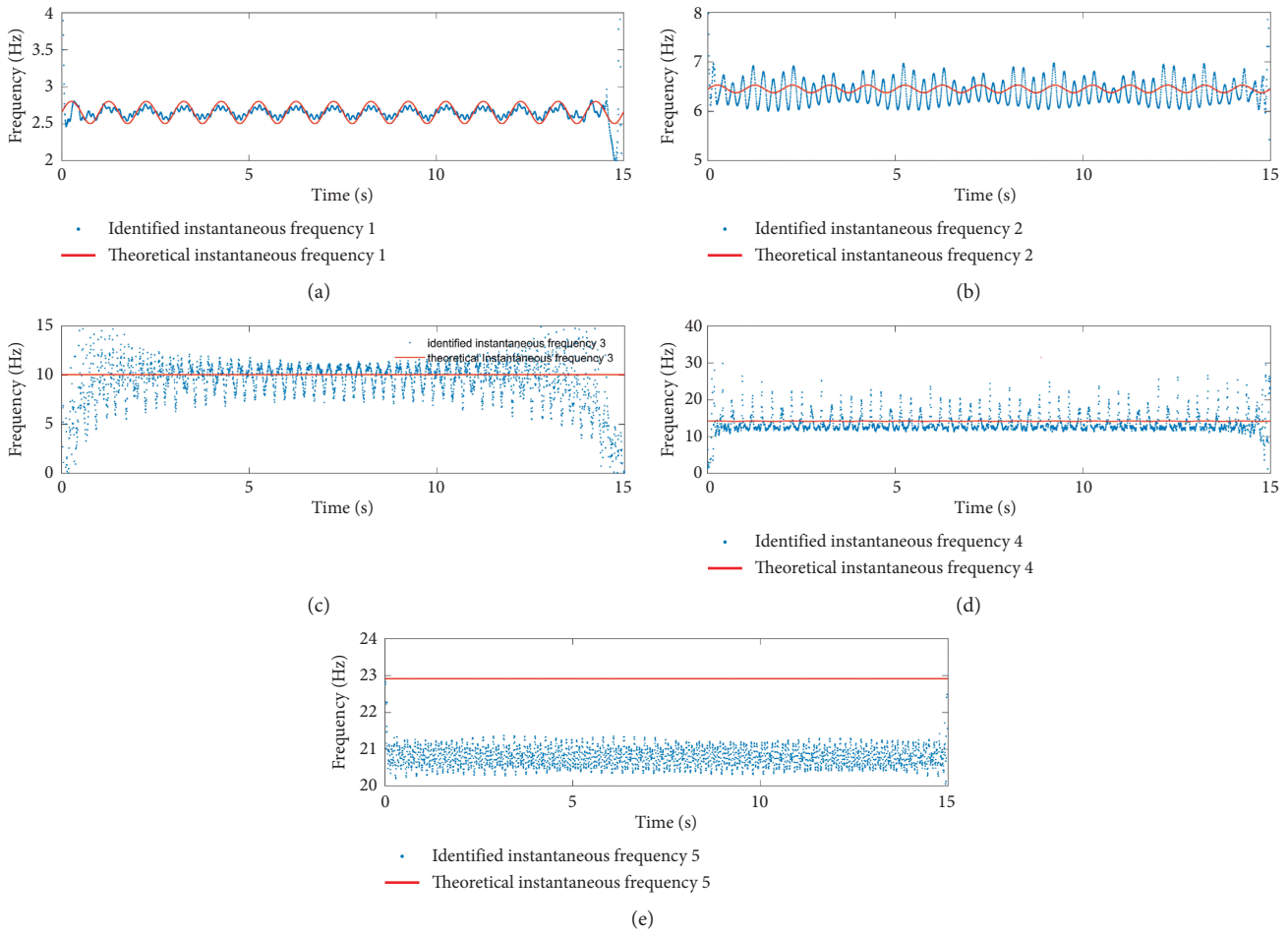

Figure 12: The results in the simulation study (Case 3): identified instantaneous frequencies by the symplectic geometric model decomposition.

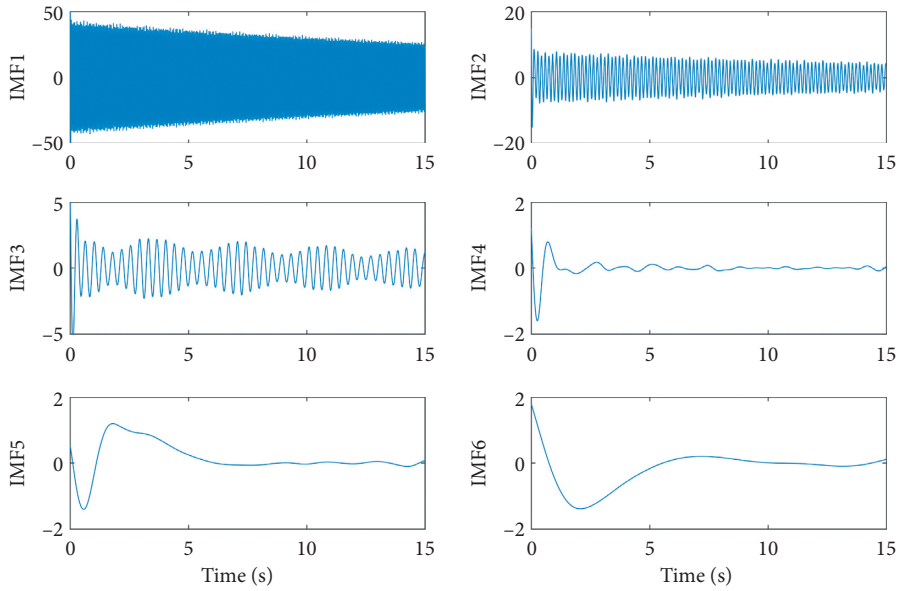

Figure 13: Extracted intrinsic model functions (IMFs) of the response signal on the basis of empirical model decomposition in the simulation study (Case 3).

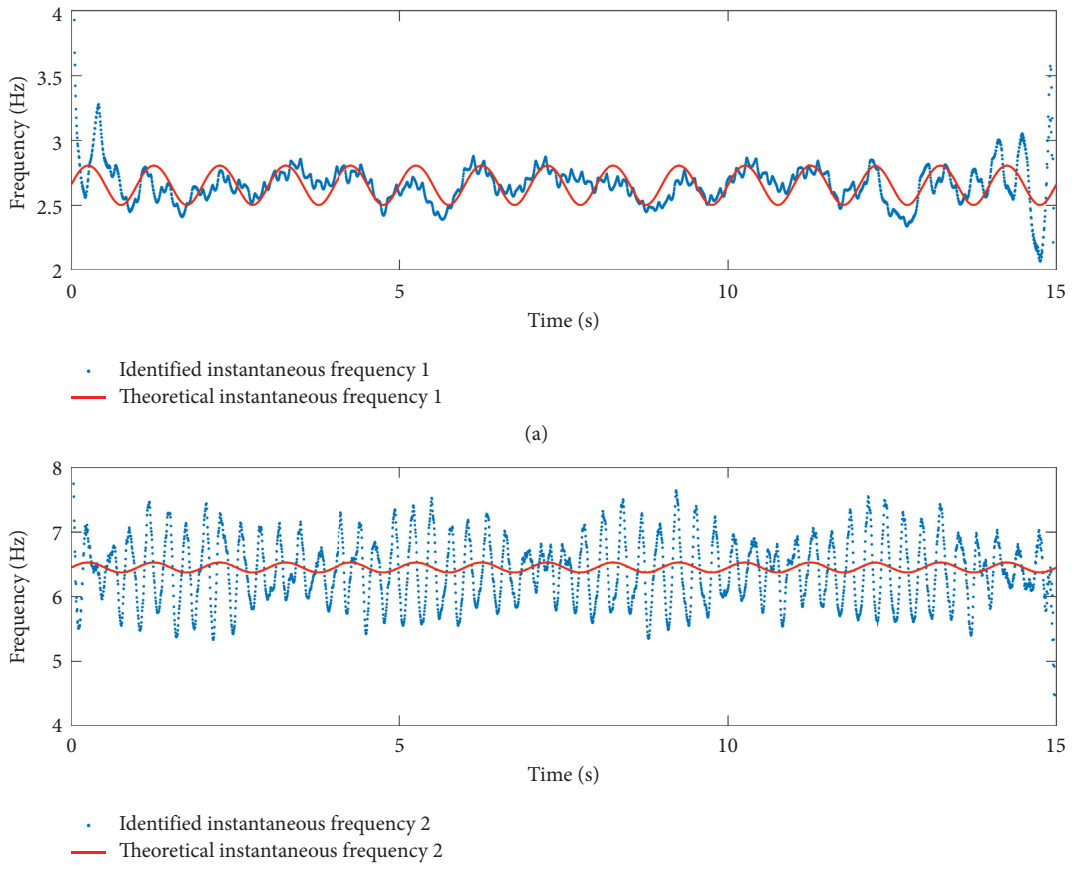

Figure 14: Continued.

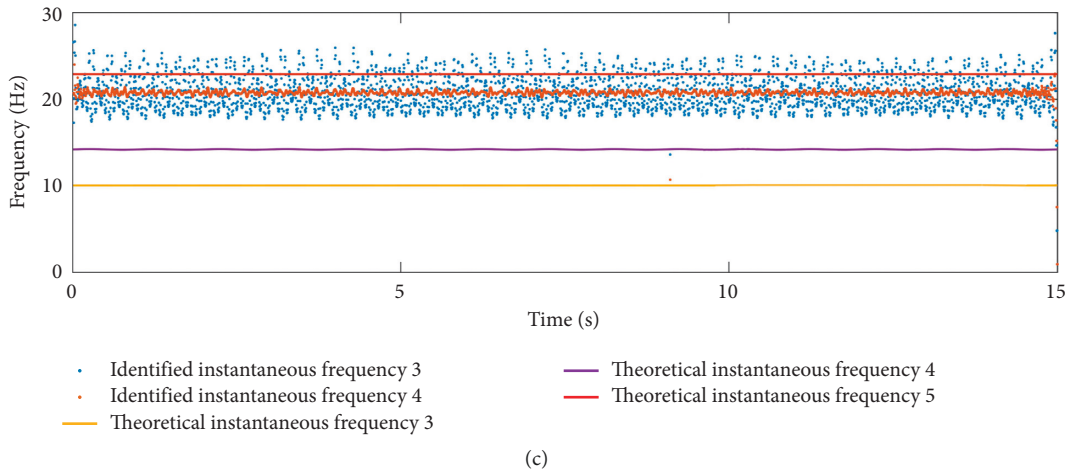

(c)

Figure 14: Identified instantaneous frequencies on the basis of empirical model decomposition in the simulation study (Case 3). (a) Identified instantaneous frequency from IMF 5. (b) Identified instantaneous frequency from IMF 4. (c) Identified instantaneous frequency from IMF 1–3.

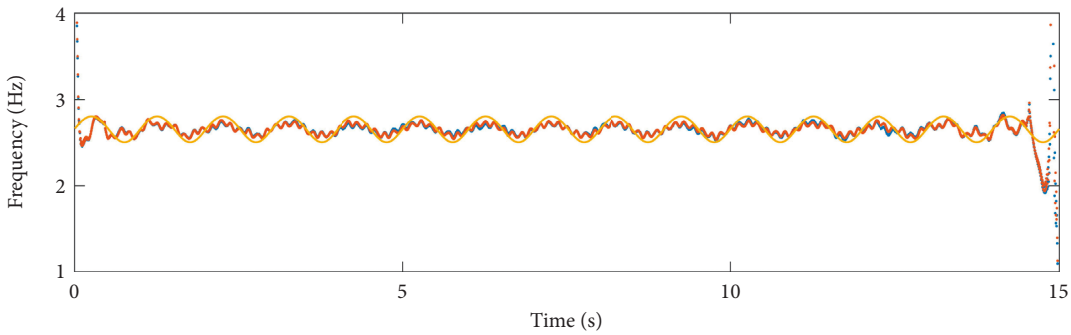

(a)

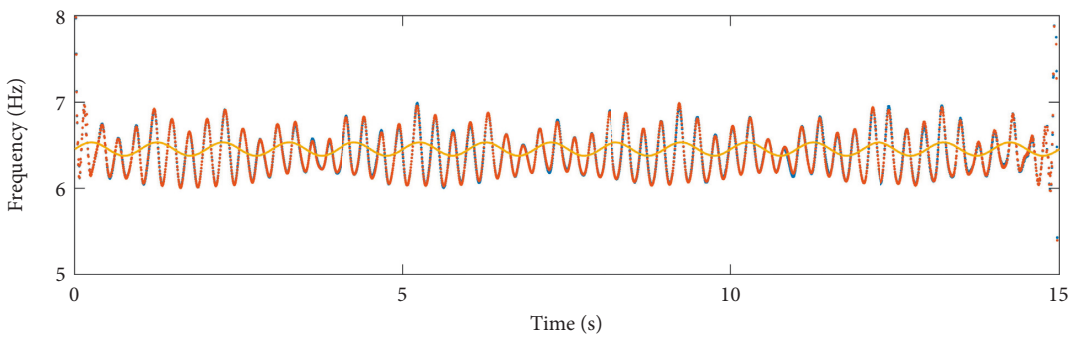

(b)

Figure 15: Continued.

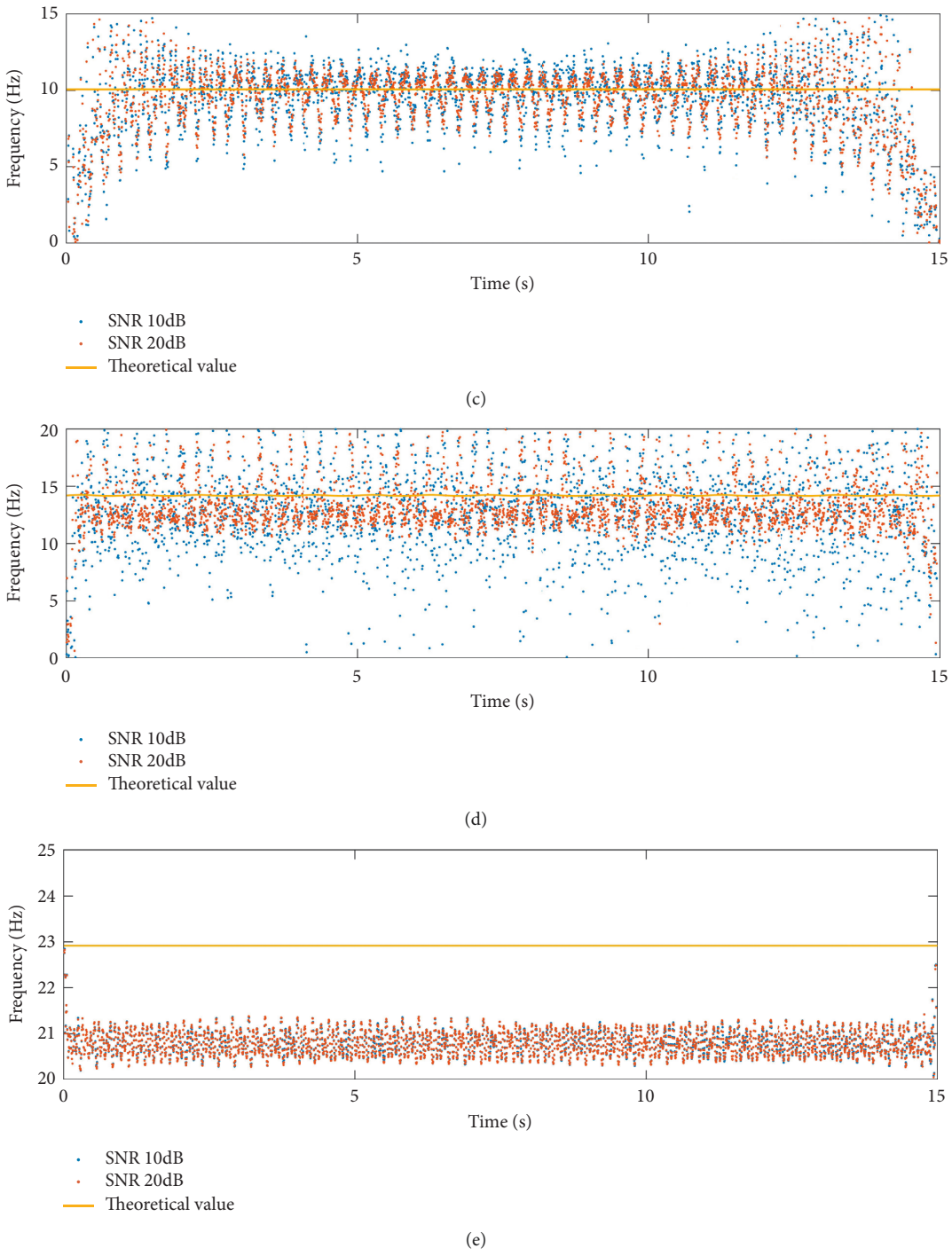

Figure 15: Identified instantaneous frequencies under different noise levels with symplectic geometric model decomposition in the simulation study (Case 3). (a) Identified instantaneous frequency of Mode 1. (b) Identified instantaneous frequency of Mode 2. (c) Identified instantaneous frequency of Mode 3. (d) Identified instantaneous frequency of Mode 4. (e) Identified instantaneous frequency of Mode 5.

proposed method to implement a better result. The second example is a time-variant structure, a wheel and rail vehicle system. Moreover, the signals measured from a moving vehicle are nonstationary. Those experiments can be implemented to prove the applicability and efficiency of instantaneous frequency identification and signal decomposition via SGMD.

4.1. Modal Identification of a Time-Invariant Structure. The applicability of the method proposed in this paper is demonstrated by the first example given in this section. A dissected vehicle under-frame crossbeam of high-speed train has been selected as the test object; usually the CRH3 high-speed train car body with 20 toes in crossbeams can improve the stiffness of car body and inhibit the chassis vertical

deformation. By adjusting the chassis beam, the natural frequency resonance of bodywork and bogie can be effectively avoided. To verify the accuracy of recognition results of experimental modal parameters, the finite element software Hypermesh and Nastran were used to complete the model grid division and modal calculation of the bottom crossbeams in this section. The material property was as follows: elastic modulus $E = 70$ GPa, density of rho = 2710 kg/m^3, and Poisson's ratio $\mu = 0.33$.

This paper mainly analyzes the modal parameters of the crossbeam below 500 Hz, and the simulation results are shown in Figure 16. Considering the actual testing samples had two constraints, the vertical constraints are applied at the same position on geometry modal. The results of finite element analysis indicate that the first three models of vibration are larger in each sequence at the upper corner of the crossbeam, and the transverse response is larger than the vertical response because of the applied constraints. Therefore, as shown in Figure 17, an acceleration sensor is placed above the crossbeam to obtain vertical and horizontal vibration signals during the experiment. The testing material was made of aluminum alloy, but the sensor mass was closed to 1% of the beam mass. Therefore, to decrease the mass effect from the sensor in measurement, only one acceleration sensor was placed. The crossbeam was divided into 68 tapping points, and five times excitation induced by a hammer were applied on each tapping point. This hammer was connected to the 24 bit NI USB-6255DAQ board via a charge amplifier. The accelerometer is directly connected to the NI USB-6255 for signal acquisition. The acquisition duration is 5 s per test, and the sampling frequency is 10 kHz.

Before applying the method of this paper, the test results firstly need to be carried into preprocess for better identification of modal parameters. The acoustic and vibration output signals are as shown in Figure 18(a), and the Fourier transform is performed on the input hammer signal and the output signal; also, the ratio of self power spectrum to the cross power spectrum is obtained to get the estimated frequency response function of $H1$. These results are shown in Figure 18(b). Then, the means of 5 times $H1$ for each measurement point have been calculated and then inverse fast Fourier transform was performed; the time-domain response curve obtained by the preprocessing is subjected to modal parameter identification according to the symplectic geometric model decomposition method described above, and it is shown in Figure 18(c).

The method proposed in the Section 2.4 is used to identify the time-domain response signal of bottom crossbeam. The modal parameters of right singular value matrix after decomposition are shown in Table 2. Since the laboratory test is conducted by means of SISO multiple measurements, the cumulative error of the vibration model of the measuring point is large, and the result of vibration model is not ideal. Therefore, it would not be shown here. There is a large difference between the experimental and simulation results, and this error is caused by the damping here, which is not added in the simulation model.

The vibration of structure causes a change in the sound pressure of the surrounding medium. For a vibrating plate structure in the sound field, the plate can be divided into a limited number of small units. Those small units which are closely positioned on the surface of the plate can be assumed as point sources in the sound pressure measurement. Therefore, where the distances are relatively close, the sound pressure of the measuring point is proportional to the vibration acceleration of the reference point. Prezelj et al. [31] have also verified the relationship between the near-field sound pressure generated by the vibrational radiation of flat structure and dynamic response of the structure.

In addition, Table 3 shows that the first- and third-order modal recognition results are closer to the simulation results than those of the vibration recognition. However, the second-order errors are larger. According to those results, the method is applicable to the identification of structural modal parameters of near-field sound pressure signals. It should be noted that when applying the sound pressure signal to identify the structural modal parameters, the distance between the microphone and the structure should be as small as possible so that effectiveness of the air damping can be ignored during the sound wave propagation process.

Both simulation and experimental results confirm that the method proposed in this paper can be used to achieve the accuracy and consistency of modal parameters. However, in the data processing, since each layer of SGC is extracted, it is necessary to repeat the construction matrix. Therefore, a large number of repeated calculations are required. Actually, this method is a time-domain decomposition method and it is very sensitive to the data length, as shown in the time-domain diagram in Figures 19 and 20, when the time-domain response signal is decomposed. However, the test of output signal length is 5 s. If the data length of the decomposed SGC signal is greater than 1 s, the vibration signal has been attenuated to a very small value, and the modal identification will contribute to increase the identify accuracy under the appropriate adjustment of data length after decomposition. However, in this paper, there are much more points in the experimental model, and all response time is unified to 2.5 s.

4.2. Instantaneous Frequency Identification of a Time-Variant System. The second example is shown in Figure 21, which is a time-variant wheel-rail coupling system. A field braking test was carried out here on the tangent ballast track. The test line's length was close to 1500 m. The test train comprised three HX-type heavy haul locomotives which are widely employed in 10,000 t freight trains connected by 100-type coupler and draft gear systems. It was reported that a bogie frame had a natural frequency similar to the excitation frequencies which were included in the time-variant loads and that this similarity resulted in fatigue damage in the bogie frame [32]. If the track clearance on the track is large, the natural frequency of the bogie will be frequently excited, and thus detecting the excitation frequency of bogie frame and time-variant load has vital engineering values. According to the literature [33], any interaction between external excitations and natural vibration models is primarily located at relatively low-frequency regime below 200 Hz. Four acceleration sensors are placed above the bogie frame to record the

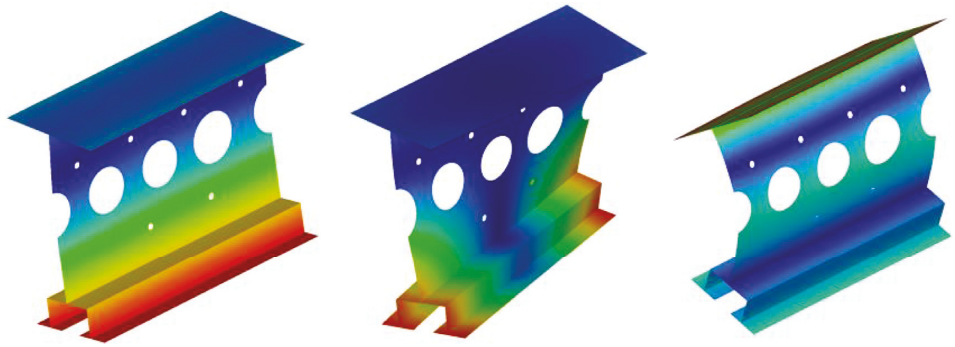

Figure 16: The first three models of simulation. (a) Mode Frequency = 65.0 Hz. (b) Mode Frequency = 214.1 Hz. (c) Mode Frequency = 447.1 Hz.

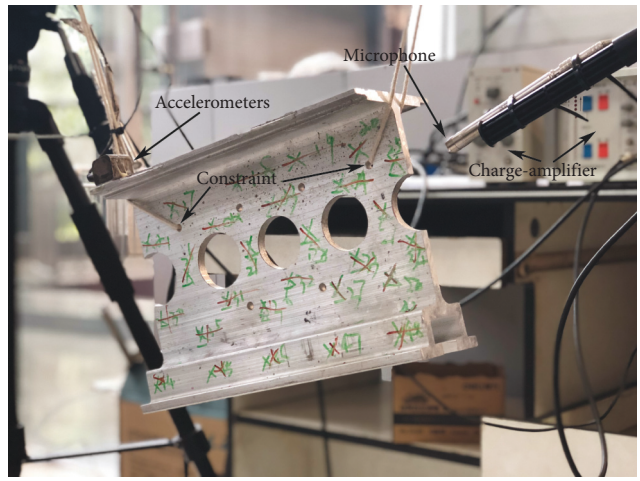

Figure 17: Experimental setup.

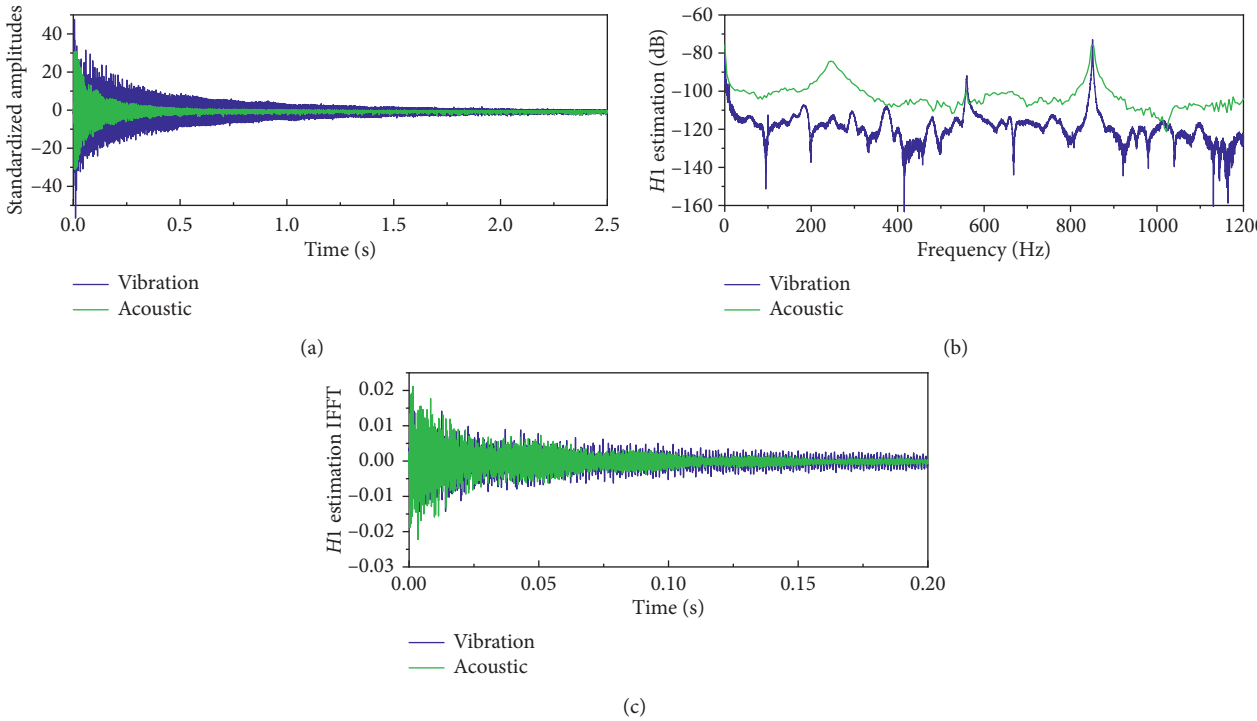

Figure 18: The acoustic and vibration signals. (a) Time series of acoustic and vibration signals. (b) $H1$ estimation frequency response functions. (c) $H1$ estimation inverse fast Fourier transform.

Table 2: The modal identification of vibration signals.

	Natural frequency	Error (%)	Damping ratio
Model 1	62.92	3.2	0.00213
Model 2	215.82	0.80	0.00073
Model 3	397.11	11.18	0.00029

Table 3: The results of acoustic identification.

	Natural frequency	Error (%)	Damping ratio
Model 1	69.0	6.15	0.0012
Model 2	246.3	15.04	0.0010
Model 3	425.3	4.88	0.0005

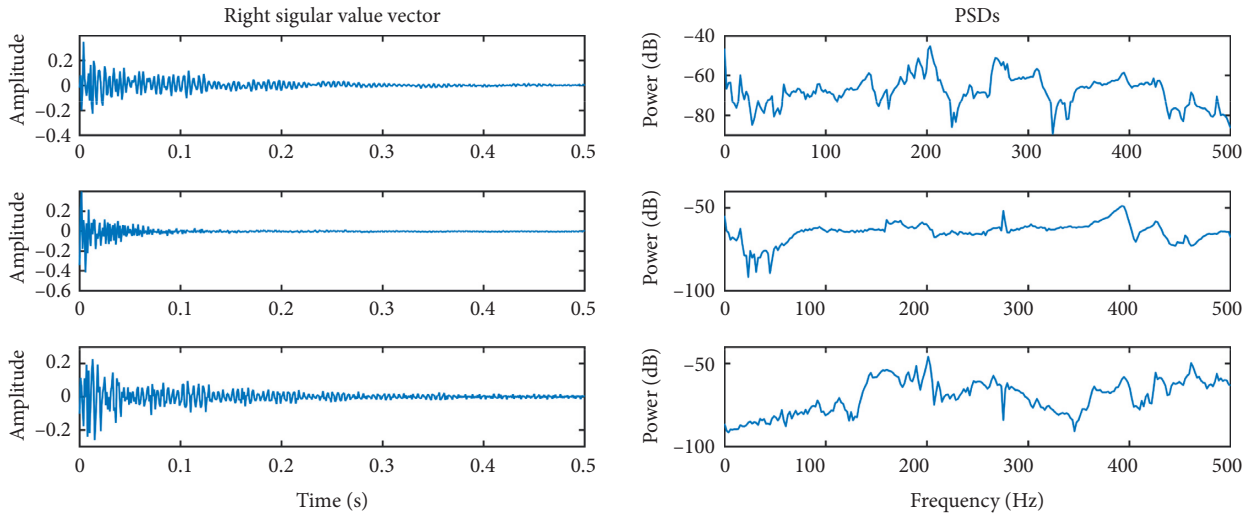

Figure 19: The first three models of vibration signal identification results.

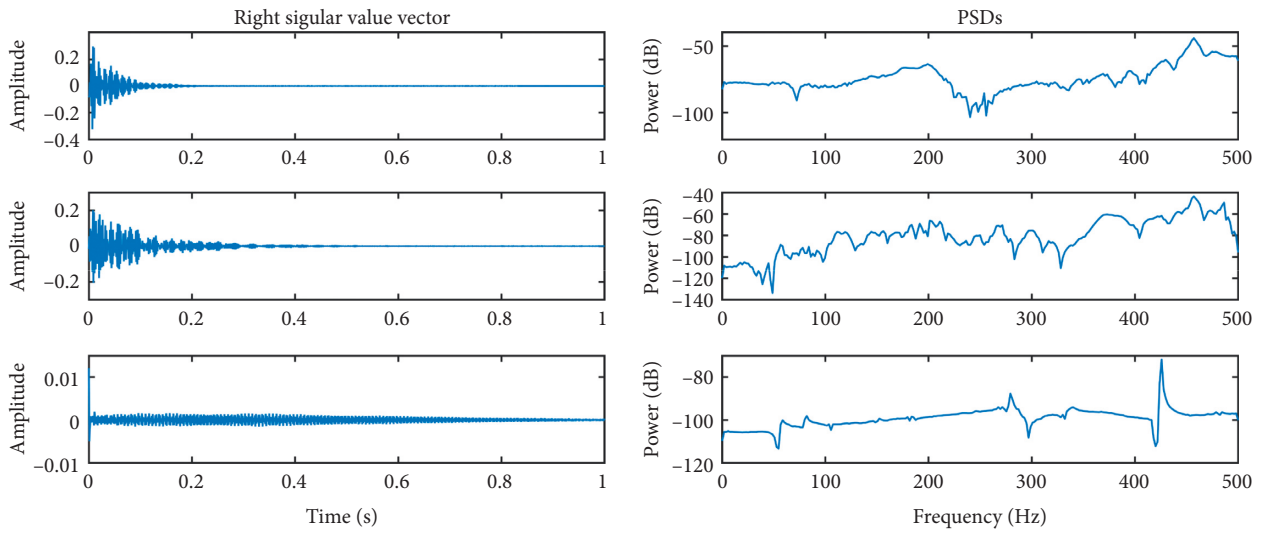

Figure 20: The first three models of acoustic signals identification results.

dynamic response of the moving vehicle. When the vehicle speed reached 80 km/h, resistance braking was performed and response data of about 9 seconds were recorded. The band-pass range is set to 0–100 Hz, with a sampling frequency of 5000 Hz. The time history of the acceleration response on the bogie during braking of the vehicle and its Fourier spectrum are shown in Figure 22. Moreover, we can see that the energy is primarily within a scope of 2–80 Hz. Approximately 63 Hz

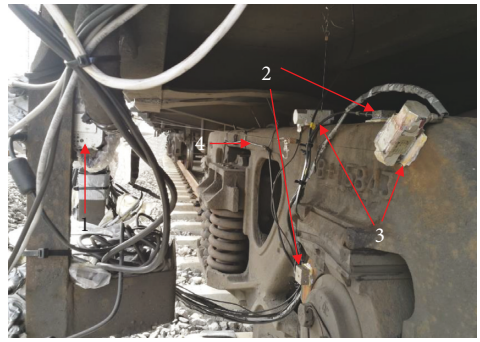

Figure 21: Test device for wheel and rail system in field test. 1: signal acquisition device; 2: acceleration sensor; 3: displacement sensor; 4: bogie.

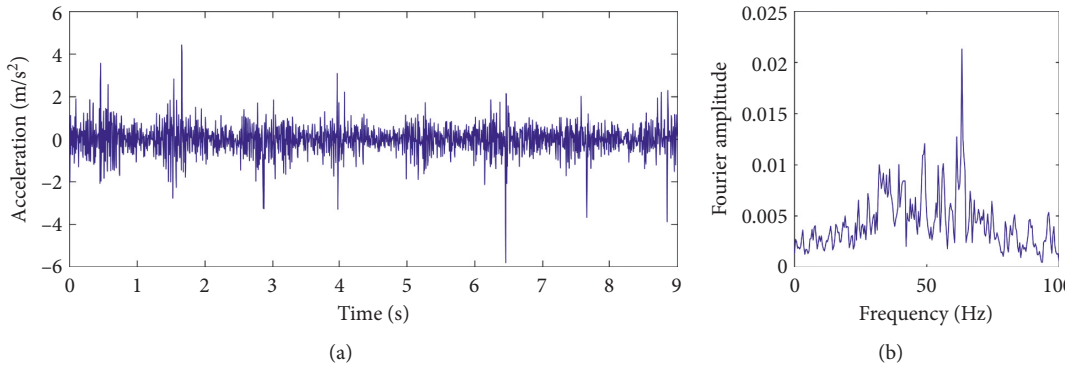

Figure 22: Wheel-rail coupling system: time history and fast Fourier transform spectrum of measured response.

corresponds to the maximum energy, and the frequency range from 30 to 70 Hz corresponds to the significant vibrations. It is obvious from the time history that there is a significant time-variant load excitation when the vehicle passes near the rail joint gap. If the moving vehicle locations are changed, the vibration characteristics of the system are also changed. During the running process of the vehicle, there are significant fluctuations and noise in the response signal.

Hence, the method proposed and the conventional EMD method, as well as the measured acceleration response, were used for the identification of the instantaneous frequency of time-variant systems. Figures 23 and 24 show the identified results from these two methods, respectively. The EMD method has a large number of ripple phenomena and overlaps at the instantaneous frequency, and there is no significant continuous frequency near the main frequency of 63 Hz in the Fourier spectrum. Meanwhile, the SGMD method described in this paper can effectively suppress the ripple phenomenon and overlap. Based on the results of past studies [33–35], the response reason for each SGC is determined. Also, the SGMD decomposes the acceleration response signal into 10 SGCs components. As shown in Figure 24, SGC_2 is the second-order natural frequency of the frame and external excitation (80 Hz–100 Hz); SGC_3 causes the bounce of the bogie frame (6–8 Hz); SGC_4 and SGC_7 are the wheel noncircular excitation (13.67 Hz, 27.73 Hz); SGC_5 and SGC_6 correspond to 0.39 Hz and 1.56 Hz, which are related to the low-frequency body and bogie rigid motion; SGC_8 is the rail surface excitation (3.12 Hz); SGC_9 450 is the first-order natural frequency of bogie frame (63.28 Hz). Among them, the first-order natural frequency of the bogie frame has obvious endpoint problems. SGC_1 and SGC_{10} instantaneous frequency distribution is in the entire analysis frequency band, so it is considered as noise and is not shown. Obvious fluctuations are observed within the identified instantaneous frequencies, which are caused by the uncertainties of wheel-rail coupling and measurement noise. Therefore, the efficiency and effectiveness of this method have been verified on identifying the instantaneous frequency of time-variant systems which have measurement noise as well as significant uncertainties.

5. Conclusions

The iterative method is introduced in the decomposition process of the symplectic geometry model decomposition, replacing the traditional similarity direct combination. Compared with other decomposition methods, SGMD does not need user-defined parameters and has better robustness and suppresses modal aliasing. The results show that better decomposition performance and robustness can be obtained by the proposed SGMD method, without setting user-defined parameters.

Moreover, a new modal parameter identification method is proposed for modal parameter identification using

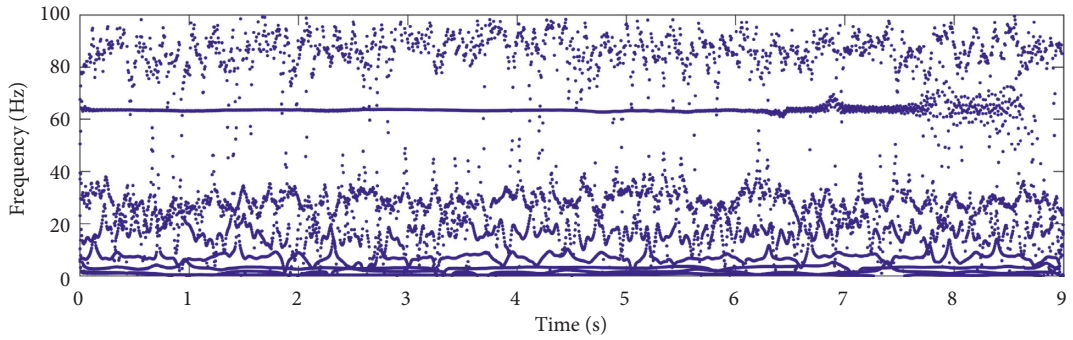

Figure 23: Identified instantaneous frequencies of wheel-rail coupling systems on the basis of empirical model decomposition.

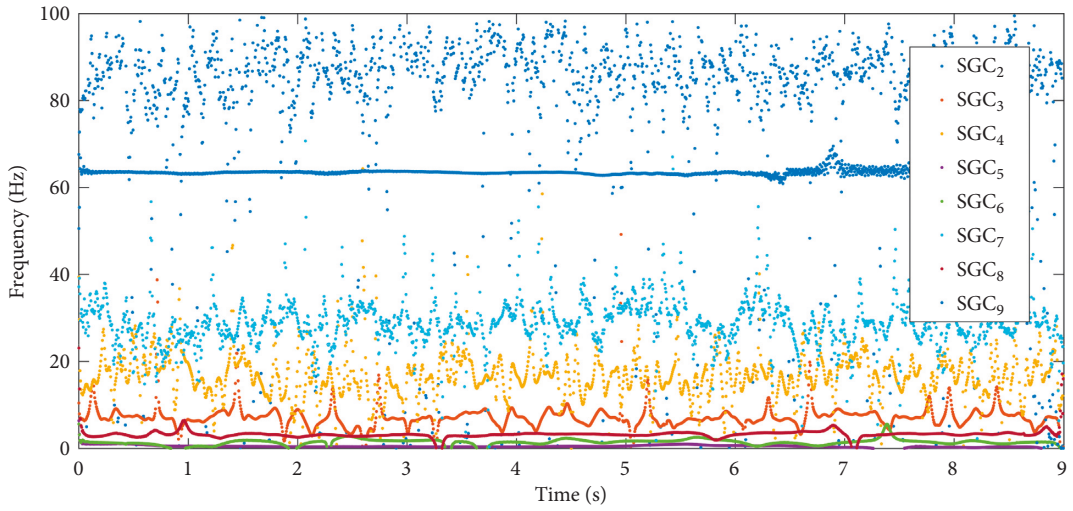

Figure 24: Identified instantaneous frequencies of wheel-rail coupling systems on the basis of symplectic geometry model decomposition.

symplectic geometry model decomposition. The core of this method is to solve the eigenvalues of Hamiltonian matrix by using symplectic geometric similarity transformation, and at the same time, the essential characteristics of the original signal can still be unchanged. It is proposed to calculate the normalized mean absolute errors which are between residual signals and original signals as the termination condition of decomposition. For the time-invariant structural model parameters, SVD is applied to decouple the modal, realize the identification of modal shape, and improve the recognition accuracy of the natural frequency and damping ratio directly via SGMD. Also, it is suitable to identify instantaneous frequencies of time-variant structures. The real response signal is decomposed into several SGCs, after which the Hilbert transform is utilized to recognize instantaneous frequency. Considering the three models of stiffness variation, simulation studies are carried out on time-invariant systems and time-variant systems to study the ability of the proposed method. Test and verification have been applied on the time-variant vehicle-rail beam and test line wheel-rail coupling system in the laboratory; also, the proposed method should been confirmed for applying the analysis of time-frequency and the instantaneous frequency identification of time-variant systems with non-stationary variable signal.

The experiments using simulated and real data show that the proposed method can make good use of the limited bandwidth of each model for signal decomposition, and it can also accurately extract the instantaneous frequency of the time-variant system. This method can be applied to signal decomposition as well as the modal identification of structures under environment excitation, whereas, it is not the key problem in this article. Further research will be performed to study the applicability of modal identification time-invariant and variant structures under environment excitation. In addition, compared with the same signal-based adaptive method (such as EMD), the SGMD-based system identification method has better robustness to noise and sampling frequency. There are still many problems in modal parameter identification for symplectic geometry decomposition, such as how to further improve the MAC of the mode, speeding up the calculation of SGMD, and solving reconstruction constraints and their end effects. Hence, in future research, the authors will pay more attention to these issues.

Data Availability

The data used to support the findings of this study have been deposited in the FIGSHARE repository (https://doi.org/10.6084/m9.figshare.7610429.v1).

Conflicts of Interest

The authors declare that they have no conflicts of interest.

Acknowledgments

This paper was supported by the National Key Research and Development Program of China (2016YFB1200401-102 and 2018YFB1201605) and the Sichuan Science and Technology Program (2019YFG0102).

References

[1] Z.-H. Min, L.-M. Sun, Z. Sun, and D.-H. Dan, "Modal parameter identification method based on wavelet transform and singular value decomposition," *Journal of Tongji University (Natural Science)*, vol. 37, pp. 460–465, 2009.

[2] X. Sun, M. Hao, and L. Zhang, "Research on broadband modal parameters identification under ambient excitation," *Journal of Building Structures*, vol. 32, pp. 151–156, 2011.

[3] B. H. Kim, N. Stubbs, and T. Park, "A new method to extract modal parameters using output-only responses," *Journal of Sound and Vibration*, vol. 282, no. 1-2, pp. 215–230, 2005.

[4] R. Brincker, L. Zhang, and P. Andersen, "Modal identification of output-only systems using frequency domain decomposition," *Smart Materials and Structures*, vol. 10, no. 3, pp. 441–445, 2001.

[5] L. Faravelli, F. Ubertini, and C. Fuggini, "System identification of a super high-rise building via a stochastic subspace approach," *Smart Structures and Systems*, vol. 7, no. 2, pp. 133–152, 2011.

[6] J.-N. Juang and R. S. Pappa, "An eigensystem realization algorithm for modal parameter identification and model reduction," *Journal of Guidance, Control, and Dynamics*, vol. 8, no. 5, pp. 620–627, 1985.

[7] Q. Qin, H. B. Li, L. Z. Qian, and C.-K. Lau, "Modal identification of Tsing Ma bridge by using improved eigensystem realization algorithm," *Journal of Sound and Vibration*, vol. 247, no. 2, pp. 325–341, 2001.

[8] J. M. Caicedo, S. J. Dyke, and E. A. Johnson, "Natural excitation technique and eigensystem realization algorithm for phase I of the IASC-ASCE benchmark problem: simulated data," *Journal of Engineering Mechanics*, vol. 130, no. 1, pp. 49–60, 2004.

[9] M. Doehler, X.-B. Lam, and L. Mevel, "Uncertainty quantification for modal parameters from stochastic subspace identification on multi-setup measurements," *Mechanical Systems and Signal Processing*, vol. 36, no. 2, pp. 562–581, 2013.

[10] F.-L. Zhang, Y.-C. Ni, S.-K. Au, and H.-F. Lam, "Fast Bayesian approach for modal identification using free vibration data, part I—most probable value," *Mechanical Systems and Signal Processing*, vol. 70-71, pp. 209–220, 2016.

[11] W.-J. Yan and L. S. Katafygiotis, "A novel Bayesian approach for structural model updating utilizing statistical modal information from multiple setups," *Structural Safety*, vol. 52, pp. 260–271, 2015.

[12] S. Sankararaman and S. Mahadevan, "Bayesian methodology for diagnosis uncertainty quantification and health monitoring," *Structural Control and Health Monitoring*, vol. 20, no. 1, pp. 88–106, 2013.

[13] K.-V. Yuen and J. L. Beck, "Updating properties of nonlinear dynamical systems with uncertain input," *Journal of Engineering Mechanics*, vol. 129, no. 1, pp. 9–20, 2003.

[14] G. Li and Q. Weilian, "Damage detection of bars based on strain mode and bayesian statistical method," *Journal of Wuhan University of Technology*, vol. 29, pp. 135–138, 2007.

[15] H. Pan and Z. Xie, "Modified bayesian spectral density approach and its application to modal parameter identification of super-tall building," *Journal of Building Structures*, vol. 37, no. 12, pp. 27–32, 2016.

[16] J. Hu, H.-F. Lam, and J.-H. Yang, "Operational modal identification and finite element model updating of a coupled building following Bayesian approach," *Structural Control & Health Monitoring*, vol. 25, no. 2, 2018.

[17] J. P. Noël and G. Kerschen, "Nonlinear system identification in structural dynamics: 10 more years of progress," *Mechanical Systems and Signal Processing*, vol. 83, pp. 2–35, 2017.

[18] D. J. Ewins, B. Weekes, and A. Delli Carri, "Modal testing for model validation of structures with discrete nonlinearities," *Philosophical Transactions of the Royal Society A: Mathematical, Physical and Engineering Sciences*, vol. 373, no. 2051, article 20140410, 2015.

[19] L. Faravelli, C. Fuggini, and F. Ubertini, "Toward a hybrid control solution for cable dynamics: theoretical prediction and experimental validation," *Structural Control & Health Monitoring*, vol. 17, no. 4, pp. 386–403, 2010.

[20] L. Xu and X. Chen, "Random analysis on vibration sources of train-track system," *Journal of the China Railway Society*, vol. 39, pp. 9–16, 2017.

[21] Y. Yang, Z. Peng, W. Zhang, and G. Meng, "Parameterised time-frequency analysis methods and their engineering applications: a review of recent advances," *Mechanical Systems and Signal Processing*, vol. 119, pp. 182–221, 2019.

[22] M. Mihalec, J. Slavič, and M. Boltežar, "Synchrosqueezed wavelet transform for damping identification," *Mechanical Systems and Signal Processing*, vol. 80, pp. 324–334, 2016.

[23] L. A. Montejo and A. L. Vidot-Vega, "Synchrosqueezed wavelet transform for frequency and damping identification from noisy signals," *Smart Structures and Systems*, vol. 9, no. 5, pp. 441–459, 2012.

[24] H. Li, X. Deng, and H. Dai, "Structural damage detection using the combination method of EMD and wavelet analysis," *Mechanical Systems and Signal Processing*, vol. 21, no. 1, pp. 298–306, 2007.

[25] Z. Y. Shi and S. S. Law, "Identification of linear time-varying dynamical systems using Hilbert transform and empirical mode decomposition method," *Journal of Applied Mechanics*, vol. 74, no. 2, pp. 223–230, 2007.

[26] P. Ni, J. Li, H. Hao et al., "Time-varying system identification using variational mode decomposition," *Structural Control & Health Monitoring*, vol. 25, no. 6, article e2175, 2018.

[27] H. Xie, Z. Wang, and H. Huang, "Identification determinism in time series based on symplectic geometry spectra," *Physics Letters A*, vol. 342, no. 1-2, pp. 156–161, 2005.

[28] H. Pan, Y. Yang, X. Li, J. Zheng, and J. Cheng, "Symplectic geometry mode decomposition and its application to rotating machinery compound fault diagnosis," *Mechanical Systems and Signal Processing*, vol. 114, pp. 189–211, 2019.

[29] P. Bonizzi, J. M. H. Karel, O. Meste, and R. L. M. Peeters, "Singular spectrum decomposition: a new method for time series decomposition," *Advances in Adaptive Data Analysis*, vol. 6, no. 4, article 1450011, pp. 107–109, 2015.

[30] J. E. Cooper, "Identification of time varying modal parameters," *The Aeronautical Journal*, vol. 94, no. 938, pp. 271–278, 1990.

[31] J. Prezelj, P. Lipar, A. Belšak, and M. Č.lšak, "On acoustic very near field measurements," *Mechanical Systems and Signal Processing*, vol. 40, no. 1, pp. 194–207, 2013.

[32] J. T. Pearson, R. M. Goodall, T. X. Mei, and G. Himmelstein, "Active stability control strategies for a high speed bogie," *Control Engineering Practice*, vol. 12, no. 11, pp. 1381–1391, 2004.

[33] Y. Lu, P. Xiang, P. Dong, X. Zhang, and J. Zeng, "Analysis of the effects of vibration modes on fatigue damage in high-speed train bogie frames," *Engineering Failure Analysis*, vol. 89, pp. 222–241, 2018.

[34] H. Shi, J. Wang, P. Wu, C. Song, and W. Teng, "Field measurements of the evolution of wheel wear and vehicle dynamics for high-speed trains," *Vehicle System Dynamics*, vol. 56, no. 8, pp. 1187–1206, 2018.

[35] J. Liu, Y. Zhao, L. Ling, and X.-Z. Sheng, "Operational modal analysis of bogie frame and its effect on vibration transfer of high-speed train," *Noise and Vibration Control*, vol. 35, no. 3, pp. 19–23, 2015.

Hindawi
Shock and Vibration
Volume 2019, Article ID 7513261, 18 pages
https://doi.org/10.1155/2019/7513261

Research Article

Online Modal Identification of Concrete Dams Using the Subspace Tracking-Based Method

Lin Cheng,[1] **Fei Tong**,[1] **Jie Yang**,[1] **and Dongjian Zheng**[2]

[1]*State Key Laboratory of Eco-Hydraulics in Northwest Arid Region of China, Xi'an University of Technology, Xi'an 710048, China*
[2]*State Key Laboratory of Hydrology-Water Resources and Hydraulic Engineering, Hohai University, Nanjing 210098, China*

Correspondence should be addressed to Fei Tong; tongfei921216@163.com

Received 13 October 2018; Revised 21 January 2019; Accepted 26 March 2019; Published 23 April 2019

Guest Editor: Filipe Magalhaes

To investigate the time-varying dynamic characteristics of concrete dams under the excitation of large earthquakes for online structural health monitoring and damage evaluation, an online modal identification procedure based on strong-motion records is proposed. The online modal identification of concrete dams is expressed as a subspace tracking problem, and a newly developed recursive stochastic subspace identification (RSSI) method based on the generalized yet another subspace tracker (GYAST) algorithm, which exploits both the accuracy of the subspace identification and fast computational capability, is used to extract the time-varying modal parameters of concrete dams during earthquakes. With the simulated vibration response records, a numerical example is used to verify the accuracy, robustness, and efficiency of the proposed GYAST-based, time-varying modal identification method. Then, the realistic strong-motion records of the Pacoima arch dam are analysed using the proposed modal identification procedure, and the time-varying characteristics of the concrete arch dam during three different earthquakes are analysed.

1. Introduction

The modal parameters of concrete dams, including the natural frequencies, damping ratios, and modal shape vectors, extracted from earthquake response records can be used for structural antiearthquake capacity analysis, health monitoring, and postearthquake structural damage evaluation. These parameters have obvious physical meanings and represent the practical dynamic characteristics of structures. Some researchers have made efforts to address the modal identification problem of concrete dams based on earthquake response records [1–6]. However, the modal identification methods adopted in the past studies are restricted to linear systems and stationary processes, and using such methods would require the assumption that the dam-reservoir-foundation system is linear and time invariant for the duration of a vibration measurement. The dam-reservoir-foundation system under the excitation of large earthquakes may present some time-varying characteristics, resulting from the time-varying character of the material parameters, boundary conditions, dam-reservoir-foundation interactions, and structural damage [7]. Using the offline modal identification procedure to extract the constant modal parameters cannot track the time-varying dynamic properties of a structure during a large earthquake, which may be important information for online structural health monitoring. Therefore, the online modal identification method of concrete dams is an important research topic.

The structural online modal identification problem is a research topic with many challenges that still attract significant attention for its significance in aerospace engineering [8], mechanical engineering [9], and civil engineering [10], among other fields. For time-varying structures, the assumption of the classic modal identification methods that the structure is a time-invariant system is no longer applicable. Thus, Liu [11] proposed the concept of "pseudomodal parameters," which use the time-freezing concept. Three types of methods have been developed for time-varying modal identification, i.e., the time series model

method and the recursive stochastic subspace identification (RSSI) method in the time domain and the time-frequency decomposition method in the time-frequency domain [12, 13]. For the time series model method, Gong [14] used adaptive forgetting through multiple models (AFMM) to track the time-varying modal parameters of tall buildings during a large earthquake and evaluated the structural health according to the modal identification results. Poulimenos and Fassois [15] performed an important literature review of different time-varying modal identification methods using different nonstationary time series models and point out their pros and cons. Klepka and Uhl [16] used the time-frequency domain decomposition technique to analyse the structural vibration response and identified the modal parameters. Goethals et al. [17] and Nezam Sarmadi and Venkatasubramanian [18] used the projection approximation subspace tracking (PAST) algorithm-based RSSI (PAST-RSSI), and Loh et al. [19, 20] used the extended instrumental variable version of the PAST algorithm-based RSSI (EIV-PAST-RSSI) to carry out the online modal identification of a power system, an in-flight flutter, a tall building, and a television tower. Among these methods, the RSSI method has attracted the most attention. The advantage of the RSSI method is mainly reflected in its strong numerical stability and strong robustness to noise interference. Therefore, it is suitable for the online modal identification of structures under random vibration excitation such as earthquakes. Although the online modal identification problem has been studied in many other fields, very few research works have been reported that use the online modal identification for concrete dams [21]. The dam-reservoir-foundation system is characterized by its large size, large number of degrees of freedom, and closely spaced modes, and the vibration measurement of concrete dams is usually performed with a low signal-to-noise-ratio (SNR) as a result of external disturbances. This brings great difficulties to the online modal identification of concrete dams.

In this work, the RSSI method is used to extract the modal parameters of concrete dams based on the strong-motion records of the structure. The online version eigenvalue decomposition (EVD) is solved as a subspace tracking problem using the generalized yet another subspace tracker (GYAST) algorithm [22]. GYAST is a newly proposed advanced algorithm which makes several robust modifications of the original subspace tracking algorithm. The YAST algorithm relies on an interesting idea of optimally extracting the updated subspace weighting matrix in each step. In the GYAST algorithm, computation reduction of optimal subspace extraction is achieved by an approximation. It caused the GYAST has the advantages of a low computational complexity, high computational efficiency, and strong robustness. Combining GYAST with RSSI is expected to improve the accuracy and efficiency of the online modal identification. The online time-varying modal identification procedure based on the GYAST-RSSI is verified using a numerical example to evaluate the algorithm identification accuracy, robustness, and computation efficiency. Finally, the time-varying modal identification of the Pacoima arch dam is carried out using the proposed time-varying modal identification procedure and the strong-motion records of three different earthquakes to track the time-varying characteristics of the arch dam during earthquakes.

2. Linear Time-Varying Modal Identification Using the GYAST-Based RSSI

2.1. Time-Varying State Space Expression of the Dam-Reservoir-Foundation System. In the design stage of a concrete dam, the structure is generally assumed to be linear, and the observed vibration response of the structure is stationary. However, for some reasons, the dam-reservoir-foundation system may be time-varying. As shown in Figure 1, the dynamic constitutive model of the concrete and the base rock may be nonlinear. Additionally, the joints on the dam body may close or open with variations in the amplitude of the earthquake excitation, which will change the stiffness of the connections between different dam monoliths. The effects of the structure-foundation interaction may also introduce some time-varying factors into the dynamic features of concrete dams [23]. Moreover, a damage structure normally exhibits nonlinear dynamic behaviours and a time-dependent stiffness, and the damping variations over time lead to the time-varying modal parameters of the system. In this study, the dam-reservoir-foundation system is assumed to be a linear time-varying system. The "frozen-time" assumption that consists of modelling a linear time-varying system as a piecewise linear time-invariant system is adopted. The parameters will be assumed to vary in a stepwise way; i.e., they will change abruptly at instants separated by small time intervals and will remain constant during these time intervals. If the time intervals are sufficiently small, this model can be considered an approximation of the continuously varying case [24]. The expression of this system will be discussed in this section.

It should be noted that the material characteristics, the boundary conditions, the damping, etc. may be affected by some environmental variables, such as the water level, temperature, and humidity. The impact of these variables will not be taken into account in this study since the observation time of an earthquake response record is not very long.

The equation of motion for an n degrees-of-freedom time-varying linear system S with time-varying structural parameters can be expressed as

$$S\colon \mathbf{M}[t]\ddot{\mathbf{x}}[t] + \mathbf{C}[t]\dot{\mathbf{x}}[t] + \mathbf{K}[t]\mathbf{x}[t] = \mathbf{f}[t], \tag{1}$$

where $\mathbf{M}[t]$, $\mathbf{C}[t]$, and $\mathbf{K}[t]$ are the time relevant mass matrix, damping matrix, and stiffness matrix, respectively. $\mathbf{M}[t]$, $\mathbf{C}[t]$, and $\mathbf{K}[t]$ are assumed to slowly change with time. For the dam-reservoir-foundation system, the change of mass is usually not taken into account, and thus, the mass matrix $\mathbf{M}[t] = \mathbf{M}$ is constant. $\mathbf{X}[t]$ is the displacement response of the structure, and $\mathbf{f}[t]$ is the external excitation force.

Equation (1) is a system of differential equations with time-varying coefficients. The response can be found by

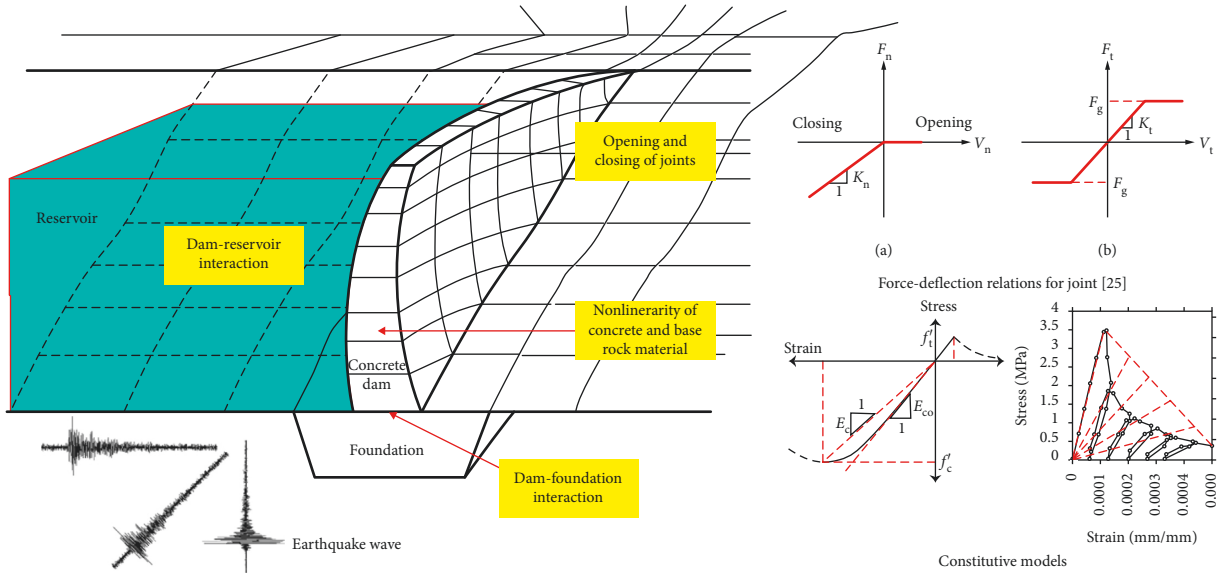

FIGURE 1: Time-varying characteristics of the dam-reservoir-foundation system under earthquake excitation: (a) normal opening; (b) tangential movement [25].

solving the differential equations using initial conditions, but in general, there is no closed-form solution set to these equations. Thus, an approximation is introduced to solve the vibration problem. In other words, the instantaneous modal parameters are obtained at each time instant under the slow-varying assumption of the structural system. According to this assumption, the continuous "frozen" time-varying structure is made up of the mass, damping, and stiffness of every instantaneous moment $\tau \in [0, t_{\text{end}}]$, which can be expressed as follows:

$$\begin{cases} S' = \{S'(\tau):\ \mathbf{M}[\tau]\ddot{\mathbf{x}}[t] + \mathbf{C}[\tau]\dot{\mathbf{x}}[t] + \mathbf{K}[\tau]\mathbf{x}[t] = \mathbf{f}[t]\}, \\ \tau = t_k, \quad k = 1, 2, \ldots, N, \\ t \in [0, t_{\text{end}}], \end{cases} \tag{2}$$

where t_{end} is the end time of the time series of the vibration response signal, $S'(\tau)$ represents the time-invariant structure of $t = \tau$, and S' is a set of the time-freezing descriptions of the linear time-varying structure. Analytically, during the time interval $[t_k, t_{k+1})$, the parameter matrices of equation (2) have entries with constant values. When $t = t_{k+1}$, the matrices may suddenly change from $\mathbf{M}[t_k]$, $\mathbf{C}[t_k]$, and $\mathbf{K}[t_k]$ to $\mathbf{M}[t_{k+1}]$, $\mathbf{C}[t_{k+1}]$, and $\mathbf{K}[t_{k+1}]$ since the system during the time interval $[t_k, t_{k+1})$ is time invariant. The state space expression for the time-varying system at discrete time intervals is as follows [26]:

$$\begin{cases} \mathbf{z}_{k+1} = \mathbf{A}_k \mathbf{z}_k + \mathbf{u}_k, \\ \mathbf{y}_k = \mathbf{G}_k \mathbf{z}_k + \mathbf{v}_k, \end{cases} \tag{3}$$

where $\mathbf{A}_k$ and $\mathbf{G}_k$ are the discrete state space matrix and observation matrix of the time interval $[t_k, t_{k+1})$, respectively. $\mathbf{z}_k$ is a vector of state variables, and the observation vector $\mathbf{y}_k$ is a vector of l channels and can be any or some of the three types of structural vibration responses, i.e., the displacement, velocity, and acceleration. $\mathbf{u}_k$ is the stochastic excitation, and $\mathbf{v}_k$ is the observational noise.

The expression of the structural vibration response for a time-varying system during a time instant $t \in [t_k, t_{k+1})$ is discussed first. Since the system during the interval $[t_k, t_{k+1})$ is assumed to be time invariant, a basic expression for the linear vibration system is applicable during the time interval.

To identify the complex modal shape vector, the double-sized mixing model is adopted [27]. It is well known that the shift of the phase angle between the displacement and velocity and the velocity and acceleration is 90°. The acceleration response is generally measured for the structural strong-motion response observation system. Since the physical parameters vary slowly with time, component $\mathbf{y}_0[t]$ is an asymptotic signal. To track the time-varying characteristics of a structure with n degrees-of-freedom, the Hilbert transformation is performed to obtain the pseudoresponse of the structure with a 90° transferred phase angle $\mathbf{y}_{90}[t]$. Then, in the discrete time domain, the augmented response vector $\tilde{y}(k) \in \Re^{2l\times 1}$ can be obtained as follows:

$$\tilde{y}(k) = \begin{bmatrix} \mathbf{y}^{\text{R}}(k) \\ \mathbf{y}^{\text{I}}(k) \end{bmatrix} = \begin{bmatrix} \mathbf{y}_0(k) \\ \mathbf{y}_{90}(k) \end{bmatrix}. \tag{4}$$

Equation (4) is equivalent to the representation of the original signal in the analytical form $\mathbf{y}'[t]$ as follows:

$$\mathbf{y}'[t] = \mathbf{y}_0[t] + jH\{\mathbf{y}_0[t]\} = \mathbf{y}^{\text{R}}[t] + j\mathbf{y}^{\text{I}}[t], \tag{5}$$

where $\mathbf{y}^{\text{R}}[t] = \mathbf{y}_0[t] = \mathbf{y}[t]$ and $\mathbf{y}^{\text{I}}(t) = H\{\mathbf{y}_0[t]\}$ are the real and imaginary parts of the analytical signal, respectively, and $j = \sqrt{-1}$ is the imaginary unit; $H\{\cdot\}$ is the mathematical operator of the Hilbert transformation.

Based on the derivation by McNeill [28] and Masuda et al. [29], the free acceleration vibration of a structure can be expressed as

$$\ddot{\mathbf{x}}[t] = 2\mathrm{Re}\{\boldsymbol{\Phi}(k)\ddot{\mathbf{q}}'[k,t]\}, \quad t \in [t_k, t_{k+1}), \tag{6}$$

where k represents the kth time interval, i.e., $\boldsymbol{\Phi}(k) = \boldsymbol{\Phi}[t_k]$. The complex modal acceleration response matrix is defined as $\ddot{\mathbf{q}}'[k,t] = \ddot{\mathbf{q}}^{\mathrm{R}}[k,t] + j\ddot{\mathbf{q}}^{\mathrm{I}}[k,t]$ and is composed of the modal acceleration responses of all the activated modes. The terms $\ddot{\mathbf{q}}^{\mathrm{R}}[k,t]$ and $\ddot{\mathbf{q}}^{\mathrm{I}}[k,t]$ are the real and imaginary parts of the modal acceleration response, respectively. $\mathrm{Re}\{\cdot\}$ is the real part of a number.

If the acceleration response is measured and the output selection matrix is $\mathbf{C}_a$, the analytical expression of the acceleration response signal is

$$\begin{aligned}\mathbf{y}'[t] &= \mathbf{C}_{\mathrm{a}}\left\{\ddot{\mathbf{x}}^{\mathrm{R}}[t] + j\ddot{\mathbf{x}}^{\mathrm{I}}[t]\right\} \\ &= \mathbf{C}_{\mathrm{a}}\boldsymbol{\Phi}(k)\ddot{\mathbf{q}}'[k,t], \quad t \in [t_k, t_{k+1}).\end{aligned} \tag{7}$$

Based on the coordinate transformation shown in equation (6), the augmented response vector $\tilde{y}(t)$ shown in equation (4) is expressed as

$$\tilde{\mathbf{y}}[t] = \begin{Bmatrix}\mathbf{y}^{\mathrm{R}}[t] \\ \mathbf{y}^{\mathrm{I}}[t]\end{Bmatrix} = \mathbf{L}(k)\tilde{\ddot{\mathbf{q}}}[k,t] + \mathbf{v}[t], \quad t \in [t_k, t_{k+1}), \tag{8}$$

where $\mathbf{L}(k) = \begin{bmatrix}\mathbf{C}_{\mathrm{a}}\boldsymbol{\Phi}(k)^{\mathrm{R}} & -\mathbf{C}_{\mathrm{a}}\boldsymbol{\Phi}(k)^{\mathrm{I}} \\ \mathbf{C}_{\mathrm{a}}\boldsymbol{\Phi}(k)^{\mathrm{I}} & \mathbf{C}_{\mathrm{a}}\boldsymbol{\Phi}(k)^{\mathrm{R}}\end{bmatrix} \in \mathfrak{R}^{2l\times 2n}$ and $\tilde{\ddot{\mathbf{q}}}[k,t] = \begin{bmatrix}\ddot{\mathbf{q}}^{\mathrm{R}}[k,t] \\ \ddot{\mathbf{q}}^{\mathrm{I}}[k,t]\end{bmatrix} \in \mathfrak{R}^{2n\times 1}$.

Assume the observational noise components are independently identically distributed with a variance σ_n^2. Then, the covariance matrix of $\tilde{\mathbf{y}}[t]$ can be expressed as

$$\mathbf{R}_{\tilde{\mathbf{y}}\tilde{\mathbf{y}}}(k,0) = E\left\{\tilde{\mathbf{y}}[t]\tilde{\mathbf{y}}[t]^{\mathrm{H}}\right\} = \mathbf{L}(k)\mathbf{R}_{\tilde{\ddot{\mathbf{q}}}\tilde{\ddot{\mathbf{q}}}}(k,0)\mathbf{L}(k)^{\mathrm{H}} + \sigma_n^2\mathbf{I}_{2pl}, \quad t \in [t_k, t_{k+1}), \tag{9}$$

where the superscript $^{\mathrm{H}}$ denotes the conjugate transpose of a matrix and $\mathbf{R}_{\tilde{\ddot{\mathbf{q}}}\tilde{\ddot{\mathbf{q}}}}(k,0)$ is the covariance matrix of the modal acceleration responses. For a structure system with weak damping,

$$\mathbf{R}_{\tilde{\ddot{\mathbf{q}}}\tilde{\ddot{\mathbf{q}}}}(k,0) \approx \begin{bmatrix}\mathbf{R}_{\ddot{\mathbf{q}}^{\mathrm{R}}\ddot{\mathbf{q}}^{\mathrm{R}}}(k) & \mathbf{0}_{n_0\times n_0} \\ \mathbf{0}_{n_0\times n_0} & \mathbf{R}_{\ddot{\mathbf{q}}^{\mathrm{I}}\ddot{\mathbf{q}}^{\mathrm{I}}}(k)\end{bmatrix}. \tag{10}$$

After the discrete sampling of the physical acceleration of the l channels at N identical time intervals, a time-delayed vector $\mathbf{Y}(k) \in \mathfrak{R}^{2pl\times 1}$, which is composed of $\tilde{y}(k)$ and its time-delayed data, can be written as follows:

$$\mathbf{Y}(k) = \left(\tilde{\mathbf{y}}(k)^{\mathrm{T}} \;\; \tilde{\mathbf{y}}(k)^{\mathrm{T}} \;\; \cdots \;\; \tilde{\mathbf{y}}(k+p-1)^{\mathrm{T}}\right)^{\mathrm{T}}, \quad k = 1, 2, \ldots, N, \tag{11}$$

in which the number of time delays should satisfy $2pl > n$.

Then, the Hankel matrix $\mathbf{H}_0(k) \in \mathfrak{R}^{2pl\times 2pl}$ can be defined as follows:

$$\begin{aligned}\mathbf{H}_0(k) &= E\left[\mathbf{Y}(k)\mathbf{Y}(k)^{\mathrm{T}}\right], \\ &= \begin{bmatrix}\mathbf{R}_{\tilde{\mathbf{y}}\tilde{\mathbf{y}}}(k,0) & \mathbf{R}_{\tilde{\mathbf{y}}\tilde{\mathbf{y}}}(k,1) & \cdots & \mathbf{R}_{\tilde{\mathbf{y}}\tilde{\mathbf{y}}}(k,p-1) \\ \mathbf{R}_{\tilde{\mathbf{y}}\tilde{\mathbf{y}}}(k,1) & \mathbf{R}_{\tilde{\mathbf{y}}\tilde{\mathbf{y}}}(k,2) & \cdots & \mathbf{R}_{\tilde{\mathbf{y}}\tilde{\mathbf{y}}}(k,p) \\ \vdots & \vdots & \cdots & \vdots \\ \mathbf{R}_{\tilde{\mathbf{y}}\tilde{\mathbf{y}}}(k,p-1) & \mathbf{R}_{\tilde{\mathbf{y}}\tilde{\mathbf{y}}}(k,p) & \cdots & \mathbf{R}_{\tilde{\mathbf{y}}\tilde{\mathbf{y}}}(k,2p-2)\end{bmatrix}.\end{aligned} \tag{12}$$

Based on the derivation of the free acceleration response shown in equation (9), the Hankel matrix $\mathbf{H}_0(k)$ can be decomposed into the following form:

$$\begin{aligned}\mathbf{H}_0(k) &= \begin{bmatrix}\mathbf{L}(k) \\ \mathbf{L}(k)\sum(k) \\ \vdots \\ \mathbf{L}(k)\sum(k)^{p-1}\end{bmatrix}\mathbf{R}_{\tilde{\ddot{\mathbf{q}}}\tilde{\ddot{\mathbf{q}}}}(k)\left[\mathbf{L}(k)^{\mathrm{H}} \;\; \sum(k)\mathbf{L}(k)^{\mathrm{H}} \;\; \cdots \;\; \sum(k)^{p-1}\mathbf{L}(k)^{\mathrm{H}}\right] + \sigma_n^2\mathbf{I}_{2pl}, \\ &= \tilde{L}(k)\mathbf{R}_{\tilde{\ddot{\mathbf{q}}}\tilde{\ddot{\mathbf{q}}}}(k)\tilde{L}(k)^{H} + \sigma_n^2\mathbf{I}_{2pl},\end{aligned} \tag{13}$$

where $\boldsymbol{\Sigma}(k) = \exp\{\boldsymbol{\Lambda}t_k\} \in \mathfrak{R}^{n\times n}$. $\Lambda = \mathrm{diag}(\lambda_1, \ldots, \lambda_{n0})$, $\lambda_1, \ldots, \lambda_{n0}$ are the eigenvalues of the continuous system matrix.

For the free vibration response of a structure system without damping, the modal acceleration responses of the different modes are independent of each other. However, the damping effect and the disturbance of the noise result in the matrix $\mathbf{R}_{\tilde{\ddot{\mathbf{q}}}\tilde{\ddot{\mathbf{q}}}}(k)$ being approximately a diagonal matrix. Since the damping of concrete structures is usually weak, the error caused by the approximation is acceptable.

At the time instant t_k, new observational data $\mathbf{y}(k)$ are available, and the Hankel matrix $\mathbf{H}_0(k)$ should be updated online. One way to update the Hankel matrix is called the exponential forgetting method. Using this matrix, the Hankel matrix $\mathbf{H}_0(k)$ at the time $t = t_k$ is expressed as

$$\mathbf{H}_0(k) = \beta\mathbf{H}_0(k-1) + \mathbf{Y}(k)\mathbf{Y}(k)^{\mathrm{T}}, \tag{14}$$

in which β is the forgetting factor, with a suggested value between 0.995 and 0.999 [30].

2.2. Modal Subspace Tracking Using GYAST. For each time step, the EVD of $\mathbf{H}_0(k)$ (where $\mathbf{H}_0(k)$ is a square matrix) should be performed at each time instant as follows:

$$\mathbf{H}_0(k) = [\,\mathbf{Q}_1(k)\ \ \mathbf{Q}_2(k)\,]\begin{bmatrix}\boldsymbol{\Delta}_1(k) & \mathbf{0}\\ \mathbf{0} & \boldsymbol{\Delta}_2(k)\end{bmatrix}\begin{bmatrix}\mathbf{Q}_1(k)^{\mathrm{T}}\\ \mathbf{Q}_2(k)^{\mathrm{T}}\end{bmatrix},$$
$$= \mathbf{Q}_1(k)\boldsymbol{\Delta}_1(k)\mathbf{Q}_1(k)^{\mathrm{T}} + \mathbf{Q}_2(k)\boldsymbol{\Delta}_2(k)\mathbf{Q}_2(k)^{\mathrm{T}}. \tag{15}$$

If $\mathbf{Q}_1(k)$ contains the first n dominant eigenvectors of $\mathbf{H}_0(k)$, it can be taken as the dominant signal subspace, which represents the contributions of different modes. $\boldsymbol{\Delta}_1(k)$ is a diagonal matrix that is composed of the first n dominant eigenvalues of $\mathbf{H}_0(k)$. $\mathbf{Q}_2(k)$ and $\boldsymbol{\Delta}_2(k)$ correspond to the remaining eigenvectors and eigenvalues. However, the total computation time will then be very large and is not suitable for online applications. Thus, the online version of the EVD algorithm should be adopted. Since only the left part of the EVD is needed to retrieve an estimate of the observability matrix, an economical (so-called thin) EVD, which computes only that left part, can be used. Using the subspace tracking procedure, the GYAST, in each time step, a sufficient approximation of the dominant subspace, namely,

$$\prod(k)\prod(k)^{\mathrm{H}} \approx \mathbf{Q}_1(k)\mathbf{Q}_1(k)^{\mathrm{H}}, \tag{16}$$

can be obtained. It has been proven that, in a stationary situation, the desired steady-state weights $\boldsymbol{\Pi}(k) = \mathbf{Q}_1(k)^H$ can be obtained by maximizing the mean square value of the output of the combiners, given by

$$J\Big(\prod(k)\Big) = E\Big[\mathrm{trace}\big(\tilde{\tilde{\mathbf{q}}}(k)^{\mathrm{H}}\tilde{\tilde{\mathbf{q}}}(k)\big)\Big],$$
$$= E\Big[\mathrm{trace}\Big(\prod(k)^{\mathrm{H}}\mathbf{Y}(k)\mathbf{Y}(k)^{\mathrm{H}}\prod(k)\Big)\Big],$$
$$= \mathrm{trace}\Big(\prod(k)^{\mathrm{H}}\mathbf{Y}(k)\mathbf{Y}(k)^{\mathrm{H}}\prod(k)\Big), \tag{17}$$

in which the operator trace $(\cdot)$ stands for the trace of a matrix.

To ensure the orthogonality of $\boldsymbol{\Pi}(k)$, a maximization optimization problem with constraints is expressed as follows:

$$\max_{\boldsymbol{\Pi}(t)}: \quad J\Big(\prod(k)\Big) = \mathrm{trace}\Big(\prod(k)^{\mathrm{H}}\mathbf{H}_0(\mathrm{k})\prod(k)\Big),$$
$$\text{subject to}: \quad \prod(k)^{\mathrm{H}}\prod(k) = \mathbf{I}_n. \tag{18}$$

To reduce the computational cost of updating $\boldsymbol{\Pi}(k)$ online, the ideal subspace projection- (SP-) type algorithm limits the search space to the range space of $\boldsymbol{\Pi}(k-1)$ plus one additional search direction, i.e., $\mathbf{Y}(k)$. Then, the n-dimensional range space of $\boldsymbol{\Pi}(k)$ is found as a subspace of the $(n+1)$-dimensional space spanned by $\mathbf{V}(k) \in \Re^{2pl\times(n+1)}$:

$$\mathbf{V}(k) = \Big[\prod(k-1), \mathbf{Y}(k)\Big]. \tag{19}$$

If $\underline{\boldsymbol{\Pi}}(k)$ is an orthonormal basis of the $(n+1)$-dimensional range space $\mathbf{V}(k)$, then $\boldsymbol{\Pi}(k)$ can be expressed as

$$\prod(k) = \underline{\prod}(k)\mathbf{U}(k), \tag{20}$$

in which $\mathbf{U}(k) \in \Re^{(n+1)\times n}$.

Then, replacing equation (20) with the optimization problem shown in equation (18), the following new optimization problem is obtained:

$$\max_{\mathbf{U}(t)}: \quad J(\mathbf{U}(k)) = \mathrm{trace}\Big(\mathbf{U}(k)^{\mathrm{H}}\underline{R}_{\tilde{\tilde{\mathbf{q}}}\tilde{\tilde{\mathbf{q}}}}(k)\mathbf{U}(k)\Big),$$
$$\text{subject to}: \quad \mathbf{U}(k)^{\mathrm{H}}\mathbf{U}(k) = \mathbf{I}_n. \tag{21}$$

in which the matrix $\underline{R}_{\tilde{\tilde{\mathbf{q}}}\tilde{\tilde{\mathbf{q}}}}(k) = \underline{\boldsymbol{\Pi}}(k)^{\mathrm{H}}\mathbf{H}_0(\mathrm{k})\,\underline{\boldsymbol{\Pi}}(k)$.

For the GYAST algorithm, an approximation is introduced that calculates the modal acceleration responses $\tilde{\tilde{\mathbf{q}}}(k) = \tilde{\tilde{\mathbf{q}}}[k, t_k]$ as

$$\tilde{\tilde{\mathbf{q}}}(k) = \prod(k-1)^{\mathrm{H}}\mathbf{Y}(k). \tag{22}$$

Then, the orthonormal basis $\underline{\boldsymbol{\Pi}}(k)$ of the augmented $(n+1)$-dimensional range space $\mathrm{span}(\mathbf{V}(k))$ is given by

$$\underline{\prod}(k) = \Big[\prod(k-1), \mathbf{u}(k)\Big], \tag{23}$$

where $\mathbf{u}(k)$ is the unit-norm variant of $\mathbf{Y}_\perp(k)$, $\mathbf{Y}_\perp(k) = \mathbf{Y}(k) - \boldsymbol{\Pi}(k-1)\tilde{\tilde{\mathbf{q}}}(k) = \sigma(k)\mathbf{u}(k)$ is the complement of the orthonormal projection of $\mathbf{Y}(k)$, and $\sigma(k) = \|\mathbf{Y}_\perp(k)\|_2 = \sqrt{\mathbf{Y}(k)^{\mathrm{H}}\mathbf{Y}(k) - \tilde{\tilde{\mathbf{q}}}(k)^{\mathrm{H}}\tilde{\tilde{\mathbf{q}}}(k)}$ is the L_2-norm of $\mathbf{Y}_\perp(k)$.

Define the matrix $\underline{R}_{\tilde{\tilde{\mathbf{q}}}\tilde{\tilde{\mathbf{q}}}}(k) = \underline{\boldsymbol{\Pi}}(k)^{\mathrm{H}}\mathbf{H}_0(k)\,\underline{\boldsymbol{\Pi}}(k)$. Based on equation (14) and equations (22) and (23), $\underline{R}_{\tilde{\tilde{\mathbf{q}}}\tilde{\tilde{\mathbf{q}}}}(k)$ can be deduced as

$$\underline{R}_{\tilde{\tilde{\mathbf{q}}}\tilde{\tilde{\mathbf{q}}}}(k) = \underline{\prod}(k)^{\mathrm{H}}\mathbf{H}_0(k)\underline{\prod}(k) = \begin{bmatrix}\mathbf{R}'_{\tilde{\tilde{\mathbf{q}}}\tilde{\tilde{\mathbf{q}}}}(k) & \mathbf{r}(k)\\ \mathbf{r}(k)^H & \gamma(k)\end{bmatrix}, \tag{24}$$

in which $\mathbf{r}(k) = \sigma(k)\tilde{\tilde{\mathbf{q}}}(k)$, $\gamma(k) = \beta\sigma_n(k)^2 + \sigma(k)^2$, and $\mathbf{R}'_{\tilde{\tilde{\mathbf{q}}}\tilde{\tilde{\mathbf{q}}}}(k) = \beta\mathbf{R}_{\tilde{\tilde{\mathbf{q}}}\tilde{\tilde{\mathbf{q}}}}(k-1) + \tilde{\tilde{\mathbf{q}}}(k)\tilde{\tilde{\mathbf{q}}}(k)^{\mathrm{H}}$.

For the subspace tracking algorithm, GYAST, to track the signal subspace of $\mathbf{H}_0(k)$, four basic steps must be performed, which are (i) calculating the orthonormal basis $\underline{\boldsymbol{\Pi}}(k)$ of the range space $\mathbf{V}(t)$, (ii) constructing the matrix $\underline{R}_{\tilde{\tilde{\mathbf{q}}}\tilde{\tilde{\mathbf{q}}}}(k)$, (iii) conducting the online updating of $\boldsymbol{\Pi}(k)$, and (iv) conducting the online updating of $\mathbf{R}_{\tilde{\tilde{\mathbf{q}}}\tilde{\tilde{\mathbf{q}}}}(k)$. Using equations (14) and (22)–(24) and the following equations (25a)–(25k), these calculations can be realized online in a recursive way, and $\boldsymbol{\Pi}(k)$ can be updated online for each time instant [23, 31]:

$$\mathbf{q}_n(k) = \text{minor eigenvector of } \underline{R}_{\tilde{\tilde{\mathbf{q}}}\tilde{\tilde{\mathbf{q}}}}(k)$$
$$= \begin{bmatrix}\mathbf{q}\\ r_n(k)\end{bmatrix}, \tag{25a}$$

$$b(k) = \frac{1}{1+|r_n(k)|}, \tag{25b}$$

$$s(k) = \frac{r_n(k)}{|r_n(k)|\sigma(k)}, \tag{25c}$$

$$\mathbf{e}'(k) = \prod(k-1)\left(b(k)\mathbf{q} - s(k)\tilde{\tilde{\mathbf{q}}}(k)\right) + s(k)\mathbf{Y}(k), \tag{25d}$$

$$\prod(k) = \prod(k-1) - \mathbf{e}'(k)\mathbf{q}^{\mathrm{H}}, \tag{25e}$$

$$\mathbf{q}'(k) = \mathbf{R}'_{\tilde{\tilde{\mathbf{q}}}\tilde{\tilde{\mathbf{q}}}}(k)\mathbf{q}, \tag{25f}$$

$$\mathbf{C}_2(k) = \left(\frac{r_n(k)}{|r_n(k)|}\mathbf{R}(k) + b(k)\mathbf{q}'(k)\right)\mathbf{q}^{\mathrm{H}}, \tag{25g}$$

$$c(k) = b(k)^2\mathbf{q}^{\mathrm{H}}\mathbf{q}'(k) + \gamma(k) + 2\frac{b(k)}{|r_n(k)|}\mathrm{Re}\left\{r_n(k)\mathbf{q}^{\mathrm{H}}\mathbf{r}(k)\right\}, \tag{25h}$$

$$\mathbf{R}_{\tilde{\tilde{\mathbf{q}}}\tilde{\tilde{\mathbf{q}}}}(k) = \mathbf{R}'_{\tilde{\tilde{q}}\tilde{\tilde{q}}}(k) + c(k)\mathbf{q}\mathbf{q}^{\mathrm{H}} - \mathbf{C}_2(k) - \mathbf{C}_2(k)^{\mathrm{H}}, \tag{25i}$$

$$\lambda_m(k) = \mathrm{trace}\left\{\underline{R}_{\tilde{\tilde{\mathbf{q}}}\tilde{\tilde{\mathbf{q}}}}(k)\right\} - \mathrm{trace}\left\{\mathbf{R}_{\tilde{\tilde{\mathbf{q}}}\tilde{\tilde{\mathbf{q}}}}(k)\right\}, \tag{25j}$$

$$\sigma_n(k+1)^2 = \min\left\{\lambda_m(k), \sigma_n(k)^2\right\}. \tag{25k}$$

2.3. Flowchart of the Online Modal Identification Method Using the GYAST-RSSI. The proposed online modal identification procedure based on the GYAST-RSSI is shown in Figure 2. Some basic steps of this procedure are summarized as follows:

(1) Initialize some parameters of the procedure, such as the number of time delays p, the system order n, the forgetting factor β, and the initial data length N_1. The system order n can be determined using the SVD spectrum method. The number of time delays should satisfy $2pl > n$. The forgetting factor β is set within the range of [0.995–0.999]. Through some numerical experiments, the choice of N_1 will have an effect on the calculation result of the initial Hankel matrix, but considering that GYAST is an iterative algorithm, the result of $\mathrm{H}(N_1)$ only affects the results of the previous steps. Here, for convenience, set $N_1 = 100$ and $k = N_1$ and use the initial strong-motion records of l channels with data length N_1 to calculate the initial Hankel matrix $\mathbf{H}_0(k)$ as $\mathbf{H}_0(k) = (1/\tilde{p})\sum_{k=1}^{N_1}\mathbf{Y}(k)\mathbf{Y}(k)^{\mathrm{T}}$.

(2) GYAST is a recursive subspace tracking algorithm, and it should first be initialized. Perform EVD on the Hankel matrix $\mathbf{H}_0(k)$ and initialize the orthonormal matrix $\mathbf{\Pi}(t)$ as follows:

$$\prod(k) = \mathbf{Q}_1(k), \tag{26a}$$

$$\mathbf{R}_{\tilde{\tilde{\mathbf{q}}}\tilde{\tilde{\mathbf{q}}}}(k) = \mathbf{Q}_1(k)^{\mathrm{T}}\mathbf{H}_0(k)\mathbf{Q}_1(k), \tag{26b}$$

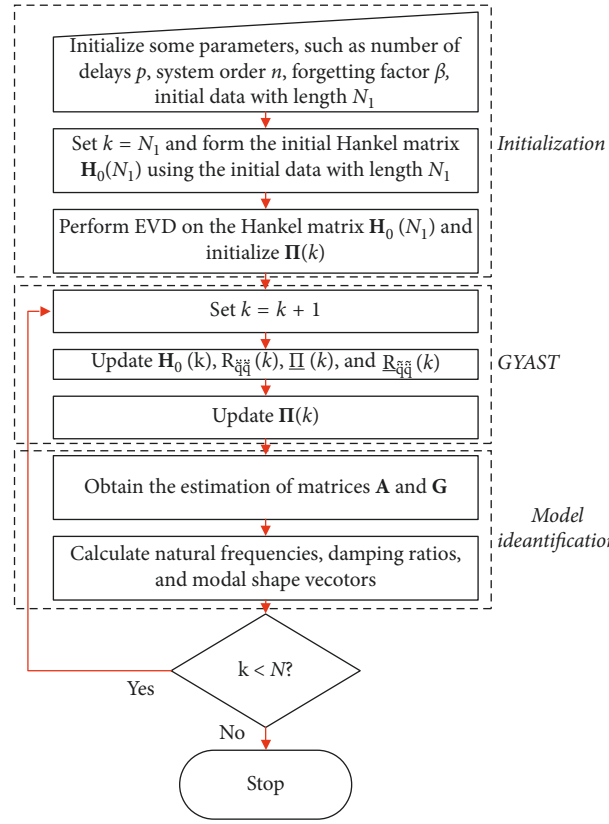

Figure 2: Flowchart of the proposed online modal identification using the GYAST-RSSI method and strong-motion records.

$$\sigma_n(k)^2 = \text{smallest eigenvalue of } \mathbf{H}_0(k). \tag{26c}$$

(3) Set $k = k+1$ and update $\mathbf{\Pi}(k)$ using the GYAST algorithm to calculate the orthonormal basis $\underline{\mathbf{\Pi}}(k)$, $\underline{H}(k)$, $\mathbf{R}_{\tilde{\tilde{\mathbf{q}}}\tilde{\tilde{\mathbf{q}}}}(k)$, etc., using equation (14) and equations (22)–(24).

(4) Since $\mathbf{\Pi}(k) \sim \mathrm{O}_{i,k}$, the two matrices have the same eigenvalues and eigenvectors, and so we set $\mathrm{O}_{i,k} = \mathbf{\Pi}(k)$. From the above recursive procedures, the orthonormal matrix $\mathbf{\Pi}(k)$ can be updated. Then, at the kth time interval, the discrete state space matrix $\mathbf{A}_k$ and the observation matrix $\mathbf{G}_k$ are realized using the following expressions:

$$\mathbf{G}_k = \mathrm{O}_{i,k}(1:2l,:), \qquad \mathbf{A}_k = \left(\underline{\mathrm{O}}_{i,k}\right)^{+}\overline{\mathrm{O}}_{i,k}, \tag{27}$$

where $\underline{\mathrm{O}}_{i,k} = \mathbf{O}_{i,k}(1:2l(p-1),:)$ and $\overline{\mathrm{O}}_{i,k} = \mathbf{O}_{i,k}(2l+1:2lp,:)$.

(5) After we obtain the modal identification results at time instant t_k, some meaningless mathematical poles should first be discarded. If the identified natural frequencies $f_{i,k}$ and damping ratios $\xi_{i,k}$ at time instant t_k satisfy the following criteria, then mode i is deemed to be a real structural mode:

$$\begin{cases} f_{\min} < f_{i,k} < f_{\max}, \\ \xi_{\min} < \xi_{i,k} < \xi_{\max}, \end{cases} \tag{28}$$

in which $f_{\min}$ and $f_{\max}$ are the minimum and maximum natural frequencies of the active modes of the structure and $\xi_{\min}$ and $\xi_{\max}$ are the minimum and maximum damping ratios.

(6) Continue with step 3~step 5 of the above calculation procedure until reaching the end of the strong-motion records.

3. Examples

3.1. Numerical Example. Using the mass-spring-damper system with 4 degrees-of-freedom shown in Figure 3, the time-varying modal identification method proposed in this work is validated for its identification accuracy, robustness, and computation efficiency. Some parameters of the system are set as follows: $m_1 = m_2 = m_3 = 1.0\,\text{kg}$, $m_4 = 0.9\,\text{kg}$, $k_3 = 7000\,\text{N/m}$, $k_2 = k_4 = 8000\,\text{N/m}$, $c_1 = c_2 = 0.6\,\text{N·s}^2/\text{m}$, and $c_3 = c_4 = 0.55\,\text{N·s}^2/\text{m}$. The time-varying stiffness coefficients k_1 are simulated as follows. The time intervals are in seconds.

Case 1: abrupt change of k_1:

$$k_1 = \begin{cases} 8000, & 0 \le t < 4, \\ 6000, & 4 \le t < 8, \\ 9000, & 8 \le t < 12, \\ 7000, & 12 \le t \le 16, \end{cases} \quad \text{(unit: N/m)}. \tag{29}$$

Case 2: continuous linear change of k_1:

$$k_1 = 6000 + 125t, \quad \text{(unit: N/m)}. \tag{30}$$

The initial state of the system is zero, and the support excitation $a_g(t)$ is simulated using a white noise signal. The structural vibration response is obtained by adding some white noise to the calculated responses using a Runge–Kutta algorithm (using MATLAB code ODE45). The sampling frequency of the simulated structural vibration response is 1000 Hz. Figures 4 and 5 show the support excitation and the acceleration response of m_1 for two simulation cases of k_1.

Setting $\beta = 0.995$, $p = 50$, and $N_1 = 100$ and using the simulated structural vibration responses (SNR = 40 dB) of case 1 and case 2, the time-varying modal identification results for the frequencies and damping ratios are shown in Figures 6 and 7. The identification accuracy of the frequencies is sufficient, but the identification accuracy of the damping ratios needs to be further improved.

The forgetting factor is an important parameter in the GYAST-RSSI method proposed in this paper. To verify its influence on the recognition result, different values of β are selected for a parameter sensitivity analysis. Under simulation case 1, the analysis results are shown in Figure 8. It can be seen from Figure 8 that when β is in the interval of [0.995 0.999], the result does not change much. In this example, the result of $\beta = 0.995$ is better.

Based on the simulated vibration response (SNR = 40 dB), the identification results for frequencies f_1 and f_2 of mode 1 and mode 2 using the EIV-PAST-RSSI and GYAST-RSSI methods are plotted in Figures 9 and 10 to make a comparison. Figures 9 and 10 show that the difference between the identification results of the EIV-PAST-RSSI and GYAST-RSSI methods is small, but the identification results of GYAST-RSSI are more stable.

To verify the robustness of the proposed time-varying modal identification method, simulated vibration response signals with different SNRs are used to perform the time-varying modal identification. The modal identification results of the first two frequency orders f_1 and f_2 for simulation cases 1 and 2 are shown in Figures 11 and 12, respectively. Figures 11 and 12 show that, with the increase in the noise level (decrease in the SNR), the identification accuracy of the frequencies is still very high.

The modal assurance criterion (MAC) indexes between the identified modal shape vectors and the theoretical modal shape vectors are calculated and shown in Figure 13. In addition to some sudden changes in the MAC value at 4 s, 8 s, and 12 s, which is caused by the instability of the algorithm, the identification results of the modal shape vectors indicate the sufficient accuracy of the GYAST-RSSI method of tracking the time-varying structural modal shape vectors.

To evaluate the identification accuracy of the proposed time-varying modal identification method, the average relative error (ARE) of the frequencies is calculated and is shown in Table 1. The ARE of the certain order frequency is defined as

$$\text{ARE} = \frac{1}{N} \sum_{m=1}^{N} 100\% \times \frac{\left| f_m^t - f_m^c \right|}{f_m^t}, \tag{31}$$

in which f_m^t and f_m^c are the identification results and the theoretical value of the certain order frequency at time instant m, respectively.

From Table 1, it can be seen that the identification accuracy is good for the two time-varying modal identification methods since the maximum ARE is 2.11%. With the decrease in the SNR, the identification accuracy for the frequencies has become low. Moreover, the GYAST-RSSI has better identification than the EIV-PAST-RSSI method in most cases.

3.2. Time-Varying Modal Identification of the Pacoima Arch Dam. The Pacoima dam is a 113 m high arch dam located near Los Angeles, California. Since the Pacoima arch dam is near the famous San Fernando earthquake-prone area, it has experienced several earthquakes of different magnitudes. The dam experienced two severe earthquakes: the San Fernando earthquake (1971) and the Northridge earthquake (1994). Due to the damage caused by the San Fernando earthquake and the opening of the joints near the thrust block at the left abutment, rehabilitation operations were

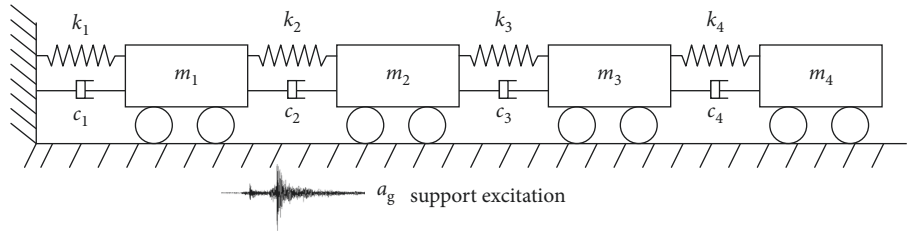

FIGURE 3: Concentrated mass system with 4 degrees-of-freedom.

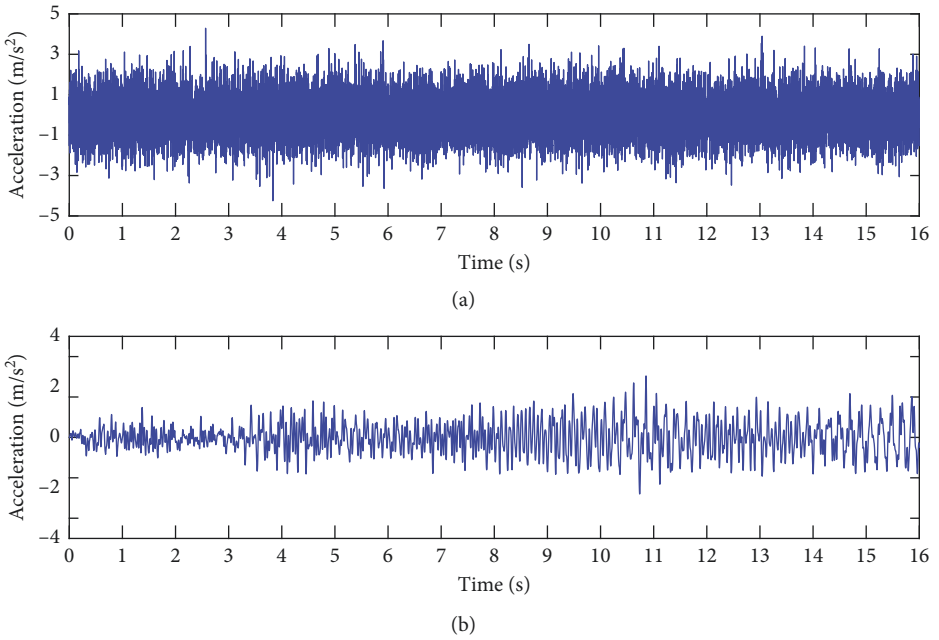

FIGURE 4: Support excitation and vibration response of m_1 (SNR = 40 dB) for simulation case 1: (a) support excitation $a_g(t)$; (b) acceleration response of m_1.

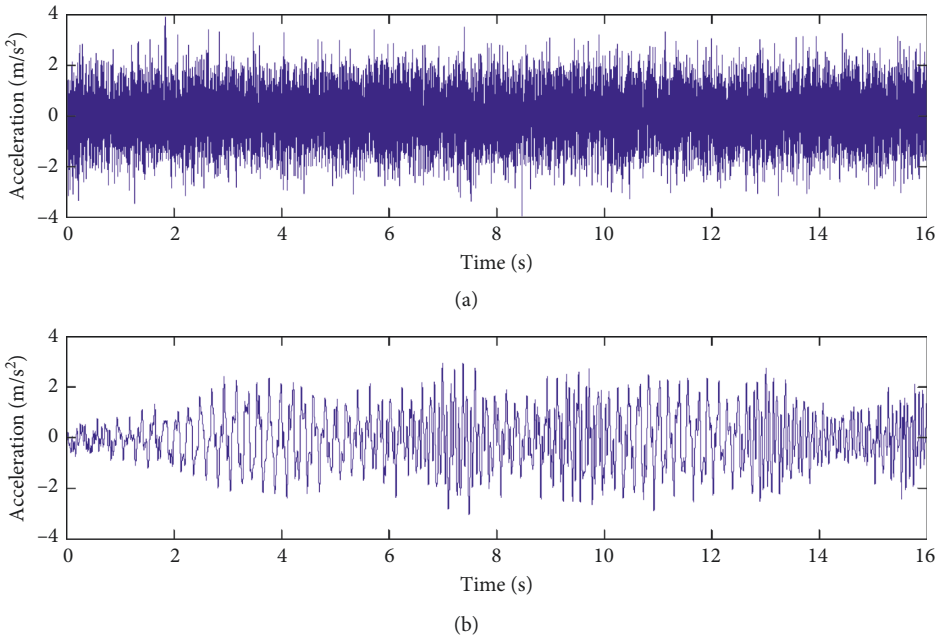

FIGURE 5: Support excitation and acceleration response of m_1 (SNR = 40 dB) for simulation case 2: (a) support excitation $a_g(t)$; (b) response of m_1.

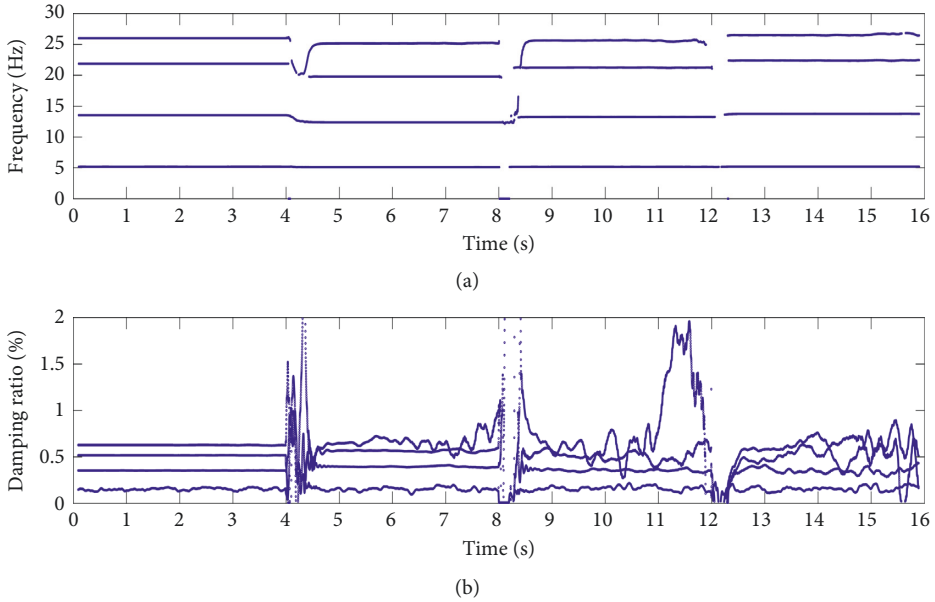

Figure 6: Frequency (f_1~f_4) and damping ratio (ξ_1~ξ_4) identification results of simulation case 1 (SNR = 40 dB): identification results for (a) natural frequencies using GYAST-RSSI and (b) damping ratios using GYAST-RSSI.

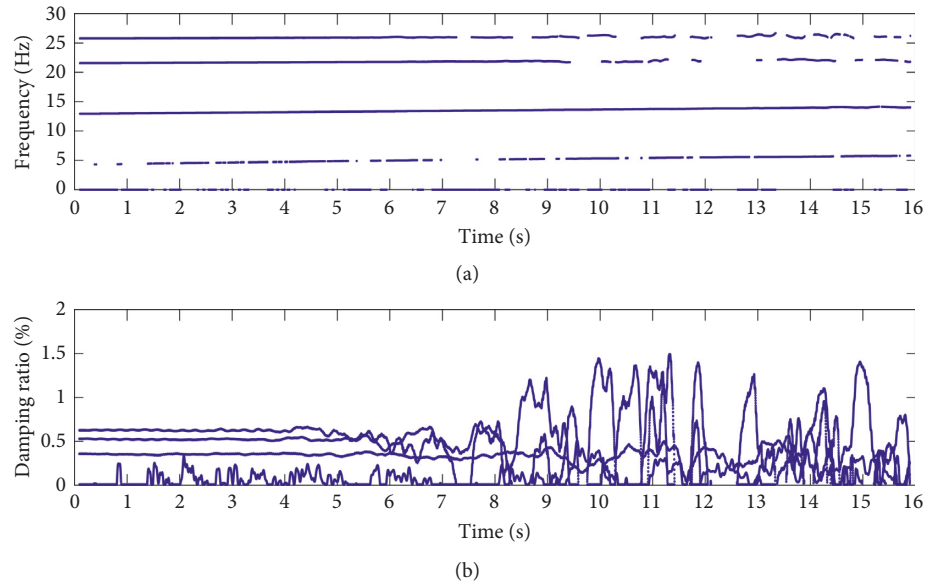

Figure 7: Frequency (f_1~f_4) and damping ratio (ξ_1~ξ_4) identification results of simulation case 2 (SNR = 40 dB): identification results for (a) natural frequencies and (b) damping ratios.

performed afterward, and an array of 17 accelerometers were installed on the dam in 1977 [32]. The arrangement of the 10 acceleration sensors with 17 measurement channels is shown in Figure 14. Among the 17 measurement channels, channels 1~8 are located on the dam body and channels 9~17 are located on the base rock. The measurement directions of channels 1, 2, 5, 6, 7, 8, 9, 12, and 15 are in the radial direction; channels 4, 11, 14, and 17 are in the tangential direction; and channels 3, 10, 13, and 16 are in the vertical direction. After the Northridge earthquake, the strong-motion observation system was updated, and the strong-motion responses of the three different earthquakes were recorded. The information of the three earthquakes is shown in Table 2.

The strong-motion records of the Pacoima arch dam for channels 1, 2, 5, 6, 7, and 8 in the radial direction during the Newhall earthquake are shown in Figure 15. The sampling frequency of the strong-motion monitoring data is 200 Hz. Thus, the cutoff frequency of the data is 50 Hz.

Time-invariant modal identification results of the Pacoima dam using different methods are shown in Table 3. These identification results are used to make a comparison with the following time-varying modal identification results.

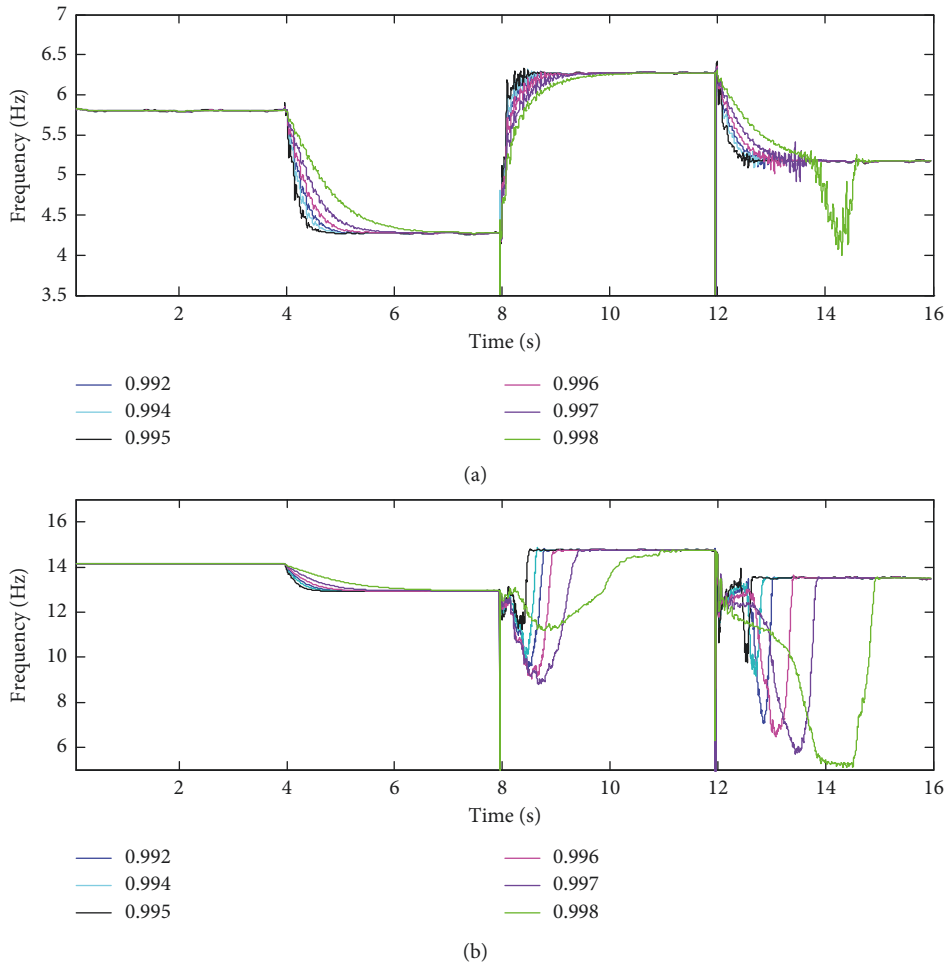

Figure 8: Frequency (f_1, f_2) identification results of simulation case 1 under different forgetting factors (SNR = 40 dB): (a) mode 1; (b) mode 2.

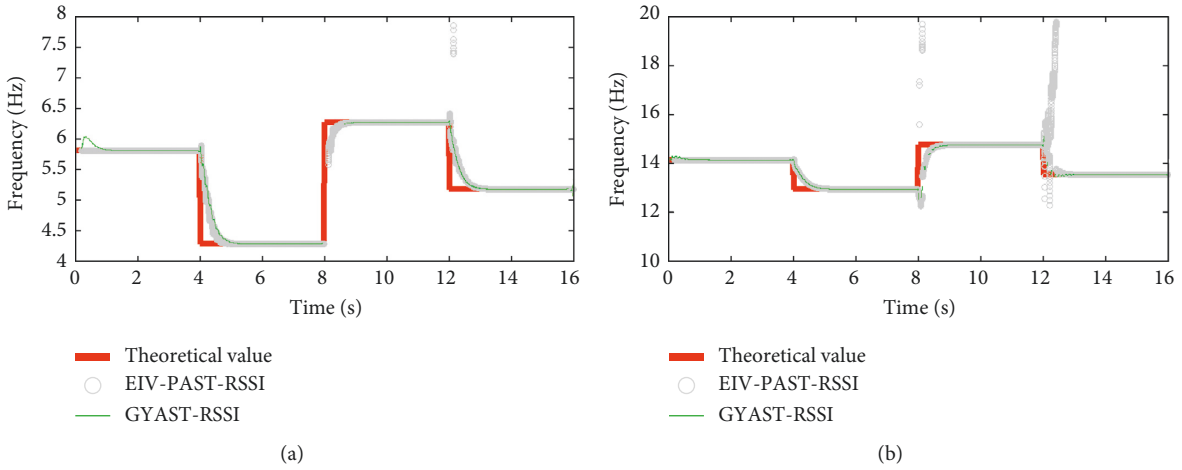

Figure 9: Frequency identification results of the first two modes using the different methods for simulation case 1 (SNR = 40 dB): (a) mode 1; (b) mode 2.

Channels 9~17 are located on the base rock. The strong-motion records of channel 9 in the radial direction during the three major California earthquakes and the corresponding power spectrums are shown in Figure 15. As seen from Figure 15, for the San Fernando earthquake and the Chino Hills earthquake, the dominant frequencies of the earthquake excitations are less than 3.32 Hz. It can be seen from Table 3 that the dominant frequencies of the earthquake excitation are

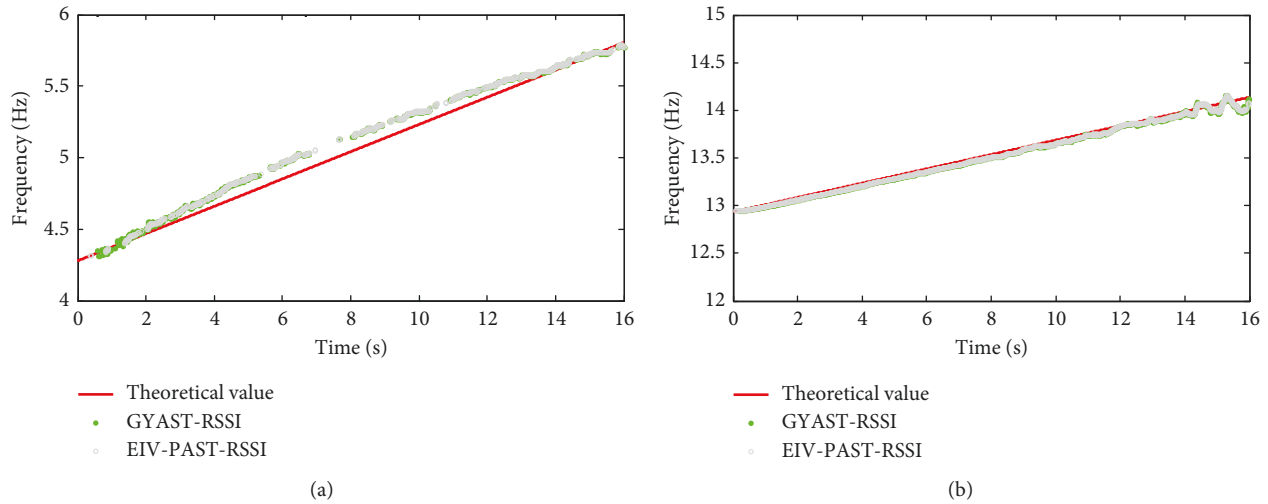

Figure 10: Frequency identification results of the first two modes using different methods for simulation case 2 (SNR = 40 dB): (a) mode 1; (b) mode 2.

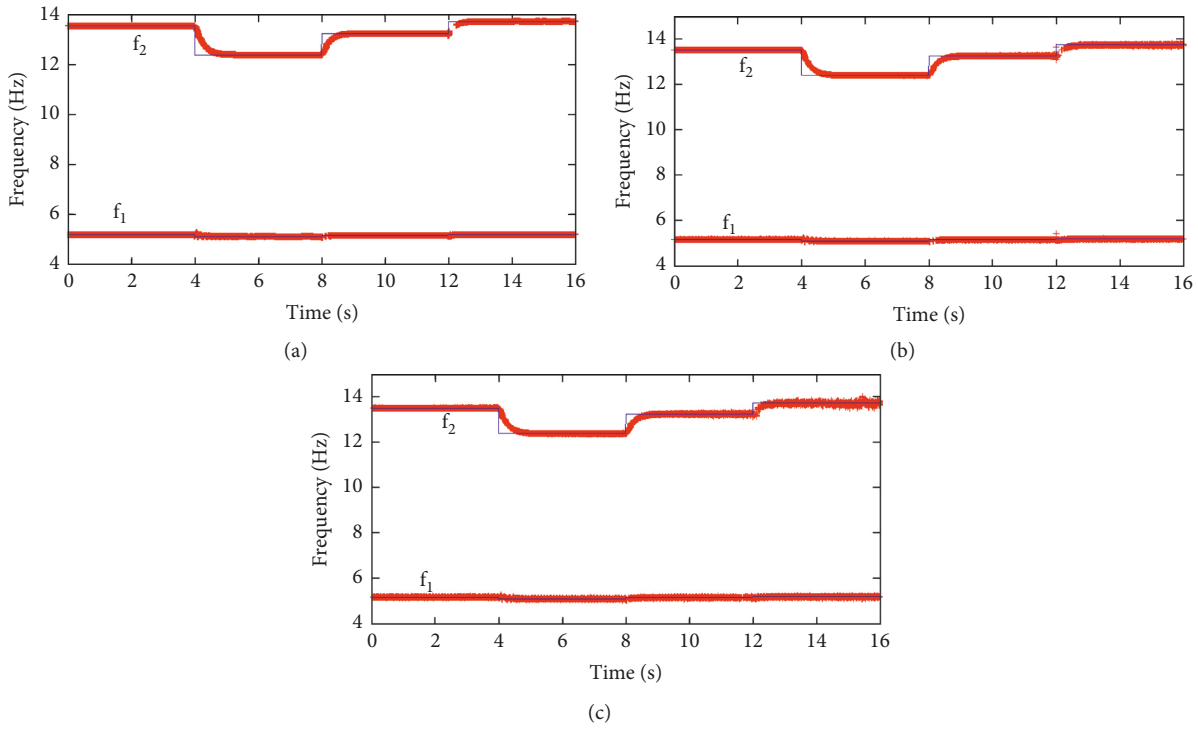

Figure 11: Frequency identification results of the first two modes using vibration signals with different SNR values for simulation case 1 (blue line represents the theoretical value of the frequency, and red line represents the identified value of the frequency): (a) no noise; (b) SNR = 50 dB; (c) SNR = 40 dB; (d) SNR = 30 dB.

less than the first-order modal frequency of the dam. However, for the Newhall earthquake, the range of the dominant frequencies of earthquake excitation is much wider than those of the other two earthquakes. Therefore, for the Newhall earthquake, the final modal identification results of the dam should not include these dominant frequencies of excitation shown in Figure 16(f).

By setting $\beta = 0.995$, $p = 100$, and $N_1 = 200$, the structural frequencies and damping ratios are identified using the proposed time-varying modal identification method based on GYAST-RSSI, and the identification results are shown in Figures 17–19. The vibration response of channel 1 is plotted to show the variation of the modal parameters with the acceleration amplitude. From Figures 17–19, the time-varying characteristics of the arch dam during earthquakes are clearly observed, especially when the amplitude of the acceleration response is relatively large. According to Figures 17–19, the frequency after the earthquake tends to be

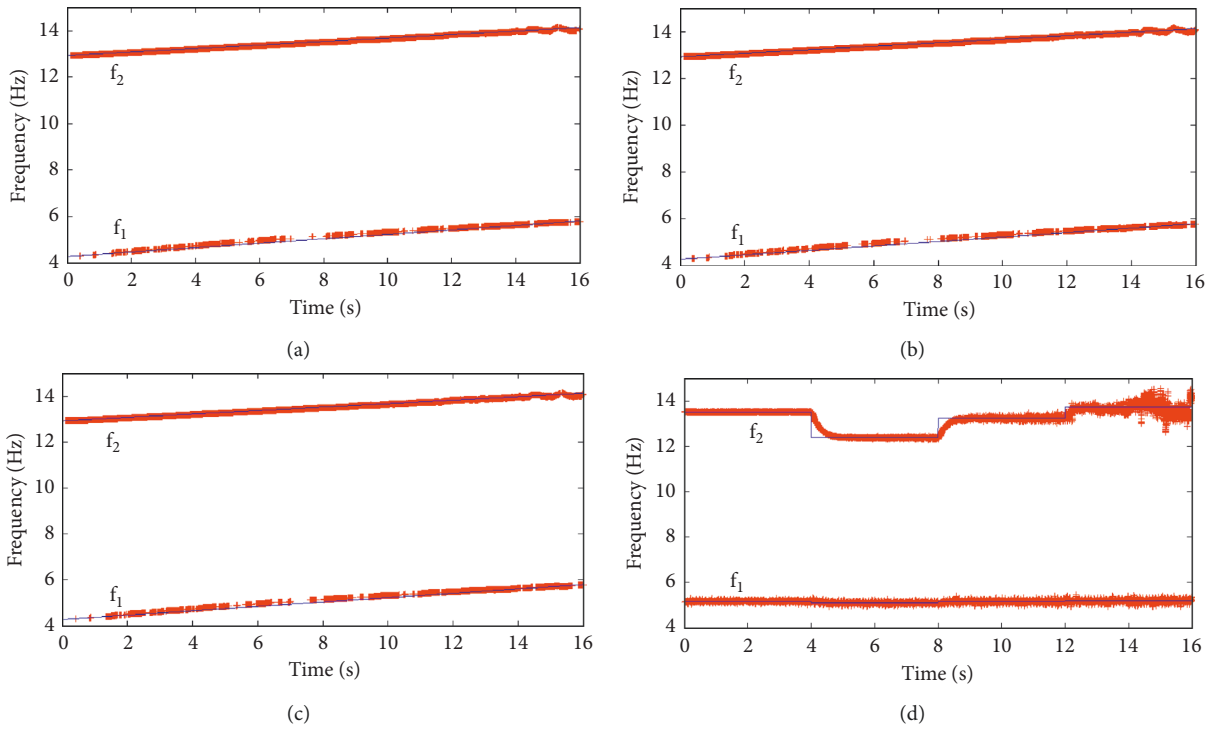

Figure 12: Frequency identification results of the first two modes using vibration signals with different SNR values for simulation case 2 (blue line represents the theoretical value of the frequency, and red line represents the identified value of the frequency): (a) no noise; (b) SNR = 50 dB; (c) SNR = 40 dB; (d) SNR = 30 dB.

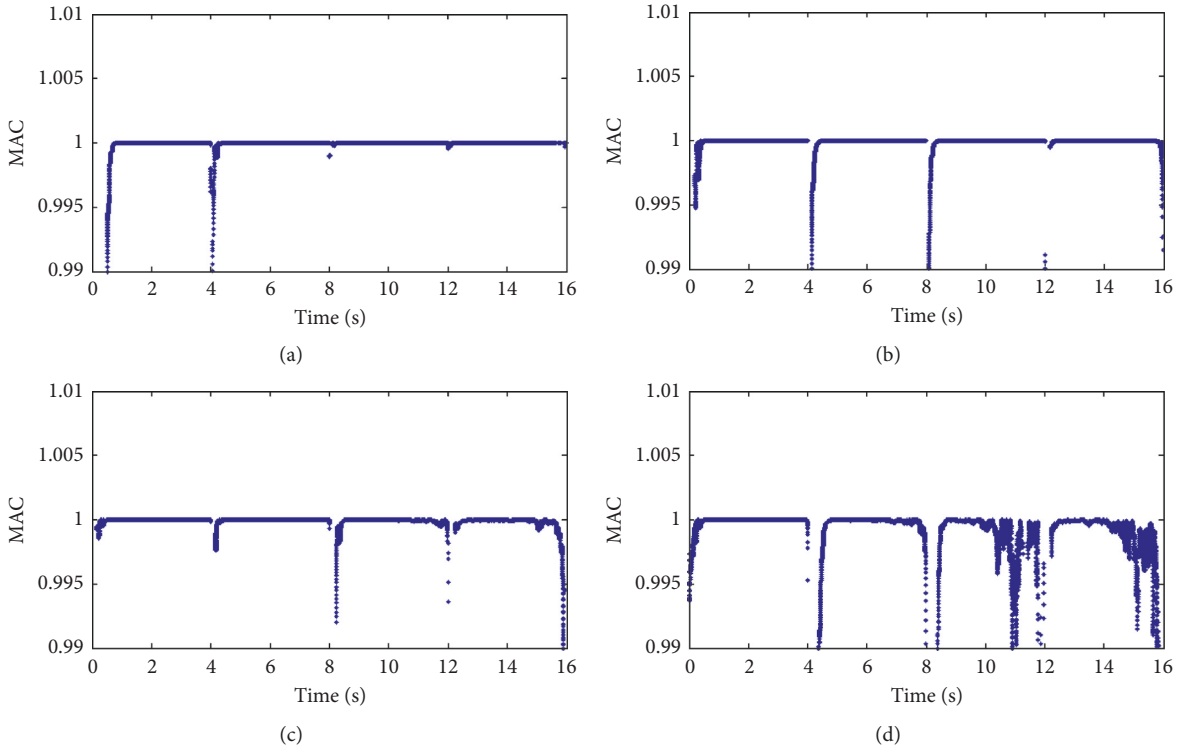

Figure 13: The MAC between the identified and theoretical values of the modal shape vectors for simulation case 1 (SNR = 40 dB): (a) mode 1; (b) mode 2; (c) mode 3; (d) mode 4.

Table 1: A comparison of the ARE of time-varying modal identification results for frequencies using the EIV-PAST-RSSI and GYAST-RSSI methods.

Case	Mode	Method	No noise (%)	SNR = 50 dB (%)	SNR = 40 dB (%)	SNR = 30 dB (%)
I	1	EIV-PAST-RSSI	0.25	0.41	0.63	0.88
		GYAST-RSSI	0.23	0.44	0.51	0.75
	2	EIV-PAST-RSSI	0.32	0.64	1.58	2.05
		GYAST-RSSI	0.29	0.60	1.47	2.11
	3	EIV-PAST-RSSI	0.30	0.83	1.02	1.37
		GYAST-RSSI	0.36	0.80	0.97	1.22
	4	EIV-PAST-RSSI	0.42	0.77	1.29	1.58
		GYAST-RSSI	0.58	0.69	1.36	1.77
II	1	EIV-PAST-RSSI	0.11	0.20	0.59	0.92
		GYAST-RSSI	0.21	0.34	0.48	0.85
	2	EIV-PAST-RSSI	0.32	0.41	0.68	1.09
		GYAST-RSSI	0.47	0.59	0.50	1.32
	3	EIV-PAST-RSSI	0.79	0.86	1.25	1.73
		GYAST-RSSI	0.79	0.86	1.25	1.73
	4	EIV-PAST-RSSI	0.54	0.99	1.43	1.92
		GYAST-RSSI	0.48	0.87	1.51	1.77

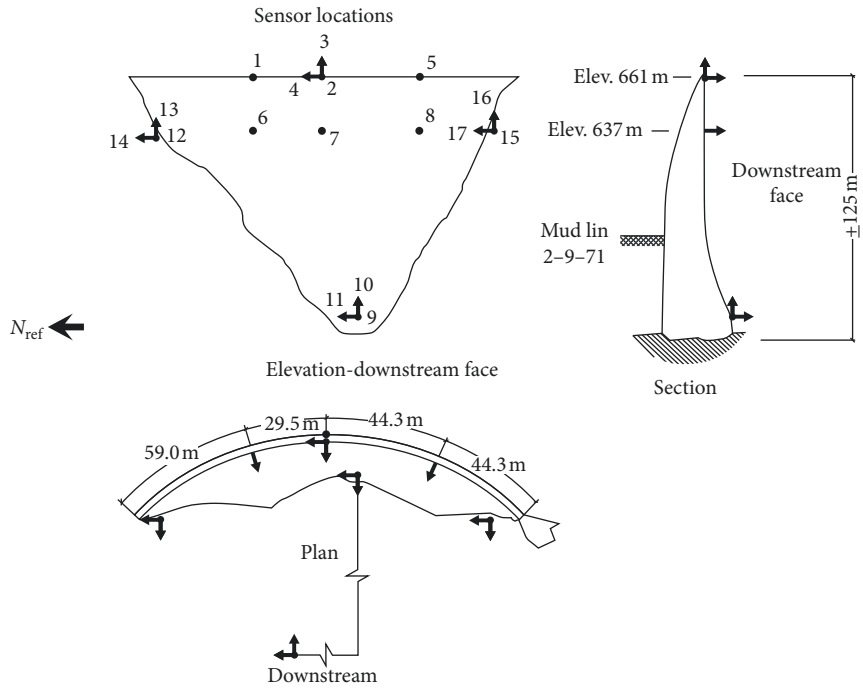

Figure 14: The arrangement of the accelerographs on the Pacoima arch dam.

Table 2: Information about three major California earthquakes.

Earthquake name	Date	Earthquake magnitude	Location of earthquake source	Depth of the earthquake source (km)
San Fernando	2001-01-13	4.3	—	—
Chino Hills	2008-07-29	5.5	3.5 km northwest of Los Angeles	13.6
Newhall	2011-09-01	4.2	12 km away from Los Angeles	—

stable, indicating that none of the three earthquakes may cause any damage to the dam.

For the three earthquakes, the frequencies of the dam show a decreasing trend after the earthquake, which may be caused by the solid-water interaction and the reduction of the structural stiffness. As was shown in some previous works, the solid-water interaction can be simulated by the simple adding-mass method. The additional mass that is added to the structural system will reduce the frequencies of the dam-reservoir-foundation system. However, the decrease in the frequencies can also be caused by the reduction of the structural stiffness during earthquakes, which needs to be

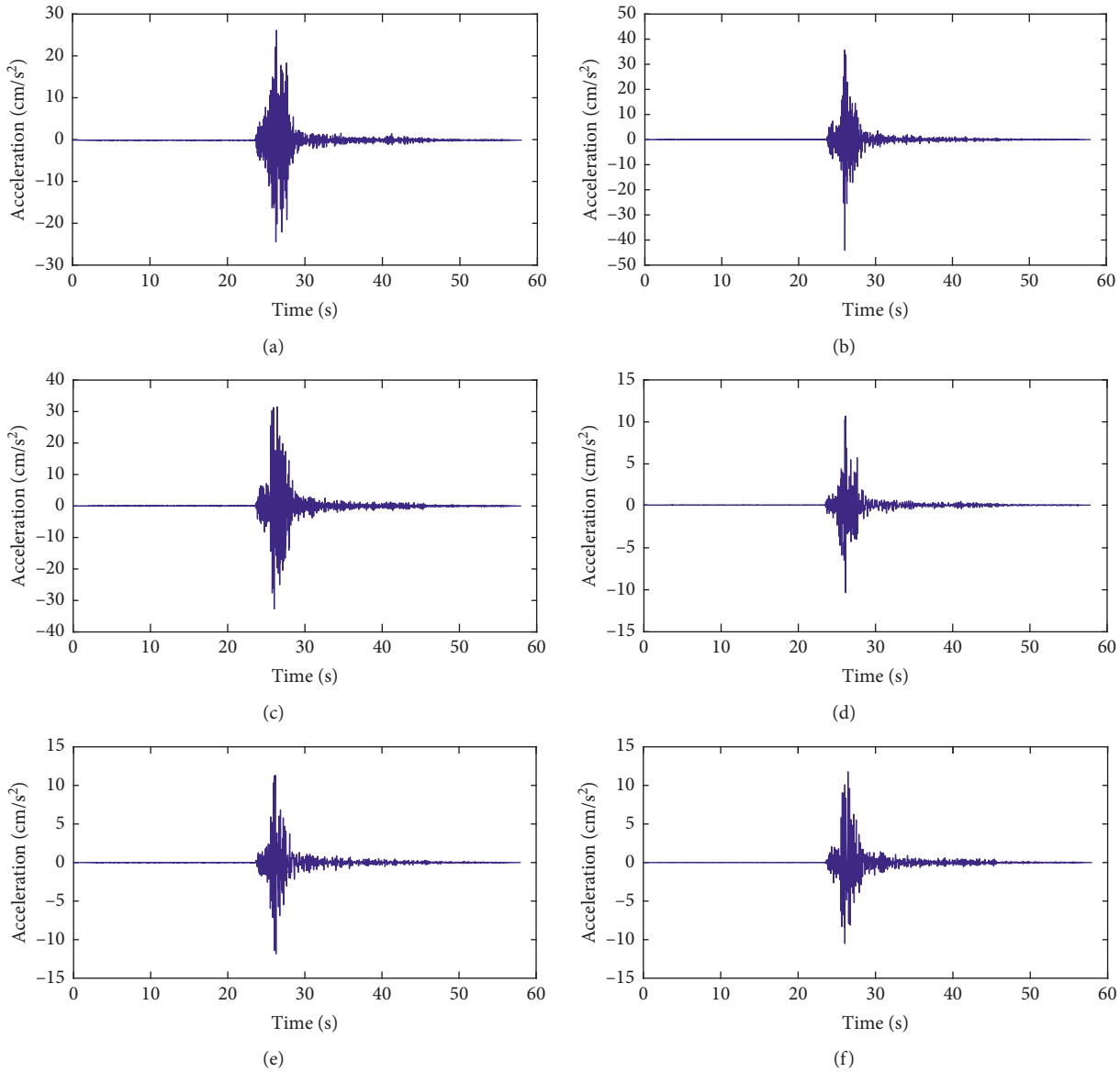

Figure 15: Strong motion of Pacoima arch dam of channels in the radial direction during the Newhall earthquake: (a) channel 1; (b) channel 2; (c) channel 5; (d) channel 6; (e) channel 7; (f) channel 8.

Table 3: Some time-invariant modal identification results of the Pacoima dam.

Earthquake	Identification method	Frequency (Hz)			Damping ratio		
		Mode 1	Mode 2	Mode 3	Mode 1	Mode 2	Mode 3
San Fernando	Optimization method [8]	—	4.73	5.06	—	6.2%	6.6%
San Fernando	4 spectra [32]	3.6–3.7	4.8–5.0	5.1–5.3	2.74%	2.48%	2.41%
Chino Hills	ARX model [22]	—	5.40	5.75			

studied in the future. When the amplitude of the acceleration is very low, the modal identification results tend to be time variant. These time-varying modal identification results demonstrate that the dynamic characteristics of concrete dams during large earthquakes are time-varying indeed.

For four typical time instants, $t = 20$ s, 25 s, 30 s, and 35 s, the identification results of the modal shape vectors using the strong-motion records of the Newhall earthquake are shown in Figure 20. Figure 20 shows the time-varying characteristics of the arch dam's modal shape vectors during the earthquake.

4. Conclusions

The online modal identification method of concrete dams proposed in this work has been verified using a numerical example and an engineering example. The GYAST is a good

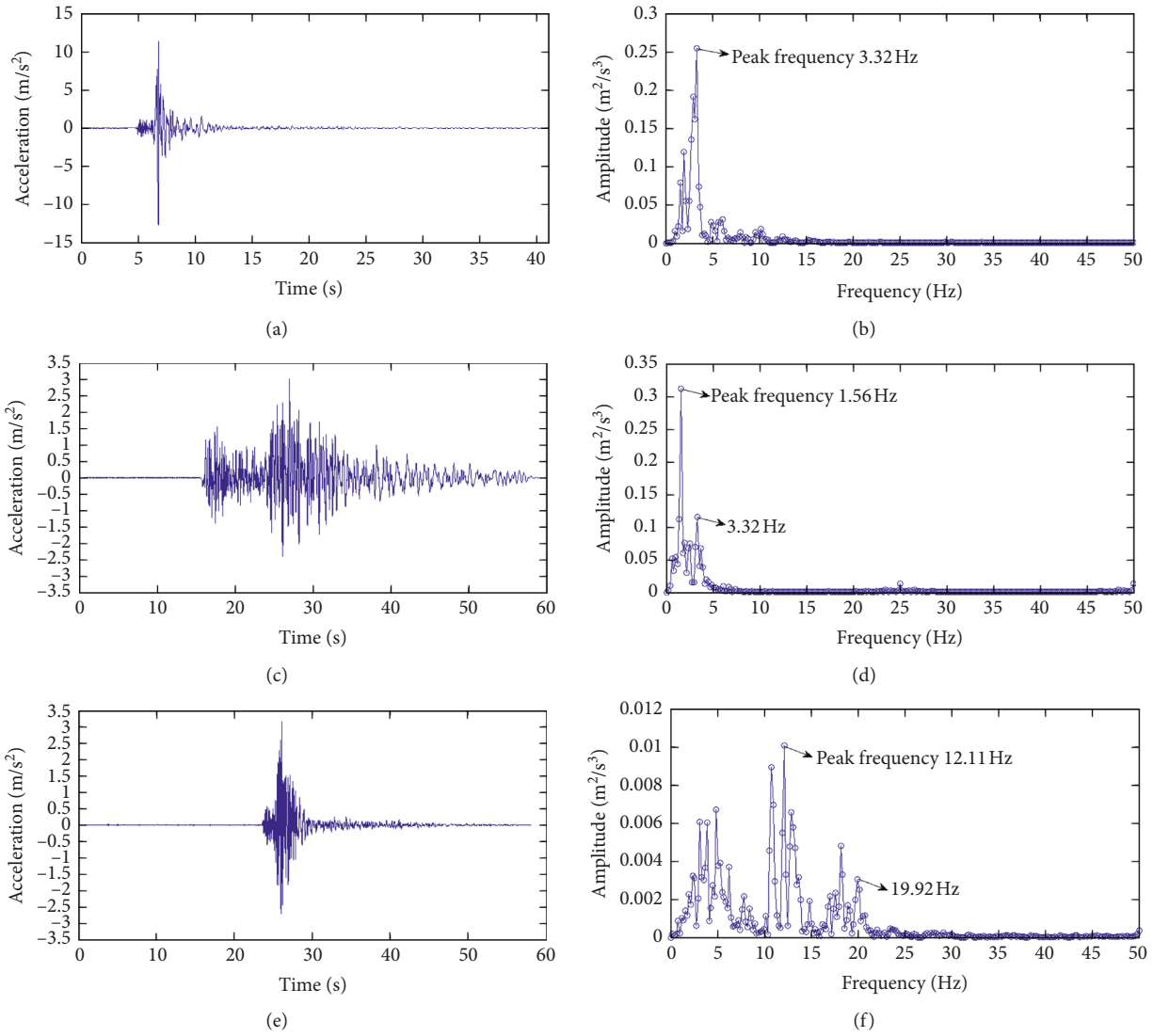

Figure 16: The strong-motion records of channel 9 and the corresponding power spectrums during three major California earthquakes: (a) the strong-motion record of channel 9 during the San Fernando earthquake; (b) the power spectrum of the strong-motion record of channel 9 during the San Fernando earthquake; (c) the strong-motion record of channel 9 during the Chino hill earthquake; (d) the power spectrum of the strong-motion record of channel 9 during the Chino hill earthquake; (e) the strong-motion record of channel 9 during the Newhall earthquake; (f) the power spectrum of the strong-motion record of channel 9 during the Newhall earthquake.

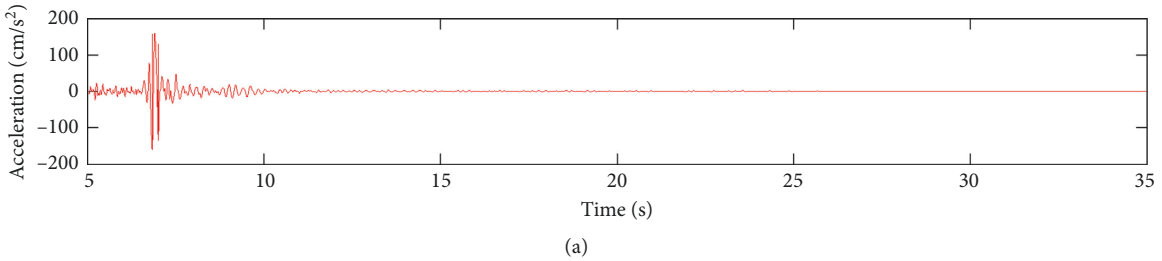

Figure 17: Continued.

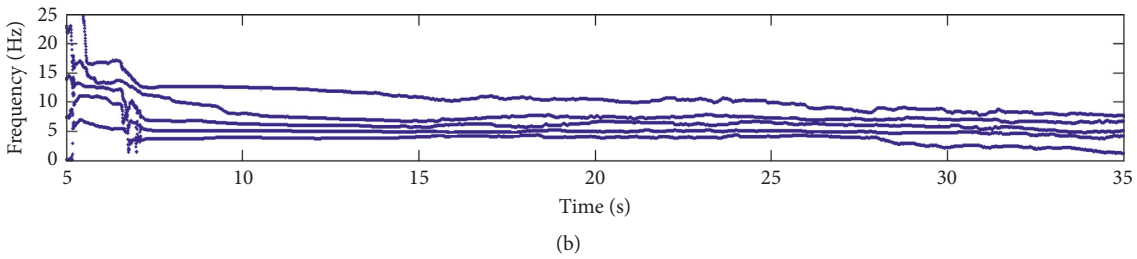

(b)

Figure 17: Time-varying modal identification results of the Pacoima dam using the San Fernando earthquake data: (a) vibration response of channel 1; (b) identification results for frequencies.

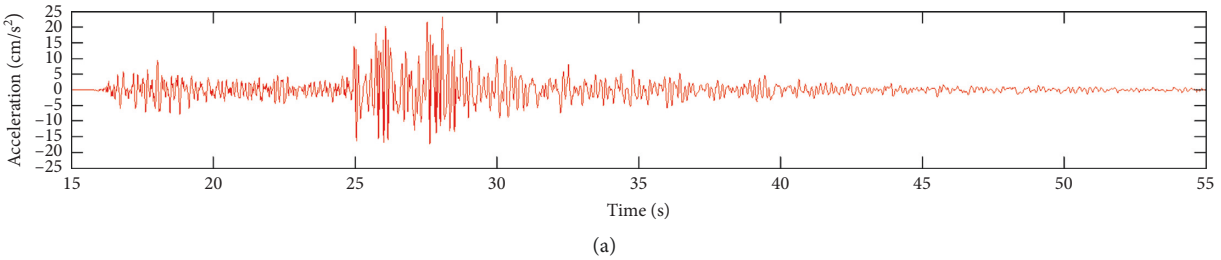

(a)

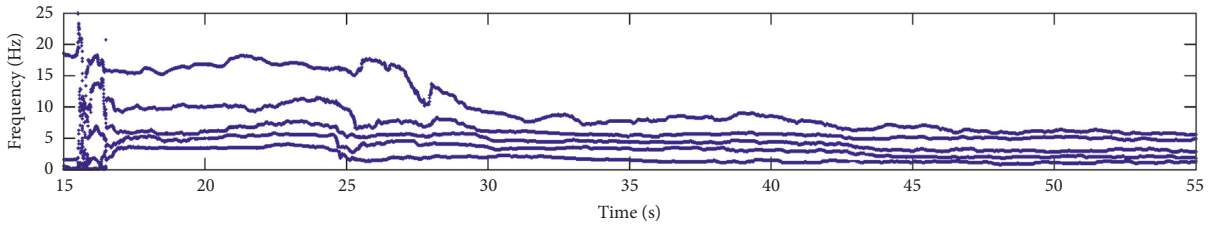

(b)

Figure 18: Time-varying modal identification results of the Pacoima dam using the Chino Hills earthquake data: (a) vibration response of channel 1; (b) identification results for frequencies.

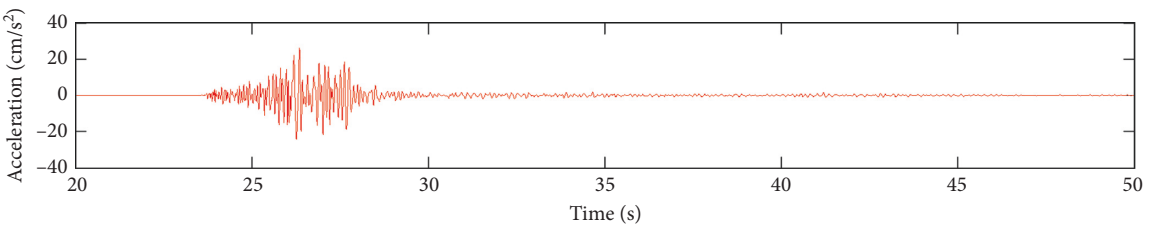

(a)

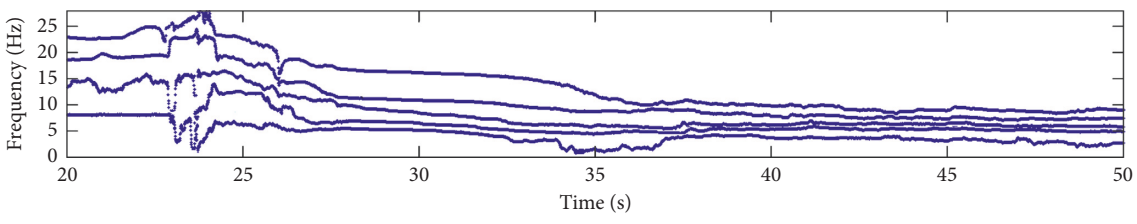

(b)

Figure 19: Time-varying modal identification results of the Pacoima dam using the Newhall earthquake data: (a) vibration response of channel 1; (b) identification results for frequencies.

tool to track the signal subspaces of different modes to reduce the disturbance of the observation noise and stochastic excitation since it shows good identification accuracy, robustness, and computation efficiency. The identification accuracy of the frequencies and modal shape vectors is sufficient, while for the damping ratios, the

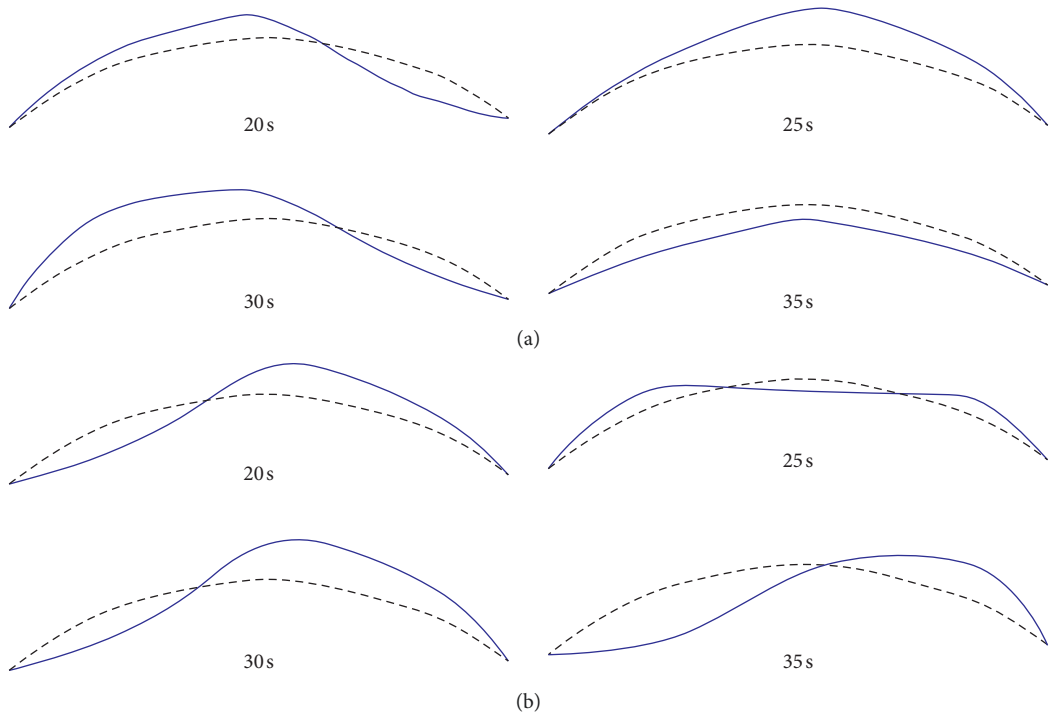

Figure 20: Time-varying modal shape vectors of the Pacoima dam using the strong-motion records of the Newhall earthquake (dash line represents the original arch circle, and blue line represents the modal shape): (a) mode 1; (b) mode 2.

performance of the proposed online modal identification method still needs to be improved. Some possible ways to obtain a better identification result of the damping include improving the robustness of the subspace tracking algorithms, signal denoising, and adopting input-output modal identification methods. The time-varying modal parameters identified using the strong-motion records of concrete dams can be used as important features to study the real dynamic characteristics of structures during large earthquakes, which is our research direction in the future.

Data Availability

The strong earthquake records data used to support the findings of this study may be released upon application to the Center for Engineering Strong Motion Data at https://strongmotioncenter.org. The MATLAB code for the GYAST algorithm online to support the findings of this study is available from the Professor Mostafa Arjomandi-Lari [22]. The numerical simulation and other data used to support the findings of this study are available from the corresponding author upon request.

Conflicts of Interest

The authors declare that they have no conflicts of interest.

Acknowledgments

This work was supported by the National Natural Science Foundation of China (Grant nos. 51409205, 51279052, 51409018, and 51309189), the National Natural Science Foundation for Excellent Young Scientists of China (Grant no. 51722907), a project funded by the China Postdoctoral Science Foundation (Grant no. 2015M572656XB), and the Open Foundation of the State Key Laboratory of Hydrology-Water Resources and Hydraulic Engineering (Grant no. 2014491011). The authors appreciate Professor Mostafa Arjomandi-Lari for providing the MATLAB code for the GYAST algorithm online. The authors also appreciate the Center for Engineering Strong Motion Data; all strong earthquake records used in this article are derived from this centre.

References

[1] C.-H. Loh and T.-C. Wu, "System identification of Fei-Tsui arch dam from forced vibration and seismic response data," *Journal of Earthquake Engineering*, vol. 4, no. 4, pp. 511–537, 2000.

[2] G. R. Darbre, C. A. M. de Smet, and C. Kraemer, "Natural frequencies measured from ambient vibration response of the arch dam of Mauvoisin," *Earthquake Engineering & Structural Dynamics*, vol. 29, no. 5, pp. 577–586, 2000.

[3] J. Proulx, P. Paultre, J. Rheault, and Y. Robert, "An experimental investigation of water level effects on the dynamic behaviour of a large arch dam," *Earthquake Engineering & Structural Dynamics*, vol. 30, no. 8, pp. 1147–1166, 2001.

[4] N. Okuma, Y. Etou, and K. Kanazawa, "Dynamic property of a large arch dam after forty-four years of completion," in *Proceedings of the Fourteenth World Conference on Earthquake Engineering*, Beijing, China, October 2008.

[5] L. Cheng and D. J. Zheng, "The identification of a dam's modal parameters under random support excitation based on the Hankel matrix joint approximate diagonalization

technique," *Mechanical Systems and Signal Processing*, vol. 42, no. 1-2, pp. 42–57, 2014.

[6] J. Yang, F. Jin, J.-T. Wang, and L.-H. Kou, "System identification and modal analysis of an arch dam based on earthquake response records," *Soil Dynamics and Earthquake Engineering*, vol. 92, pp. 109–121, 2017.

[7] S. W. Alves and J. F. Hall, "System identification of a concrete arch dam and calibration of its finite element model," *Earthquake Engineering & Structural Dynamics*, vol. 35, no. 11, pp. 1321–1337, 2006.

[8] Z. Ni, R. Mu, G. Xun, and Z. Wu, "Time-varying modal parameters identification of a spacecraft with rotating flexible appendage by recursive algorithm," *Acta Astronautica*, vol. 118, pp. 49–61, 2016.

[9] A. Velazquez and R. A. Swartz, "Output-only cyclo-stationary linear-parameter time-varying stochastic subspace identification method for rotating machinery and spinning structures," *Journal of Sound and Vibration*, vol. 337, pp. 45–70, 2015.

[10] G. Ruocci, G. Cumunel, T. Le, P. Argoul, N. Point, and L. Dieng, "Damage assessment of pre-stressed structures: a SVD-based approach to deal with time-varying loading," *Mechanical Systems and Signal Processing*, vol. 47, no. 1-2, pp. 50–65, 2014.

[11] K. Liu, "Extension of modal analysis to linear time-varying systems," *Journal of Sound and Vibration*, vol. 226, no. 1, pp. 149–167, 1999.

[12] K. Yang and K. P. Yu, "The currently existing methods of modal parameter estimation for time-varying structures can be classified into two categories: parametric time-domain methods and non-parametric time–frequency-domain methods," in *Proceedings of the 15th ASCE Engineering Mechanics Conference*, New York, NY, USA, June 2002.

[13] K. Yu, S. W. Pang, and J. Zhao, "Advances in method of time-varying linear/nonlinear structural system identification and parameter estimate," *CSB*, vol. 54, no. 20, pp. 3147–3156, 2009.

[14] M. S. Gong, *Structural modal parameters identification and application based on earthquake response data*, Ph.D. Dissertation, Institute of Engineering Mechanics China Earthquake Administration, Harbin, China, 2005.

[15] A. G. Poulimenos and S. D. Fassois, "Parametric time-domain methods for non-stationary random vibration modelling and analysis—a critical survey and comparison," *Mechanical Systems and Signal Processing*, vol. 20, no. 4, pp. 763–816, 2006.

[16] A. Klepka and T. Uhl, "Identification of modal parameters of non-stationary systems with the use of wavelet based adaptive filtering," *Mechanical Systems and Signal Processing*, vol. 42, no. 1-2, pp. 21–34, 2014.

[17] I. Goethals, L. Mevel, A. Benveniste, and B. D. Moor, "Recursive output only subspace identification for in-flight flutter monitoring," in *Proceedings of the 22nd International Modal Analysis Conference*, Dearborn, MI, USA, January 2004.

[18] S. A. Nezam Sarmadi and V. Venkatasubramanian, "Electromechanical mode estimation using recursive adaptive stochastic subspace identification," *IEEE Transactions on Power Systems*, vol. 29, no. 1, pp. 349–358, 2014.

[19] C.-H. Loh and Y.-C. Liu, "Application of recursive SSA as data pre-processing filter for stochastic subspace identification," *Smart Structures and Systems*, vol. 11, no. 1, pp. 19–34, 2013.

[20] Y.-C. Liu, C.-H. Loh, and Y.-Q. Ni, "Stochastic subspace identification for output-only modal analysis: application to super high-rise tower under abnormal loading condition," *Earthquake Engineering & Structural Dynamics*, vol. 42, no. 4, pp. 477–498, 2013.

[21] R. Tarinejad, "Modal identification of an arch dam during various earthquakes," in *Proceedings of the 1st International Conference On Dams And Hydropower*, Tehran, Iran, January 2012.

[22] M. Arjomandi-Lari and M. Karimi, "Generalized YAST algorithm for signal subspace tracking," *Signal Processing*, vol. 117, pp. 82–95, 2015.

[23] S. W. Alves, *Nonlinear analysis of pacoima dam with spatially non-uniform ground motion*, Ph.D. Dissertation, California Institute of Technology, Pasadena, CA, 2004.

[24] S.-D. Zhou, W. Heylen, P. Sas, and L. Liu, "Parametric modal identification of time-varying structures and the validation approach of modal parameters," *Mechanical Systems and Signal Processing*, vol. 47, no. 1-2, pp. 94–119, 2014.

[25] M. A. Raja and B. K. Maheshwari, "Seismic performance evaluation and analysis of major arch dams considering material and joint nonlinearity effects," *ISRN Civil Engineering*, vol. 2012, Article ID 681350, 10 pages, 2012.

[26] X. Xu and Z. Y. Zhang, "Identification of time-varying modal parameters using linear time-frequency representation," *Chinese Journal of Mechanical Engineering (English Edition)*, vol. 16, no. 4, pp. 445–448, 2003.

[27] S. I. McNeill, *Modal identification using blind source separation techniques*, Ph.D. Dissertation, University of Houston, Houston, TX, USA,, 2007.

[28] S. McNeill, "An analytic formulation for blind modal identification," *Journal of Vibration and Control*, vol. 18, no. 14, pp. 2111–2121, 2012.

[29] A. Masuda, M. Noori, A. Sone, and Y. Yamashita, "Time varying modal identification by Monte Carlo filter," in *Proceedings of 15th ASCE Engineering Mechanics Conference*, New York, NY, USA, June 2002.

[30] Z. Li and C. C. Chang, "Tracking of structural dynamic characteristics using recursive stochastic subspace identification and instrumental variable technique," *Journal of Engineering Mechanics*, vol. 138, no. 6, pp. 591–600, 2012.

[31] R. Badeau, G. Richard, and B. David, "Fast and stable YAST algorithm for principal and minor subspace tracking," *IEEE Transactions on Signal Processing*, vol. 56, no. 8, pp. 3437–3446, 2008.

[32] R. Tarinejad and M. Damadipour, "Extended FDD-WT method based on correcting the errors due to non-synchronous sensing of sensors," *Mechanical Systems and Signal Processing*, vol. 72-73, pp. 547–566, 2016.

Hindawi
Shock and Vibration
Volume 2019, Article ID 6581516, 14 pages
https://doi.org/10.1155/2019/6581516

Research Article

An Introduction of a Robust OMA Method: CoS-SSI and Its Performance Evaluation through the Simulation and a Case Study

Fulong Liu[2], **Jigang Wu**[1,2], **Fengshou Gu**[2] and **Andrew D. Ball**[2]

[1]*Hunan Provincial Key Laboratory of Health Maintenance for Mechanical Equipment, Hunan University of Science and Technology, Xiangtan, China*
[2]*Centre for Efficiency and Performance Engineering (CEPE), School of Computing and Engineering, University of Huddersfield, Huddersfield, UK*

Correspondence should be addressed to Jigang Wu; jwu@cvm.ac.cn

Received 27 October 2018; Revised 11 January 2019; Accepted 19 January 2019; Published 31 January 2019

Academic Editor: Carlo Rainieri

Operational modal analysis (OMA) is a powerful vibration analysis tool and widely used for structural health monitoring (SHM) of various system systems such as vehicles and civil structures. Most of the current OMA methods such as pick-picking, frequency domain decomposition, natural excitation technique, stochastic subspace identification (SSI), and so on are under the assumption of white noise excitation and system linearity. However, this assumption can be desecrated by inherent system nonlinearities and variable operating conditions, which often degrades the performance of these OMA methods in that the modal identification results show high fluctuations. To overcome this deficiency, an improved OMA method based on SSI has been proposed in this paper to make it suitable for systems with strong nonstationary vibration responses and nonlinearity. This novel method is denoted as correlation signal subset-based SSI (CoS-SSI) as it divides correlation signals from the system responses into several subsets based on their magnitudes; then, the average correlation signals with respective to each subset are taken into as the inputs of the SSI method. The performance of CoS-SSI was evaluated by a simulation case and was validated through an experimental study in a further step. The results indicate that CoS-SSI method is effective in handling nonstationary signals with low signal to noise ratio (SNR) to accurately identify modal parameters from a fairly complex system, which demonstrates the potential of this method to be employed for SHM.

1. Introduction

Operational modal analysis (OMA) is, in fact, not really a new discipline. The beginning of OMA could be going back to the sixties and early seventies, which was developed along with the experimental modal analysis (EMA) [1]. However, OMA has been developed rapidly since the last two decades. One main reason for this is the availability of a large quantity of new powerful system identification techniques, which are the basis of OMA approaches available as a complementary tool [2–7]. Another reason is the rapid development of computer technology, which can compute the mass measured data in less time. Compared to EMA, the OMA has attracted a more considerable attention in mechanical engineering, aerospace engineering, and civil engineering since 1990s due to its many aspects. The main advantages of OMA are highlighted as follows [5, 8–10]:

(1) OMA is cheaper and faster to conduct since it only measures the responses
(2) The dynamic characteristics of the whole structural system can be obtained instead of its small parts
(3) A linear model of structural systems under operational conditions can be obtained since the random excitations are of broadband in nature
(4) OMA is suitable for complex and complicated structures due to the fact that the close modes can be identified through multi-input/multioutput (MIMO) modal identification algorithm

Because of these advantages, there are numerous OMA methods that have been developed in last decades. Generally, they can be classified into two categories: frequency domain (FD) and time domain (TD). The earliest FD technique is

based on the power spectrum density (PSD) peak-picking algorithm. The natural frequencies are directly obtained from the choice of peaks in the PSD graph. The peak-picking technique has proved its effectiveness in the modal identification method when system's modes are well separated [4, 5]. This technique is simple to use. However, it has less accuracy because of the limitation of the frequency resolution in the PSD spectrum [4]. Therefore, peak-picking technique is unsuitable for the modal identification of the system with close modes [5]. However, the realistic complex structures are always encountered with close modes. Consequently, a new FD technique, named frequency domain decomposition (FDD), was developed to meet the challenge of the identification of the close modes [11]. In FDD, the response is derived into a set of single-degree-of-freedom systems by introducing a decomposition of the spectral density function matrix. The major drawback of the FDD is that it can only estimate the modal frequencies and the mode shapes but not the damping ratios. In order to extract the damping ratio, an enhanced FDD (EFDD) was then proposed [12]. The EFDD method extracts the damping of a particular mode by computing the autocorrelation and cross-correlation functions. However, all of the referred methods are under assumptions that the input signals are stationary Gaussian white noise and the structure is very lightly damped.

Besides the FD techniques, the TD techniques were also developed very quickly in the last decades. For instance, the natural excitation technique (NExT) is a popular and powerful TD method, which was proposed in 1990s [13]. It is based on the principal that the correlation functions can be expressed as the sum of exponentially decayed sinusoids assuming the ambient excitation as a white noise. The correlation functions perform the similar role like the impulse response functions in EMA, which consists of the information of the modal parameters [5, 14]. On the basis of this principle, some other traditional EMA techniques such as polyreference complex exponential (PRCE), Ibrahim time domain (EITD), and eigen realization algorithm (ERA) were also successfully extended and applied for the OMA.

Furthermore, stochastic subspace identification (SSI) method is another widely employed TD technique for OMA. It was proposed as an extension of the subspace state-space system identification method [5]. A systematic description of SSI and its applications can be found in [15–17]. However, the SSI method follows the same assumption like other OMA techniques; the excitations have to be stationary. Yet this is not always true for the field test of OMA. For example, the vehicle responses are always nonstationary resulted by frequently acceleration and deceleration. In addition, road humps and nonlinearity will also lead nonstationarity of the vehicle responses. In order to meet the challenge of nonstationarity, some improved SSI methods were proposed by the combining traditional SSI method with other methods, or preprocessing the measured responses before applying them in the SSI. For instance, empirical mode decomposition (EMD) was combined with SSI to extract modal parameters of civil structure from nonstationary signals [18]. What is more, a preprocess step was conducted in [19–21] by averaging the obtained correlation signals, which is denoted as average correlation signal-based SSI (ACS-SSI). The effectiveness of ACS-SSI has been proved by the experimental study of the extraction of the modal parameters of a chassis frame of a heavy-duty dump vehicle under normal operational condition.

Because of the effectiveness of the ACS-SSI method, it was employed to identify the modal parameters related to the vehicle suspension system. However, it was found that the ACS-SSI method was unable to accurately extract the target modal parameters due to the severer excitation condition. Consequently, a new method is needed to extract the modal parameters linked to the suspension parameters. In this study, the main objective of this paper is to present a novel method based on the ACS-SSI method [19, 20], denoted as the correlation subset-based SSI (CoS-SSI), for OMA of system under high noise scenery and with extreme nonstationary responses.

The rest of this paper has been divided into four sections. Section 2 outlines the enhanced method, CoS-SSI. Section 3 verifies the performance of this method through a vibration simulation of a typical 3-DOF system and Section 4 presents an experimental investigation of CoS-SSI to validate the simulation results. Finally, the conclusions are given in Section 5.

2. CoS-SSI Method

As referred previously, most of the OMA techniques were developed under the assumption that the measured responses are stationary. However, the field-monitored data are usually nonstationary such as the platform under the wave impacts and the bridge with the time-varying traffic loading [22]. The nonstationary responses will result in the variation of identified modal parameters from time to time, which may cause the monitoring process to be unreliable in many cases. Moreover, the nonstationary signals may lead to time-varying frequency contents characterized by modal components participating at different times and hence, part of the modes could be missed [19, 22].

The nonstationary problem has been addressed in [23, 24] by introducing the correlation technique, which demonstrates that the nonstationary procedure can be transferred into the stationary problem if the correlation functions are evaluated at a fixed time instant. A theoretical justification can be found in [13, 25]. Based on this theory, a method employing the correlation signals and combined with the framework of covariance driven SSI (Cov-SSI), denoted as ACS-SSI, was proposed in [19, 20]. The main steps of ACS-SSI are listed as follows [19–21, 26]:

(1) Obtain K numbers of data segments from the measurements of l channels.

(2) Calculate the correlation functions of each segment for different channels. The correlation functions can be calculated as follows when the reference is p channel:

$$r^{ip}(m) = \frac{1}{N}\sum_{n=0}^{N-1-|m|} y^{p}(n)y^{i}(n+m), \quad (1)$$

where $i = 1, 2, \ldots, l$ is the channel number; N is the length of each segment; n is the time sequence; and m is the delayed time. The FFT fast Fourier transform (FFT) algorithm can be used to calculate the correlation signals to improve the calculation efficiency.

(3) Conduct average step to all of the obtained correlation functions to calculate the corresponding average correlation functions of each channel. It can be expressed as the following equation:

$$\overline{r^{ip}(m)} = \frac{1}{K}\sum_{k=1}^{K} r_k^{ip}(m), \quad (2)$$

where K is the number of segments.

The averaged correlation functions are employed as the measured responses to construct the Hankel matrix in the SSI method. The reason for the correlation signals obtained from different data sets can be averaged is based on the fact that the phase information between different records is preserved by the reference-based correlation signals. The average step will thus enhance the contents with regular or periodic components by suppressing the irregular random contents in different data records; the regular and periodic components contain the information of modal parameters [19, 20]. The effectiveness of this method has been proved in [19–21, 26]. However, the amplitudes of the correlation signals can be spread in an extremely wide dynamic range due to the strong nonstationary characteristics of the responses, whereas the ACS-SSI method helps in averaging all correlation signals at one time and therefore, takes less account to the signals with low amplitudes.

However, the low-amplitude correlation signals are often related with the vibration modes with higher damping coefficients; in other words, they are less frequently excited. It indicates that such an averaging technique over a full set of data may lead to an inadequate identification result for these modes with high damping properties. As a result, less-excited modes cannot be identified reliably. Moreover, the variation of the amplitude of the correlation signals may result from the inevitable effects of the system nonlinearity.

Based on the above analysis, the deficiency of the ACS-SSI method is evident. Therefore, the performance of ACS-SSI has to be enhanced to make it suitable for extreme nonstationary and quasi-nonlinear scenarios. In this paper, a novel method "correlation subset-based SSI" (CoS-SSI) was proposed which is based on the algorithm of ACS-SSI. Although ACS-SSI has deficiency, it has been proved that the average step conducted to the correlation signals calculated from the short segments of signal are effective in suppressing nonstationary effect, and that is why the same step is applied in the CoS-SSI method. However, the correlation signals are divided into several subsets according to their amplitudes, and each subset of correlations signals are averaged rather than considering all correlation signals as a full set. Finally, the system modal parameters can be obtained by merging the similar modal parameters identified by ACS-SSI with respective to each subset. Moreover, the merging step is performed according to the discrepancy of the identified frequencies and modal assurance criterion (MAC).

Furthermore, unlike ACS-SSI, the main contribution of the CoS-SSI is dividing the correlation signals into different subsets according to their magnitudes. This key step is fulfilled by calculating the root mean square (RMS) value of each correlation signal segment and later identifying the correlation signal segments that belong to the respective subsets based on those corresponding RMS values. Particularly, if l channels of vibration signals have been collected and they have been segregated into K segments, yet $K \times l^2$ of correlation signal segments can be obtained. Each segment has an RMS value, consequently, an RMS value matrix is obtained and its size is $K \times l^2$. The next step is obtaining the minimum RMS value from each segment, and this will yield a vector with K elements. The follow-up step is to obtain the minimum and maximum values from the vector and then calculating the difference of the obtained values. After that, using the calculated difference value, divide the number of subsets by it to calculate the interval of correlation segments. Finally, all of correlation signal segments are categorized into different subsets according to the obtained interval. The value of subset number is always set at 3 or 4 considering the accuracy of identification and the calculation efficiency.

For clarity, the CoS-SSI method is further summarized with a flow chart, shown in Figure 1. The improvement of the steps made in this study is highlighted with red boxes. In this study, a simulation study has been carried out to verify the performance of this newly proposed method by comparing with classical Cov-SSI and ACS-SSI methods. Furthermore, an experimental study has also been conducted to validate the simulation model and to evaluate the effectiveness of this novel method.

In plenty of OMA progress, stabilization diagram (SD) is a popular and efficient tool to filter out the false modes. The SD is performed to check the consistency of the modal properties by setting threshold values for the frequency, damping ratio, and the modal assurance criterion (MAC) between two adjacent orders; only the mode which satisfies all of the three thresholds will be allowed to plot a point on the SD. Moreover, the system's true modes will produce stable points but the spurious modes will not. The tolerance can be calculated based on the following equations:

$$\begin{aligned} &\frac{f_i - f_{i-1}}{f_i} \times 100\% < \varepsilon_{\mathrm{f}}, \\ &\frac{\xi_i - \xi_{i-1}}{\xi_i} \times 100\% < \varepsilon_{\xi}, \\ &1 - \mathrm{MAC}(i : i-1) < \varepsilon_{\mathrm{MAC}}, \\ &\mathrm{MAC}(i : i-1) = \frac{\left|(\Psi_i)^{\mathrm{T}}\Psi_i\right|^2}{(\Psi_i)^{\mathrm{T}}(\Psi_i)(\Psi_{i-1})^{\mathrm{T}}\Psi_{i-1}}, \end{aligned} \quad (3)$$

where f_i, ξ_i, Ψ_i are the frequencies, damping ratios, and mode shapes obtained when the Hankel matrix has i rows

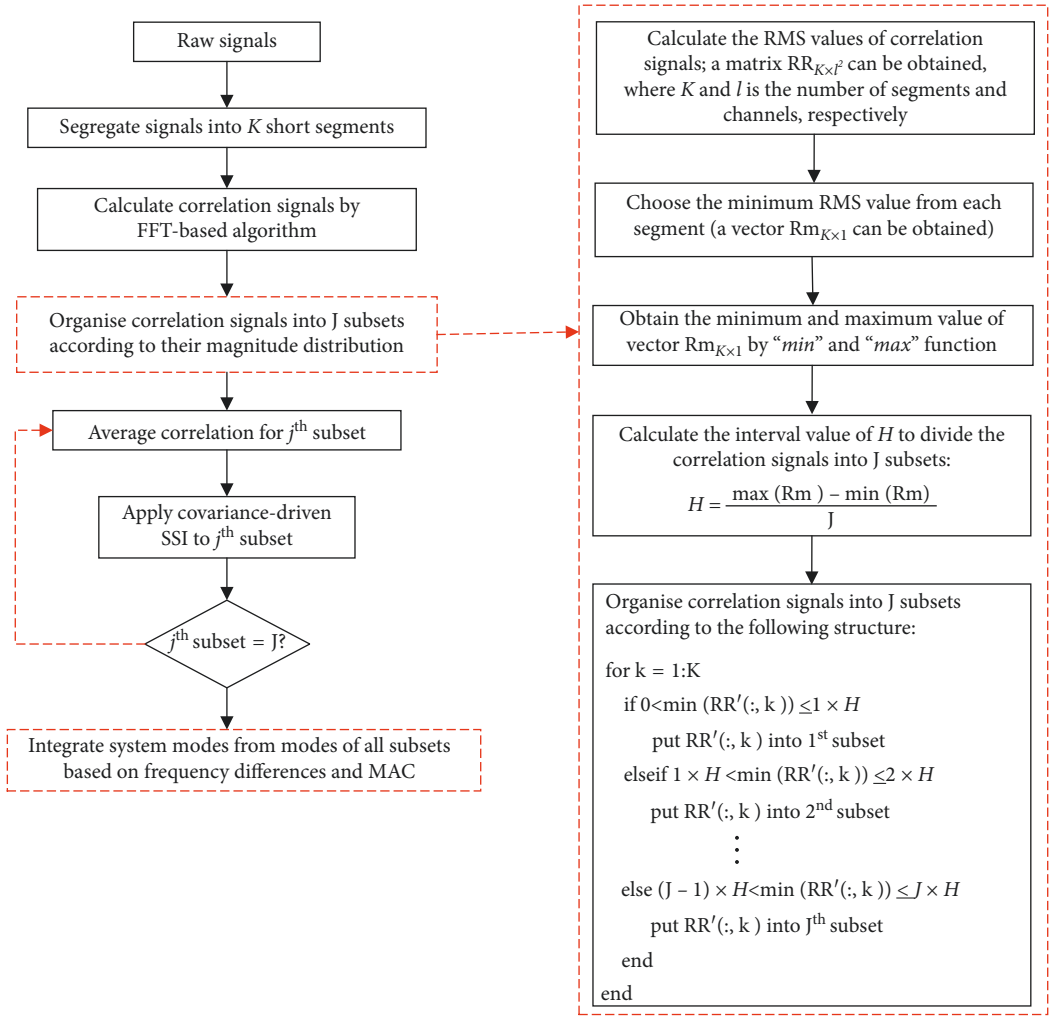

Figure 1: Flow chart of CoS-SSI.

(orders) and $\varepsilon_f, \varepsilon_\xi, \varepsilon_{MAC}$ are the threshold (tolerance) values for the true modes. In this study, $\varepsilon_f, \varepsilon_\xi, \varepsilon_{MAC}$ were set at the values of 0.1, 0.2, and 0.5, respectively. Finally, the system's real modes can be identified based on adequate stable points in the SD. The percentage of the stable points over the calculated number of orders is performed as the second threshold to indicate the corresponding mode with adequate stable points to be chosen as true or false one.

3. Numerical Simulation

3.1. 3-DOF Model Description. In this section, a classical 3-DOF vibration system, shown in Figure 2, was employed to generate simulation signals with a different level of noise to evaluate the performance of the proposed scheme by comparing with traditional Cov-SSI and ACS-SSI methods. The parameters for the 3-DOF system are of $m_1 = m_2 = m_3 =$ 200 kg, $k_1 = k_2 = k_3 = 1.96 \times 10^6$ N/m, and $c_1 = c_2 = c_3 = 1.0 \times 10^3$ N.s/m; the theoretical modal parameters such as natural frequencies and damping ratios of this system can be calculated by using the parameters tabulated in Table 1.

In the simulation case, the 3-DOF system has been excited by three independent random inputs from a band-pass stationary white noise and a number of multiple random impulsive impacts. The impulsive excitations attempt to mimic the occasionally pulse inputs in real applications, such as the bump on the road. The responses $y(k)$ of this 3-DOF vibration system can be obtained through the "*lsim*" function in MATLAB. Moreover, the responses $y(k)$ of this system add more random signals to mimic the measurement noise, shown the following equation:

$$y_n(k) = y(k) + \delta\sigma(k), \tag{4}$$

where $\sigma(k)$ is a band-pass white noise with $\sigma(0, 1)$ and the amplitude factor of measurement noise is defined in equation (5). It allows the performance of CoS-SSI to be evaluated under various scenarios that the output signals with different signal to noise ratios (SNRs).

$$\delta = \frac{\sqrt{\sum_{k=1}^{N} y(k)^2}}{\mathrm{SNR}\sum_{k=1}^{N} \sigma(k)^2}. \tag{5}$$

According to the theoretical resonance frequency of the third mode, the sampling frequency for the numerically solving system model was set at 500 Hz and sampling time was 60 s for each occasion. An example of the acceleration

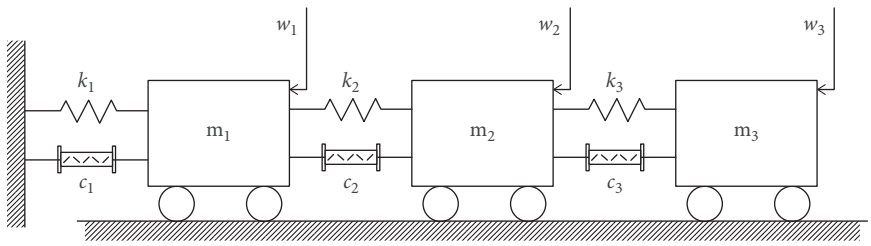

Figure 2: 3-DOF vibration system.

Table 1: Theoretical modal parameters of a 3-DOF system.

	Mode 1	Mode 2	Mode 3
Frequency	7.01 Hz	19.65 Hz	28.39 Hz
Damping ratio	1.12%	3.15%	4.55%

responses of the 3-DOF system with measurement noise is shown in Figure 3. The mean values of every 2 seconds (1000 points) of the responses were calculated when the SNR was 10. It can be seen from Figure 3 that the mean values are changed over the time, which indicates the nonstationarity characteristic of the response signals.

The corresponding power spectrum density (PSD) of each block has been presented under the time-domain signals. It shows that only the first and second modes at the frequencies of 7.06 Hz and 19.65 Hz are clear, whereas the third mode is not that much prominent due to the damping ratio is higher (shown in Table 1). Moreover, it can be seen from the PSD of SNR = 0.5 that the noise has its effect on the energy distribution. Although the main peak values have not been affected, the second and third modes of m_2 have been submerged. Based on this result, it is reasonable to suppose that the noise may cause the modal parameters hard to be identified.

3.2. Identification Results and Analysis. In this section, to illustrate the superiority of CoS-SSI, the other two methods, Cov-SSI and ACS-SSI methods, are also employed in this simulation case. For the Cov-SSI, the dataset used to identify the modal parameters is of 60 seconds time duration for the 3-DOF system with measurement noise; the sampling frequency is 500 Hz. Apart from that, twenty more Monte Carlo simulations were carried out to generate the sufficient signals for modal parameters identification by the ACS-SSI and the CoS-SSI methods. Moreover, the correlation signals were calculated in each Monte Carlo simulation and therefore, twenty correlation signal segments were obtained. For the ACS-SSI, the twenty segments were averaged in single time, and then the averaged signals were employed to identify the modal parameters. However, as referred previously, the ensemble average might loss some significant signatures of the correlation signals with small amplitudes. Therefore, the twenty segments of correlation signals were divided into three subsets according to their magnitudes in the CoS-SSI, and the modal parameters were identified with respective to each subset of correlation signals. The SD identified by the three methods for the 3-DOF system under two SNR scenarios, SNR = 10 and 0.5, are presented in Figures 4–6, respectively.

It can be seen from Figures 4(a) and 5(a) that Cov-SSI and ACS-SSI have the ability to identify three relative stable modes when the SNR is 10. However, the SDs identified by CoS-SSI are messier than the previous two, which can be seen from Figure 6 ($a_{i,i=1,2,3}$). These results might be caused by the classification of correlation signals before the averaging step which improved the SNR in a further step; the signals quality has been improved greatly. Therefore, the threshold should be stricter (with smaller value). It implies that CoS-SSI has no superiority when the signal quality is good. However, the advantage of CoS-SSI can be illustrated with poor quality signals (SNR = 0.5). The SDs identified by the three methods when the SNR is 0.5 are presented in Figures 4(b) and 5(b) and Figure 6 ($b_{i,i=1,2,3}$). It can be seen from Figure 4(b) that Cov-SSI is unable to identify any stable modes. From Figure 5(b), it can be seen that ACS-SSI has the ability to identify first two stable modes, whereas the third mode is unstable. In contrast, CoS-SSI has identified three relative stable modes in the three subsets.

As referred earlier, a second threshold is set up to filter out the spurious modes. In this simulation case, 60 orders (rows) of the Hankel matrix are calculated, which can be seen from the left-y axle. The stable modes are chosen as the percentage of stable points over 50% of the SDs for Cov-SSI and ACS-SSI; this threshold for CoS-SSI is stricker which is set at 70%. An example of the second threshold result identified by Cov-SSI of the signal with SNR = 10 is shown in Figure 7.

Based on these two thresholds, the natural frequency and damping ratio identified by Cov-SSI, ACS-SSI, and CoS-SSI methods are listed in Tables 2–4, respectively. Moreover, the identification errors compared with the theoretical values are also listed in the tables. There are three noticeable things that can be found in the three tables. The first one is that the Cov-SSI cannot identify any mode when the SNR is 0.5; the second one is that the ACS-SSI can only identify first two modes but not the third mode under the same noise condition; and the third thing is that CoS-SSI has the ability to identify all the three modes with the acceptable errors.

In order to better illustrate the identification results, the identification errors of frequency and damping are presented in bar figures, which are shown in Figures 8 and 9, respectively. It can be seen from Figure 8(a) that the frequency identification errors are extremely small. Particularly, when the SNR is 10, most of the frequency identification errors are below 1%. Although the frequency identification errors from CoS-SSI are bigger than those of

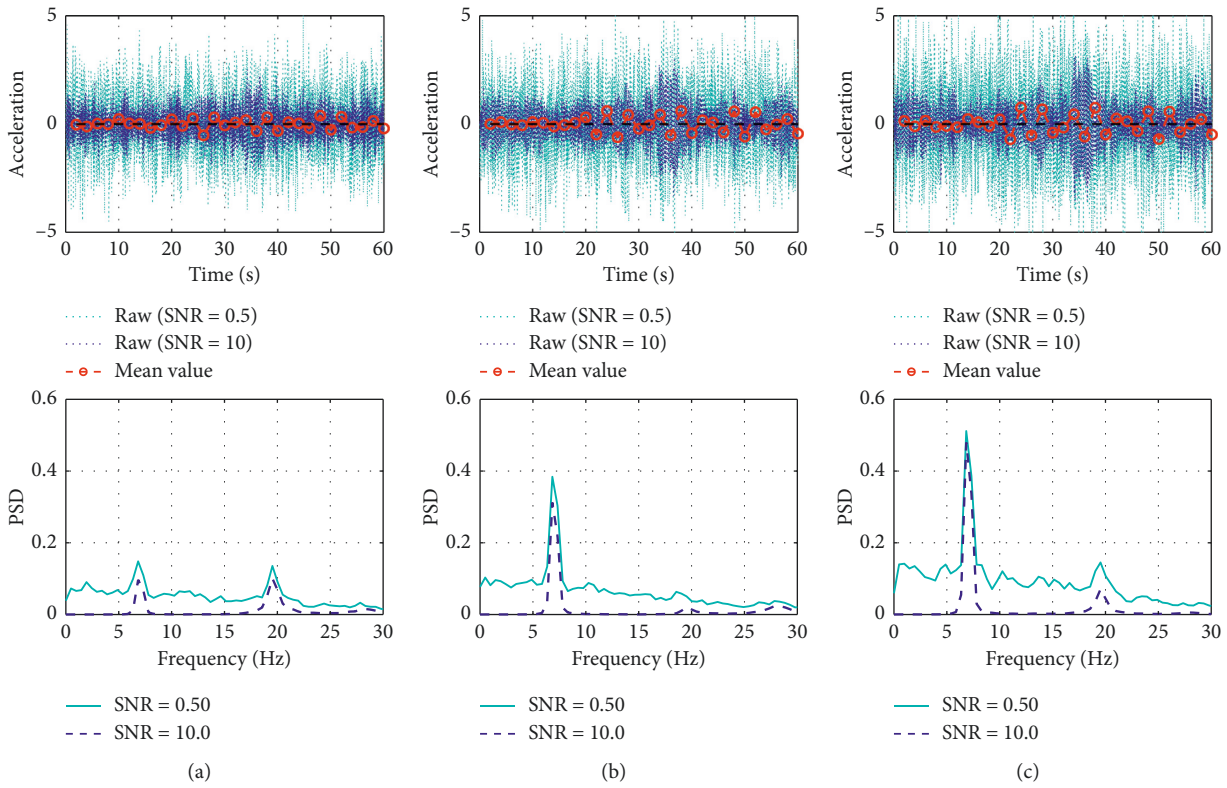

Figure 3: Example of the time-domain responses and corresponding PSD.

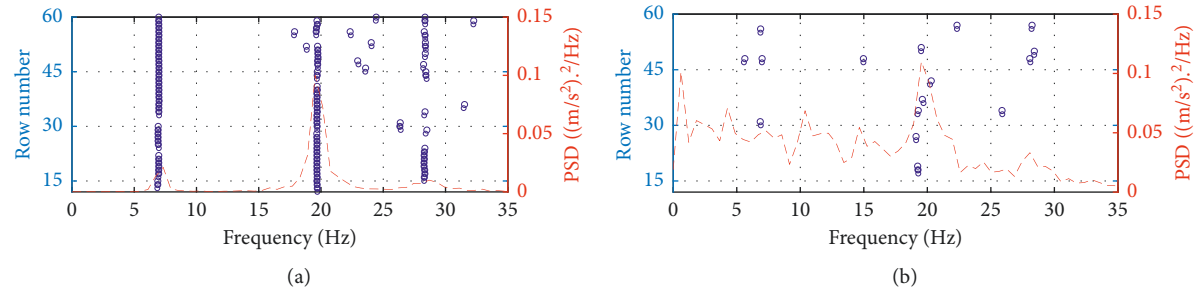

Figure 4: Stabilization diagram of Cov-SSI. (a) SD of Cov-SSI (SNR = 10). (b) SD of Cov-SSI (SNR = 0.5).

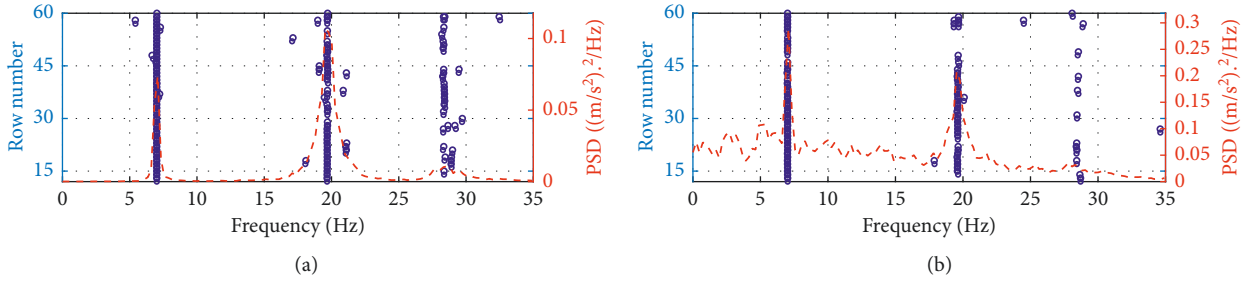

Figure 5: Stabilization diagram of ACS-SSI. (a) SD of ACS-SSI (SNR = 10). (b) SD of Cov-ACS (SNR = 0.5).

ACS-SSI, the errors are still quite small, which are around 1.5%. The main reason for the bigger error of frequency identification from CoS-SSI is the average step accounted with less signals due to the signals are divided into three groups according to their amplitudes. Moreover, it can be seen from Figure 8(b) that the frequency identification accuracy of ACS-SSI and CoS-SSI methods has not been affected regardless of the measurement noise added.

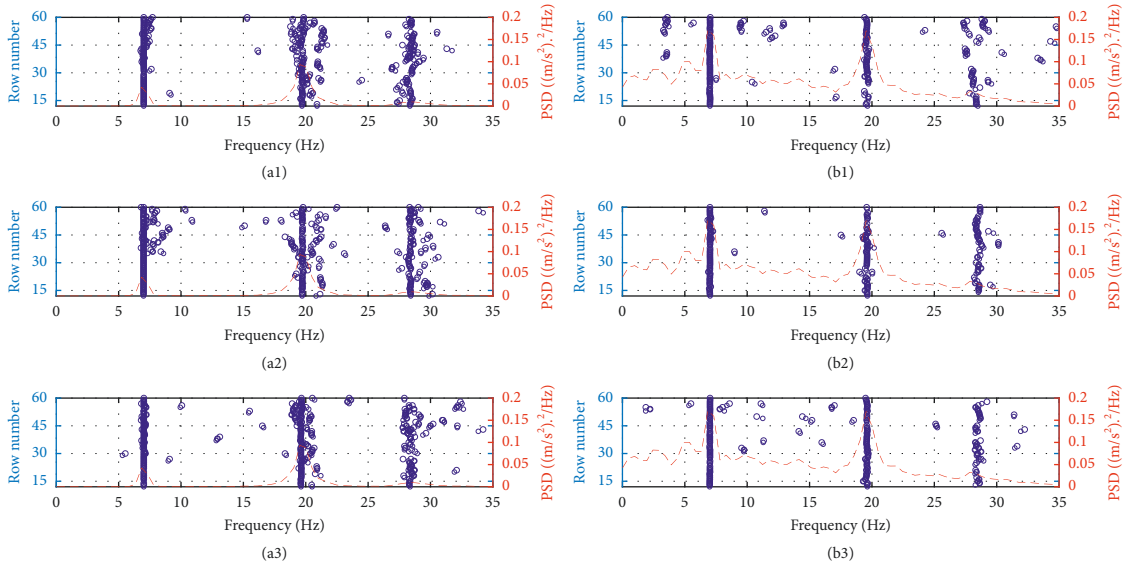

Figure 6: Stabilization diagram of CoS-SSI. (a1) CoS-SSI (SNR = 10, J = 1/1st subset). (a2) CoS-SSI (SNR = 10, J = 2/2nd subset). (a3) CoS-SSI (SNR = 10, J = 3/3rd subset). (b1) CoS-SSI (SNR = 0.5, J = 1/1st subset). (b2) CoS-SSI (SNR = 0.5, J = 2/2nd subset). (b3) CoS-SSI (SNR = 0.5, J = 3/3rd subset).

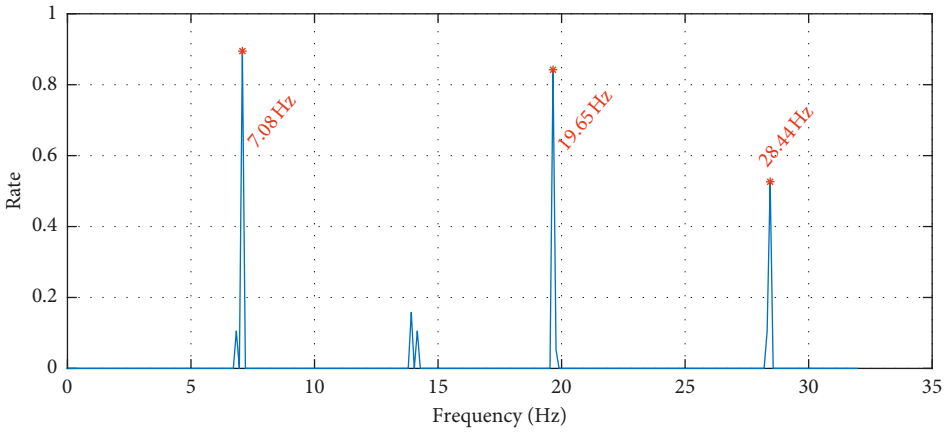

Figure 7: Example of selecting modes by the rate of stable points over orders (CoS-SSI, SNR = 10).

Table 2: Cov-SSI results.

	Mode 1				Mode 2				Mode 3			
	f_1 (Hz)	Error (f)	ξ_1	Error (ξ)	f_2 (Hz)	Error (f)	ξ_2	Error (ξ)	f_3 (Hz)	Error (f)	ξ_3	Error (ξ)
Theoretical value	7.0129	Null	1.12%	Null	19.6468	Null	3.15%	Null	28.3904	Null	4.55%	Null
SNR = 10	7.0380	0.37%	1.25%	11.61%	19.6663	0.09%	3.11%	1.27%	28.4377	0.17%	4.3%	5.49%
SNR = 0.5	*Null*	*Null*	*Null*	*Null*	*Null*	*Null*	*Null*	*Null*	*Null*	*Null*	*Null*	*Null*

Table 3: ACS-SSI results.

	Mode 1				Mode 2				Mode 3			
	f_1 (Hz)	Error (f)	ξ_1	Error (ξ)	f_2 (Hz)	Error (f)	ξ_2	Error (ξ)	f_3 (Hz)	Error (f)	ξ_3	Error (ξ)
Theoretical value	7.0119	Null	1.12%	Null	19.6468	Null	3.15%	Null	28.3904	Null	4.55%	Null
SNR = 10	7.0090	0.04%	1.08%	3.57%	19.6889	0.21%	3.29%	4.44%	28.3172	0.26%	4.81%	5.71%
SNR = 0.5	7.0093	0.04%	1.19%	6.25%	19.6797	0.17%	3.41%	8.25%	***Null***	***Null***	***Null***	***Null***

Table 4: CoS-SSI results.

		Mode 1				Mode 2				Mode 3			
		f_1(Hz)	Error (f)	ξ_1	Error (ξ)	f_2 (Hz)	Error (f)	ξ_2	Error (ξ)	f_3 (Hz)	Error (f)	ξ_3	Error (ξ)
Theoretical value		7.0119	Null	1.12%	Null	19.6468	Null	3.15%	Null	28.3904	Null	4.55%	Null
SNR = 10	S1	7.0275	0.22%	2.17%	93.75%	19.3324	1.60%	4.45%	41.27%	28.5183	0.45%	6.53%	43.52%
	S2	7.0118	0	1.97%	75.89%	19.3377	1.57%	5.91%	87.62%	28.5781	0.66%	6.71%	47.47%
	S3	7.0405	0.41%	5.17%	361.61%	19.3322	1.6%	3.92%	24.44%	28.5076	0.41%	5.83%	28.13%
SNR = 0.5	S1	7.0170	0.07%	3.47%	209.82%	19.5947	0.27%	5.14%	63.17%	28.4288	0.14%	6.53%	43.52%
	S2	7.0234	0.16%	2.58%	130.36%	19.5935	0.27%	3.74%	18.73%	28.5125	0.43%	3.50%	23.08%
	S3	7.0220	0.14%	4.45%	297.32%	19.5887	0.30%	3.51%	11.43%	28.4736	0.29%	5.53%	21.54%

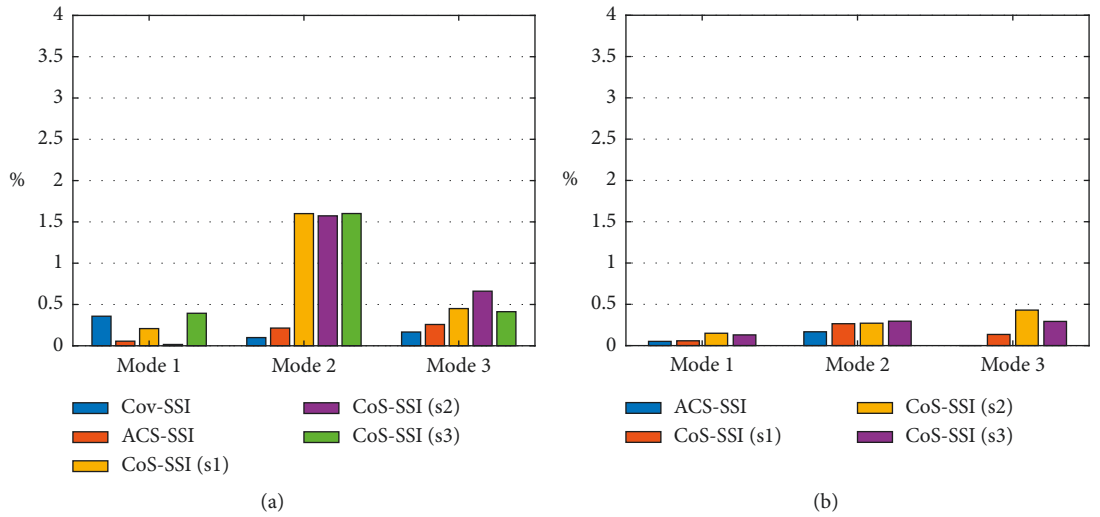

Figure 8: Identified frequency errors. (a) Identified frequency errors (SNR = 10). (b) Identified frequency errors (SNR = 0.5).

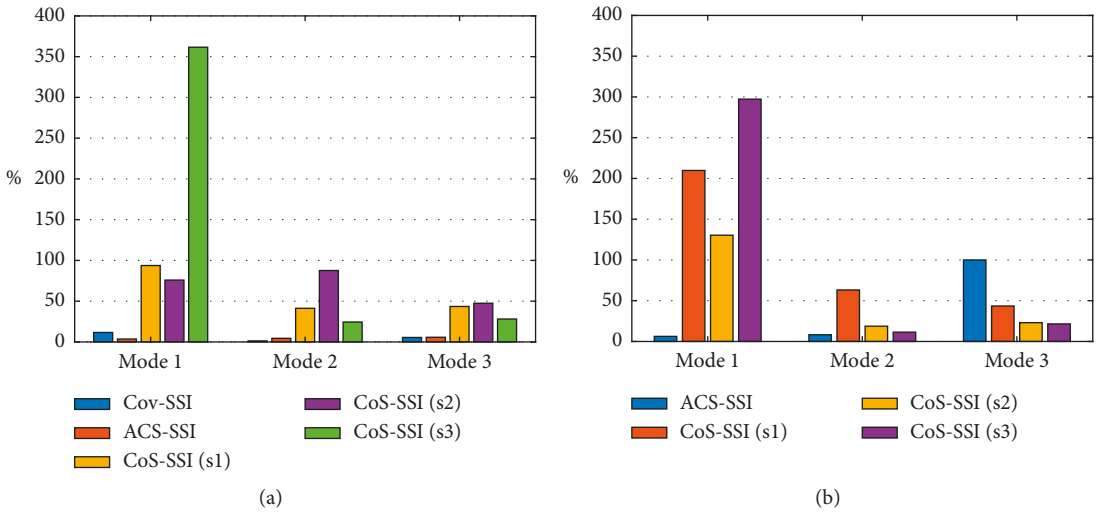

Figure 9: Identified damping errors. (a) Identified damping errors (SNR = 10). (b) Identified damping errors (SNR = 0.5).

However, the damping ratios are identified with huge errors in spite of the signal quality, which can be seen in Figure 9. This is reasonable because the damping estimation is a common challenge for all the system identification methods. In addition, it is evident from the theoretical results that the value of damping ratios are much smaller than the frequency; this could also lead the error of damping ratios becoming much more evident, especially for the first mode. Therefore, the damping ratio will not be chosen as a vital reference for structural health monitoring (SHM).

However, the mode shape is the most significant index for SHM whenever we adopt any modal parameters identification methods. It is well-known that MAC values are widely employed to compare two mode shapes to see

whether they are close or not. In this simulation study, all of the identified mode shapes are illustrated by the MAC values by comparing with the theoretical mode shapes, shown in Figures 10–12. From these figures, it can be seen that all of the MAC values for the identified modes are close to 1. Furthermore, the result of ACS-SSI can only identify two modes when the SNR is 0.5 and has been illustrated in Figure 11. Based on these results, it could recognise the powerful ability of the MAC value to indicate the mode shapes.

All of the three methods have been evaluated by using a 3-DOF vibration system. It seems highly probable that CoS-SSI is superior to other two methods, especially treating high noise signals; however, signals collected under operational conditions always contained with high noise.

4. Experiment Study

4.1. Experiment Setup. The experiments carried out in this paper are to identify the vehicle suspension-related modal parameters by collecting the vibration signal from a car body at four corners. The experimental car is a commercial car, and its model is Vauxhall Zafira. The signals were collected during car running on a traditional UK rustic road. Moreover, four accelerometers were employed to collect the vibration signals from the vehicle body which caused by the road excitation. The four transducers are piezoelectric accelerometers which are produced by SINOCERA and the model is CA-YD-185. This is a widely used kind of transducer because of its wide frequency measurement range, which is from 0.5 Hz to 5000 Hz. A four-channel data acquisition system and a laptop were adopted to collect and store the signals, respectively. The data acquisition system model is YE6231 and is also manufactured by SINOCERA with maximum sampling frequency of 96,000 Hz.

In this experiment, the accelerometers were mounted at the four corners of the car, and they were kept much close to the connection point of suspension. This is to obtain better quality vibration signals from the suspension system which are related to the road excitation. The tested car and a schematic of data acquisition system are presented in Figure 13.

4.2. Signal Characteristics. The purpose of the method proposed in this paper is to identify the modal parameters of vehicle under running condition. Therefore, the data were collected when the vehicle was driven on the typical UK suburb roads with speed limits from 20 to 40 miles/hr. In order to confirm no loss of information in the modal identification process, the sampling frequency was set much higher than the requirement of Nyquist sampling theory; the sampling frequency was 4000 Hz, and each test sample was recorded with the time duration of 240 s. Moreover, the test was repeated 4 times by driving on the same road section. Although the sensors were installed close to the suspension, the collected signals still contained high noise because this is a field test and there are thousands of reasons that can introduce unwanted measurement noise. Furthermore, the vehicle was running on the real road, not on a test platform; therefore, the speed was not always constant. The changing

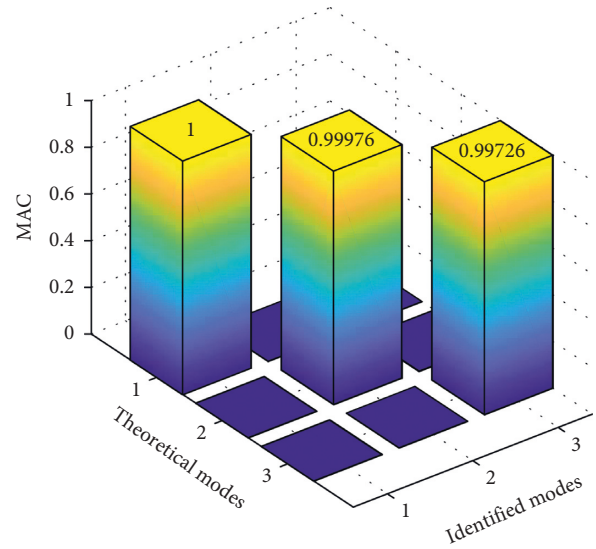

Figure 10: MAC of Cov-SSI results. (a) CoV-SSI (SNR = 10).

speed will cause nonstationary vibration. In addition, the random big excitations such as the hump on the road will also result in nonstationary responses of the vehicle.

An example of the collected signals is presented in Figure 14, and the corresponding power spectrum densities (PSD) were presented below. From the time-domain waveform analysis, it can be seen that the car body vibration is highly nonstationary. In addition, it can be seen from the PSD that the main power of the signal is around the frequency of 2 Hz, and a small peak appears around the frequency of 12 Hz, which are related to the car body and the wheel bounce, respectively. Moreover, it is noticeable from the PSD that the vibration amplitudes from the front part of the vehicle are smaller than its rear part. The main reason is the engine located in the front part of the vehicle. As a result, the pitch mode of the vehicle is easier to be excited.

4.3. Identification Results. In this section, only ACS-SSI and CoS-SSI methods are applied to identify the modal parameters of the car when it was in normal operation. As referred previously, the vehicle test was repeated four times with the sampled time duration of 240 s and sample rate of 4000 Hz. Firstly, the data of each test were segregated into six segments (40 s for each segment). Therefore, there are 24 (4 times × 6 segments = 24) data segments in total. Secondly, the correlation signals of each data segment were calculated. Then, for the ACS-SSI method, the correlation signals were averaged in a single time; for the CoS-SSI, the correlation signals were categorised into three subsets according to their amplitudes, and each subset was averaged. During the identification process of these two methods, the same threshold $(\varepsilon_f, \varepsilon_\xi, \varepsilon_{MAC})$ was set when developing the SDs; $\varepsilon_f, \varepsilon_\xi, \varepsilon_{MAC}$ were set at 0.1, 0.2, and 0.5, respectively. Moreover, the orders (rows) of Hankel matrix were 100 to develop the SDs.

The SD identified by ACS-SSI is presented in Figure 15(a). It is apparent that two relative stable modes

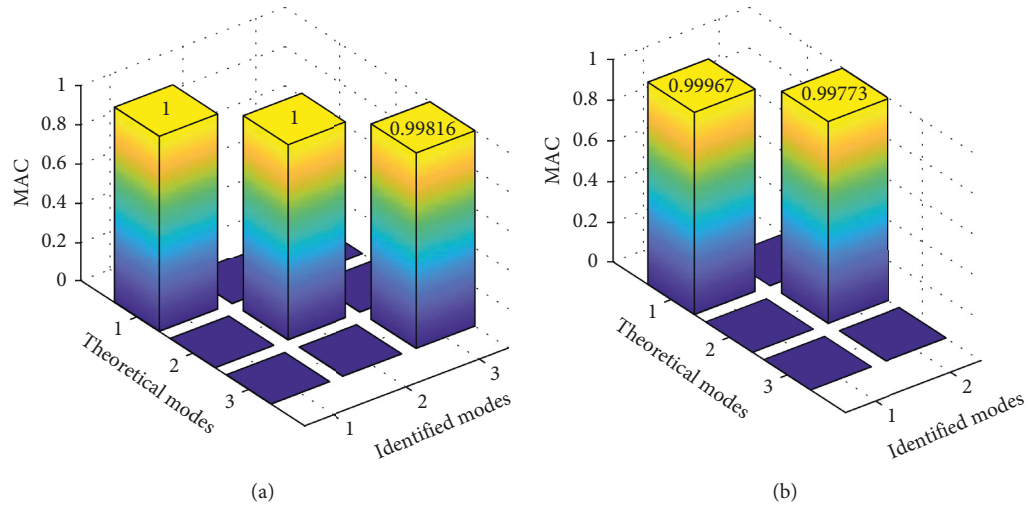

Figure 11: MAC of ACS-SSI results. (a) ACS-SSI (SNR = 10). (b) ACS-SSI (SNR = 0.5).

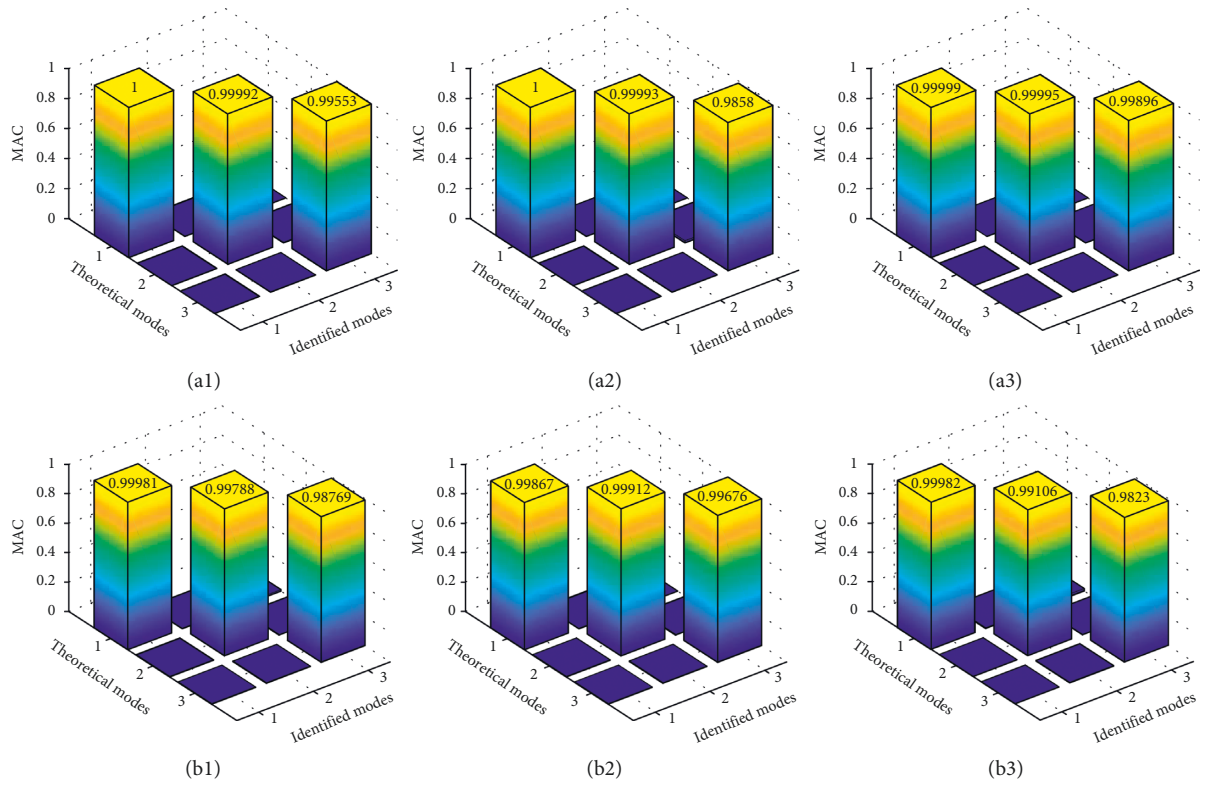

Figure 12: MAC of CoS-SSI results. (a1) CoS-SSI (SNR = 10). (a2) CoS-SSI (SNR = 10). (a3) CoS-SSI (SNR = 10). (b1) CoS-SSI (SNR = 0.5). (b2) CoS-SSI (SNR = 0.5). (b3) CoS-SSI (SNR = 0.5).

around 2 Hz were identified. Figure 15(b) shows the rate of identified stable points over the calculated orders. It can be observed from Figure 15(b) that the stable points for the first two modes are at 60% and 40%, respectively. This indicated that the second mode cannot be identified when we set the second threshold at 50% which is the same as the simulation case. In order to present the mode shapes of the two relative stable modes, the second threshold was set at 40% and the ACS-SSI identified modal parameters are given in Figure 16. These two modes seem like pitch. However, the first mode should bounce according to the theoretical modal parameters [27]. The reason for it looks like pitch mode could be because of the front part of the vehicle is heavier and therefore it has smaller amplitude vibration. Moreover, the nonstationary responses and high measurement noise will also have effect on the identified mode shapes.

In the second place, the SDs identified by CoS-SSI are presented in Figures 17(a1), 17(b1), and 17(c1). It can be seen that the SDs identified from the first two subsets are bit messier than the third one. Furthermore, the rate of the

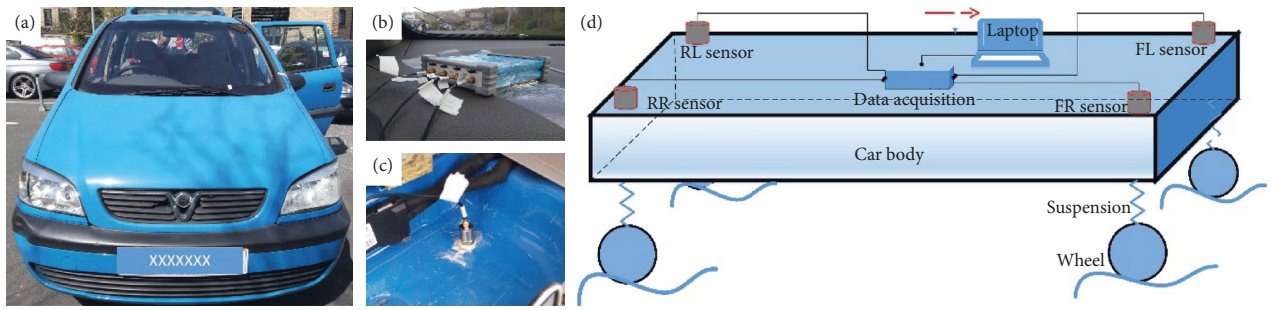

Figure 13: (a) Test car; (b) data acquisition equipment; (c) accelerometer; (d) schematic of test system.

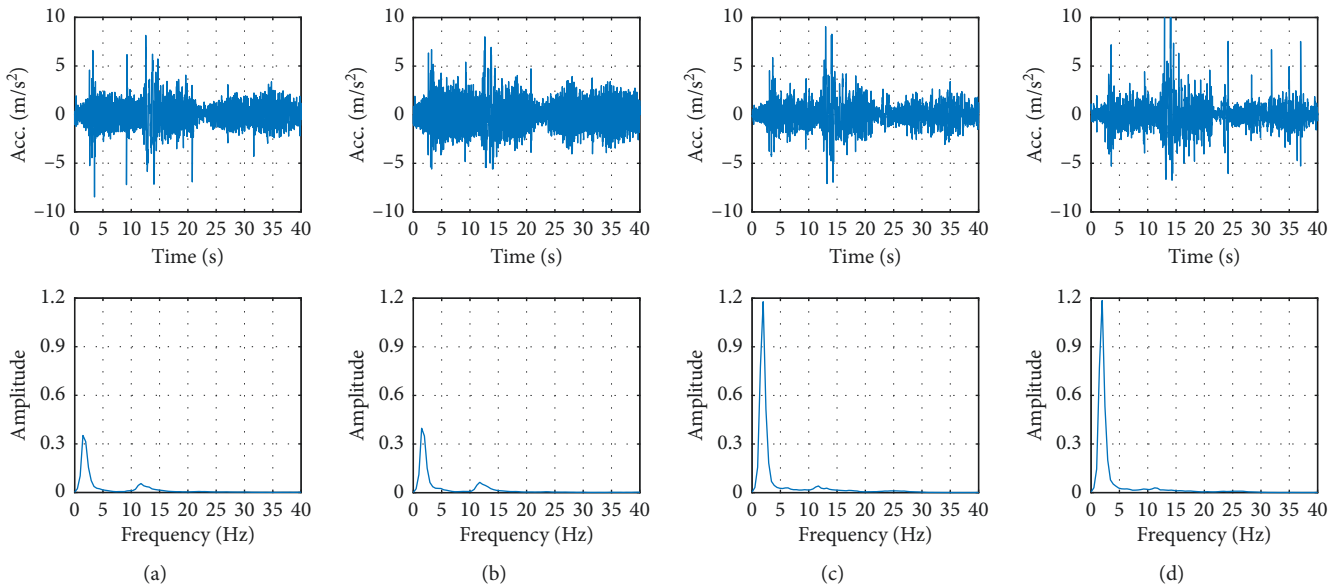

Figure 14: Time-domain signal and corresponding PSD. (a) Ch = FL. (b) Ch = FR. (c) Ch = RL. (d) Ch = RR.

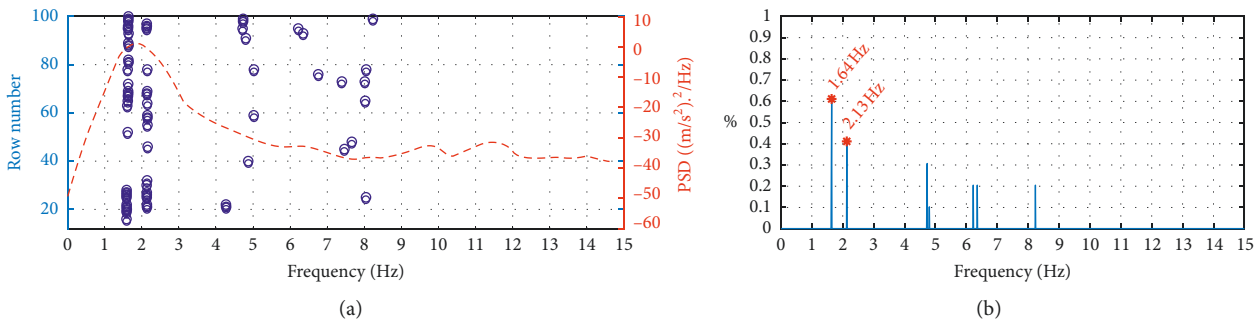

Figure 15: Stabilization diagram identified by ACS-SSI. (a) SD of ACS-SSI. (b) Selecting modes by the rate of the frequency over orders for on road vehicle modal identification.

stable modes over calculated orders is presented in Figures 17(a2), 17(b2), and 17(c2). It can be seen that the rates of the stable modes are much higher than the rates of modes identified by ACS-SSI. Therefore, a higher second threshold can be selected to obtain the target modes, which means the identified results are more reliable than the results identified by the ACS-SSI method. At the end, the second threshold value was found at 80%. It can be seen from Figures 17(a2), 17(b2), and 17(c2) that a mode around the frequency of 1.58 Hz was selected in the first subset, and two modes around 2.34 Hz and 9.02 Hz were identified in the second subset. Furthermore, the modes around 1.58 Hz and 2.06 Hz were identified in the third subset. The corresponding mode shapes identified from each subset are shown in Figure 18. It can be observed that the mode identified from the first subset is similar to the bounce mode

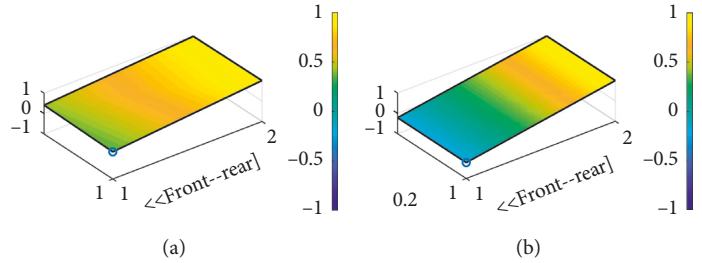

Figure 16: Modal parameters identified by ACS-SSI. (a) 1.64 Hz, 21%. (b) 2.133 Hz, 17%.

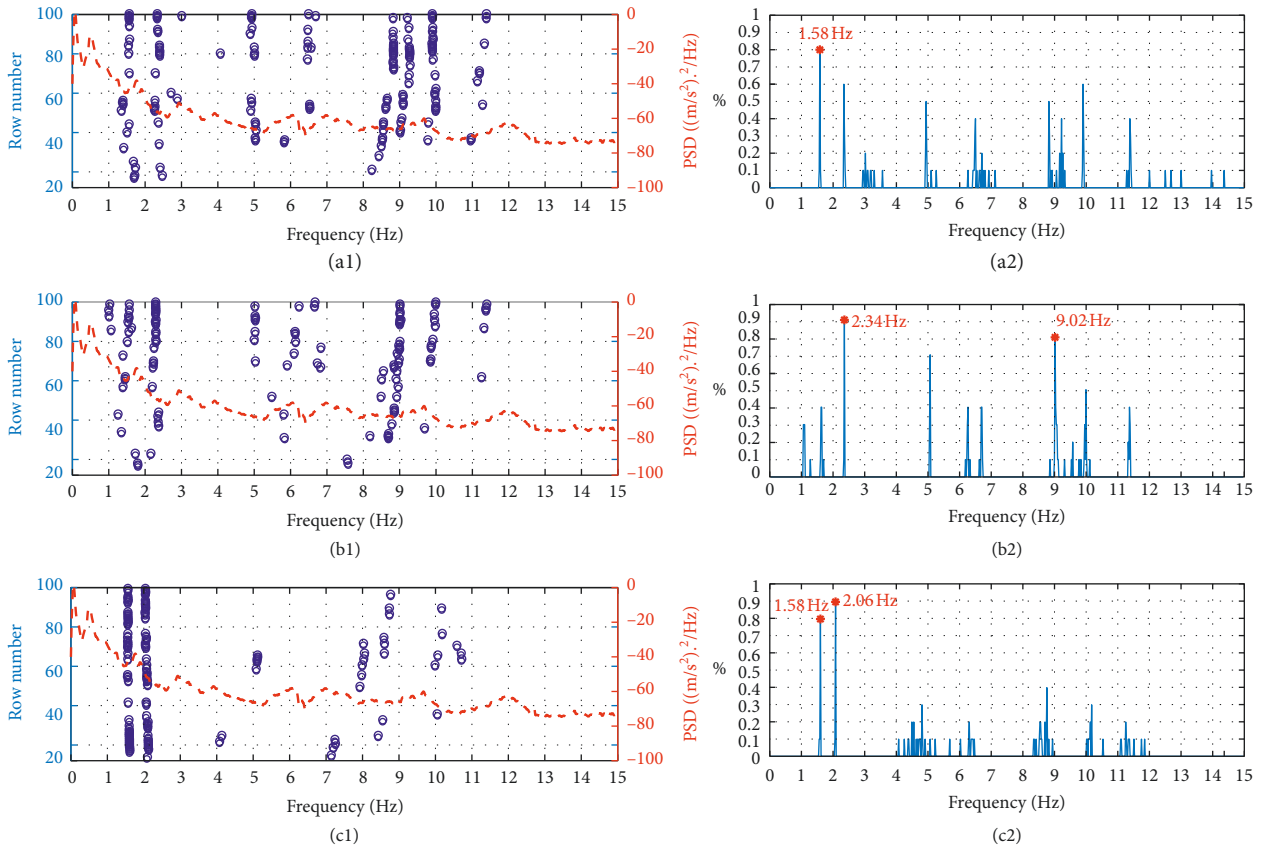

Figure 17: Stabilization diagram identified by CoS-SSI. (a1) SD of CoS-SSI (J = 1/1st subset). (a2) Selecting mode by the rate of the stable frequency over orders for on road vehicle modal identification (J = 1). (b1) SD of CoS-SSI (J = 2/2nd subset). (b2) Selecting mode by the rate of the stable frequency over orders for on road vehicle modal identification (J = 2). (c1) SD of CoS-SSI (J = 3/3rd subset). (c2) Selecting mode by the rate of the stable frequency over orders for on road vehicle modal identification (J = 3).

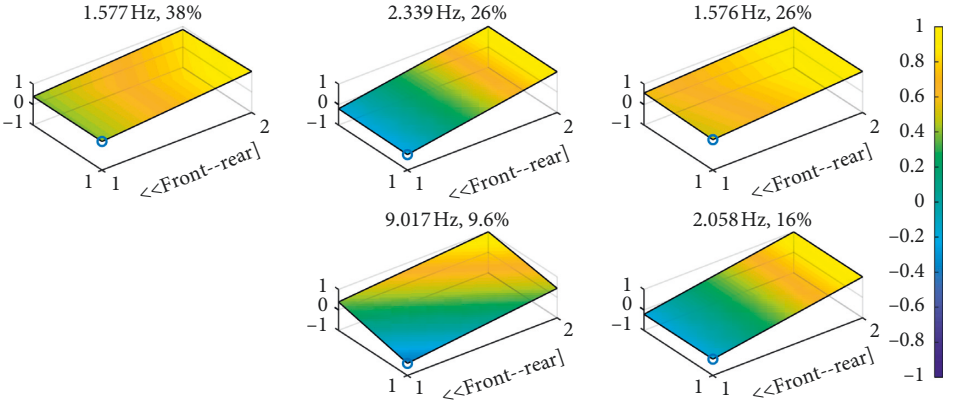

Figure 18: Modal parameters identified by CoS-SSI. (a) J = 1(1st subset). (b) J = 2(2nd subset). (c) J = 3(3rd subset).

identified from third subset; the first mode identified from the second subset is similar to the pitch mode identified from the last subset. Furthermore, it can be seen that a mode around 9 Hz was identified in the second subset which can be linked to the wheel bounce according to theoretical dynamic analysis in [27].

What is more, roll is a significant mode in the theoretical vertical vehicle dynamic analysis. However, it is noticeable that the roll mode has not appeared in the identification results. In view of the vehicle and road design requirements, the roll mode has to be avoided for the safety. The results demonstrating no roll mode has illustrated the robustness of the proposed method in a further step. Consequently, the CoS-SSI method has identified all of the vehicle suspension system-related modes under a high second threshold (80%), which indicates the reliability of the identified results.

5. Conclusions

An improved OMA method, denoted as CoS-SSI, was proposed in this paper to accurately identify the modal parameters when the system responses are highly nonstationary and contained high noise. As the inherent nonlinearity of engineering systems often results in nonstationary vibration responses due to changes in modal properties under different operating conditions, the method then categories such responses into a number of subsets based on energy levels and implement SSI subsequently on the ensample averaged data for accurate and consistent identification. The performance of CoS-SSI was evaluated by a 3-DOF typical vibration system under various SNR condition. Then, an experimental study of vehicle running on the practical suburb roads was carried out to verify the performance of CoS-SSI in a further step. Both simulation analysis and the experimental results provide compelling evidence that the CoS-SSI method is superior to the traditional Cov-SSI and ACS-SSI methods. In other words, the CoS-SSI method can provide a more accurate and reliable modal identification results when the structure is under severe situations; the accurate results ensure the reliability of the SHM.

Data Availability

The experimental data used to support the findings of this study are available from the corresponding author upon request.

Conflicts of Interest

The authors declare that there are no conflicts of interest regarding the publication of this paper.

Acknowledgments

The authors would like to thank the China Scholarship Council (CSC; grant no. 201608060041) and the National Natural Science Foundation of China (NSFC; grant no. 51775181) for the sponsorship of the project carried out in this study. Moreover, the authors would like to express their appreciation to Mr. Debanjan Modal for his work to improve English in this paper.

References

[1] R. Brincker and P. H. Kirkegaard, "Special issue on operational modal analysis," *Mechanical Systems and Signal Processing*, vol. 24, no. 5, pp. 1209–1212, 2010.

[2] H. Sohn, C. R. Farrar, F. M. Hemez et al., *A Review of Structural Health Monitoring Literature: 1996–2001*, Los Alamos National Laboratory, Santa Fe, NM, USA, 2003.

[3] L. Zhang, "An overview of operational modal analysis," in *Proceedings of 1st International Operational Modal Analysis Conference*, pp. 179–190, Copenhagen, Denmark, April 2005.

[4] M. H. Masjedian and M. Keshmiri, "A review on operational modal analysis researches: classification of methods and applications," in *Proceedings of 3rd International Operational Modal Analysis Conference (IOMAC'09)*, pp. 707–718, Portonovo, Italy, May 2009.

[5] L. Zhang, T. Wang, and Y. Tamura, "A frequency-spatial domain decomposition (FSDD) method for operational modal analysis," *Mechanical Systems and Signal Processing*, vol. 24, no. 5, pp. 1227–1239, 2010.

[6] E. Reynders, J. Houbrechts, and G. De Roeck, "Fully automated (operational) modal analysis," *Mechanical Systems and Signal Processing*, vol. 29, pp. 228–250, 2012.

[7] E. Reynders, "System identification methods for (operational) modal analysis: review and comparison," *Archives of Computational Methods in Engineering*, vol. 19, no. 1, pp. 51–124, 2012.

[8] B. Peeters, H. Van der Auweraer, F. Vanhollebeke, and P. Guillaume, "Operational modal analysis for estimating the dynamic properties of a stadium structure during a football game," *Shock and Vibration*, vol. 14, no. 4, pp. 283–303, 2007.

[9] L. Soria, B. Peeters, J. Anthonis, and H. V. der Auweraer, "Operational modal analysis and the performance assessment of vehicle suspension systems," *Shock and Vibration*, vol. 19, no. 5, pp. 1099–1113, 2012.

[10] F. Magalhães and Á. Cunha, "Explaining operational modal analysis with data from an arch bridge," *Mechanical Systems and Signal Processing*, vol. 25, no. 5, pp. 1431–1450, 2011.

[11] R. Brincker, L. Zhang, and P. Andersen, "Modal identification from ambient responses using frequency domain decomposition," in *Proceedings of 18th International Modal Analysis Conference (IMAC)*, San Antonio, TX, USA, February 2000.

[12] R. Brincker, C. Ventura, and P. Andersen, "Damping estimation by frequency domain decomposition," in *Proceedings of 19th International Modal Analysis Conference*, pp. 698–703, Orlando, FL, USA, February 2001.

[13] G. H. James, T. G. Carne, J. P. Lauffer, and A. R. Nord, "Modal testing using natural excitation," in *Proceedings of International Modal Analysis Conference*, p. 1208, San Diego, CA, USA, February 1992.

[14] R. Brincker, "Some elements of operational modal analysis," *Shock and Vibration*, Article ID 325839, 11 pages, 2014.

[15] B. Peeters and G. De Roeck, "Reference-based stochastic subspace identification for output-only modal analysis," *Mechanical Systems and Signal Processing*, vol. 13, no. 6, pp. 855–878, 1999.

[16] B. Peeters and G. De Roeck, "Stochastic system identification for operational modal analysis: a review," *Journal of Dynamic Systems, Measurement, and Control*, vol. 123, no. 4, pp. 659–667, 2001.

[17] E. Reynders, K. Maes, G. Lombaert, and G. De Roeck, "Uncertainty quantification in operational modal analysis with stochastic subspace identification: validation and applications," *Mechanical Systems and Signal Processing*, vol. 66-67, pp. 13–30, 2016.

[18] D.-J. Yu and W.-X. Ren, "EMD-based stochastic subspace identification of structures from operational vibration measurements," *Engineering Structures*, vol. 27, no. 12, pp. 1741–1751, 2005.

[19] Z. Chen, T. Wang, F. Gu, and R. Zhang, "Characterizing the dynamic response of a chassis frame in a heavy-duty dump vehicle based on an improved stochastic system identification," *Shock and Vibration*, vol. 2015, Article ID 374083, 15 pages, 2015.

[20] Z. Chen, T. Wang, F. Gu, R. Zhang, and J. Shen, "The average correlation signal based stochastic subspace identification for the online modal analysis of a dump truck frame," *Journal of Vibroengineering*, vol. 17, no. 4, pp. 1971–1988, 2015.

[21] F. Liu, F. Gu, A. D. Ball, Y. Zhao, and B. Peng, "The validation of an ACS-SSI based online condition monitoring for railway vehicle suspension systems using a SIMPACK model," in *Proceedings of 23rd International Conference on Automation and Computing (ICAC)*, pp. 1–6, Huddersfield, UK, September 2017.

[22] Y. Guo and A. Kareem, "System identification through nonstationary data using time-frequency blind source separation," *Journal of Sound and Vibration*, vol. 371, pp. 110–131, 2016.

[23] C.-S. Lin, D.-Y. Chiang, and T.-C. Tseng, "An extended time series algorithm for modal identification from nonstationary ambient response data only," *Mathematical Problems in Engineering*, vol. 2014, Article ID 391815, 12 pages, 2014.

[24] C.-S. Lin, "Ambient modal identification using non-stationary correlation technique," *Archive of Applied Mechanics*, vol. 86, no. 8, pp. 1449–1464, 2016.

[25] G. H. James, T. G. Carne, and J. P. Lauffer, "The natural excitation technique (NExT) for modal parameter extraction from operating structures," *International Journal of Analytical and Experimental Modal Analysis*, vol. 10, no. 4, p. 260, 1995.

[26] F. Liu, F. Gu, Y. Zhao, and A. Ball, "A validation study of ACS-SSI for online condition monitoring of vehicle suspension systems," *Vibroengineering Procedia*, vol. 10, pp. 369–375, 2016.

[27] M. Hamed, *Characterisation of the dynamics of an automotive suspension system for on-line condition monitoring*, Ph.D Thesis, University of Huddersfield, Huddersfield, England, 2016.

Hindawi
Shock and Vibration
Volume 2019, Article ID 1362954, 12 pages
https://doi.org/10.1155/2019/1362954

Research Article

One-Step FE Model Updating Using Local Correspondence and Mode Shape Orthogonality

Martin Ø. Ø. Jull,[1] **Sandro D. R. Amador**,[2] **Anders Skafte**,[3] **Jannick B. Hansen**,[3] **Manuel L. Aenlle**,[4] **and Rune Brincker**[2]

[1]*Brincker and Georgakis ApS, Department of Engineering, Inge Lehmanns Gade 10, 8000 Aarhus, Denmark*
[2]*Technical University of Denmark, Department of Civil Engineering, Brovej, Building 118, DK-2800 Kongens Lyngby, Denmark*
[3]*Aarhus University School of Engineering, Department of Engineering, Inge Lehmanns Gade 10, 8000 Aarhus, Denmark*
[4]*University of Oviedo, Department of Construction and Manufacturing Engineering, C/ Pedro Puig Adam, s/n, 33204 Gijón, Spain*

Correspondence should be addressed to Sandro D. R. Amador; sdio@byg.dtu.dk

Received 14 August 2018; Accepted 31 October 2018; Published 2 January 2019

Academic Editor: Filippo Ubertini

In this paper, it is described how the matrix mixing model updating technique can be combined with the local correspondence (LC) mode shape expansion algorithm, to give a new finite element (FE) model updating method. The matrix mixing method uses that the inverse mass and stiffness matrices can be expressed as a linear combination of outer products of FE mode shape vectors, where the low-frequency part of these sums are substituted with expanded test modes. The approach is meant to update FE models in one-step and is exact, except for the following two approximations: the mode shape smoothing and the mass scaling of the expanded experimental mode shapes. A simulation study illustrates the errors from the two approximations and shows the ability of the technique to improve the modal assurance criterion (MAC) values so that they get very close to unity. Finally, the performance of the proposed updating method is assessed by means of an application example in which the FE model is updated based on the test modes of a real structure.

1. Introduction

Finite element models are numerical idealizations of real structures used in structural design or to predict the structural response under operational conditions. The accuracy of these models is highly dependent on how precise the localized and distributed imperfections are accounted for in the model. For example, joints and boundary conditions tend to be inaccurately modelled by standard components embedded in the FE software that may be different from the ones in the actual structure. Many other examples of inaccurate modelling can be found, and, in general, we accept that the discrepancies between the model and the modelled structure are not significant.

We do expect, however, that the model can simulate the structural behaviour of the modelled structure in every respect that matters. When the structure is built, we can improve the model by adjusting the model parameters to match a subset of measured responses of the structure. This can be done by using the dynamic response of the structure [1]. A review of the existing updating techniques prior to 1993 is found in [2]. Nowadays, a commonly used updating technique is a sensitivity-based method explained in [3], in which the FE model spatial matrices are both parametrically and iteratively updated to match the experimental modal parameters estimated from vibration tests.

In this paper, a novel approach is proposed to update the FE model based on the test modal properties coming from an operational modal analysis (OMA) test [4]. Contrary to sensitivity-based updating techniques, the main advantage of this approach relies on the fact that the spatial matrices of the FE model are updated in one step, hence the name "one-step approach" was framed. The idea behind this approach is basically to replace the modal properties estimated with the FE

model by their experimental counterparts so that a good correlation between the updated FE and the test modal parameters is obtained.

In this proposed approach, the method of matrix mixing [5, 6] is used in combination with the local correspondence (LC) expansion technique [7]. The idea is to expand experimental mode shapes in a limited number of degrees of freedom (DOFs) to an entire structure using modes shapes from a FE model. Since the expansion procedure is a crucial task carried out by the one-step approach, it is also herein extensively and detailed described. In order to update the FE model in one step, the technique takes advantage of the matrix mixing method in which the inverse mass and stiffness matrices are written as a sum of outer products of mode shapes. This updating procedure is also discussed in [8, 9]. By making use of such method, the FE model modes in these sums can be replaced by the corresponding expanded test modes, yielding the updated inverse mass and stiffness matrices.

Since the inverse stiffness matrix is of interest in its own right in structural health monitoring (SHM) as shown in [10, 11], the accurate updating of $\mathbf{K}^{-1}$ will also be of interest in SHM. The one-step algorithm presented in this paper is a perturbation technique since it relies on the LC principle [7]. The LC principle is a first-order perturbation technique based on the sensitivity equations created by Fox and Kapoor [12]. This means that one-step requires normal model updating to be done before the algorithm can be applied. The idea is that, after the application of the one-step updating approach, the updated FE model completely recreates all natural frequencies and mode shapes found from test measurements. Since no explicit mass scaling is done in the technique, errors in the modal mass are not adjusted by the technique.

Thus, the one-step technique ensures that the modal properties of the updated FE model match the ones estimated from measurements. The technique is meant to be applied only after classical FE model updating takes place, i.e., after the FE model is updated by making use of the analyst's engineering knowledge and/or of a classic sensitivity-based FE updating technique. This is to assure that the FE model being updated by the one-step approach is physically equivalent to the tested structured and that the discrepancies between model and real structure are caused by perturbations distributed over the FE model. Once these assumptions are fulfilled, the one-step approach can be applied to remove the existing discrepancies and bring the FE model closer to the experimental results.

It is worth also highlighting that, similarly to any sensitive-based FE model updating technique, the one-step FE updating approach herein proposed is suitable for cases where the structural system being updated can be modelled by a linear FE model with orthogonal mode shape vectors. This implies that the one-step technique cannot be used to update FE models of nonlinear structural systems with nonorthogonal mode shape vectors. This is the case of a fairly amount of constructed systems whose structural dynamic behaviour is dominated by nonlinearities.

The paper can be basically divided into three different parts. In the first part, the derivation and description of the one-step approach is presented. In order to illustrate the efficiency and accuracy of the technique from a practical point of view, four application examples are presented in the second part. Finally, some remarks regarding the results obtained from the application examples are presented in the last part of the paper.

2. The One-Step Updating Approach

In the one-step updating approach, it is considered that the discrepancies between the modelled and the real structure are small. If this condition is satisfied, the LC will enable the mixing technique to directly update the mass and stiffness matrices of the FE model. This can be done by using the expanded test modal vectors, without introducing errors in the matrices. An iterative scaling technique ensures that the test mode shapes are correctly mass scaled relative to the new updated mass matrix. Once the test modal vectors are expanded and mass scaled, they are used to replace the modal properties estimated with the FE in order to improve the correlation between the FE and the test modal parameters. The derivation and the detailed description of the one-step approach are presented in the following subsections.

2.1. Basic Equations. An undamped multiple degree of freedom (MDOF) system in structural dynamics is described by the equation of motion:

$$\mathbf{M}\ddot{\mathbf{y}} + \mathbf{K}\mathbf{y} = \mathbf{0}, \tag{1}$$

where $\mathbf{M}$ and $\mathbf{K}$ are the $N \times N$ mass and stiffness matrices, respectively. $\mathbf{y}$ is an N-dimensional column vector containing the deformations in all DOFs of the system. $\mathbf{y}$ is a function of time t, so we have $\mathbf{y} = \mathbf{y}(t)$ for every instance in time. The solution of this linear system of equations is thoroughly explained in [4].

The solution $\mathbf{y}$ is a linear combination of N mode shapes multiplied by harmonics at the corresponding eigenfrequencies. We order the mode shapes as the columns of the $N \times N$ mode shape matrix $\mathbf{B}$, and the squares of the angular frequencies as the nonzero elements of the diagonal matrix $[\omega_n^2]$, where $n \in 1, 2, \ldots, N$. The ordering of the frequencies on the diagonal corresponds to the ordering of the columns in the mode shape matrix. With this solution, we obtain the following orthogonality relations:

$$\mathbf{B}^T\mathbf{M}\mathbf{B} = \mathbf{I}, \tag{2}$$

$$\mathbf{B}^T\mathbf{K}\mathbf{B} = \left[\omega_n^2\right], \tag{3}$$

when the mode shapes are mass normalized [4].

2.2. One-Step Updating Equations. Pre- and postmultiplying equations (2) and (3), respectively, by $\mathbf{B}^{-T}$ and $\mathbf{B}^{-1}$, and inverting the resulting equations yields

$$\mathbf{M}^{-1} = \mathbf{B}\mathbf{B}^T, \tag{4}$$

$$\mathbf{K}^{-1} = \mathbf{B}\left[\omega_n^{-2}\right]\mathbf{B}^T. \tag{5}$$

Equation (4) can be written as a sum of outer products:

$$\mathbf{M}^{-1} = \sum_{i=1}^{N} \mathbf{b}_i \mathbf{b}_i^T, \tag{6}$$

where $\mathbf{b}_i$ is the i-th column in the mode shape matrix $\mathbf{B}$. If we split this sum into a sum containing contributions from the first m mode shapes, and a sum containing the remaining contributions, we have

$$\mathbf{M}^{-1} = \sum_{i=1}^{m} \mathbf{b}_i \mathbf{b}_i^T + \sum_{i=m+1}^{N} \mathbf{b}_i \mathbf{b}_i^T, \tag{7}$$

where the second sum has $N-m$ elements.

Letting $\mathbf{B}_1$ be the $N \times m$ matrix with the first m mode shapes as columns and $\mathbf{B}_2$ be the $N \times (N-m)$ matrix with the remaining $N-m$ mode shapes, we can write equation (7) as

$$\mathbf{M}^{-1} = \mathbf{B}_1 \mathbf{B}_1^T + \mathbf{B}_2 \mathbf{B}_2^T. \tag{8}$$

Using the same techniques, the stiffness equation (5) can be rewritten as

$$\mathbf{K}^{-1} = \mathbf{B}_1 \left[\omega_{m_1}^{-2}\right] \mathbf{B}_1^T + \mathbf{B}_2 \left[\omega_{m_2}^{-2}\right] \mathbf{B}_2^T, \tag{9}$$

where $[\omega_{m_1}^{-2}]$ is an $m \times m$ diagonal matrix containing the first m inverses of the squared angular frequencies and $[\omega_{m_2}^{-2}]$ is an $(N-m) \times (N-m)$ diagonal matrix containing the remaining $N-m$ inverses of the squared angular frequencies. Equations (8) and (9) are central in the one-step updating approach.

2.3. Mode Shape Expansion. Using the notation from [4], we know from structural modification theory [13] that if we have a system with mode shape matrix $\mathbf{B}$, any perturbed system with mode shape matrix $\mathbf{A}$ can be written as

$$\mathbf{A} = \mathbf{B}\mathbf{T}, \tag{10}$$

where $\mathbf{T}$ contains the weights when writing the modes of $\mathbf{A}$ as a linear combination of modes in $\mathbf{B}$. This is always possible for any modification.

Provided that $\mathbf{A}$ has only a few columns and that the modes in $\mathbf{A}$ are well described by the first m modes of $\mathbf{B}$, we can let $\mathbf{B}$ be an $N \times m$ matrix and use a smaller $\mathbf{T}$ matrix of size $m \times N$.

If we measure the responses of the structure at a set of DOFs, we can represent the mode shape matrix $\mathbf{B}$ as

$$\mathbf{B} = \begin{bmatrix} \mathbf{B}_\mathrm{a} \\ \mathbf{B}_\mathrm{d} \end{bmatrix}, \tag{11}$$

with $\mathbf{B}_\mathrm{a}$ and $\mathbf{B}_\mathrm{d}$ containing the modal coordinates of the FE mode shapes at the measured and unmeasured DOFs, respectively. We, hereinafter, designate them as active and deleted DOFs and denote them with subscripts a and d, respectively.

We can write an experimentally identified mode shape column vector $\mathbf{a}$ as

$$\mathbf{a} \approx \mathbf{B}_\mathrm{a} \mathbf{t}, \tag{12}$$

where the column vector $\mathbf{t}$ is the linear combination of modes from $\mathbf{B}_\mathrm{a}$ that gives the identified mode. This is known from the system equivalent reduction-expansion process (SEREP) [14]. Having identified the mode shape $\mathbf{a}$, we solve equation (12) to get

$$\hat{\mathbf{t}} = \mathbf{B}_\mathrm{a}^\dagger \mathbf{a}, \tag{13}$$

where $\mathbf{B}^\dagger$ is the Moore–Penrose pseudoinverse [15] of matrix $\mathbf{B}$.

Inserting $\hat{\mathbf{t}}$ into (12) gives the least squares smoothed identified mode shape:

$$\hat{\mathbf{a}} = \mathbf{B}_\mathrm{a} \hat{\mathbf{t}} = \mathbf{B}_\mathrm{a} \mathbf{B}_\mathrm{a}^\dagger \mathbf{a}. \tag{14}$$

Extending equation (14) to all identified modes $\mathbf{A}_\mathrm{a}$ gives

$$\hat{\mathbf{A}}_\mathrm{a} = \mathbf{B}_\mathrm{a} \hat{\mathbf{T}}, \tag{15}$$

where $\hat{\mathbf{T}} = \mathbf{B}_\mathrm{a}^\dagger \mathbf{A}_\mathrm{a}$. Equation (15) that assumes that $\mathbf{A}$ can be written as a linear combination of the first m modes of the full mode shape matrix is a reduced version of equation (10).

Equation (15) can now be used for expanding the measured mode shapes in $\mathbf{A}_\mathrm{a}$. This is accomplished by appending the unmeasured or deleted DOFs to the linear combinations and holding $\hat{\mathbf{T}}$ constant. This gives

$$\hat{\mathbf{A}} = \begin{Bmatrix} \hat{\mathbf{A}}_\mathrm{a} \\ \hat{\mathbf{A}}_\mathrm{d} \end{Bmatrix} = \begin{Bmatrix} \mathbf{B}_\mathrm{a} \\ \mathbf{B}_\mathrm{d} \end{Bmatrix} \hat{\mathbf{T}} = \mathbf{B}\hat{\mathbf{T}}. \tag{16}$$

Inserting $\hat{\mathbf{T}}$ into (16) gives

$$\hat{\mathbf{A}} = \mathbf{B}\mathbf{B}_\mathrm{a}^\dagger \mathbf{A}_\mathrm{a}, \tag{17}$$

where $\mathbf{B}\mathbf{B}_\mathrm{a}^\dagger$ is the global mapping transformation matrix obtained by means of SEREP expansion [14]. The matrix $\hat{\mathbf{A}}$ consists of the expanded test modes. The assumption in equation (16) is that the estimate of $\hat{\mathbf{T}}$ based on the active subset is close to $\mathbf{T}$ for the full set of DOFs. Solving equation (12) requires $\mathbf{B}_\mathrm{a}$ to have fewer mode shapes than DOFs to make this an overdetermined system. In case of few active DOFs, only a small set of modes can be used. A better way to solve equation (12) is to use the LC approach [7], which gives an alternative way to compute $\hat{\mathbf{t}}$.

2.4. LC Expansion. Based on the sensitivity equations [12], the LC principle [7] expands an experimental mode shape by selecting an optimal subset of the FE mode shapes in $\mathbf{B}_\mathrm{a}$ as expansion basis. Only FE mode shapes with frequencies close to those of the test mode shapes are considered to make sure that the number of modes is lower than the number of active DOFs. The idea behind this strategy is to obtain an overdetermined set of equations in (12) by selecting a small subset of FE modes that locally correspond to an experimentally estimated mode shape.

The best subset, or cluster, is chosen based on a resampling technique known as leave-one-out cross validation (LOOCV) [16]. The LOOCV technique leaves out one of the mode shape parameters, selects a subspace $\mathbf{B}_{\mathrm{a,s}}$, of $\mathbf{B}_\mathrm{a}$,

and measures how well the expansion predicts the missing parameter. In this way, the LC principle chooses the optimal cluster based on optimality of predicting unknown responses. Each of the measured responses takes on the role of being unknown test data, one at a time. Using the LOOCV technique enables LC to do a high-level mode shape smoothing since the noise in the subspace of the optimal cluster is completely removed. This has been shown to be a significant advantage over SEREP.

It is possible to use the LC expansion in a simpler way, by only selecting a subspace of $\mathbf{B}_a$ whose frequencies are located around that of the test mode **a**. This subspace, containing a fixed number of modes, should then be used to compute the least squares fit and remove the elements of **t** associated with the smallest contributions to **a**. This is a kind of "noise floor" alternative to the traditional LC principle. The LOOCV technique will give its own optimality, and this is the principle used here.

In the simulation and test cases in this paper, there is no significant change, in terms of results, by choosing a fixed subspace of 5 modes locally around all test modes and solving equation (12) in a least-squares sense using the LC LOOCV technique. An illustration of using a 5-mode subspace in the LC expansion is shown in Figure 1. The subspace of modes used in the LC expansion of each experimental mode consists of a FE modal vector with the same natural frequency of the test modal vector being expanded, of one FE modal vector above this, and by three FE modal vectors below, giving a total of five modes. Once the subspace is defined, the LOOCV technique is then used to identify the modes that actually contribute to the expansion of the test mode shape. The empty circles indicate the modal vectors that do not contribute to expansion and, therefore, are not included in the (actual) subspaces used to expand the test mode shapes. The filled circles, on the contrary, show the modes used in the actual expansion. For test modes 1–3 fewer than 5 modes are shown since this gives a better visual illustration of the narrow-band nature of LC. The modes that are not shown are effectively unused in the expansion.

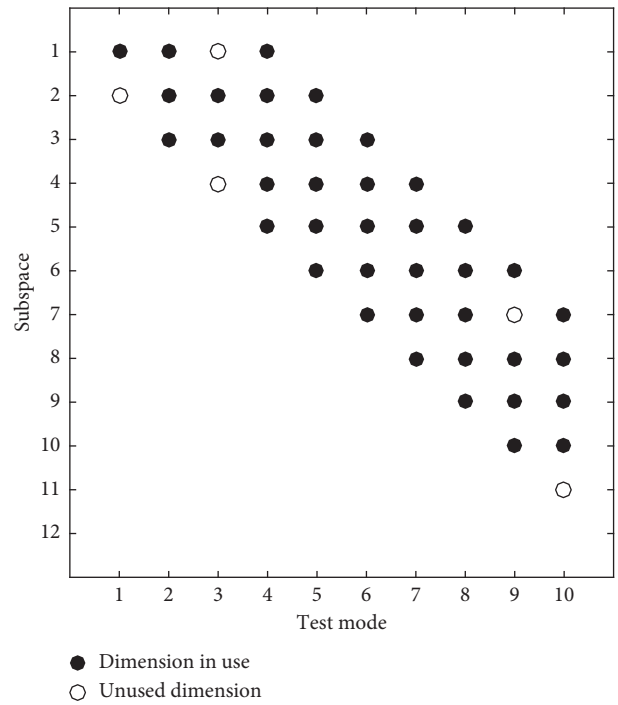

Figure 1: Plot of the structure of the 12×10 matrix **T** from equation (15). Only a limited number of FE mode shapes around the frequency of the test mode shape are used in LC. This means that the **T** matrix will have nonzero entries in a narrow band only, illustrated by black circles. If the mode actually contributes to the expansion in this experiment, the circle is filled. Thus in this experiment, we use a 5-dimensional subspace for expansion and use anywhere from one to all five modes in the expansion, corresponding to columns of **T**.

2.5. One-Step Principle. Referring to equation (8), the idea of one-step updating is to let the mode shapes corresponding to the lower m eigenfrequencies of a dynamical system be contained in $\mathbf{B}_1$ and the remaining $N - m$ mode shapes stored in $\mathbf{B}_2$. By modal testing, experimental modes shapes can be found. Using equation (16) or LC, the test modes can be expanded to the full set of FE DOFs. Since the modal properties of the physical structure are estimated from responses measured in a vibration test, the test mode shapes can be considered as the exact mode shapes contaminated with disturbances from, amongst other sources, measurement noise, identification errors, and errors in the expansion process. Despite these disturbances, the test mode shapes are expected to be more accurate than the FE model mode shapes contained in $\mathbf{B}_1$, whose accuracy is fairly affected by the modelling errors. Thus, we can use $\widehat{\mathbf{A}}$ as a substitute for $\mathbf{B}_1$ and get an $\mathbf{M}^{-1}$ that better corresponds to the physical structure for the lower frequencies. The same substitution can be made in equation (9), where the experimentally identified frequencies are also used.

The substitution is done by firstly using (8) to find $\mathbf{B}_2\mathbf{B}_2^T$:

$$\mathbf{B}_2\mathbf{B}_2^T = \mathbf{M}^{-1} - \mathbf{B}_1\mathbf{B}_1^T, \tag{18}$$

and then determining an updated mass matrix, $\mathbf{M}_{\text{upd}}$, by inserting $\widehat{\mathbf{A}}$ and equation (18) into (8)

$$\mathbf{M}_{\text{upd}}^{-1} = \widehat{\mathbf{A}}\widehat{\mathbf{A}}^T + \mathbf{B}_2\mathbf{B}_2^T. \tag{19}$$

Finally, the updated mass matrix is found by computing the inverse in equation (19). An analogous procedure is followed to determine the updated stiffness matrix, $\mathbf{K}_{\text{upd}}$, yielding

$$\mathbf{M}_{\text{upd}} = \left(\widehat{\mathbf{A}}\widehat{\mathbf{A}}^T - \mathbf{B}_1\mathbf{B}_1^T + \mathbf{M}^{-1}\right)^{-1}, \tag{20}$$

$$\mathbf{K}_{\text{upd}} = \left(\widehat{\mathbf{A}}\left[\omega_{\text{exp}}^{-2}\right]\widehat{\mathbf{A}}^T - \mathbf{B}_1\left[\omega_{m_2}^{-2}\right]\mathbf{B}_1^T + \mathbf{K}^{-1}\right)^{-1}, \tag{21}$$

where the diagonal matrix $[\omega_{\text{exp}}^{-2}]$ contains the experimentally determined angular frequencies of the first m modes.

After updating, the mode shapes $\widehat{\mathbf{A}}$ are not mass scaled. This is done using the updated mass matrix $\mathbf{M}_{\text{upd}}$. When $\widehat{\mathbf{A}}$ has been mass scaled using the updated mass matrix from

equation (20), the scaled $\widehat{\mathbf{A}}$ can be used in equation (19) instead. Iterating this way will give correctly scaled test mode shapes in $\mathbf{M}_{\text{upd}}$. Only one loop is required in this fixed point iteration [17]. When correct mass scaling has been done, the frequency content of the new model, at the lower modes, can be found using the orthogonality relation in (3).

The one-step updating principle works best when the discrepancies between FE model and physical structural system are small. The reason for this is that the LC principle relies on locality coming from the sensitivity equations [12]. For small changes, only local modes contribute to the expansion of FE mode shape changes onto all the FE model mode shapes.

3. Application Examples

In the following sections, we explain the one-step principle by simulation and by experiment. Firstly, we show the simplest possible simulation based on a FE model. Then, we show a second simulation case in which a FE model is updated from the noise-contaminated FE mode shapes expanded with the LC expansion technique. Finally, we illustrate the technique by means of a complete experimental test case on a small specimen, where we update the FE model based on experimental modal parameters estimated from vibration measurements.

3.1. FE Model. For doing simulations, we have built an FE model of a T structure using FEMtools [18]. Figure 2 shows an image of the FE model from FEMtools. The model has 126 normal beam3d construction steel elements, and a spring element connecting the structure to the base. The spring has 3 rotational and 3 translational DOFs and connects the T structure to the base at the origin: $(x, y, z) = (0, 0, 0)$. These 127 elements are defined by 127 nodes on the structure and 1 boundary node. Each of the beam3d elements in the model has a total of 6 DOFs, i.e., three translational and three rotational DOFs. This gives a total of $6 \times 127 = 762$ DOFs. Thus, the mass and stiffness matrices are of size 762×762. Half of the DOFs are rotational and half are translational.

The FEMtools model was imported into MATLAB [19] using SDTools [20], and the corresponding eigenvalue problem is solved to get the frequencies $[\omega_n^2]$ the and mode shapes $\mathbf{B}$. A perturbed version of the model was obtained by increasing the mass of some of the elements of the model and solving it again to get the new frequencies $[\omega_{n,\text{exp}}^2]$ and the mode shapes $\mathbf{A}$. As in [4], we also use $\mathbf{A}$ to indicate experimental mode shapes and $\mathbf{B}$ to indicate model mode shapes. FE model updating using the one-step principle is done using equations (20) and (21), and the updated mass matrix $\mathbf{M}_{\text{upd}}$ is adopted to mass scale the mode shape vectors in $\mathbf{A}$.

3.2. Simulation without Noise. An idealized noise-free simulation to illustrate updating using the one-step principle can be performed by using any FE model as the reference model and a perturbed version of the model as the "real" physical object. This setup is the same as having a FE

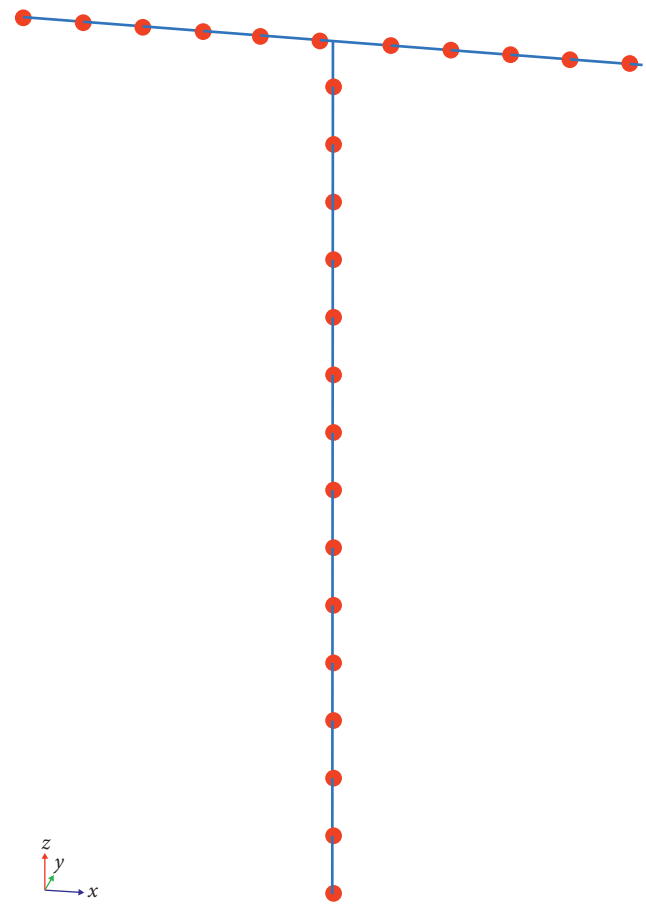

Figure 2: FE model of the T structure. To illustrate element size, every fifth node is marked with a red dot. The model contains 127 nodes and 1 boundary node, 126 beam elements, and one spring element. The spring has 3 rotational and 3 translational DOFs and connects the T structure to the base at the origin: $(x, y, z) = (0, 0, 0)$.

model which is always slightly different from the modelled structural system. In the terminology of equation (8), we start out by considering a model mass matrix $\mathbf{M}$ constructed using outer products of all mode shapes in $\mathbf{B}_1$ and $\mathbf{B}_2$ combined. The mass matrix is perturbed to give $\mathbf{M}_{\text{pert}}$, and the stiffness matrix is unchanged.

Figure 3 shows the change in the mass matrix, $\Delta\mathbf{M}$, for a perturbation of the FE model corresponding to doubling the mass of one branch of the T structure. To make an intelligible plot of all 762×762 entries in the mass matrix, the matrix was divided into submatrices of size 15×15. This division provides 51×51 submatrices. Then, the maximum absolute value was chosen to describe each submatrix. Thus, the 762×762 mass matrix is represented by the 51×51 matrix shown in Figure 3. Note that the perturbation added to the mass mass matrix cannot be considered small and, therefore, the FE model does not correspond very well to the structure.

Figure 4 shows the MAC [21] value of $\mathbf{B}_1$ and $\mathbf{A}$, where $\mathbf{A}$ contains mode shapes of the perturbed system.

The one-step operation consists of substituting the mode shapes $\mathbf{B}_1$ in $\mathbf{M}$ by the mode shapes $\mathbf{A}$ from the perturbed model. To do this, the perturbed model is solved and the first modes are extracted. This operation is synthesized by

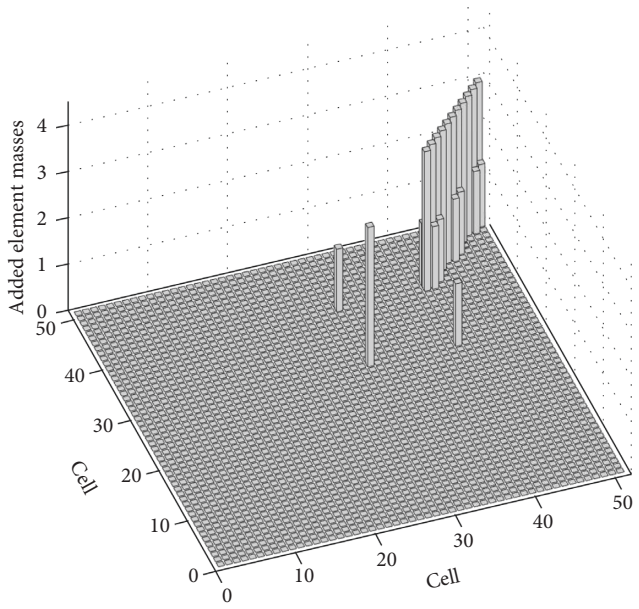

Figure 3: $\Delta\mathbf{M}$ for increasing the mass of one of the top branches of the T structure. The figure shows 51 × 51 cells where the maximum absolute value in the cell is shown. Each cell is a 15 × 15 submatrix of the 762 × 762 matrix $\Delta\mathbf{M}$. Every second element on the arm had its mass increased by 300% or three times the mass of a single element.

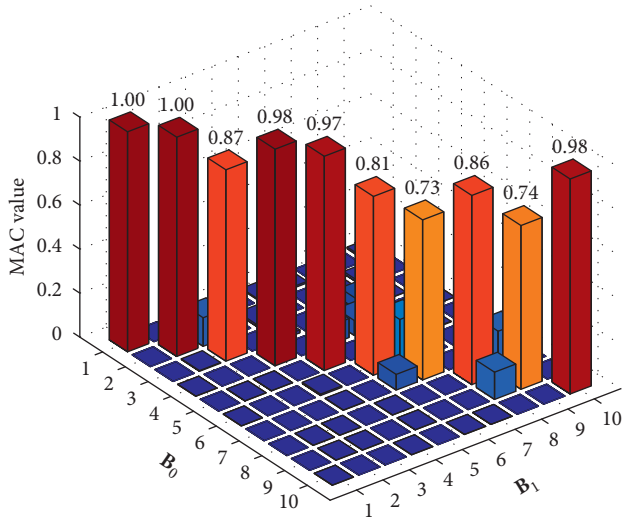

Figure 4: MAC value between the original and perturbed FE models before one-step updating. The perturbation added to the original FE model corresponds to an increase of mass on every second element on an arm of the T structure by 300%.

equation (20). The MAC values between the first modes of the updated and perturbed models are shown in Figure 5.

This procedure previously described constitutes one of the main ideas of the one-step approach, i.e., updating the mass and stiffness matrices so that the MAC values between the mode shapes of the updated and tested systems get close to 1. The example illustrates that, in the idealized case, this can be done perfectly. Note that since no update is done to high-frequency mode shapes, this part of the system will not be improved after updating.

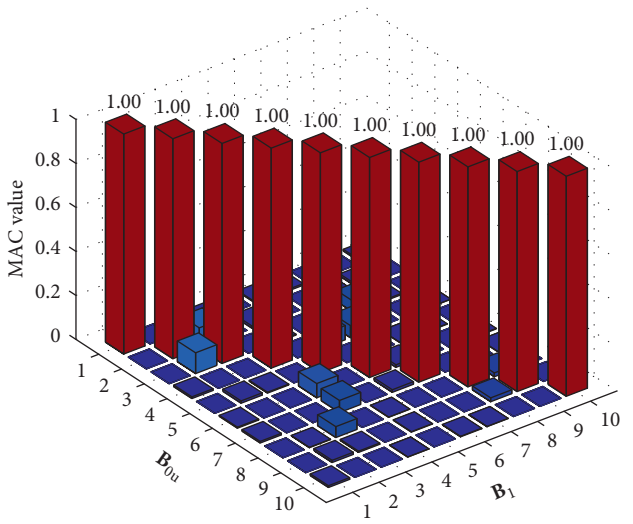

Figure 5: MAC value between the modal vectors from the FE model updated with the one-step updating approach and the modal vectors from the perturbed FE model. The perturbation added to the original FE model corresponds to an increase of mass on every second element on an arm of the T structure by 300%.

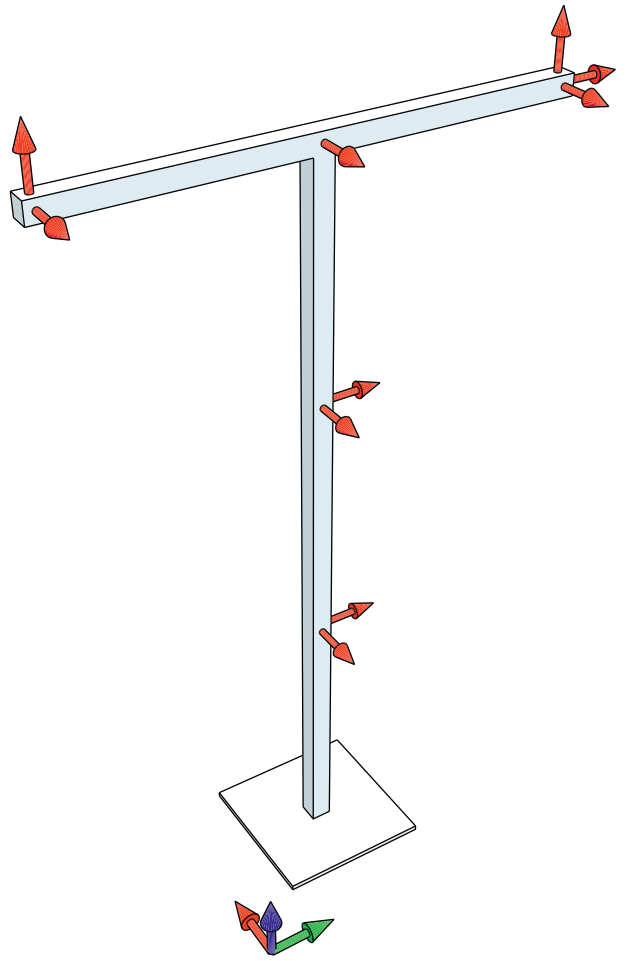

Figure 6: Measurement locations and directions indicated by red arrows on the T structure. Sensor groups are separated by 0.5 m. The green-red-blue arrows at the bottom of the figure denote the reference coordinate system of the T structure.

3.3. Simulation with Noise and LC. In this example, we extend the previous example to a complete one-step update of a structure. The example is also based on the FE model used in the previous example.

The test mode shapes in $\mathbf{A}$ are generated as in the previous example by adding mass to one arm of the T structure and solving the eigenvalue problem to obtain the mode shapes and eigenfrequencies for the model with additional mass. In order to mimic modal parameter estimates obtained from measurements, white Gaussian noise was added to the mode shape coordinates with a standard deviation of 1%.

Since the perturbed model is known only in a relatively small subset of the 762 DOFs, in this particular case, we have used the 10 DOFs of the FE model that correspond best to the locations and directions shown in Figure 6. The 10 chosen DOFs have directions that coincide with the coordinate axes in the FE model. The chosen subset of the mode shapes $\mathbf{A}$ are the active DOFs. This gives the test mode shapes $\mathbf{A}_a$. The MAC values between the test mode shapes $\mathbf{A}_a$ from the perturbed system and the active DOFs of the model mode shapes $\mathbf{B}_a$ from the unperturbed system are shown in Figure 7. The simulated data consisting of mass and stiffness matrices, eigenfrequencies, model mode shapes, and mode shapes from the 10 measured DOFs of the perturbed system constitute a complete setup required for one-step updating.

The FE model updating with the one-step approach is carried out in two phases. Firstly, the mode shape vectors in $\mathbf{A}_a$ are expanded to the same size as the FE mode shape vectors of 762×1. This is done using LC, essentially by following the procedure synthesized by equation (17). This gives the smoothed and expanded test modes $\widehat{\mathbf{A}}$. The MAC value between the expanded mode shapes and the original unperturbed model is shown in Figure 8.

Finally, the expanded mode shapes are inserted into equations (20) and (21) to update the mass and stiffness matrices of the unperturbed FE model. The MAC value between the mode shapes of the updated system and the perturbed system is shown in Figure 9.

This illustrates that the LC expansion has been able to express almost all perturbation of the system in terms of components of the local model modes. Thus, when updating the model with the LC expanded modes, model and test modes are very well correlated. The small drop in the MAC value visible for the 8-th mode is due to a perturbation in this mode that cannot be explained by expanding into the local modes, and therefore, LC misses a little of the perturbation. For perturbations that are significantly smaller than those related to doubling the mass of the arm of the T structure, the update can be expected to be much better. This is explained by the fact that the LC expansion technique relies on the sensitivity equations [12] that are a first-order approximation of the mode shape change under small perturbations.

The procedure previously described can be summarized in the following steps:

(1) Extract $\mathbf{M}$, $\mathbf{K}$, $\mathbf{B}$, and ω from the FE model

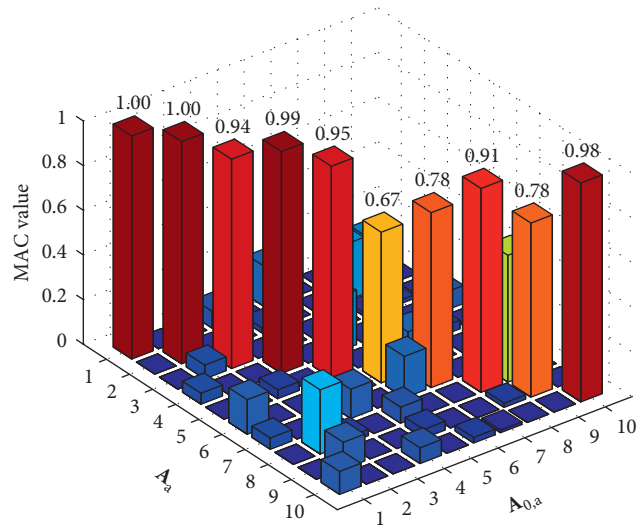

Figure 7: MAC between the measured mode shapes $\mathbf{A}_a$ and unperturbed model $\mathbf{B}_{0,a}$.

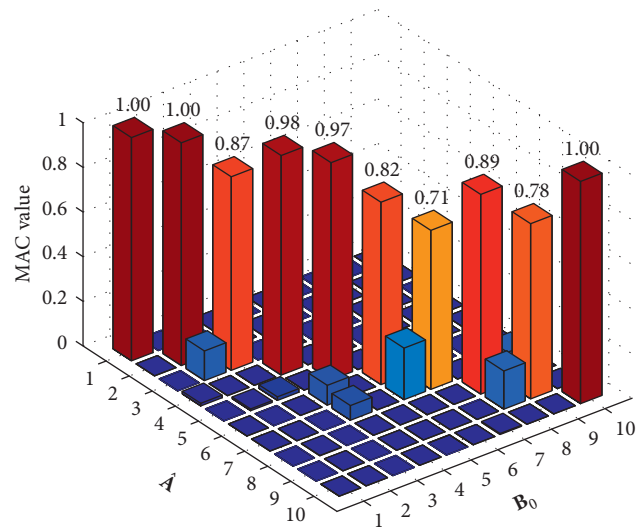

Figure 8: MAC between the LC expanded measured mode shapes $\mathbf{A}$ and incomplete model $\mathbf{B}_{0,a}$.

(2) Chose the subset $\mathbf{B}_1$ and calculate $\mathbf{M}^{-1}$ and $\mathbf{K}^{-1}$

(3) Determine $\mathbf{A}_a$ and ω_{exp} based on test data

(4) Find LC subspace size and do LC expansion

(5) Update $\mathbf{M}$ and $\mathbf{K}$ using equations (20) and (21)

(6) Mass scale test mode shapes $\mathbf{A}$ using the updated mass matrix in equation (20) and redo the one-step update using equations (20) and (21)

The number of modes used for LC expansion is chosen as described in [7]. For a dataset with 10 active DOFs, 4–6 modes are usually a good choice.

3.4. Updating Test Case T Structure. For illustrating the one-step technique for a real test case, we have used the T structure in Figure 10. It is a welded tubular steel structure constituted

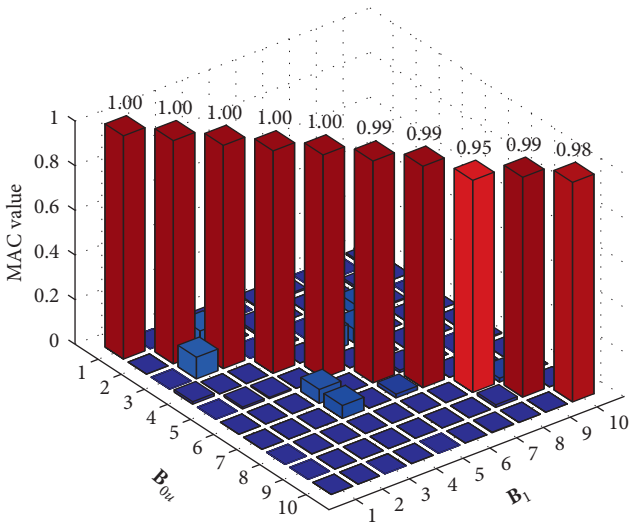

Figure 9: MAC values between the mode shapes from the updated FE model and the mode shapes from the perturbed FE model. The updating was done using 10 LC expanded modes. The LC expansion used 12 model modes from the unperturbed system.

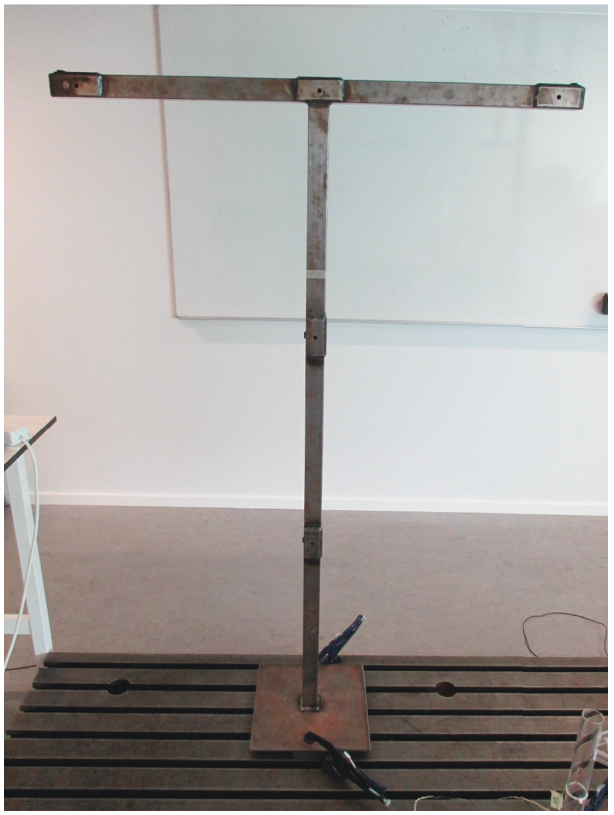

Figure 10: T structure used in the test experiment. The structure is a welded tubular steel structure of 2mm thick square pipes. Small masses are welded on in the areas where the sensors are placed. Sensor placement is shown in Figure 6. Close-ups of the additional masses at the sensor positions are shown in Figures 11 and 12.

of 2mm thick square pipes, with small additional masses welded on at the areas where the sensors are placed. Figures 11 and 12 show how the masses are welded on. The structure

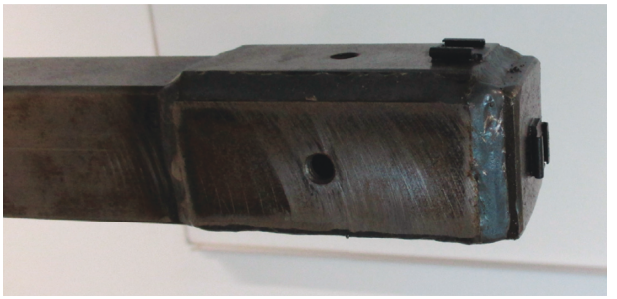

Figure 11: Close-up of the right arm of the T structure from Figure 10.

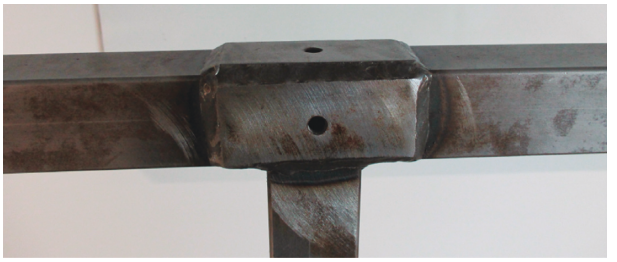

Figure 12: Close-up of the center of the T structure from Figure 10.

closely resembles the FE model used in the previous simulation cases, except for the small additional masses that are not included in the model. Sensor placement and directions are shown in Figure 6. They are identical to the positions and directions chosen in the FE simulation case. For clamping, a 10 mm thick steel plate is welded to the bottom of the vertical pipe. The lower 8 modes are used to update the FE model of the T structure in this experiment.

Compared to the ideal FE model, the perturbation considered in Section 3.3 consisted of an increase of mass on one branch of the FE model of the T structure. In this section, however, the perturbation of the structure, with regard to the ideal FE model, is the small imperfections on the real T structure that are not captured by the FE model.

An output-only vibration test was conducted to estimate the experimental vibration modes of the structure. The vibration responses of the T structure were collected using three National Instruments (NI) 9234 DAQ modules with four channels each, placed in a NI cDAQ-9178 8 module carrier, with a total of 10 channels. Each channel consisted of a Brüel and Kjær 4508 Piezoelectric CCLD 100mV/g accelerometer mounted in Brüel and Kjær UA-1407 mounting clips. The NI-DAQmx driver from NI was used. The sampling frequency was set to 1652Hz. The structure was excited by air pressure coming from three different directions, to excite the structure along x, y, and z directions. As expected, it was verified that the output data followed a Gaussian distribution. The modal identification was carried out using operational modal analysis (OMA) as described in [4]. A LabView [22] program was developed to automate the complete cycle of data collection, system identification, and saving to disk. The identification algorithms were written in MATLAB [19], and the LabView interface to MATLAB was used to make use of the algorithms.

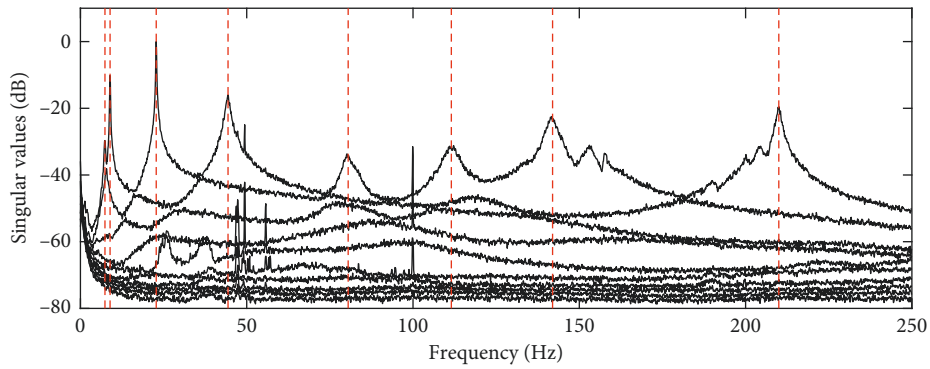

Figure 13: Plot of the singular values of the spectral matrix estimated from the vibration responses of the T structure. The natural frequencies of the identified modes are shown as the vertical dashed red lines.

System identification based on the Time Domain Poly Reference (TDPR) [4] algorithm was carried out to extract the natural frequencies and modal vectors from the test data. Bands containing approximately three natural frequencies were selected by filtering, and the TDPR algorithm with 10 poles was run on this block of filtered data. The physical natural frequencies of the T structure were selected, and the corresponding identified parameters were saved to the disk. For each block of data, 9 modes were saved, each consisting of a natural frequency, a damping ratio, and a 10 DOF mode shape vector. One of the 9 mode shapes was disregarded after identification as it was considered nonphysical by inspecting the mode shape animation, by comparing to the FE model modal vectors and by assessing the noise level of the identified parameters of the mode. The 8 identified physical modes physical are shown in Figure 13 as vertical dashed red lines.

The blocks of vibration data used for identification were 2 minutes long, where the length of each block was chosen according to the formula found in [4]:

$$T_{\text{recording}} > \frac{10}{\zeta f_{\min}} \approx \frac{10}{0.01 f_{\min}} \approx \frac{1000}{8}\ \text{s} \approx 2\ \text{min}, \qquad (22)$$

where $f_{\min}$ is the lowest natural frequency of the structure and ζ its corresponding damping ratio. The final identified modes were obtained as an average of 192 identifications. Typical standard deviations on the final parameters of the mode shapes were below 1/10000 for parameters of unit-scaled mode shapes.

One-step updating works best for FE models that are already in good correspondence with the modelled structure. Therefore, the FE model of the T structure was manual and iteratively updated using FEMtools [18] prior to the application of the one-step approach. This manual updating was done by placing a spring at the bottom of the model of the T structure, and optimizing stiffness in x- and y-axis directions. The Young's modulus of the steel beams was also used in the parametric optimization with FEMtools. The spring stiffness parameters and Young's modulus of the beams were updated based on the natural frequencies and mode shape vectors experimentally identified from the test data.

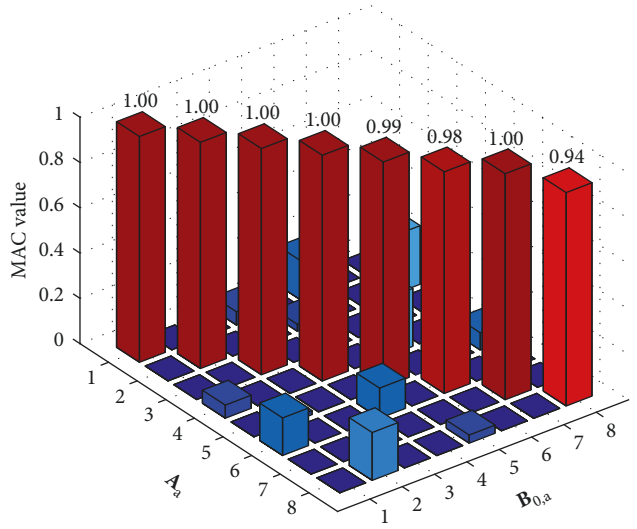

Figure 14: MAC between the measured mode shapes **A** and model $\mathbf{B}_{0,a}$.

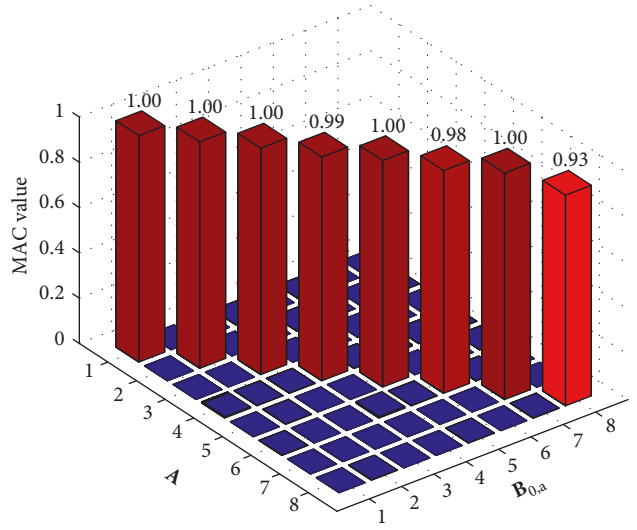

Figure 15: MAC between the LC expanded measured mode shapes **A** and model $\mathbf{B}_{0,a}$.

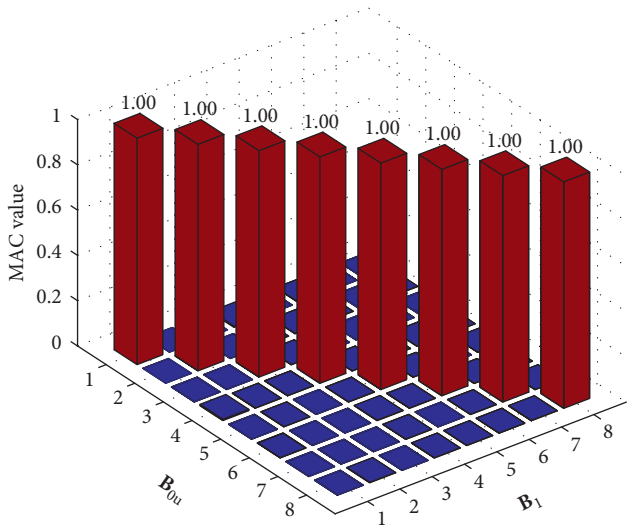

Figure 16: MAC values between the mode shape vectors of the FE model updated with the one-step principle and the test mode shapes. The FE model was updated with 8 modes using LC expansion for the actual test case.

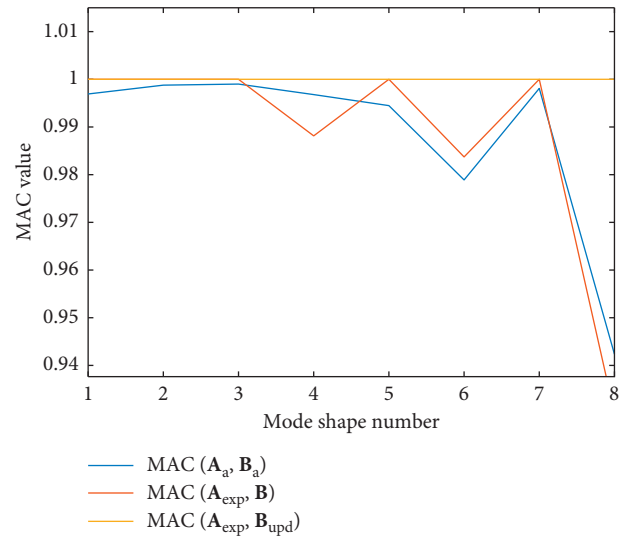

Figure 17: Variation of the MAC values between test and FE model mode shapes over the vibration modes: MAC values between the test and FE mode shapes (at the active DOFs only) before updating with one-step approach (blue line), MAC values between the LC expanded test mode shapes and the FE mode shapes before updating with the one-step approach (red line), and MAC values between the LC expanded test mode shapes and the FE mode shapes after updating with the one-step approach (yellow line).

The MAC values between the first 8 mode shapes estimated from test data and the corresponding modes from FE model updated with FEMtools are shown in Figure 14. These values were computed between modal vectors containing 10 modal components that correspond to the active DOFs. Doing LC expansion removes noise on the off-diagonal terms of the mass and stiffness matrices. The resulting MAC values between the model and the expanded test modes are shown in Figure 15. The MAC values between the mode shapes computed from the FE model updated with the one-step approach and the test mode shapes are shown in Figure 16. To clearly see the result of this procedure, a plot of the diagonal MAC values of Figures 14–16 are shown in Figure 17. Analysing the latter, we see that if the LC technique successfully expands the mode, the updated system is in complete accordance with its perturbed counterpart.

Table 1: Results obtained, in terms of natural frequencies, after one-step updating.

Mode	f_{exp} (Hz)	f_{model} (Hz)	f_{upd} (Hz)
1	7.38	7.22	7.38
2	8.91	8.91	8.91
3	22.79	19.03	22.79
4	44.38	46.15	44.38
5	80.50	80.14	80.50
6	111.52	113.88	111.52
7	141.96	153.68	141.96
8	209.98	212.94	209.98
9	—	274.01	274.01
10	—	274.06	274.06
11	—	515.52	515.52
12	—	526.40	526.40
13	—	560.75	560.75
14	—	589.77	589.77
15	—	705.80	705.80

First column has experimentally determined frequencies. Second column contains frequencies from the original linear system $\mathbf{M}\ddot{x} + \mathbf{K}\mathbf{x} = 0$. The third column contains frequencies from the updated linear system $\mathbf{M}_{upd}\ddot{x} + \mathbf{K}_{upd}\mathbf{x} = 0$. After updating, the frequencies in the upper part of column three coincide with the frequencies in the first experimental column.

The results obtained, in terms of natural frequencies, after one-step updating are presented in Table 1. The natural frequencies in the third column illustrates that, for the unscaled test mode shapes in $\mathbf{A}$, the frequencies $\mathbf{A}_{unsc.}^{T}\mathbf{K}_{0,u}\mathbf{A}_{unsc.} = [\omega_{u,n}^{2}]$ should not be used. The frequencies in the updated model, however, are in perfect accordance with their experimental counterparts, as verified in column 1. It is worth highlighting that the frequencies below the second horizontal line in Table 1, i.e., from mode 9 onwards, have not been subjected to model updating and, thus, remained the same after updating.

4. Discussion

The one-step technique uses a limited number of modes and is therefore better suited to update FE models with distributed rather than with localized modelling errors. This implies that, in order to remove or minimize the localized imperfections, many experimental modes will be required. The reason for this is that higher frequency mode shapes carry more localized information than lower modes.

We have seen in Section 3.3 that when the perturbation is very large, the one-step technique will not handle all the imperfections in the FE model. This is illustrated by mode 8 in Figure 9 that has an MAC below one. The reason for this is that the LC expansion assumes small distributed

perturbations. When this assumption is not fulfilled, the one-step updating based on LC expansion can fail.

When updating a FE model using the one-step technique, the modes used for updating are mass scaled with respect to the original mass matrix. To scale the mode shapes using the updated mass matrix, the fixed point iteration explained in Section 2.5 is used. Since this procedure introduces only small changes in the mass matrix, the scaling of the mode shapes is only changed by a tiny amount, so almost no physical information in the system is lost by the fixed-point iteration.

The updating equations (20) and (21) require inversion of potentially very large matrices. Effective algorithms to do this inversion can be implemented by exploring the fact that the matrices **M** and **K** are sparse, symmetrical, and positive semidefinite. Alternatively, one could consider the following strategy: (1) reduce the FE spatial matrices using SEREP; (2) update the reduced compliance matrices with the test modal parameters; (3) invert the updated compliance matrices; and (4) finally, expand the resulting matrices with SEREP to obtain the full updated matrices. This strategy provides much better updating performance, both in terms of computational time and memory requirements.

Structural-change localization using the one-step technique could be developed by using a FE model to simulate the expected changes in the mass and stiffness matrices and by comparing with the changes suggested by the one-step updating procedure.

5. Conclusion

We have presented a method for updating finite element mass and stiffness matrices directly from experimentally identified mode shapes using FE models with local correspondence principle. The method uses the smoothed and expanded mode shapes to improve the correlation between FE model and test results. It is shown that, after mass scaling using the new updated mass matrix, the correct frequencies are found from the stiffness matrix. The method proved to work both with simulations and real vibration tests. One-step requires a fix-point mass scaling iteration and works well for non-localized changes that can be considered small distributed perturbations. It is also observed that, thanks to the LC approach, the one-step procedure introduces no errors in the higher frequency band of the model. Moreover, it is verified that, if the perturbations are small and globally distributed along the structure, the one-step technique is able to completely update the vibration modes with lower natural frequencies while keeping the modes with higher frequencies unaltered.

Data Availability

The experimental data, i.e., the vibration responses of the T structure, used to support the findings of this study are available from the corresponding author upon request.

Conflicts of Interest

The authors declare that they have no conflicts of interest.

Acknowledgments

The work in this article was partly funded by the Innovation Fund Denmark under contract number 54-2014-3, project name Innomill.

References

[1] M. Friswell and J. E. Mottershead, *Finite Element Model Updating in Structural Dynamics*, Springer Science & Business Media, Vol. 38, Springer Science & Business Media, Berlin, Germany, 1995.

[2] J. E. Mottershead and M. I. Friswell, "Model updating in structural dynamics: a survey," *Journal of Sound and Vibration*, vol. 167, no. 2, pp. 347–375, 1993.

[3] J. E. Mottershead, M. Link, and M. I. Friswell, "The sensitivity method in finite element model updating: a tutorial," *Mechanical Systems and Signal Processing*, vol. 25, no. 7, pp. 2275–2296, 2011.

[4] R. Brincker and C. Ventura, *Introduction to Operational Modal Analysis*, Wiley, Hoboken, NJ, USA, 2015.

[5] M. Link, M. Weiland, and J. M. Barragan, "Direct physical matrix identification as compared to phase resonance testing-an assessment based on practical application," in *Proceedings of the 5th International Modal Analysis Conference (IMAC)*, vol. 1, pp. 804–811, London, UK, April 1987.

[6] B. Caesar, "Updating system matrices using modal test data," in *Proceedings of the 5th International Modal Analysis Conference (IMAC)*, London, UK, April 1987.

[7] R. Brincker, A. Skafte, M. López-Aenlle, A. Sestieri, W. D'Ambrogio, and A. Canteli, "A local correspondence principle for mode shapes in structural dynamics," *Mechanical Systems and Signal Processing*, vol. 45, no. 1, pp. 91–104, 2014.

[8] S. D. R. Amador, M. Juul, T. Friis, and R. Brincker, "Finite element model updating using the local correspondence principle," in *Proceeding of the 36th International Modal Analysis Conference (IMAC 2018)*, Orlando, FL, USA, 2018.

[9] M. Jull, *Operational modal analysis in the InnoMill project*, Ph.D. thesis, Department of Civil Engineering, Aarhus University, Aarhus, Denmark, 2018.

[10] Z. Zhang and A. E. Aktan, "Application of modal flexibility and its derivatives in structural identification," *Journal of Research in Nondestructive Evaluation*, vol. 10, no. 1, pp. 43–61, 1998.

[11] F. N. Catbas, D. L. Brown, and A. E. Aktan, "Use of modal flexibility for damage detection and condition assessment: case studies and demonstrations on large structures," *Journal of Structural Engineering*, vol. 132, no. 11, pp. 1699–1712, 2006.

[12] R. L. Fox and M. P. Kapoor, "Rates of change of eigenvalues and eigenvectors," *AIAA Journal*, vol. 6, no. 12, pp. 2426–2429, 1968.

[13] A. Sestieri, "Structural dynamic modification," *Sadhana*, vol. 25, no. 3, pp. 247–259, 2000.

[14] J. O'Callahan, P. Avitabile, and R. Riemer, "System equivalent reduction expansion process (serep)," in *Proceedings of the 7th International Modal Analysis Conference*, vol. 1, pp. 29–37, Union College Schnectady, Las Vegas, NV, USA, January-February 1989.

[15] P. C. Hansen, V. Pereyra, and G. Scherer, *Least Squares Data Fitting with Applications*, JHU Press, Baltimore, MD, USA, 2012.

[16] G. James, D. Witten, T. Hastie, and R. Tibshirani, *An Introduction to Statistical Learning*, Springer, Berlin, Germany, 2013.
[17] S. Banach, "Sur les opérations dans les ensembles abstraits et leur application aux équations intégrales," *Fundamenta Mathematicae*, vol. 3, no. 1, pp. 133–181, 1922.
[18] N.V. Dynamic Design Solutions (DDS), *FEMtools 3.8.2*, 2016, http://www.femtools.com.
[19] MathWorks Inc., *MATLAB R2015b*, 2015, http://www.mathworks.com/.
[20] SDTools, *SDT Structural Dynamics Toolbox 6.8*, 2016, http://www.sdtools.com/.
[21] R. J. Allemang and D. L. Brown, "A correlation coefficient for modal vector analysis," in *Proceedings of the 1st International Modal Analysis Conference (IMAC 1982)*, vol. 1, pp. 110–116, SEM, Orlando, FL, USA, November 1982.
[22] National Instruments (NI), *LabView 15.0*, 2015, http://www.ni.com.

Hindawi
Shock and Vibration
Volume 2018, Article ID 6595841, 12 pages
https://doi.org/10.1155/2018/6595841

Research Article

The Tunnel Structural Mode Frequency Characteristics Identification and Analysis Based on a Modified Stochastic Subspace Identification Method

Biao Zhou,[1,2] **Xiongyao Xie**,[1,2] **and Xiaojian Wang**[1,2]

[1]*Key Laboratory of Geotechnical & Underground Engineering, Ministry of Education, Tongji University, Shanghai 200092, China*
[2]*Department of Geotechnical Engineering, Tongji University, Shanghai 200092, China*

Correspondence should be addressed to Biao Zhou; zhoubiao@tongji.edu.cn

Received 2 August 2018; Accepted 22 October 2018; Published 2 December 2018

Academic Editor: Filippo Ubertini

With the rapid development of underground engineering in China, the heavy structural maintenance work followed is expected to be a great challenge in the future. The development also provides a promising application prospect for the newly developed vibration-based health assessment and monitoring methods. However, the fact that tunnels are embedded in soil makes collecting and identifying the vibration characteristics more difficult, especially for the online monitoring. In this paper, a new identification method that combines the natural excitation technique (NExT) and stochastic subspace identification (SSI) method is developed. The new method is compared with the traditional SSI method, and mode frequency analysis is made based on a series of field tests carried out at the subway and power tunnel. It is found that both stability and efficiency of the mode frequency identification have been greatly improved, and it more suitable for online monitoring. Meanwhile, a mathematical model is used to analyze the original mode characteristics and the influence of soil coupling. The results are also compared with the field tests results by using the NExT-SSI method, and some recommendations are also made for how to choose the vibration modals for vibration-based monitoring in the tunnel.

1. Introduction

At present, the underground engineering is gradually moving from the large-scale construction stage into the following heavy maintenance stage in China. The safe operation of underground facilities is threatened by the increasing servicing time and the increasing number of the surrounding construction activities, such as the large excavation. Therefore, the health monitoring system is greatly needed to determine the service state of underground facilities in real time. The static level gauge and crack meter are frequently used to monitor tunnel settlement and joint opening [1, 2], which can effectively prevent large deformation and leakage accidents caused by improper construction behavior such as deep excavation around subway tunnels. However, the related static health monitoring method can only characterize the structural behavior near the monitoring points, and the dense layout is thus needed and difficult to obtain the structural elastic modulus and other indicators directly. It can be used instead of some nondestructive testing methods, but the detection efficiencies of these methods are difficult to meet the real-time requirements for large-scale applications. Therefore, there is a strong need of developing health monitoring methods based on vibration or wave propagation characteristics which have sensing capability of the overall underground structure and the surrounding soil.

The present wave or vibration-based methods can utilize characteristics of wave propagation within the structures or the normal vibration modes to identify structural performance. Examples of current structural healthy monitoring (SHM) techniques include using fiber optics, ultrasonics, piezoelectrics and acoustic emissions, thermography, and embedded thin film [4–6]. For these methods, the effective

identification and extraction of vibration characteristics become very important. For applications in bridges and high-rise buildings, the vibration modes and related methods are more commonly used, e.g., the natural frequency and frequency response function (FRF) spectrum-based methods [7], the mode shape-based methods [8], the model and related matrix-based methods [9], and the data driven methods [10]. Some signal processing techniques have also been proposed for vibration characteristics extraction [11].

It is well known that the soil-structure interaction will change the wave propagation characteristics [12, 13], since the underground structures are strongly coupled with the surrounding soil, and the constraining and damping effects and the dynamic behaviors of surrounding soil will cause major challenges for the identification of vibration characteristics [14]. In previous studies, the difference between frequency and dispersion characteristics of the subway tunnel with or without surrounding soil is studied by numerical calculation [15–17]. It is found that the mode frequency is more difficult to identify from the frequency spectrum under the condition of soil coupling. Health monitoring of underground pipelines is mostly based on wave propagation characteristics and related methods [18–20]. Leinov et al. [21], Vogt et al. [22], and Eybpoosh et al. [23] found that the propagation modes and their dispersion characteristics of the propagating ultrasonic-guided waves changed from the pipeline to the surrounding medium. Meanwhile, a series of signal processing and modal parameter identification methods have been proposed, such as the peak-picking method, the random decrement technique (RAMA) [24], the natural excitation technique (NExT) [25], and the stochastic subspace identification (SSI) method [26]. The NExT is a method of mode testing that allows structures to be tested in their ambient environments, where the auto- or cross-correlation function is used for mode identification. The SSI method is originally presented by van Overschee and de Moor [27], and an extension of the original SSI method that does not require output covariance was proposed by Peeters and de Roeck [28, 29] as the reference-based SSI. The stochastic realization algorithm mainly focused on the data-driven method (SSI-DATA) that considers the problem of identifying a stochastic state-space model from output-only data. As opposed to SSI-DATA, the covariance-driven stochastic subspace identification (SSI-COV) algorithm is also developed to avoid the computation of orthogonal projection. Furthermore, to reduce the effect of noise on the results of identification, some filtering techniques need to be used to enhance the early emergence of a stable diagram for the identifiable modes. For instance, SSI is combined with multivariate singular spectrum analysis (MSSA) for vibration monitoring of the rotating turbine system [30]. These methods are widely used in bridges and high-rise buildings, but their applicability in the underground engineering remains to be explored.

An equally important consideration in developing the monitoring system is minimizing the amount of data processing and improving the stability and robust of the monitoring network. Automatic processing technology is also used to reduce the amount of data transmission from the terminal nodes to the server. Therefore, the following key problems need to be considered in the application of the vibration-based monitoring method to tunnels and other underground structures:

(1) Understanding of the tunnel-soil coupling effect on the tunnel dynamic characteristics, and selection of the appropriate vibration characteristics for determining the current structural state

(2) Proper signal processing and vibration characteristics identification methods with high stability and accuracy

(3) Development of the self-processing and automatic identification capability of terminal nodes to meet the low energy cost and robust needs of the wireless network transmission

In this paper, to explore the vibration characteristics of the tunnel and its identification method, a series of field tests are carried out at the subway and power tunnels with different diameters of 6.4 m and 3.2 m. The SSI-COV method is used, and the NExT is also combined as the filtering techniques to identify tunnel mode natural frequency, and some comparisons on the difference between using SSI-COV and NExT-SSI-COV method on the result of identification are carried out through the stability diagram. At last, a theoretical pipe-in-pipe (PiP) model [31] is employed to study the distribution of the vibration modes, and some scientific suggestions for the tunnel mode parameters identification are provided at last.

2. The NExT-SSI-COV Method

The SSI-COV method is a well-known multivariate identification technique. However, the uncertainty of parameter selection, such as the Toeplitz matrix row number [32] and the long input data will result in the sharp drop of the computational efficiency and stability. In this study, the NExT method is employed and combined with the SSI-COV method to reduce the singularity of covariance matrix and improve the calculation efficiency and stability. The details and process of this method are shown in Figure 1.

Step 1. Form the input matrix $\mathbf{N}$ by the NExT method.

The autocorrelation function a_{mm} of every measurement points and cross-correlation function a_{mn} for any two measurement points were calculated by the NExT method [33], and the formed matrix is denoted as $\mathbf{N} \in \mathbb{R}^{l \times n}$, where l is the number of autocorrelation and cross-correlation functions and n is the sampling number of the NExT method. The n value is always less than 2048 for identifying the low-frequency modes. Therefore, compared with the conventional SSI-COV method, the size and singularity of the input matrix will be greatly reduced and the computational efficiency and stability can be obviously improved.

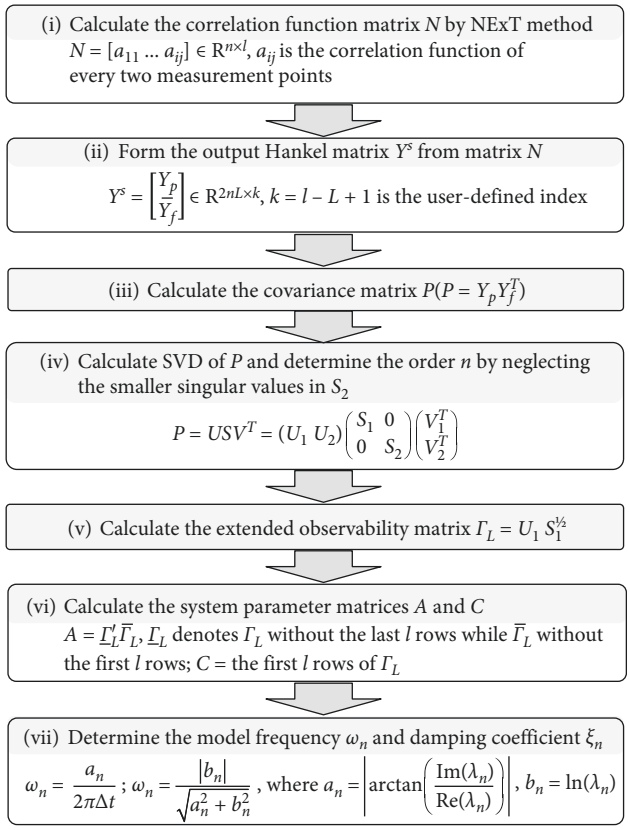

Figure 1: The flowchart of the NExT-SSI-COV method.

Step 2. Form the output Hankel matrix $\mathbf{Y}^s$ from input matrix $\mathbf{N}$.

Firstly, as Equation (1) shows, a series of block matrix $\mathbf{y}_i$ are obtained with a time lag i from the input matrix $\mathbf{N}$, and every block matrix $\mathbf{y}_i$ has l lines same as $\mathbf{Y_N}$. And the data Hankel data matrix is established by the future measurements matrix $\mathbf{Y}_\mathrm{f}$ and past measurements $\mathbf{Y}_\mathrm{p}$ as Equation (1) shows:

$$\mathbf{Y}^s = \frac{1}{\sqrt{j}}\begin{bmatrix} y_0 & y_1 & \cdots & y_{j-1} \\ y_1 & y_2 & \cdots & y_j \\ \vdots & \vdots & \ddots & \vdots \\ y_{i-1} & y_i & \cdots & y_{i+j-2} \\ y_i & y_{i+1} & \cdots & y_{i+j-1} \\ y_{i+1} & y_{i+2} & \cdots & y_{i+j} \\ \vdots & \vdots & \ddots & \vdots \\ y_{2i-1} & y_{2i} & \cdots & y_{2i+j-2} \end{bmatrix} = \begin{pmatrix} \mathbf{Y}_\mathrm{p} \\ \mathbf{Y}_\mathrm{f} \end{pmatrix} \begin{matrix} \text{“past”} \\ \text{“future”} \end{matrix}. \quad (1)$$

Step 3. Obtain covariance-driven Hankel matrix $\mathbf{P}$ by the conventional matrix and then form the block Toeplitz matrix by a multiplication between future measurements matrix $\mathbf{Y}_\mathrm{f}$ and transpose of past measurements $\mathbf{Y}_\mathrm{p}$ based on Equation (2):

$$\begin{aligned} \mathbf{P} &= \begin{bmatrix} R_i & R_{i-1} & \cdots & R_1 \\ R_{i+1} & R_i & \cdots & R_2 \\ \vdots & \vdots & \ddots & \vdots \\ R_{2i-1} & R_{2i-2} & \cdots & R_i \end{bmatrix} \\ &= \begin{pmatrix} C \\ CA \\ \cdots \\ CA^{i-1} \end{pmatrix} \begin{pmatrix} A^{i-1}G & \cdots & AG & G \end{pmatrix} = \mathbf{Y}_\mathrm{f}\left(\mathbf{Y}_\mathrm{p}\right)^T, \end{aligned} \quad (2)$$

$$R_i = E\begin{bmatrix} y_{k+i} & y_k^T \end{bmatrix} = \lim_{j\longrightarrow\infty} \frac{1}{j}\sum_{k=0}^{j-1} y_{k+i} y_k^T.$$

Step 4. Perform singular value decomposition (SVD) on the Hankel covariance matrix $\mathbf{P}$ and obtain eigenmatrix $\mathbf{S}$ [28, 29]. Then, separate the matrix $\mathbf{S}$ into two submatrices $\mathbf{S}_1$ and $\mathbf{S}_2$ by reducing the eigenvalues. The smallest singular values in the matrix $\mathbf{S}$ are grouped as $\mathbf{S}_2$ and will be neglected in the following steps by parameters Csvd. The Csvd can be calculated by the following equations:

$$\begin{aligned} \mathbf{P} = USV^T &= \begin{pmatrix} U_1 & U_2 \end{pmatrix}\begin{pmatrix} S_1 & 0 \\ 0 & S_2 \end{pmatrix}\begin{pmatrix} V_1^T \\ V_2^T \end{pmatrix} \\ &= U_1 S_1 V_1^T, \end{aligned} \quad (3)$$

$$\mathrm{Csvd} = \frac{\sum V_{S_\mathrm{n}}}{\sum V_S}, \quad (4)$$

where $\sum V_{S_\mathrm{n}}$ is the cumulative value of the first n eigenvalues for the $\mathbf{S}$ matrix and $\sum V_S$ is the cumulative value of all eigenvalues.

Steps 5~7. Based on the conventional SSI-COV method, the extended observability matrix Γ_L is firstly calculated according to Equation (5), and then the system parameter matrices $\mathbf{A}$ and $\mathbf{C}$ and mode frequency ω_n and damping coefficient ξ_n. are obtained separately by Equations (6) and (7) [34, 35]:

$$\Gamma_L = S_1^{1/2} V_1^T, \quad (5)$$

$$\begin{aligned} A &= \underline{\Gamma}_L' \overline{\Gamma}_L, \\ C &= \text{the first } L \text{ rows of } \Gamma_L, \end{aligned} \quad (6)$$

where $\underline{\Gamma}_L$ and $\overline{\Gamma}_L$ denote Γ_L without the last L rows and the first L rows, respectively:

$$\omega_n = \frac{a_n}{2\pi\Delta t},$$
$$\omega_n = \frac{|b_n|}{\sqrt{a_n^2 + b_n^2}},$$
$$\text{where } a_n = \left|\arctan\left(\frac{\text{Im}(\lambda_n)}{\text{Re}(\lambda_n)}\right)\right|, \quad (7)$$
$$b_n = \ln(\lambda_n).$$

3. Field Test and Mode Frequency Identification of a Power Tunnel

3.1. Measurement Site and Arrangement. As Figure 2 shows, the measured power tunnel is a pipe jacking tunnel, which consists of concrete pipes with a length of 2.5 m. The outer diameter is 3.2 m, and inner diameter is 2.7 m. Nine accelerometers (LANCE 130 series) are installed at the wall and the bottom of the tunnel. Three of them are equipped at each measured point to collect the response from the radical, longitudinal, and tangential directions, and the letter R means the sensor is installed in the radial direction; L means the longitudinal direction, while T is the tangential direction.

3.2. Ambient Vibration Test. To compare the response characteristics of the tunnel in daytime and nighttime, the ambient vibration test is continued for seven days. Acceleration response records of 30 minutes in the nighttime and daytime, respectively, at the measurement point B-1 are shown in Figure 3. For the measured power tunnel close to a subway, the vibration from the operational trains makes the vibration amplitude at daytime about 4 times than that at night. Based on the above data, the tunnel mode frequency characteristics are studied, and a comparison on the difference between using SSI-COV and NExT-SSI-COV on the result of identification is carried out through the construction of a stability diagram. The stability diagram has been proved very helpful to identify the dominant frequencies of the vibration mode while using the SSI-COV method [32].

3.2.1. The Tunnel Response Characteristics at Night. To analyze the tunnel response characteristics at night, with the 30-minute records collected from nine accelerometers, the input matrix dimension will be 3600000 × 9 using the traditional SSI method. The stability diagram can be obtained and is shown in Figure 4 after running for three hours on a microcomputer with an Intel i5 processor. While the NExT method is employed, based on the procedures of Step 1 and Step 2 introduced in Section 2, the auto- and cross-correlation functions of every degree of freedom were calculated with a sampling window of 2048 points and the input matrix **N** is formed with the matrix dimension of 2048 × 28. The operation time of the stability diagram on the same microcomputer then can be reduced to less than 2 minutes. The calculation results are shown in Figure 5.

By comparing the stability diagrams of Figures 4 and 5, it was observed that several modes between 10 and 15 Hz can be found in Figure 4 by using the SSI-COV method directly, but the data fluctuation along the number of rows makes it difficult to identify the natural frequency automatically and accurately. It thus will limit its application of SHM at the underground structure. However, as the NExT method is combined, there is only one mode left with the frequency of 10.5 Hz. In addition, in the implementation of SSI-COV, the selecting Csvd in Step 4 at Section 2 can lead to a change in the number of the vibration modes and their identification accuracy. From Figure 5, it is observed that there is almost no change on the identified model frequencies as the Csvd value changes from 0.815 to 0.915 by using the NExT-SSI-COV method. Therefore, the NExT method can develop the mode frequency identification stability and accurately and make it much suitable for application in the underground structure.

3.2.2. The Tunnel Response Characteristics at Daytime. The tunnel response characteristics are analyzed during the daytime, especially for considering those vibration modes excited by the train-induced vibration from the nearby subway. By employing the method both of traditional SSI-COV method and NExT-SSI-COV method, a 30-minute record is used and the stability diagrams are shown in Figure 6. By comparing Figures 6(a) and 6(b), the mode frequency identification accuracy and stability are improved by using the NExT-SSI-COV method. Meanwhile, it also can be observed that besides 10.5 Hz, there are much more recognition results that can be found from Figure 6, and several modes of which are around 48 Hz of which is close to the subway track-rail resonant frequency.

From the ambient test at the power tunnel both at daytime and nighttime and by comparing the stability diagrams of using the traditional SSI method and modified method, it is found that the NExT-SSI-COV method has better mode natural frequency recognition accuracy and stability, and several mode frequencies can be clearly identified around 10.5 Hz, 48 Hz, and 71 Hz from the ambient test. Especially for the frequency of 10.5, stability can be recognized both at daytime and nighttime.

3.3. Hammering Test. The mode hammering test is a commonly used method to study the mode characteristics and has a wider test frequency band than the ambient test. Thus, it was also carried out at the power tunnel along the radial, longitudinal, and tangential directions. The impulse load is applied at the connecting steel ring of the tunnel segment (Figure 7(a)), the time history of the pulse load is shown in Figure 7(b), and the frequency test band is around 300 Hz as shown in Figure 7(c).

The NExT-SSI-COV method is also used here to analyze the acceleration response, and the stability diagrams are shown in Figure 8. From Figure 8(a), the modes at 53 Hz,

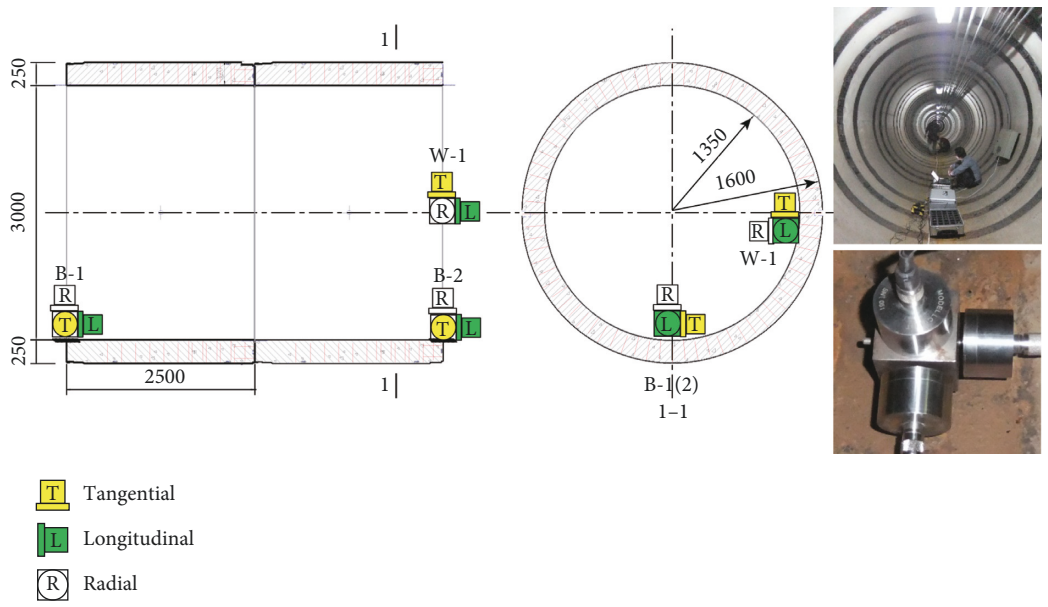

Figure 2: Arrangement map for the site measurement at the Xizang Road power tunnel.

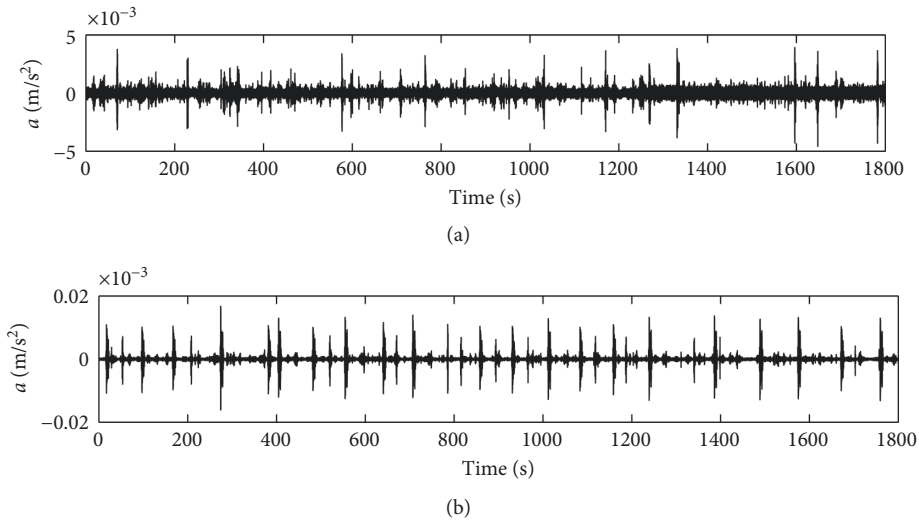

Figure 3: The time history of the acceleration for the measurement points B-1: (a) at nighttime; (b) at daytime.

203 Hz, and 223 Hz can be identified from the radical responses as hammered along the radial direction of the tunnel. And much more modes can be found from the longitudinal direction response as hammered along the longitudinal direction, and there are stable recognition results at 10.5 Hz, 15 Hz, 108 Hz, 123 Hz, 203 Hz, and 223 Hz. When the excitation is applied along the tangential direction along the top pipe, from the stability diagram of longitudinal directional response, four modes at 10.5 Hz, 123 Hz, 203 Hz, and 223 Hz can be clearly identified.

By comparing with the results of the ambient test, besides the first mode of 10.5 Hz, there are much more modes at 53 Hz, 123 Hz, 203 Hz, and 223 Hz that can be found by hammering excitation. Among them, the stability determination of the mode at 53 Hz means that the modes around 48 Hz that are found from the ambient test in Figure 6 are false modes, and it is generated by the train vibration of the nearby subway.

4. Field Test and Mode Frequency Identification of a Subway Tunnel

For analysis of the tunnel mode characteristics with different sizes, a mode hammer test is also applied in the nearby subway tunnel. As shown in Figure 9(b), the internal diameter of the tunnel is 5.5 m, and the outer diameter is 6.2 m. The structure of each ring is assembled from six segments, and the thickness of the segment is 35 cm. There is one bidirectional (1-3) and three radial acceleration sensors (1-1, 1-2, and 2-1) placed on the tunnel structure to collect the response from different directions as shown in Figure 9. The hammer pulse's frequency spectrum is shown in Figure 10.

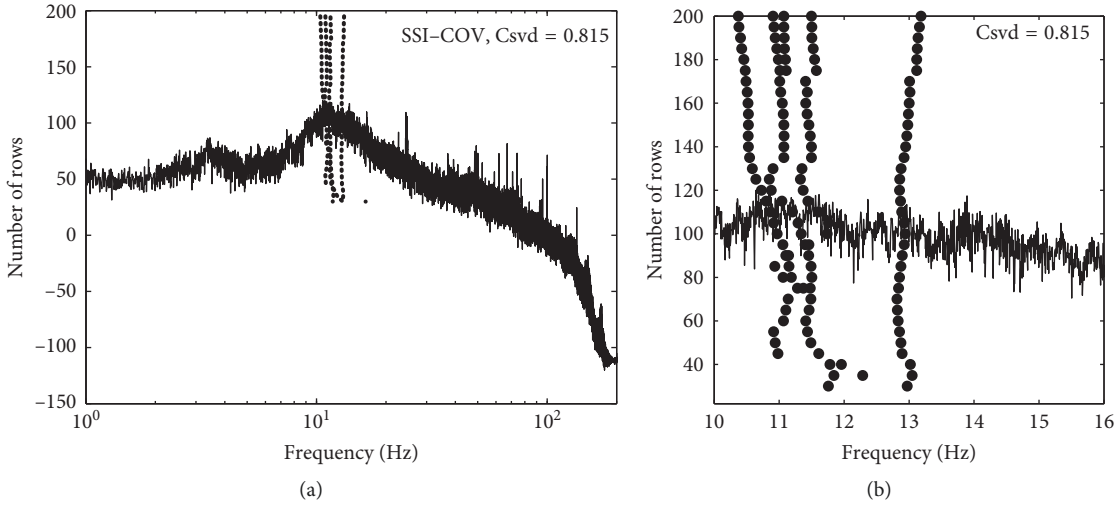

Figure 4: The stability diagram of the data collected at night by using the traditional SSI COV method.

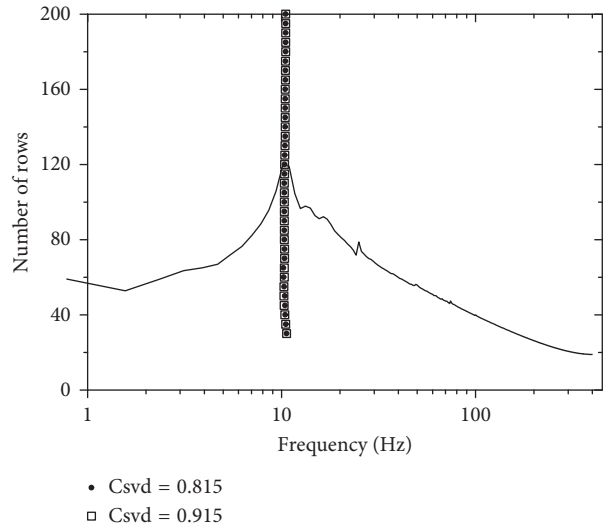

Figure 5: The stability diagram of the data collected at night by using the NExT-SSI-COV method.

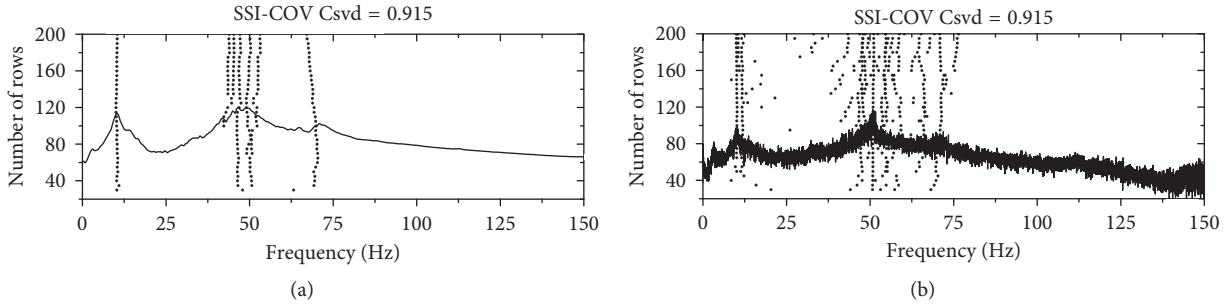

Figure 6: The comparison of the stability diagram of the data collected at daytime: (a) NExT-SSI-COV method; (b) traditional SSI-COV method.

The SSI-NExT method is employed to the acceleration response collected in the tunnel, and the stability diagrams are shown in Figure 11. From Figure 11(a), two modes can be found from the radial response at 142.5 Hz and 233 Hz. And relatively stable recognition results can be obtained at 23.5 Hz and 128.5 Hz in the longitudinal response (Figure 11(b)) and 119 Hz and 128.5 Hz in the tangential direction (Figure 11(c)). In addition, it is also observed that there are two peaks at 10.75 Hz and 176 Hz which appear at the spectrum function from Figure 11 and 10.75 Hz of

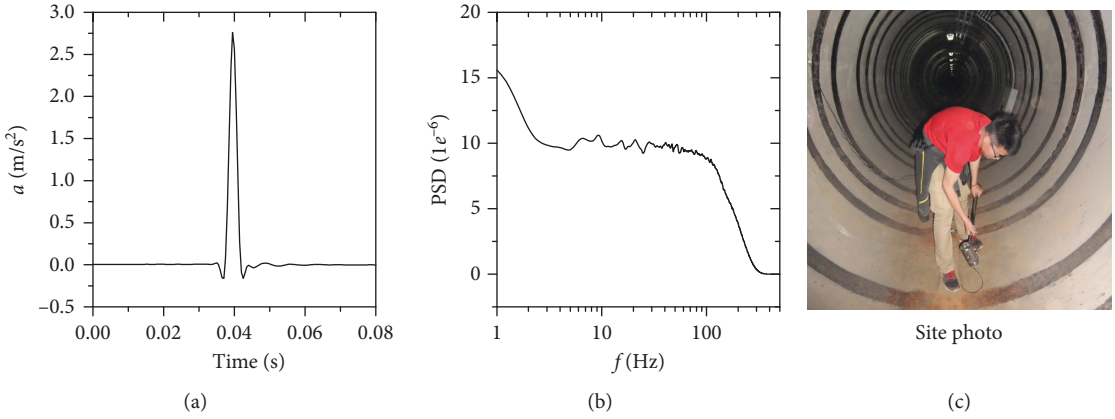

Figure 7: The hammer mode test at the power tunnel.

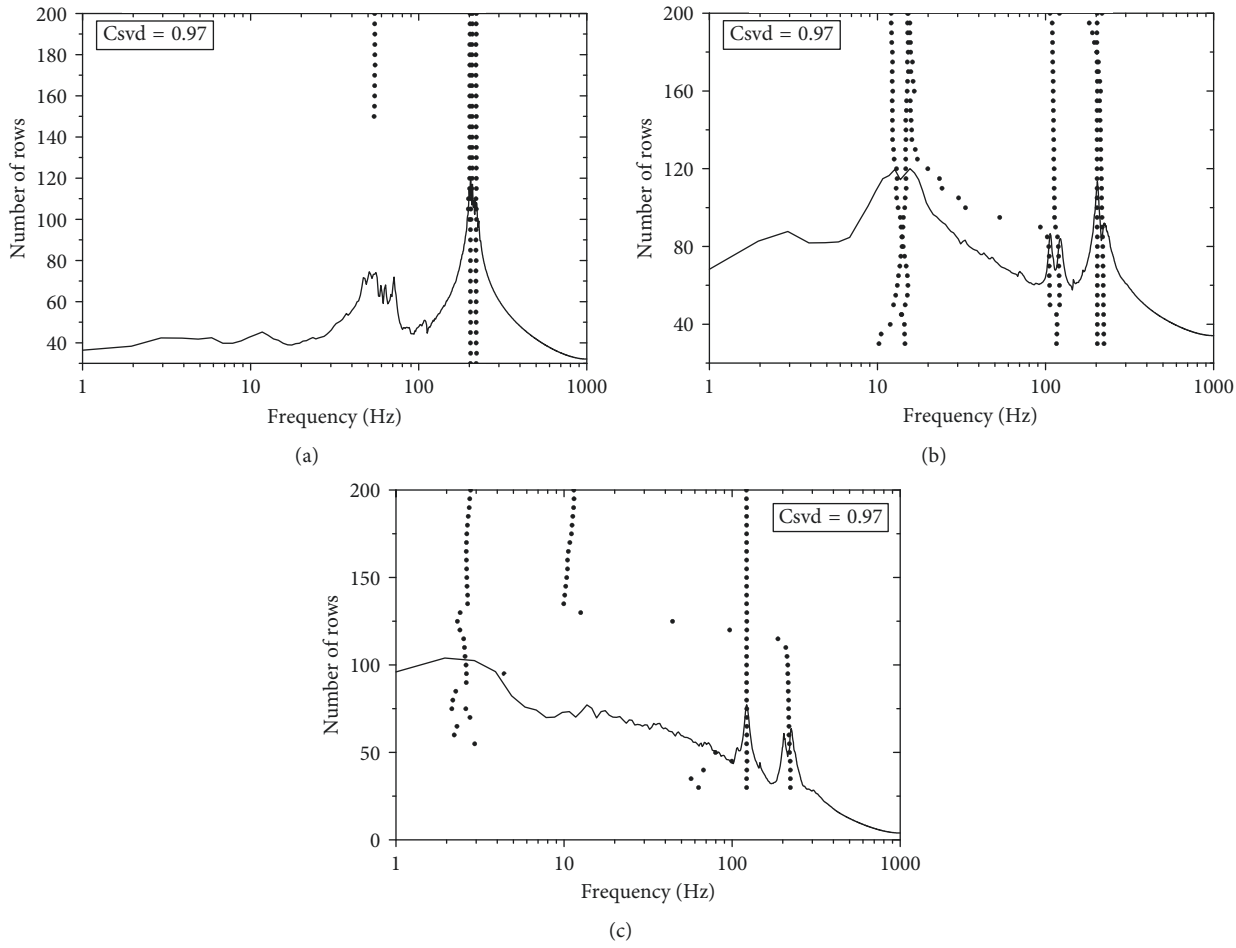

Figure 8: The stability diagrams of the response by applying impulse along different directions at the power tunnel: (a) radical; (b) longitudinal; (c) tangential directions.

which is close to one of the power tunnel's natural frequency at 10.5 Hz.

From the tests and analysis introduced at above, it can be seen that the modes of the tunnel can be stably identified from the hammer test by using the NExT-SSI-COV method.

5. Numerical Verification and Analysis

As the SSI method may generate false mode, the dispersion analysis is thus carried out in this section to explore the vibration modes distribution both of the tunnel mentioned above based on the pipe-in-pipe (PiP) model [31]. By

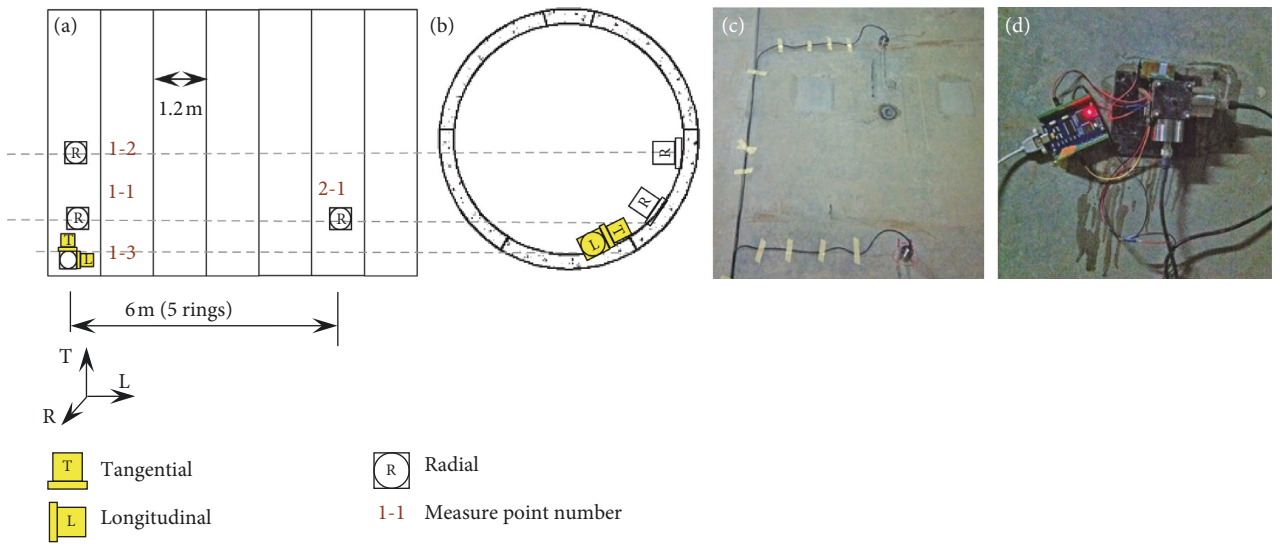

Figure 9: Arrangement map for the site measurement at the subway tunnel.

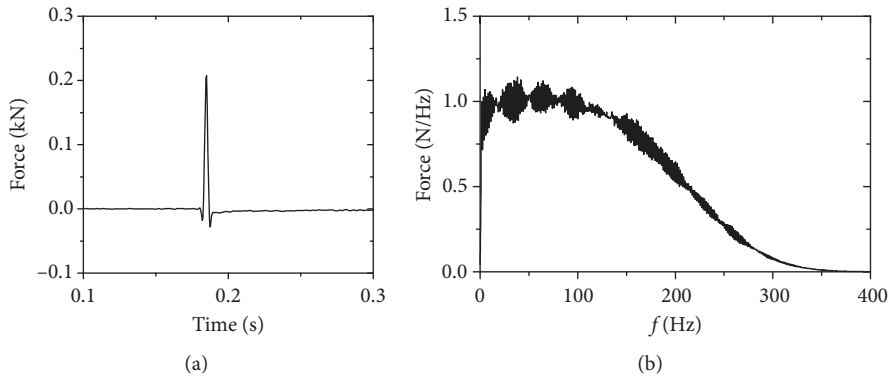

Figure 10: The hammer impulse load applied in the subway tunnel: (a) time spectrum; (b) frequency spectrum.

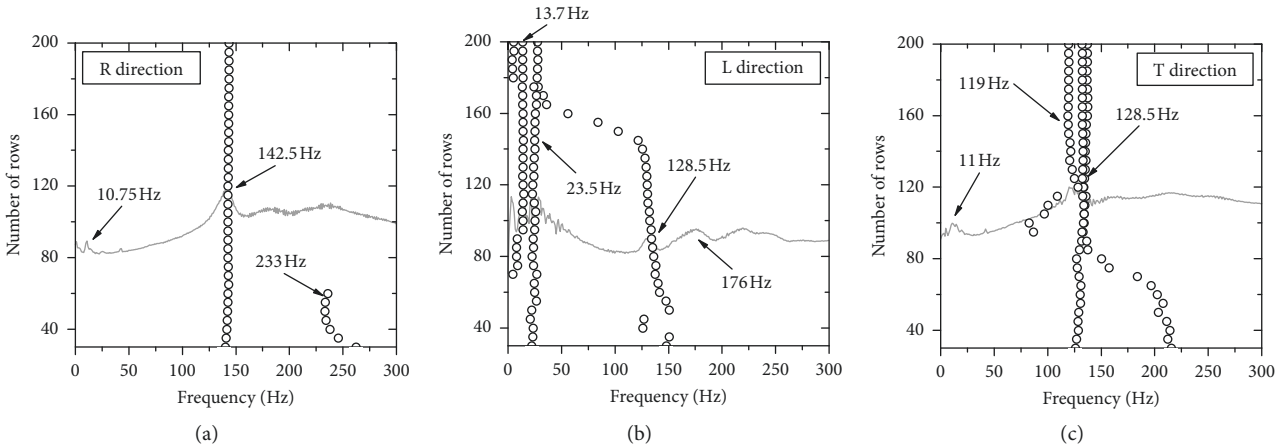

Figure 11: The stability diagrams of the response by applying impulse along different directions at the subway tunnel: (a) radical; (b) longitudinal; (c) tangential directions.

comparing the calculated cut-off frequencies with the results from the field test, the structural and soil-body coupling vibration characteristics will be analyzed.

5.1. The PiP Model and Dispersion Analysis. The shield or pipe-jacking tunnel is an assembled structure composed of segments. As Figure 12(a) shows, when only the low frequency response is concerned, it can be approximately analogous to an infinite continuous concrete hollow cylinder due to the wavelength greater than the tunnel segment size. Therefore, the PiP model is introduced here, and the details are given in [17] based on dispersion and wave propagation theories. In this model, as shown in Figure 12(a), the tunnel structure is analogous to an infinite continuous concrete hollow cylinder, and the homogeneous surrounding soil is considered by coupling a concentric 3D thick-walled cylinder outside the tunnel in the PiP model, with its inner diameter set equal to the diameter of the tunnel and outer diameter set to infinity.

The PiP model is established based on the 2.5D periodic approach [31]. By assuming constant material and geometric properties along the infinite extended direction x, and from Figures 12(b) and 12(c), the loads supplied in the tunnel invert can be treated as a sum of sequence of unit harmonic loads along the direction of x and θ. The function can be expressed as shown in Equation (8) in the frequency-wavenumber domain:

$$\widetilde{F}(r,\theta,x,t) = \sum_{n=0}^{\infty} \begin{bmatrix} \widetilde{Q}_{rn} \cos n\theta \\ \widetilde{Q}_{\theta n} \sin n\theta \\ \widetilde{Q}_{xn} \cos n\theta \end{bmatrix} e^{i(kx+\omega t)}, \tag{8}$$

where $\widetilde{Q}_{xn}$, $\widetilde{Q}_{\theta n}$, and $\widetilde{Q}_{rn}$ are the force components, whose elements are given in [31].

And for a steady response system, it is known that the displacement response can be expressed as the same style with the applied load. Finally, for a given wavenumber n, when applying an impulse load at the tunnel invert along different directions, the displacement components of $\widetilde{U}_n$, $\widetilde{V}_n$, and $\widetilde{W}_n$ for the tunnel structure only is shown in Equation (9), and for the tunnel-soil coupled system, the displacement components of $\widetilde{U}_{rn}$, $\widetilde{U}_{\theta n}$, and $\widetilde{U}_{zn}$ can be calculated by Equation (10) in the frequency-wavenumber domain:

$$[\mathbf{A}] \begin{Bmatrix} \widetilde{U}_n \\ \widetilde{V}_n \\ \widetilde{W}_n \end{Bmatrix} = \frac{-r(1-v^2)}{Eh} \begin{Bmatrix} \widetilde{Q}_{rn} \\ \widetilde{Q}_{\theta n} \\ \widetilde{Q}_{xn} \end{Bmatrix}, \tag{9}$$

where matrix $\mathbf{A}$ is the coefficients matrix, whose elements are given in [31].

$$\begin{Bmatrix} \widetilde{U}_{rn} \\ \widetilde{U}_{\theta n} \\ \widetilde{U}_{zn} \end{Bmatrix}_{r=R+(h/2)} = \mathbf{M}^{\mathrm{T}} \cdot \begin{Bmatrix} \widetilde{Q}_{rn} \\ \widetilde{Q}_{\theta n} \\ \widetilde{Q}_{xn} \end{Bmatrix}_{r=R+(h/2)},$$

$$\mathbf{M} = \frac{-Eh}{a(1-v^2)}[\mathbf{A}] + \begin{bmatrix} 1 & & \\ & -1 & \\ & & -1 \end{bmatrix} [\mathbf{T}_{\infty}]_{r=R+(h/2)} \cdot [\mathbf{U}_{\infty}]^{T}_{R+(h/2)} \begin{bmatrix} -1 & & \\ & 1 & \\ & & 1 \end{bmatrix}, \tag{10}$$

where matrix $\mathbf{T}_{\infty}$ and $\mathbf{U}_{\infty}$ are the 3×3 complex matrix, whose elements are given in [31].

It is known that the dispersion curves are useful in investigating the mechanism of wave propagation in a medium, which are plotted as the wavenumber k of propagating modes versus the frequency ω. And the mode frequency can be obtained by searching for the cut-on frequency of each propagation mode. There are different methods to calculate the dispersion curves [36]. The most commonly used method is to solve the determinant of the coefficient matrix of the equilibrium equation. As Equation (11) shows, the dispersion relation of the tunnel structure can be obtained by defining the coefficient matrix $\mathbf{A}$ of Equation (9) to zero:

$$\det(\mathbf{A}) = 0, \tag{11}$$

where $\mathbf{A}$ is a 3×3 matrix with the parameters of wavenumber k, tunnel density (ρ), Poisson ratio (ν), segment thickness (h), and tunnel radius which is equal to the average of the inner and outer radii. The detailed description of the matrix $\mathbf{A}$ can be found in [31].

5.2. The Power Tunnel Dispersion Characteristics and Comparison with the Field Test. Based on the PiP model, the dispersion characteristics of the power tunnel will be obtained. According to Equation (4), the parameters are Young's modulus $E_t = 2.25 \times 10^4$ MPa, Poisson's ratio $v = 0.2$, density $\rho = 2500\ \mathrm{kg/m^3}$, the outer diameter = 3.2 m, and inner diameter = 2.7 m. The tunnel dispersion curves within the range of 0–300 Hz are obtained and plotted in Figure 13. By dispersion analysis theory, every curve in Figure 13 corresponds to one vibration mode, and the starting frequency at the x-axis is the cut-on frequency of the corresponding vibration mode. The vibration modes arise when the excited frequency is higher than the corresponding cut-on frequency. The cut-on frequencies of the 2nd–4th propagation modes and the comparison with the field test results are listed in Table 1.

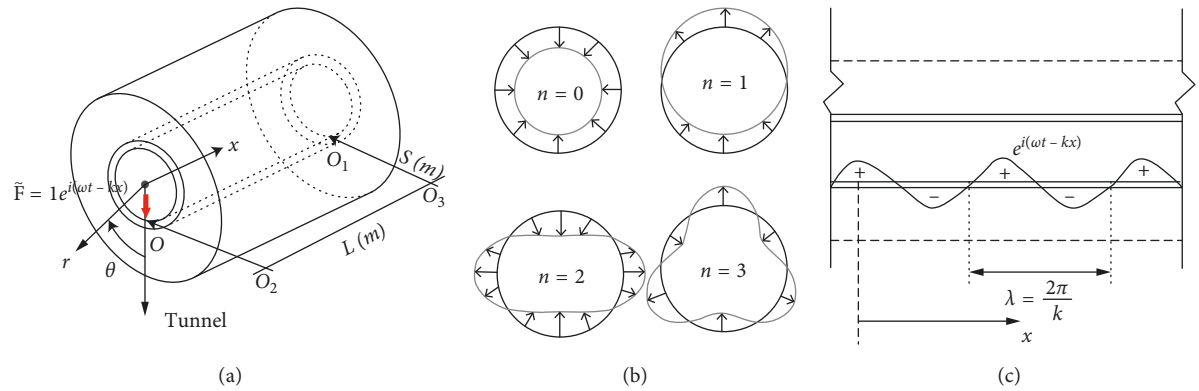

(a) (b) (c)

Figure 12: Decomposition of a radial line load and the resulting tunnel response: (a) the first four Fourier components in cross section; (b) schematic map of the steady response system of the tunnel structure; (c) spatial distribution along the x direction [31].

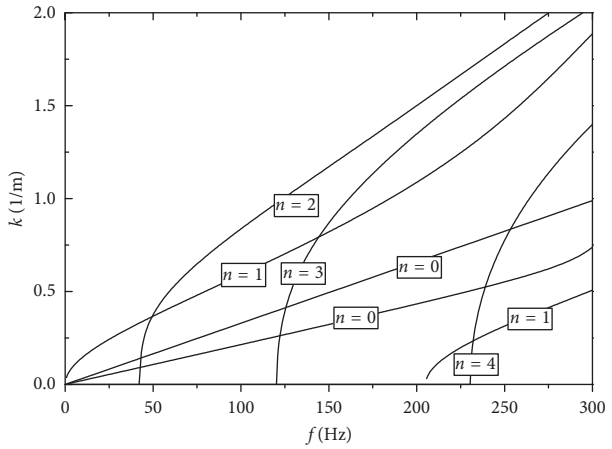

Figure 13: Dispersion curves of the power tunnel modeled as a hollow cylinder shell by the PiP model.

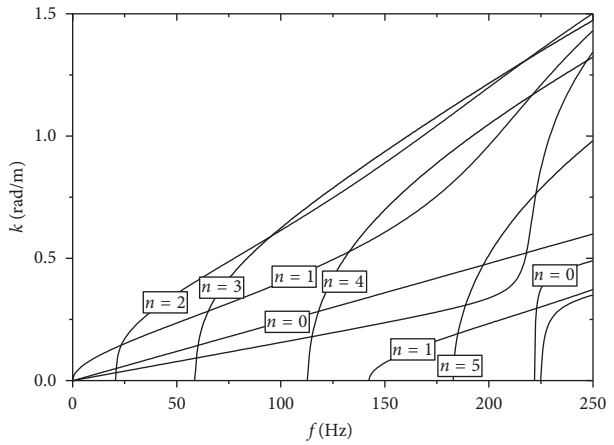

Figure 14: Dispersion curves of the subway tunnel modeled as a hollow cylinder shell by the PiP model.

Table 1: The dispersion analysis of the power tunnel mode frequency distribution and comparison with the field test results.

Number	1	2	3	4	5
Dispersion analysis	—	48	121	203	231
Field test	10.5	53	123	203	223

From Table 1, it is found that most mode frequency plotted in the field test can be found by dispersion analysis. However, 10.5 Hz has not matched, which can be clearly identified in the ambient vibration test. This may be caused by the coupling effect of the tunnel and surrounding soil, and the discussion will be continued in the following section.

5.3. The Subway Tunnel Dispersion Characteristics and Comparison with Field Test. Similarly, the dispersion of the subway tunnel is studied and plotted in Figure 14. Here, Young's modulus $E_t = 4.35 \times 10^4$ MPa, Poisson's ratio $\upsilon = 0.2$, density $\rho = 2500$ kg/m^3, the outer diameter = 6.2 m, and inner diameter = 5.5 m. The dispersion curves within the range of 0–250 Hz are obtained and plotted in Figure 14. And the cut-on frequencies of the propagation modes are compared with the field test results in Table 2.

Table 2: The dispersion analysis of the subway tunnel mode frequency distribution and comparison with the field test results.

Number	1	2	3	4	5	6	7	8	9
Dispersion analysis	—	21	58	115	—	142	183	222	225
Field test	10.75	23.5	—	119	128.5	142	176	203	233

From Table 2, the most cut-on frequencies from dispersion analysis can well match with the field test results. Similarly, the first mode frequency 10.75 Hz cannot be obtained by dispersion analysis which is close 10.5 Hz found in the field test of the power tunnel. It is further confirmed that the first mode comes from the surrounding soil or the coupled mode of the tunnel and surrounding soil.

From the analysis above, it can be found that, except the first mode, most of the modes natural frequency identified by the SSI-COV and NExT method are well consistent with the dispersion analysis results. It is proved that the method proposed in this paper has a good accuracy in mode frequency identification. And these modes can be used to track structural changes in tunnels by combing some inversion algorithms.

And the mismatch of the first mode at 10.5 Hz of the power tunnel and 10.75 Hz of the subway tunnel means that it may come from the surrounding soil or generate from the coupling of the tunnel and surrounding soil, and further analysis on the mechanism needs to be discussed in future and is not include here. What is more meaningful is that the first mode can be stability recognized, and it is the only one mode from the ambient test at night, and therefore, it very suitable for monitoring the natural frequency changes caused by soil excavation around the tunnel.

6. Conclusions

In this paper, in order to explore the mode frequency distribution of the tunnel and its automatic recognition method, the SSI and NExT methods are combined and applied to analyze the recorded response from ambient and hammer tests and have been proved very suitable for the mode frequency identification in the underground structure. The recognition results are also verified by dispersion analysis based on the PiP model, and some conclusions and suggestion for vibration-based monitoring are obtained as follows:

(1) The first-order mode frequencies can be clearly and stably identified by the ambient test, which has great application potential for monitoring the natural frequency changes caused by soil excavation around the tunnel

(2) Traffic environment excitation in the daytime will interfere with the recognition of structural mode characteristics and result in some false modes

(3) Most of the higher-order vibration modes can be found by the hammer test and are well consistent with the dispersion analysis results. It provides conditions for the analysis of the structural service condition more accurately by some inversion algorithms

Data Availability

The data used to support the findings of this study are available from the corresponding author upon request.

Conflicts of Interest

The authors declare that they have no conflicts of interest.

Acknowledgments

This research was supported by the National Key R&D Program of China under the grant no. 2018YFC0808702, National Natural Science Foundation of China under the grant nos. 51608379 and 51778476, and Shanghai Science and Technology Innovation Plan Funds under the grant nos. 17DZ1204203 and 18DZ1205200. These supports are greatly appreciated.

References

[1] H. Zhang, J. Chen, F. Fan, and J. Wang, "Deformation monitoring and performance analysis on the shield tunnel influenced by adjacent deep excavations," *Journal of Aerospace Engineering*, vol. 30, no. 2, article B4015002, 2015.

[2] J. Y. Han, J. Guo, and Y. S. Jiang, "Monitoring tunnel deformations by means of multi-epoch dispersed 3D LiDAR point clouds: an improved approach," *Tunnelling and Underground Space Technology*, vol. 38, pp. 385–389, 2013.

[3] T. Hao and C. D. F. Rogers, "Condition assessment of the buried utility service infrastructure," *Tunnelling and Underground Space Technology*, vol. 28, pp. 331–344, 2012.

[4] X. Y. Xie and L. Feng, "Real-time health monitoring system for power tunnel," in *Proceedings of Geo Congress*, pp. 3099–3108, Oakland, CA, USA, March 2012.

[5] D. Delaloye, M. S. Diederichs, and G. Walton, "Sensitivity testing of the newly developed elliptical fitting method for the measurement of convergence in tunnels and shafts," *Rock Mechanics and Rock Engineering*, vol. 48, no. 2, pp. 651–667, 2015.

[6] M. Wilcock, K. Soga, and P. Wright, "Monitoring mechanisms of tunnel lining settlement using instrumented bolts and conventional survey method: assessing neutral axis of longitudinal flexure," Unspecified, pp. 398–407, 2012.

[7] D. Bindi and B. Petrovic, "Seismic response of an 8-story RC-building from ambient vibration analysis," *Bulletin of Earthquake Engineering*, vol. 13, no. 7, pp. 2095–2120, 2015.

[8] D. Daniele and C. Gabriele, "Damage identification techniques via mode curvature analysis: overview and comparison," *Mechanical Systems and Signal Processing*, vol. 52-53, pp. 181–205, 2016.

[9] F. Musafere, A. Sadhu, and K. Liu, "Towards damage detection using blind source separation integrated with time varying auto-regressive modeling," *Smart Materials and Structures*, vol. 25, no. 1, article 015013, 2016.

[10] J. A. Goulet, C. Michel, Kiureghian, and A. D. Kiureghian, "Data-driven post-earthquake rapid structural safety assessment," *Earthquake Engineering and Structural Dynamics*, vol. 44, no. 4, pp. 549–562, 2015.

[11] J. P. Amezquita-Sanchez and H. Adeli, "Signal processing techniques for vibration-based health monitoring of smart structures," *Archives of Computational Methods in Engineering*, vol. 23, no. 1, pp. 1–15, 2016.

[12] Z. N. Ba and X. Gao, "Soil-structure interaction in transversely isotropic layered media subjected to incident plane SH waves," *Shock and Vibration*, vol. 2017, Article ID 2834274, 13 pages, 2017.

[13] A. Anvarsamarin, F. R. Rofooei, and M. Nekooei, "Soil-structure interaction effect on fragility curve of 3D models of concrete moment-resisting buildings," *Shock and Vibration*, vol. 2018, Article ID 7270137, 13 pages, 2018.

[14] B. Zhou, F. S. Zhang, and X. Y. Xie, "Vibration characteristics of underground structure and surrounding soil underneath high speed railway based on field vibration tests," *Shock and Vibration*, vol. 2018, Article ID 3526952, 13 pages, 2018.

[15] S. Gupta, M. F. M. Hussein, G. Degrande, H. E. M. Hunt, and D. Clouteau, "A comparison of two numerical models for the prediction of vibrations from underground railway traffic," *Soil Dynamics and Earthquake Engineering*, vol. 27, no. 7, pp. 608–624, 2007.

[16] B. Zhou, X. Y. Xie, Y. B. Yang, and J. C. Jiang, "A novel vibration-based structure health monitoring approach for the

shallow buried tunnel," *Computer Modeling in Engineering and Sciences*, vol. 86, no. 4, pp. 321–348, 2012.

[17] B. Zhou, X. Y. Xie, and Y. S. Li, "A structural health assessment method for shield tunnels based on torsional wave speed," *Science China Technological Sciences*, vol. 57, no. 6, pp. 1109–1120, 2014.

[18] A. Galvagni and P. Cawley, "The reflection of guided waves from simple supports in pipes," *Journal of Acoustical Society of America*, vol. 129, no. 4, pp. 1869–1880, 2011.

[19] A. B. Thien, H. C. Chiamori, J. T. Ching, J. R. Wait, and G. Park, "Model-based SHM: the use of macro-fibre composites for pipeline structural health assessment," *Structural Control and Health Monitoring*, vol. 15, no. 1, pp. 43–63, 2008.

[20] B. K. RaghuPrasad, N. Lakshmanan, N. Gopalakrishnan, K. Sathishkumar, and R. Sreekala, "Damage identification of beam-like structures with contiguous and distributed damage," *Structural Control and Health Monitoring*, vol. 20, no. 4, pp. 496–519, 2013.

[21] E. Leinov, M. J. S. Lowe, and P. Cawley, "Investigation of guided wave propagation and attenuation in pipe buried in sand," *Journal of Sound and Vibration*, vol. 347, no. 7, pp. 96–114, 2015.

[22] T. Vogt, M. Lowe, and P. Cawley, "The scattering of ultrasonic guided waves in partly embedded cylindrical structures," *Acoustical Society of America*, vol. 113, no. 3, pp. 1259–1272, 2003.

[23] M. Eybpoosh, M. Berges, and H. Y. Noh, "Sparse representation of ultrasonic guided-waves for robust damage detection in pipelines under varying environmental and operational conditions," *Structural Control and Health Monitoring*, vol. 23, no. 2, pp. 369–391, 2016.

[24] P. Andersen, *Identification of civil engineering structures using vector ARMA models*, Ph.D. thesis, Department of Building Technology and Structural Engineering, Aalborg University, Aalborg, Denmark, 1997.

[25] G. H. James, T. G. Carne, and J. P. Lauffer, "The natural excitation technique (NExT) for modal parameter extraction from operating structures," *International of Analytical and Experimental Modal Analysis*, vol. 10, no. 4, pp. 260–277, 1995.

[26] Y. C. Liu, C. H. Loh, and Y. Q. Ni, "Stochastic subspace identification for output-only mode analysis: application to super high-rise tower under abnormal loading condition," *Earthquake Engineering Structure Dynamics*, vol. 42, no. 4, pp. 477–498, 2013.

[27] P. van Overschee and B. L. R. de Moor, *Subspace Identification for Linear Systems: Theory-Implementation-Applications*, Kluwer Academic Publishers, Dordrecht, Netherlands, 1996.

[28] I. Goethals, L. Mevel, A. Benveniste, and B. D. Moor, "Recursive output only subspace identification for in-flight flutter monitoring," in *Proceedings of 22nd International Mode Analysis Conference*, Dearborn, MI, USA, 2004.

[29] B. Peeters and G. de Roeck, "Reference-based stochastic subspace identification for output-only mode analysis," *Mechanical Systems and Signal Processing*, vol. 13, no. 6, pp. 855–878, 1999.

[30] B. Peeters and G. D. Roeck, "Stochastic system identification for operational mode analysis: a review," *Journal of Dynamic Systems, Measurement, and Control*, vol. 123, no. 4, pp. 659–667, 2001.

[31] J. A. Forrest and H. E. M. Hunt, "A three-dimensional model for calculation of train-induced ground vibration," *Journal of Sound and Vibration*, vol. 294, no. 4-5, pp. 678–705, 2006.

[32] Y. Wang, X. C. Hang, D. Jiang, X. L. Han, and Q. G. Fei, "Selection method of Toeplitz matrix row number based on covariance driven stochastic subspace identification," *Journal of Vibration and Shock*, vol. 34, no. 7, pp. 71–75, 2015.

[33] R. E. Akins, "Cross-spectral measurements in the testing of wind turbines," in *Proceedings of 9th ASME Wind Energy Symposium*, New Orleans, LA, USA, 1990.

[34] J. H. Weng, C. H. Loh, J. P. Lynch, K. C. Lu, P. Y. Lin, and Y. Wang, "Output-only mode identification of a cable-stayed bridge using wireless monitoring systems," *Engineering Structures*, vol. 30, no. 7, pp. 1820–1830, 2008.

[35] C. H. Loh, K. J. Loh, Y. S. Yang, W. Y. Hsiung, and Y. T. Huang, "Vibration-based system identification of wind turbine system," *Structural Control and Health Monitoring*, vol. 24, no. 3, article e187, 2016.

[36] X. Sheng, C. J. C. Jones, and D. J. Thompson, "A theoretical study on the influence of the track on train-induced ground vibration," *Journal of Sound and Vibration*, vol. 272, no. 3–5, pp. 909–936, 2004.